Compact Capabilities: Developing and Evaluating a Field-Portable Neutron Resonance Capture Analysis System

by

Jill M. Rahon

B.S. International History, United States Military Academy, 2006
M.S. Nuclear Science and Engineering, Massachusetts Institute of Technology, 2016

Submitted to the Department of Nuclear Science and Engineering
in partial fulfillment of the requirements for the degree of

DOCTOR OF PHILOSOPHY

at the

MASSACHUSETTS INSTITUTE OF TECHNOLOGY

September 2024

Authored by:	Jill M. Rahon Department of Nuclear Science and Engineering August 23, 2024
Certified by:	Areg Danagoulian Associate Professor of Nuclear Science and Engineering, Thesis Supervisor
Accepted by:	Ju Li Chairman, Department Committee on Graduate Theses

Compact Capabilities: Developing and Evaluating a Field-Portable Neutron Resonance Capture Analysis System

by

Jill M. Rahon

Submitted to the Department of Nuclear Science and Engineering
on August 23, 2024 in partial fulfillment of the requirements for the degree of

DOCTOR OF PHILOSOPHY

ABSTRACT

Technological advances in the thorium fuel cycle and other advanced reactor concepts suggest their possible commercialization for nuclear power use in the next ten years. Although the thorium cycle shares many aspects with the uranium and plutonium fuel cycles, it introduces the requirement for the nondestructive assay of multiple isotopes (^{238}U, ^{232}Th, ^{233}U,^{235}U, or ^{239}Pu) in varied concentrations and chemical or physical forms. Current methodologies used for safeguarding the uranium and plutonium fuel cycles are either unsuitable for quantifying many of these isotopes or lack the ability to differentiate between them effectively. This work presents an experimental evaluation of a portable Neutron Resonance Capture Analysis (NRCA) system sensitive to isotopes with neutron capture resonances in the epithermal range (1-100 eV). NRCA is a technique traditionally used for nuclear data collection and nondestructive assay of archaeological materials, typically conducted at large accelerator facilities with beamlines in excess of ten meters. This research miniaturizes the system to a two-meter beamline using a portable deuterium-tritium neutron generator. It builds upon the foundation of a portable Neutron Resonance Transmission Analysis (NRTA) system, utilizing capture gamma rays to generate a signal, in contrast to the neutron transmission measurements of NRTA.

The NRCA technique is evaluated in this novel, portable configuration first using non-radioactive samples for optimization and then progressing to depleted uranium and thorium salt samples. Through a research partnership with Pacific Northwest National Laboratory, the technique was tested using highly enriched uranium, ^{233}U and high-assay, low-enrichment uranium (HALEU) samples. Field portability tests demonstrated its ability to operate safely in field conditions, with operator doses remaining well within occupational limits. The system was able to identify multiple mid- and high-Z materials by reconstructing their neutron resonance profiles in experiments as brief as 20 minutes. It successfully differentiated between nuclear fuel cycle isotopes in composite samples as small as 2 grams, with limited success in quantifying the areal densities of uranium and thorium. These results suggest that NRCA, especially when used in concert with NRTA and other neutron-interrogation techniques, has the potential to rapidly and nondestructively quantify and characterize isotopes of interest in support of safeguards material accountancy.

Thesis supervisor: Areg Danagoulian
Title: Associate Professor of Nuclear Science and Engineering

Acknowledgments

"If the neutron did not exist, it would need to be invented."
Bertram Brockhouse, 1994 Nobel Laureate in Physics

I would like to acknowledge and profusely thank:

- my advisor, Professor Danagoulian, and my committee members for the guidance and the leeway to take my research wherever it might lead.

- the MIT faculty and staff for their tireless work supporting, instructing, and mentoring students.

- the MIT Environmental Health and Safety Team and MIT Bates Research and Engineering Center Team for their professionalism and 'we'll get it done' approach to any problem.

- the National Nuclear Security Administration and the Pacific Northwest National Laboratory for supporting this work and sharing the talents of their outstanding scientists and administrators.

- the West Point Department of Physics and Nuclear Engineering and Army Functional Area 52 for their faith in my abilities and for the time and support to make this happen.

- my friends, labmates, and teammates from MIT (both the first and second time), from USMA Class of 2006, from the Army (including the 6-101 Avn Regt and the Pachyderms), and those friends from back home.

- my big, loving, weird family, including my wonderful parents who taught me anything is possible if you do the work, and to my sisters and cousins, and to my aunts and uncles, and nieces and nephews for their loving support. A significant thank you goes to the Ranalli Family for everything. Family is one of nature's greatest masterpieces.

- my unbelievable husband who not only supported us and kept us going, but challenged me to never accept anything less than the complete solution, the best product or the whole truth. I love you.

- and finally, I'd like to thank Kit and Charlie for reminding me what pure love is and for providing a daily example of insatiable curiosity, ingenuity, and sheer scrappiness: the three most important traits to carry one through a dissertation.

Contents

List of Figures

List of Tables

Chapter 1

Introduction

Interest in thorium as a source of nuclear energy is increasing worldwide as industry and governments seek abundant, low-carbon energy solutions to meet growing demand. The Shanghai Institute of Applied Physics (SINAP) received a state operating license in July 2023 for its experimental liquid fuel thorium molten salt reactor (TMSR-LF1), three years ahead of schedule [1]. The SINAP solid fuel, once-through fuel cycle design is already in the large-scale production phase [2], with expectations of widespread commercialization by 2030 for both designs (assuming successful prototype tests) [3]. In North America, Chicago-based Clean Core Thorium Energy is in pre-licensing review with Canadian regulators to produce blended thorium and high-assay, low-enriched uranium (HALEU) fuel for use in existing CANDU reactors as early as 2025 [4]. One of the first uses of thorium for commercial power generation, the Clean Core fuel will improve reactor performance, safety, and cost effectiveness [5]. The proposed United States Thorium Energy Security Act of 2022 (S.4242, 117th Congress) will require the Department of Energy to preserve existing inventories of uranium-233 to facilitate the development of thorium-based energy production [6]. Clearly, thorium as a nuclear fuel is an emerging technology with a high likelihood of employment around the world.

With the promise of thorium and its associated advanced reactor concepts comes the duty of ensuring its peaceful use. Accountancy of fissile and fertile isotopes is as critical for advanced reactor fuel cycles as it is for traditional uranium and plutonium fuel cycles – thorium fuel cycle products can be misused to produce a nuclear weapon. Although aspects of the thorium fuel cycle grant some inherent proliferation resistance [7], [8], these barriers can be circumvented by a motivated proliferator (see 1.2 for a full discussion), highlighting the need for a robust safeguards protocol. Safeguarding the thorium fuel cycle requires a layered strategy of appropriate policy and technologies for monitoring and inspections to rapidly detect fissile material diversion and other proliferation indicators [9]. The International Atomic Energy Agency (IAEA) has highlighted its capability to develop and perform process monitoring for advanced reactor concepts (e.g., small modular reactors, microreactors, molten salt or pebble fuel) as one of its core focus activities and a resource utilization priority [10].

However, safeguards technology for on-site inspections of thorium-based nuclear fuels requires significant development to match the pace of commercialization of these reactors. A 2021 multi-US national laboratory scoping study [11] identified several technological gaps that prevent the safeguards community from verifying the thorium fuel cycle to the extent that it currently does for plutonium and uranium fuels. While aspects of the thorium fuel cycle are analogous to those of uranium, the varying fundamental design types for reactors and the associated diversity of fuel isotopics and chemical arrangements necessitate a broad array of verification techniques. Furthermore, the physical attributes of thorium, the fissile driver isotopes, and their progeny in mixed samples can obscure assay (*e.g.* the similar gamma spectra of uranium-232 and thorium-232.) Several important safeguards measurement concepts require development or refinement to keep pace with the commercialization timeline of thorium reactors.

Non-destructive assay (NDA) fulfils a critical component of the safeguards regime by detecting and analyzing signals emitting from a sample and drawing inferences about the isotopics and quantities of the material [12]. Neutron resonance capture analysis (NRCA) is an established NDA method in large beamline facilities with uses primarily in elemental analysis of archaeological objects [13] and cross-section determination, but gradually expanding into forensic uses [14]. By time-correlating γ-ray emissions with incident neutron energy, it is possible to measure isotopic signatures in thorium fuel cycle products beyond the information gained through passive assay. NRCA has the ability to constrain and enhance the results from other assessment techniques, namely in the cases of neutron poisons, irregular geometries, and overlapping resonance structures.

The main goal of this research is to explore the feasibility of performing NRCA with a portable neutron source, which is a novel setup and application. In this configuration, the primary challenge was to reduce the background to a level that permits resolution of isotopic content sufficient for use in practical scenarios. This research has evaluated the feasibility of NRCA in the context of the thorium fuel cycle; however, it is a technique with a broad array of applications. The use of NRCA as an isotopic assessment method in a portable experimental setup represents a new step in on-site, active assessment for nuclear materials safeguards.

1.1 Thorium-based Nuclear Energy

Thorium-232 is a naturally occurring fertile isotope that accounts for 100% of elemental thorium in the Earth's crust[1]. It is more than three times more abundant on Earth than uranium, the element currently used for nuclear power generation [15]. Thorium is found in small amounts in soils and rocks worldwide, is geologically concentrated in the rare-earth-bearing mineral monozite, and is traditionally removed and treated as mildly radioactive waste. However, its upcoming importance as a nuclear fuel has resulted in recent commodification [16] and interest as a strategic asset [6].

Nuclear energy can be roughly classified into two broad categories: energy derived from naturally occurring primordial nuclides such as ^{235}U and energy from fissile nuclides that are bred by neutron capture on fertile materials. ^{232}Th is a fertile isotope, incapable of sustaining a fission chain reaction in a reactor, but capable of being transmuted into fissile uranium-233 under neutron bombardment as

$$^{232}_{90}\mathrm{Th} + n \rightarrow {}^{233}_{90}\mathrm{Th} \xrightarrow{-\beta} {}^{233}_{91}\mathrm{Pa} \xrightarrow{-\beta} {}^{233}_{92}\mathrm{U}\cdot \tag{1.1}$$

The source of transmutation neutrons in 1.1 must initially be provided by a driver — usually a fissile isotope (^{233}U,^{235}U, or ^{239}Pu) or possibly a spallation source or accelerator driven system [17]. In a simple example, the ^{233}U bred in a previous thorium reactor cycle is comingled in the same reactor core as fertile ^{232}Th, providing the neutron source through fission until enough thorium is transmuted to ^{233}U to sustain the reaction.

A thorium reactor characteristic of particular importance for both the power generation and the safeguards communities is the potential for a high (>1) breeding ratio of ^{233}U, depending on the design and operation of the reactor. A breeding ratio greater than one results in more ^{233}U being produced than burned and is therefore present in the outflow stream. This is a beneficial, if not a key feature of recycling-based fuel concepts, in which ^{233}U from a previous cycle provides the driver for the next [18]. It also highlights a proliferation concern, as ^{233}U is a fissile material capable of being used in a nuclear weapon. The IAEA has designated 8 kg of ^{233}U as a significant quantity, the same significant mass as plutonium and less than half the mass of ^{235}U [19]. The implications of ^{233}U not only in waste streams but also in chemically separated process flows that feed the next reactor cycle underscore the need for a robust safeguards protocol.

---

[1] Both the thorium and uranium decay series pass through other isotopes of thorium (^{228}Th, ^{230}Th, ^{234}Th) however their mass ratio is negligible compared to quantities of Th-232

After neutron capture on ^{232}Th, the half-life of ^{233}Th is 22.3 minutes, followed by ^{233}Pa with a half-life of 27 days until it decays to ^{233}U [17]. If the ^{233}Pa remains in the neutron-rich environment, the reaction

$$^{233}_{91}\mathrm{Pa} + \text{fast } n \rightarrow {}^{232}_{91}\mathrm{Pa} + 2n \xrightarrow{-\beta} {}^{232}_{92}\mathrm{U} \tag{1.2}$$

is possible for neutrons in excess of 6 MeV (peaking at a cross section of 2 barns at 11 MeV) [15]. Table A.1 in Appendix A shows the percentages of neutron energy flux above and below 6 MeV for several thorium reactor concepts. ^{233}U also has a low probability $(n,2n)$ reaction for fast neutrons that proceeds as

$$^{233}_{92}\mathrm{U} + \text{fast } n \rightarrow {}^{232}_{92}\mathrm{U} + 2n. \tag{1.3}$$

Furthermore, ^{230}Th is a product of the ^{238}U radioactive decay series and exists in secular equilibrium in natural uranium at 17 ppm [20]. In reactors containing ^{238}U or thorium mined from deposits bearing uranium, two subsequent radiative captures beginning with ^{230}Th and proceeding as

$$^{230}_{90}\mathrm{Th} + n \rightarrow {}^{231}_{90}\mathrm{Th} \xrightarrow{-\beta} {}^{231}_{91}\mathrm{Pa} + n \rightarrow {}^{232}_{91}\mathrm{Pa} \xrightarrow{-\beta} {}^{232}_{92}\mathrm{U}. \tag{1.4}$$

There is also a possible $(n,2n)$ reaction on ^{232}Th, which will enter the above equation at ^{231}Th and proceed accordingly [21][2]. The cross sections for the two radiative captures in Eqn. 1.4 are significantly higher than the $(n,2n)$ reactions, making ^{230}Th contamination an issue if the reduction of ^{232}U is desired. The decay chain of ^{232}U, which is available in Appendix B-1, proceeds through several daughter isotopes with high specific activities, including ^{208}Tl, which emits a strong 2.6 MeV γ-ray. ^{232}U is chemically identical to its valuable and fissile fellow uranium isotope, ^{233}U. If the ^{232}Pa is not removed from the reactor core or breeder blanket prior to decay, the harvested ^{233}U will be contaminated with ^{232}U, necessitating costly isotopic separation to remove it [22]. ^{232}U as a contaminant has implications for the reprocessing and handling of spent fuel, as well as for the proliferation resistance of the thorium fuel cycle, discussed in Section 1.2.1.

Despite the potential for production of the strongly radioactive ^{232}U, thorium as a source of nuclear energy has several advantages over the uranium fuel cycle. In this research, the thorium fuel cycle refers to the nuclear power derived from the ^{232}Th→^{233}U process and the uranium cycle is defined as the ^{238}U→^{239}Pu process. As a result of its natural isotopic abundance and its role as a fertile isotope, thorium

---

[2] Only the principle ^{232}U production routes for the thorium fuel cycle are described here; there are other options that become more probable in uranium or MOX cycles

Table 1.1: Fuel cycle metrics: uranium vs. thorium breeder reactors (data from [15], [18])

Fertile Isotope	Fissile Isotope	Regeneration Factor (η_{thermal})	Regeneration Factor (η_{fast})	Delayed Neutron Fraction (β)
^{238}U	^{239}Pu	2.01	2.45	0.0020
^{232}Th	^{233}U	2.24	2.30	0.0026

does not need isotopic enrichment to be fuel ready, as is the case for uranium reactor types that require some amount of ^{235}U enrichment (however, the driver isotope does require some processing to obtain from spent fuel). Thorium lends itself to a multitude of reactor designs, including molten salt (such as SINAP's TMSR-LF1), a fusion- or accelerator-driven subcritical reactor, a gas-cooled high-temperature reactor, a heavy water CANDU-like reactor (HWR), or as a fuel blanket in a light water reactor (LWR) [15]. The selection of reactor type is driven by commercial and national objectives, such as ease of maintenance, the ability to use process heat for hydrogen production, or access to natural resources, as in the case of India's massive thorium deposits [23]. Although the diversity of reactor type allows greater access to nuclear power, each reactor design has its own fuel chemistry, isotopics, and physical form, potentially requiring multiple safeguard technologies to test a molten salt versus a solid fuel pellet or TRISO ball.

Thorium also has isotopic advantages over uranium that enhance its suitability as a reactor fuel. Table 1.1 shows selected isotopic characteristics relevant to breeder reactors. Like thorium, fertile ^{238}U is converted to fissile ^{239}Pu under neutron bombardment in a similar double β decay process, but with less efficiency than thorium. The larger delayed neutron fraction of ^{233}U improves control of its core reactivity compared to ^{239}Pu. For sufficient fissile material breeding, the neutron regeneration factor[3], η, must be above a value of 2.2. Table 1.1 shows that the thermal neutron regeneration factor for ^{239}Pu fission is insufficient for breeding, whereas ^{233}U has a good neutron breeding economy at both ends of the spectrum [15]. To avoid oversimplification, there are several reactor parameters that influence the breeding ratio and economy of a reactor (e.g. hardening the neutron spectrum away from thermal and into the resonance region of ^{232}Th preferences radiative capture there and not on fissile or structural materials [24].) These factors demonstrate the versatility of the thorium fuel cycle, enhancing its attractiveness for diverse energy production applications.

---

[3] η is defined as the number of fission neutrons emitted per neutron absorbed in the fuel

Thorium fuel cycles also provide the opportunity to reduce long-lived nuclear waste products. After the first ten years of decay time, the spent fuel waste from the uranium-plutonium fuel cycle has over 10^3 times higher actinide radiotoxicity per gigawatt hour than the thorium-uranium cycle and 10^4 times higher after 300 years [23]. This is due in part to the six mass units between ^{239}Pu and ^{233}U (two protons and four neutrons), which greatly contribute to the uranium-plutonium cycle generating a significantly higher fraction of long-lived transuranic waste (TRU) from nuisance neutron captures during core life. The advantages of thorium as a reactor fuel are compelling enough to motivate renewed interest and suggest a high likelihood that it will be deployed in future reactors.

1.1.1 The Thorium Fuel Cycle

The term *thorium fuel cycle* refers to any of the many nuclear fuel cycle designs which have at least one stage utilizing natural thorium or the ^{233}U derived from thorium [25]. Entire stages in the fuel cycle may not involve the use of thorium at all, such as those devoted to the production of the fissile driver isotope required to transmute ^{232}Th in a later step, as in the case of the multistage concept for Indian reactors, shown in Table 1.2. Fuel cycles can be classified as open or closed; with an open cycle referring to one in which fuel is used only once and then disposed of [16]. Therefore, a closed cycle implies some amount of reprocessing of spent fuel to support future cycles.

A 2014 study identified 40 potential reactor designs in development, including 15 thorium-based cycles (the reader is referred to [31] for a comprehensive listing). In an effort to downselect the diverse field of thorium reactor types and their associated fuel cycles to better identify safeguards technology requirements, 1.2 presents the three leading fuel cycles selected by a tri-national lab study [25]. These cycles are most likely to be implemented on the basis of their technical maturity and ability to meet national or commercial objectives. Inspection of 1.2 reveals the diversity of reactor type and fuel form that thorium-based energy could take within the next decade. It should also be noted that China and the United States, two of the countries leading thorium energy development, are already nuclear weapon states (NWS). The need to safeguard these facilities arises not only from the export potential of reactor designs to non-NWS, but also from China and the United States' Voluntary Offer Agreements with the IAEA, permitting the implementation of safeguards in NWS nuclear facilities [25].

Table 1.2: Leading thorium fuel cycle candidates and fuel forms

Fuel Cycle Type [25]	Reactor Type	Country Developing	Fuel Form
Once-thru or continuous recycle	Pressurized water reactor (PWR)	Norway (ThorEnergy) USA (WASB, historic)[27]	Stage I: Th-Add (Th-U MOX) [26] pellets, fuel pins Stage II: Th-Pu MOX pellets, fuel pins
Multistage cycle, resulting in cont. recycle of ^{233}U	Heavy water reactor (Stage I) -Breeds Pu for Stage II Na-cooled fast breeder (II) -Breeds ^{233}U and Pu Advanced heavy water reactor (III) -^{233}U recycle	India (Bhabha Atomic Research Center)	Stage I: Enriched U Stage II: U-Pu MOX driver ThO$_2$ blanket Stage III: Th-Pu MOX ^{233}U-Pu MOX
Continuous recycle of ^{233}U (ThorCon planned once-thru) [29]	Molten salt reactor -graphite moderated	China (TMSR-LF1)	fuel: LiF-BeF$_2$-ZrF$_4$-UF$_4$-ThF$_4$ (U is 19.7% enr HALEU) coolant: FLiBe / FLiNaK [28]
		USA/Indonesia (ThorCon)	NaF-BeF$_2$-ThF$_4$-UF$_4$ [28] (76-12-10.2-1.8 mol%) (U is 19.8% enr HALEU)
		USA (Flibe Energy LFTR)	fuel: 2LiF$_2$-BeF$_2$-^{233}UF$_4$ [30] blanket: 2LiF$_2$-BeF$_2$-^{232}ThF$_4$

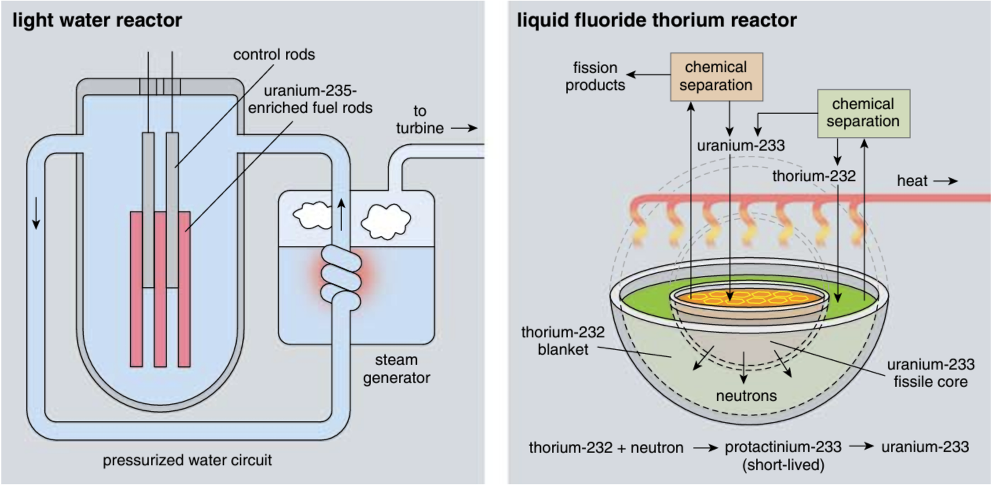

Figure 1-1: Schematic of a light water reactor versus a liquid fluoride thorium reactor [23]

1.1.2 Molten Salt Reactors

Thorium lends itself particularly well to a liquid fuel, molten salt reactor (MSR) concept. A brief discussion of MSR design and fuel forms is beneficial in understanding their impacts on safeguards applications. The goal of an MSR is to “improve thorium resource utilization, minimize nuclear waste, promote nuclear nonproliferation and finally realize a fully closed Th-U fuel cycle [18]." Design types may include solid fuel concepts with liquid coolant (as in the Chinese TMSR-SF design), liquid fuel with the fuel dissolved in the coolant, and liquid fuel cooled by a separate loop of non-fissile liquid coolant [32]. Fig. 1-1 illustrates the concept of a liquid fuel MSR with fissile isotopes dissolved in a fluoride or chloride coolant salt core, which acts as both the fuel matrix and the heat transfer fluid [15]. In the example of Fig. 1-1, a two-fluid MSR, a blanket salt laden with fertile ^{232}Th uses neutrons escaping from the core to transmute ^{233}U. In this illustration, both the core and blanket are circulated through chemical processing loops; the core circulation removes fission products, which prevents a build-up of gaseous fission product accumulation as well as neutron poisons. The blanket salt is chemically processed to remove ^{233}Pa, which is left in a holding tank until it decays to ^{233}U and then added to the fuel salt to maintain criticality. The heat exchanger loop that carries heat from the core to an energy conversion system is not pictured, which can be Rankine (steam), Brayton (gas), or supercritical fluid [15]. This is only one example; MSR variants can vary greatly in design, refueling timeline, and processing frequency.

MSR reactors have several advantages over traditional light water reactors (LWR). Chief among them are the safety features, including a low operating pressure, with most experimental designs in the range of 0.025 - 1 MPa [28]. This reduces the size of the containment facilities and prevents accidents from pressure vessel failures. Likewise, the fuel is already in a 400 -700 °C molten state, eliminating the problem of fission product leakage from the cladding, as well as hydrogen explosions from zirconium hydride formed during a loss of coolant accident. The option of removing fission products during operation improves reactivity control and also reduces core radioactivity in the event of an accident [33]. Many designs incorporate a drain plug that melts during an overheating scenario, allowing the core to flow into a subcritical geometry cooling tank. The MSR design concept is suitable for thermal or fast neutron spectra, with some concepts designed for breeding ^{238}U to ^{239}Pu or incinerating TRU [28]. MSRs may also offer economic and environmental benefits compared to LWRs, details of which go beyond the focus of this study but can be found in [15], [23]. The discussion of the proliferation advantages of MSRs will be elaborated in further detail in Section 1.2.1.

From a material and safeguards accounting perspective, the fuel and fuel handling design of MSRs is of critical importance. A molten salt is a chemical compound of an acid and an alkali that is liquid at high temperature [34]. The forefront salt of choice for many reactor designs is currently $LiF-BeF_2$ (written and pronounced "FLiBe"), into which nuclear material can be dissolved as molten fluoride salts (ThF_4, UF_4, PuF_4, etc. [35].) FLiBe is a eutectic compound[4] that is chemically stable, can dissolve nuclear isotopes of interest, and has high heat transfer capability and a low vapor pressure— properties which make it a leading candidate for use in MSRs. $LiF-NaF-KF$ (“FLiNaK") is similarly suitable with the benefit of omitting chemically toxic beryllium and is the coolant salt for the Chinese TMSR-LF1 design [28]. Naturally occurring lithium, present in both salt types, is 7.42% ^{6}Li, which has a high capture cross section for neutrons beginning in the epithermal regions. To improve neutronics and decrease tritium production, many reactor designs will require the use of isotopically separated lithium, increasing the price of the salt [35]. Molten salt reactors (MSRs) designed to produce ^{238}U from ^{239}Pu in a fast spectrum may opt for chloride salts instead, as fluoride excessively moderates neutrons [28].

Despite notable progress, MSRs have many development challenges remaining. These include the demand for exceptionally corrosion resistant materials capable of withstanding high temperatures (likely nickel-based alloys, such as Hastelloy N [15].) In addition, advances are needed in chemical separation processes and equipment suitable for high-radiation environments. The search for more cost-effective methods for lithium isotopic separation remains ongoing. Therefore, safeguard de-

---

[4] Eutectic compound: one in which the compound melting point is lower than the melting points of the constituents

velopers should incorporate redundant capabilities and adaptable procedures to be ready to respond to changes in salt chemistry, fuel handling, and reactor operations.

1.2 Safeguards

The International Atomic Energy Agency (IAEA) safeguards system is the suite of technology, legal instruments, and administrative procedures used in accordance with safeguards agreements to verify that States do not acquire nuclear material and facilities for prohibited purposes [19]. In accordance with Article III.1 of the Treaty on the Non-Proliferation of Nuclear Weapons (NPT), party States (as well as those with item-specific agreements) must accept the application of safeguards "on all source or special fissionable material in all peaceful nuclear activities... for the exclusive purpose of verifying that such material is not diverted to nuclear weapons [9]." The comprehensive safeguards agreements authorized in the NPT are enhanced by verification measures under the Additional Protocol, which provides for an inspection regime to ensure that States uphold their obligations.

These inspections are intended to verify the non-diversion of fissile materials through the accountancy of material balances, random sampling at various phases of a fuel cycle, and focusing on procedures from which weapons materials could be made or diverted [9]. On-site inspection techniques are constrained by a verification level, a predetermined quantification of confidence that a particular method can identify an event of safeguards interest [19]. The verification level and other statistical concepts are used to assess uncertainty in inspections measurements when formulating conclusions about estimates, trends, or irregularities. Nuclear reactors and related fuel cycle facilities are also required to undergo design information verification by the International Atomic Energy Agency (IAEA) throughout their entire operational life. [36].

The term *safeguards technology* is the physical equipment and measurement techniques used by the IAEA to determine material accountancy at a nuclear facility [25]. It can refer to an entire field-deployable system or individual detectors, investigation methods, data analysis techniques, and software. Thorium safeguards are therefore specific measures (physical or computational) intended to assess materials unique to the thorium fuel cycle. The IAEA classifies these isotopes as either source ($^{\text{nat}}$Th, $^{\text{nat}}$U) or direct use materials (^{233}U, ^{235}U, ^{239}Pu) [19].

Table 1.3: Comparison of dose, decay heat, and spontaneous fission rate for weapon candidate isotopes

Isotope	E [rem/5kg/h]†	P_{DH} [W kg^{-1}]	S_{f} [s^{-1} kg^{-1}]
^{233}U, 0.1% ^{232}U	12 [20]	2 [40]	2 [41]
^{233}U, 2.4% ^{232}U	300 [20]	15 [40]	30 [41]
HEU (94% ^{235}U)	0.003 [42]	1×10^{-4} [43]	0.6 [20]
WGPu (94% ^{239}Pu)	0.001 [44]	2.4 [43]	2.5×10^{4} [20]

† Effective dose at 0.5 m, 1 year after chemical processing or separation, assuming whole body exposure and a quality factor of 1.
Note: Numbers in square brackets are citations for individual values

1.2.1 Proliferation Resistance and The Need for Nuclear Safeguards

It is worthwhile to discuss the degree of inherent proliferation resistance afforded by thorium-fueled reactor concepts. A possible benefit of the thorium fuel cycle, frequently touted by advocates [7], [37], [38], is the lack of access to ^{233}U as a weapon material due to ^{232}U contamination. However, the degree of this nonproliferation advantage depends on the implementation of the reactor and recycle systems. The characteristics of the thorium fuel cycle and any other design features of nuclear systems that impede the diversion or clandestine production of nuclear material are classified by the IAEA as *proliferation resistance* [39]. Especially in the case of non-NWS possessing a thorium reactor and a desire to leave the NPT, it is beneficial for the nonproliferation regime to have dual-use nuclear materials exist in the most undesirable state for potential weapons production.

The ^{233}U generated during the use of thorium-based reactors is an attractive nuclear weapon material with a critical mass comparable to ^{239}Pu and a low spontaneous fission rate [20]. Any isotope capable of a sustained fast neutron chain reaction can, in principle, be used in a nuclear weapon. However, a material can be more or less suitable for weapons use considering three aspects of the isotope's physical characteristics: heat generation, spontaneous neutron generation, and dose rate– Table 1.3 presents these aggregated data for three weapons candidate isotopes. As Table 1.3 suggests, increasing quantities of ^{232}U have dramatic impacts on both the decay heat and the dose to workers or nuclear weapon components.

^{232}U is an isotope generated from the nuisance transmutation of various actinides present in all fission reactors, as introduced in Section 1.1 and Eqns 1.2, 1.3, and 1.4. It has a half-life of 69 years, proceeding via the thorium decay series through several short-lived, α- and β-emitting isotopes (where each daughter isotope is in a quantity approximately in secular equilibrium with the parent ^{233}U). Near the end of the decay chain (available in Fig. B-1) there is a 36% branching ratio to ^{208}Tl, which emits a 2.6 MeV γ-ray that is difficult to shield. The daughter isotopes build in over time after reactor discharge, so the dose rate of ^{232}U-contaminated ^{233}U after ten years is tripled from what it was at one year [20]. The concentration of this impurity depends on multiple reactor parameters and post-processing steps, although anywhere in the range of parts per billion to a few percent is reasonable based on thorium research history and neutronics simulations [20]. 2.4% was selected for one of the two ^{232}U concentrations in Table 1.3 as it results in the dose rate to personnel that the IAEA considers a material 'self-protecting' [43], [45]. In this ratio, a 5 kg sphere of ^{233}U/^{232}U would result in a dose of 100 rem h^{-1} to a worker at a distance of a half meter, inducing hematopoietic changes in the first half hour and severe illness or death in three hours.

Radioactivity from ^{232}U also creates a localization signal for a possible clandestine weapon and affects the high explosives placed around the sphere during the assembly of the weapon. These explosives have a tolerance of 1×10^8 Roentgen [46] before degrading due to gas evolution, crumbling, and other effects of ionizing radiation[5]. At 2.4% U-232, the high explosives would degrade in 1500 hours one year after uranium was removed from the reactor and in 550 hours at ten years [40]. Lawrence Livermore National Laboratory determined that the surface temperature of a 5 kg bare sphere of ^{233}U would exceed 100 °C at 3 W of decay power, which is reached by a contamination of 0.05% ^{232}U immediately upon reactor removal [40]. It is this excess heat generation and dose rate to personnel and weapons components that thorium cycle proponents highlight as a deterrent to would-be diverters using contaminated ^{233}U inside a nuclear weapon.

Although the presence of ^{232}U serves as a barrier to inappropriate use of ^{233}U produced in thorium cycles, it is not insurmountable. A party with access to a thorium reactor and the desire for proliferation may not consider the human dose hazards a significant concern and may be content with the short shelf life of a weapon contaminated with ^{232}U. One key advantage of the thorium fuel cycle lies in the utilization of ^{233}U generated to fuel subsequent cycles. As a result, reactor facilities are motivated to take steps to minimize ^{232}U levels, thereby reducing worker exposure. This is certainly possible: India's Bhaba Atomic Research Center reported a per-person dose of 0.2 rem (whole body) incurred by workers over 100 hours in 1993 who were fabricating a 0.6 kg ^{233}U reactor fuel assembly with 3 ppm

---

[5] For the purpose of considering high doses of gamma radiation, a rad, rem and Roentgen are effectively equal.

^{232}U [47]. This ^{233}U was well below the self-protection limits for anti-proliferation, as evidenced by its safe handling. Table A.1 in Appendix A demonstrates how the fast neutron flux responsible for many ^{233}U production pathways can be mitigated in an HWR by moving the breeding thorium from the fuel to a target channel. In the case of single-use thorium reactors that intentionally allow ^{232}U contamination as a protection measure, a 2012 study identified two chemical separation processes that can be employed with standard nuclear chemistry laboratory equipment to remove ^{233}Pa prior to its decay to pure ^{233}U [22]. The execution of this process could be carried out with the knowledge of the reactor operator or, potentially, covertly by a third party.

The detrimental aspects of ^{232}U alone are insufficient to deter the misuse of nuclear material; however, there are additional design solutions that may enhance proliferation resistance. The concept of 'denatured' thorium reactors, especially as applied to TMSR designs, began as a proliferation resistance engineering strategy in the 1970s [48]. Similar to the concept of plutonium 'spiking' [49] in which weapons-usable ^{239}Pu is made less attractive with the addition of ^{238}Pu and ^{240}Pu, denatured ^{233}U requires significant amounts of processing for use in a weapon. In this concept, fresh thorium fuel is blended with depleted uranium that does not transmute to the same extent as ^{232}Th. When the spent fuel is removed for disposal or reprocessing, the remaining ^{238}U cannot be chemically separated from the fissile ^{233}U, requiring a significant increase in workload to make it pure enough for a nuclear device [50][6]. Uranium may be considered denatured if the final mass fractions satisfy the inequality:

$$\frac{M_{\text{U-233}} + 0.6M_{\text{U-235}}}{0.12M_{\text{U-total}}} < 1 \tag{1.5}$$

which in practice is an approximately 32:1:4 ratio of ^{232}Th, ^{235}U, and ^{238}U, respectively, in the fresh fuel of a notional single-fluid MSR [52].

Denatured MSRs remain of interest today. Ahmad, *et al.* conducted a modeling study of the above fuel ratios using neutron transport and point depletion codes. They determined that with annual replenishment fuel additions of ^{235}U and ^{238}U, a denatured MSR could operate at 200 MWe for 30 years with only non-chemical removal of fission products (e.g., a gas bubbling system)[52]. Without the need for online chemical processing to remove fission products and neutron poisons

---

[6] Lovins notes that this bar is still not high enough: at approximately 12% ^{233}U 'enrichment' as opposed to the traditional isotopic separation problem of 0.7% ^{235}U natural enrichment, 85% of the separative work has been done for the nefarious party [51]. He recommends rather to approach safeguards from a predominantly politically-oriented solution and not a technical one, this research advocates for a fusion of both.

(including protactinium), it becomes significantly more difficult for proliferators to access ^{233}U or ^{235}U without including the added ^{238}U.[7] Denaturing impacts the reactivity, breeding ratio, and overall neutronics of a reactor and is not suitable for all designs. In the case of converter reactors focused solely on consuming self-produced ^{233}U rather than fueling the subsequent cycle, there exists a design margin to compensate for the reduced reactivity arising from ^{238}U additions [28]. The Japanese FUJI reactor concept is a single-fluid MSR in development by the International Thorium Molten-Salt Forum. It is based on the design of the Oak Ridge denatured MSR and could operate on denatured fuel [28]. ThorCon's fuel, which will have only 22 ppm ^{232}U after 8 years, is denatured by design from the initial load and progressively builds an increasing ratio of ^{238}U throughout use [49]. Therefore, it is possible that the assay of ^{238}U in thorium fuel for denaturation purposes becomes a safeguards requirement.

The methodologies of proliferation resistance and physical protection, which consider value and attractiveness of weapons materials in relation to barriers to access, are important design and operation criteria for all reactor concepts. However, the classification of 'proliferation resistant' does not replace the role of safeguards, which actively verify that States party to the Non-Proliferation Treaty or item-specific agreements are meeting their legally binding responsibility to prevent the misuse of nuclear materials [54]. The addition of denatured fuel blends or other design features meant to enhance nonproliferation features may become part of safeguards processes and inspections.

1.2.2 Pathways

Diversion path analysis is the study of the methods through which a 'nuclear material subject to safeguards could be diverted from a facility or by which facilities could be misused for the undeclared production or processing of nuclear material [36].' An identification of a pathway informs an IAEA technical objective to either deter or detect a particular misuse case, which in turn drives how, where, and when safeguards measures should be applied. This analysis also allows safeguards managers to prioritize the implementation of measures based on the severity and risk of a proliferation pathway. Through the identification of pathways in the thorium fuel cycle, we can assess the need for technology development and testing. To guide this initial research for portable, active neutron interrogation for the thorium fuel cycle, we will analyze pathways that influence fresh fuel source isotopes.

---

[7] Plutonium is generated in the reactor from the addition of ^{238}U, however, to a lesser extent than a traditional LWR [52]. Bathke, *et. al* discusses the proliferation implications of and solutions for plutonium produced in thorium cycles in [53].

Fissile isotopes are largely the subject of safeguards material accountancy measures; however, the quantity and ratios of source isotopes (^{232}Th and ^{238}U) are also of importance due to their potential to transmute into fissile material. The need to distinguish two source isotopes from one another is a new consequence of the thorium fuel cycle and will manifest itself in various forms due to the range of advanced reactor designs and purposes [15]. An example of a diversion pathway is the production and subsequent diversion of undeclared ^{233}U or ^{239}Pu. Methods to do so may include operating the reactor at a higher power level than declared, introducing more source isotopes, or altering the reactor design to include the addition of undeclared source isotopes, such as a new molten salt processing loop [36]. These methods drive the safeguards technical objectives, which are to detect reactor misuse, detect the introduction of undeclared ^{232}Th or ^{238}U, and detect undeclared facility design changes [36]. Finally, the safeguards measures that enable these objectives include destructive and non-destructive analysis to determine the composition of salts, environmental sampling and surveillance to track the consistency of chemical separations, IAEA presence during start-up or refueling, and periodic design information verification [36].

Similarly, regulatory impositions can be applied to enhance the proliferation resistance of certain reactor designs, such as the requirement to denature thorium fuel with ^{238}U. In such a case, the pathway would be to gain access to existing nuclear materials and the diversion method is to make available the produced ^{233}U by omitting ^{238}U. Therefore, the technical objective of the safeguards is to detect this omission and the safeguards measures might include assay of fresh fuels or the monitoring of the reactor performance to detect decreased amounts of ^{238}U. Pathways analysis is unique to each reactor design series, allowing safeguards to be tailored to the particular neutron spectrum, the presence of online or on-site reprocessing, and any regulatory impositions such as denaturing. A safeguards technique that is flexible in its application to many fuel forms and compositions is therefore of great value.

1.3 Assessment of Nuclear Materials and Current Safeguards

The selection of a method can depend on the isotope of interest, its form and structure, the treaty or regulation, and the desired level of certainty. An important characterization is the difference between NDA and destructive assay (possibly chemical assay or other forms of dismantling), in which a fuel sample is altered from its original state, rendering it unusable for its original purpose [12]. NDA encompasses a series of techniques that measure induced or spontaneously emitted particles from nuclear materials to make inferences about their isotopic composition. Although NDA is generally less precise than radiochemical assay, particularly when quantifying constituents in a mixed material [12], it preserves the sample for its intended use. INFCIRC/153 provides multiple directives that safeguards inspections will be implemented in the most prudent and economical manner possible, highlighting the utility of NDA, which does not destroy valuable reactor fuel [9].

Central to the concept of nuclear material assay is an assessment of isotopic content– ^{235}U is chemically identical to ^{238}U but has a very different purpose and importance for accurate characterization. The differences in nuclear structure between isotopes that account for their distinct behavior inside reactors are also useful for identifying them, given a system capable of resolving isotopically unique signatures. Reference [12] shows isotopically unique characteristics for nuclear materials; NDA assessment methods leverage these to make inferences about the presence and quantity of a given isotope. Material analysis techniques can be passive or active. In passive analysis, spontaneously emitted particles of a characteristic nature (for instance, a particular particle energy, intensity, or type) are measured and used to infer material composition [55]. In active nuclear NDA, a material is interrogated with a photon or neutron beam of sufficient energy and intensity to induce reactions within the material [12]. These reactions must produce some kind of secondary particle or effect that can exit the assayed sample and be measured to infer isotopic content.

The safeguards technologies used for the assessment of nuclear materials during IAEA inspections of the uranium and plutonium fuel cycles are a combination of passive and active assay (some of these methods also extend to other practical nuclear material assessments, such as in port security and weapons verification for treaty compliance)[56]. Table 1.4 presents a comparison of currently used methods for the in situ non-destructive fresh fuel assay of uranium fuels and some considerations for their application to the thorium fuel cycle.

1.4 Safeguarding the Thorium Fuel Cycle

There is limited time prior to the deployment of advanced thorium reactors to proactively address the development and application of safeguards. A complete material accounting plan and an agreement with the IAEA will be required for the licensing of a thorium reactor of any design. These agreements are likely to follow

Table 1.4: Comparison of fresh fuel measurements used in the uranium fuel cycle and considerations for use with thorium fuels, adapted from [57]

Fuel Type	Fresh ^{238}U (enrichment <5 wt% ^{235}U)	Fresh ^{232}Th, ^{233}U driver or (enrichment <20 wt% ^{235}U) Possible addition of ^{238}U for denaturing spent fuel
Measurement Quantity of Interest	Enrichment [wt% ^{235}U]	Fissile material loading [wt% ^{235}U, ^{233}U, etc]
	Active length of fuel [cm]	Active length [cm] of fuel, driver blanket (complexity with powder or molten fuels)
	Linear mass of ^{235}U	Linear mass of ^{235}U, ^{233}U, etc Fertile material loading [wt% ^{232}Th, ^{238}U, etc]
NDA Technique†	Gamma spectrum analysis -HM-5 -MGA-U	Passive gamma spectroscopy is challenging due to ^{208}Tl decay
	Active neutron counting -AWCC	Currently being researched for thorium cycle

† Only nondestructive methods used for on-site analysis of fresh fuels are presented.

the standards of existing Member State agreements in INFCIRC/153 [9], using the currently designated quantity components for bulk thorium and ^{233}U to facilitate inspection goals [19]. To set the stage, safeguards professionals work hand in hand with reactor designers to incorporate concepts such as ‘safeguards by design’ during the early stages of conceptualization [54]. This approach involves incorporating design features that enable the effectiveness and efficiency of safeguards inspections and monitoring in nuclear facilities [58]. Swift, *et al.* have identified common MSR design characteristics to suggest a basis for evaluating the diversion pathways of a specific design, which, in turn, guide safeguards technical objectives and finally method development as discussed in Section 1.2.2 [36].

The development of safeguards for the thorium fuel cycle and advanced reactors is a pivotal area in research and development. The 2021 needs assessment *Safeguards Technology for Thorium Fuel Cycles* uses the pathways analysis framework to evaluate current safeguards tools and identify technical objectives for which a thorium cycle technological gap exists [25]. The general sentiment of the safeguards experts at both the IAEA and the US national laboratories is that thorium safeguards require significant development and assessment [54], [59]–[61]. Worrall, *et al.* encourage research across all technical readiness levels, including the “verification of basic methods" and “quantification of sensitivity limits to provide the foundation for realistic expectations with respect to the implementation of safeguards techniques in a real environment [25]." The following section discusses selected safeguards challenges posed by the thorium fuel cycle, a brief survey of emerging methods development, and the proposed research into active field assay of nuclear materials using neutron resonance capture.

1.4.1 Safeguards Challenges Posed by Thorium

Advanced Reactor Complexity

The technical complexity and wide range of options for thorium-based nuclear energy generate many challenges to the use of existing safeguards techniques. Several of these obstacles are presented by the fundamental differences between most current nuclear power reactors (solid fuel, water coolant, must be shut down to refuel) and the nature of MSRs and other advanced concepts. A critical distinction to highlight is the change from what the IAEA designates as an ‘item’ to ‘bulk’ handling facility [62]. Rather than nuclear material existing as countable and contained items, such as fuel rods, fuel salt is handled and operated in bulk, lowering the barrier to diversion and misuse. In Title 10 CFR Part 74, the Nuclear Regulatory Commission (NRC) makes certain material accountancy exemptions for nuclear materials in sizes or weights too large to be concealed on a person– a fuel assembly certainly fits this criterion, but samples of MSR fissile fuels may not [63]. In an MSR, the nuclear fuel not only changes form from solid before fueling to liquid during use but also changes isotopic compositions with varying time and reactor location. To maintain reactor criticality, all MSR designs with liquid fuels will require periodic refueling [60]. This is a benefit to MSRs in that it optimizes reactor operational time compared to classic LWR designs; however, it complicates material control and accountancy (MC&A) with dynamic ratios of fissile and fertile materials.

The *Infrastructure and Testing Needs for MSR Safeguards* study recommends approaching this complex MC&A problem in MSRs via characterization of fresh fuel and synthesized fuel salts prior to reactor entry. When combined with fuel burnup simulations for a given time and set of reactor parameters, operators and inspectors could predict expected values for fissile and fertile materials measurements and flag indications of diversion [60]. This approach may be implemented as either a ‘black-box’ method, which thoroughly accounts for fresh fuel inputs and spent fuel outputs combined with “robust containment and surveillance within the facility and material balance areas" or via the material accountancy method, which quantifies nuclear material throughout reactor use [32]. Each of the MSR MC&A approaches highlights technological gaps, from assaying mixed fertile and fissile fuels at all stages, the quantification of hold-up in pipes and other reactor components, and a sophisticated modeling capability that can handle burnup calculations in a dynamic fluid with the addition of refueling [32].

Advanced thorium reactor concepts that utilize solid fuel also introduce complexities in the application of safeguards. In thorium-fueled light water reactors, pellets in the same pin of a fuel assembly may have a heterogeneous composition of micro-pins containing fertile and fissile material, the composition of which varies from pellet to pellet [64]. This arrangement may confound NDA methods designed with the assumption of a homogeneous fissile and fertile length throughout a fuel element. Solid fuel MSRs and pebble bed reactors (PBR) using fuel compacts or TRi-structural ISOtropic (TRISO) spheres must also apply careful material balance and control procedures due to the portability of each element. MC&A efforts in these facilities must rely on NDA for isotopic quantification, as direct sampling will compromise the integrity of the spheres, which requires NDA methods that are sensitive to the particular isotopic mix in question [65]. For both solid- and liquid-fuel reactor concepts, substantial research and development efforts are necessary to align safeguarding measures with existing standards.

While the design and function of thorium reactors add to the complexity of applying safeguards, nuclear physics differences between the constituents of the thorium and uranium cycles also prevent the direct application of existing safeguards measures. Two open challenges highlighted in the Oak Ridge National Laboratory thorium safeguards study are the ability to discriminate between ^{233}U and ^{235}U when in a mixed sample and the ability to quantify ^{232}Th or ^{238}U at any stage of the fuel cycle, especially when co-mingled [25]. The MC&A accounting strategies discussed above place a heavy emphasis on fresh fuel analysis; this involves an understanding of both fissile and fertile material ratios in many physical and chemical forms. To make this problem tractable, the following passive and active assay discussions focus on the discrimination of ^{232}Th and ^{238}U, with brief extensions to other isotopes.

Passive Assay

Passive assessments, specifically γ-ray spectroscopy, passive neutron counting, and coincidence neutron counting, provide some information for the differentiation of thorium fuel cycle isotopes; however, they do not provide a complete solution. The passively measurable radiation signatures of fresh fuel isotopes are either too weak or too similar to generate a complete assessment of quantity (mass or activity) or character (individual isotope species) [57]. In the case of passive neutrons, those that arise primarily from spontaneous fission occur at rates for ^{232}Th, ^{238}U, ^{235}U, ^{233}U, and ^{239}Pu that are too low to detect without large quantities of material and extended counting times[8][25]. Each of the materials of interest decays by α particle and the neutron yield generated by the (α,n) reaction when the actinide is in an oxide or other low Z compound provides some distinctive passive signature [66]. This is a mechanism of ^{233}U determination currently under investigation [67] and discussed in more detail in Section 1.4.2, however the α decay rates of ^{232}Th and ^{238}U are several orders of magnitude lower than their fissile counterparts and insufficient for this technique.

Similar to passive neutron assay techniques, passive gamma-ray and x-ray methodologies offer insight into the composition of samples. However, these techniques have limitations for several key distinctions required for thorium safeguards. In the uranium fuel cycle, the most important determination is often the ^{235}U enrichment of a sample. The workhorse of the IAEA inspector toolkit is the HM-5 IdentiFINDER, a handheld radionuclide identification device capable of good determination of uranium enrichment by comparing the observed intensity of the ^{235}U 186 keV line with a background region of interest [68]. The In-Situ Object Counting

---

[8] 20 metric tons of ^{232}Th barely generate one spontaneous fission per second [25].

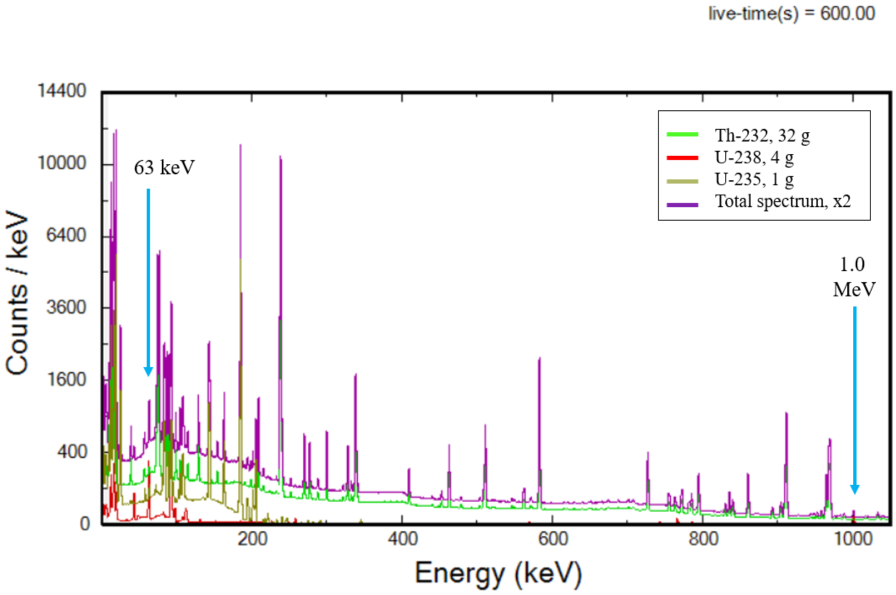

Figure 1-2: 10 minute live-time simulated spectrum of ^{235}U, ^{238}U, and ^{232}Th in nominal mass ratios for a denatured thorium MSR, as measured by an HPGe detector with 2.2 keV FWHM resolution at 1332 keV. The total or combined spectrum for all three isotopes is multiplied by two (for sufficient discrimination from the thorium spectrum). The lines from ^{238}U that distinguish it from the other isotopes in passive energy spectrum measurements are highlighted by arrows. These spectra are based on natural, non-processed, and non-irradiated signatures (therefore including daughter products of natural decay chains). Simulated by the author using GADRAS.

System (ISOCS) uses a portable high purity germanium (HPGe) detector to also perform enrichment calculations on LEU in containers or pipes [56]. There are no such readily useful comparative lines in the combined ^{238}U and ^{232}Th spectrum that can be resolved without excellent spectrometer resolution and extended counting times. Fig. 1-2 shows how the detection of ^{238}U identifying lines is confounded by the energetic range and specific activity of the progeny isotopes in the thorium decay series. Furthermore, while ^{232}Th has a distinctive γ-ray spectrum due to the γ energy and activity of its decay chain, ^{232}U shares the same decay chain, illustrated in Fig. B-1. Therefore, a reliance on passive γ assay for the characterization or quantification of either ^{232}Th or ^{232}U in the presence of one another may yield inaccurate results or falsely imply a history of reactor irradiation.

As implied in Fig. 1-2, passive gamma assay can be affected by the chemical processing history of a sample, which removes progeny isotopes and their decay lines and resets the decay chain at the parent isotope [11], [69]. The myriad stages of the fuel cycle also exacerbate the assay problem; an inspection could reasonably occur during fuel processing, reactor use, recycle processing, and in waste streams, each presenting different material forms, ratios, and therefore, different passive

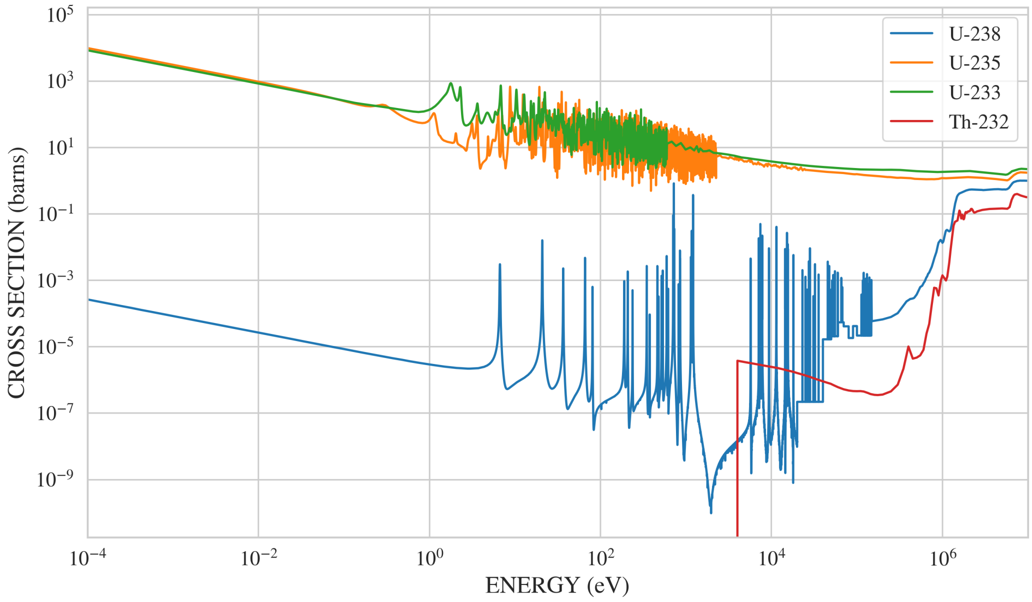

Figure 1-3: Fission cross sections for ^{235}U, ^{238}U, and ^{232}Th, suggesting induced fission methods of assay provide an incomplete assessment for the discrimination of ^{238}U and ^{232}Th, especially when co-mingled with fissile isotopes. Plot generated using data from ENDF/B-VII.1 [73].

signatures. Passive γ assay is an important tool for IAEA inspectors, but additional techniques and methodologies will be required for ambiguous situations to support the levels of confidence required by the inspection verification level.

Active Assay

In active NDA, the properties of an item are inferred based on the particles emitted after a response is induced, usually through a beam of interrogating particles generating a nuclear reaction. In the uranium cycle, this is often performed using the Active Well Coincidence Counter (AWCC), which irradiates a uranium sample with Am-Li (α,n) neutrons and measures the time-correlated neutrons arising from induced fissions [70]. This value is compared with nuclear data on ^{235}U fission cross sections and multiplicity and is used to infer the enrichment of the sample. Differential die-away (DDA) takes this process one step further by correlating isotopic content with the unique time signature of delayed fission neutrons after interrogation with a pulsed source [71]. Photon beams may also be used for active NDA of nuclear materials, such as high energy Bremsstrahlung radiation inducing photofissions in actinides. This process can identify hidden nuclear material and has been the subject of recent research to characterize photofission and delayed fission product yields toward the goal of isotopic identification [72].

Fig. 1-3 shows the fission cross sections for the driver (^{233}U and ^{235}U) and source (^{232}Th and ^{238}U) isotopes in the thorium fuel cycle. The behavior of the constituents in each pair is quantitatively similar, allowing induced fission methods to discern a source isotope from a driver isotope, but likely not ^{233}U from ^{235}U nor ^{238}U from ^{232}Th. Although ^{238}U shows fission resonances in the epithermal neutron region compared to the 4 keV threshold for ^{232}Th, the low magnitudes of ^{238}U result in a large signal-to-noise ratio arising from spurious, non-fission correlated neutrons from the interrogation source [11].

However, there are several other nuclear reactions that can provide isotope-specific data if used in an active interrogation system. Such a system must be sensitive to the isotopes of interest, be able to differentiate one from another, and preferably have little impact from sample shielding and geometry. Using neutrons as the interrogating particle leverages their ability to penetrate dense objects and interact with nuclei within, creating isotopically unique signatures that emit from the object and can be measured and interpreted. By targeting the assay to the isotope in question, not the signatures of its decay progeny, the separation and processing history issues can be circumvented.

1.4.2 Emerging Approaches to Thorium Safeguards

Several agencies and universities have risen to the verification challenges presented by the thorium fuel cycle. The following section briefly highlights selected projects to give a sense of the techniques currently under exploration. Considering the capability gap in the uranium safeguards measures evaluated for application to the thorium fuel cycle, Worrall, et al. acknowledged “the need for active neutron interrogation and development of self-interrogation neutron techniques [25]." The shift in these directions is underscored by projects under development by a consortium of Los Alamos, Oak Ridge, and Sandia National Laboratories, the Y-12 National Security Complex, and North Carolina and Michigan State Universities [66]. Throughout 2022 and 2023, the group has conducted measurement campaigns to simulate and calibrate the AWCC response to ^{233}U test articles and to determine the system’s sensitivity to mixed samples of ^{233}U and ^{235}U, with promising initial results [66].

Deuterium-tritium (DT) generators as a portable source of neutrons for active interrogation are also a theme of current research. A December 2023 study by the above group reported the DDA time profile and the long timescale delayed neutron profile for ^{233}U, suggesting that DDA using a DT pulsed neutron source is a possible candidate method for ^{233}U confirmation [67]. This group also reported the passive ^{233}U self-interrogation neutron signature arising from (α,n) reactions in the sample, showing that passive neutron intensity is proportional to mass for low levels of ^{232}U contamination [67]. At MIT, a DT generator-based system for performing field neutron resonance transmission analysis (NRTA) has also been demonstrated for several nuclear materials, including many in the thorium fuel cycle [74], [75]. This work, discussed in more detail in Section 2.3.1, pioneered the portable neutron resonance analysis concept on which this thesis research is based.

1.5 Proposed Solution

1.5.1 Neutron Resonance Capture Analysis

Given a pulsed neutron source with a sufficiently short neutron production time, the neutron energy at a known flight path can be determined based on its arrival time at a target. At certain neutron energies for specific isotopes, the neutron interaction cross section experiences a resonance— a local peak in magnitude, which corresponds to excited states in the compound nucleus. For the epithermal neutron energies (1-100 eV), in which many medium and heavy elements have resonances, the neutron capture cross section resonance structure creates istopically unique resonance profiles. These resonance signatures may be reconstructed by measuring the time signal of the γ-rays emitted from the target relative to the neutron pulse. This forms the basis of neutron resonance capture analysis (NRCA), a technique used for nondestructive material analysis at large beamline facilities [76]. It is possible to miniaturize the neutron production and moderation assembly and the beam path to create a compact experimental setup that preserves sensitivity to epithermal resonances, as shown in previous NRTA research [74], [77]. This thesis examines the additional requirements and considerations for performing NRCA on a portable system: a novel setup and application.

1.5.2 Research Proposal and Hypotheses

This research proposes the development and testing of an active neutron interrogation method for elements in the thorium fuel cycle to support the safeguard assessment of source isotopes (^{238}U and ^{232}Th) in co-mingled fuel forms. The objective of this research is to experimentally assess the feasibility of portable neutron-induced gamma analysis, specifically NRCA, to non-destructively gain information on the composition of thorium fuel cycle products. It will accomplish this objective by quantifying the sensitivity of the technique, testing in particular the significance with which it can distinguish between ^{232}Th and ^{238}U in mixed samples and its sensitivity to the isotopic quantity for a sample of known geometry.

This research will also assess the portability of the technique and associated system and determine its suitability for practical application for safeguards.

In order to evaluate the objective of assessing the feasibility of portable neutron capture gamma analysis, the following hypotheses will be tested:

- the γ-ray signature arising from epithermal neutron capture on resonances in ^{232}Th and ^{238}U can be measured to a significant degree above background,
- the γ-ray signature from resonance capture in ^{232}Th and ^{238}U is differentiable for each material in stand-alone and mixed samples,
- the γ-ray counts from resonance capture in ^{232}Th can be used determine a bulk quantity of the isotope for a known sample geometry,
- the technique is sensitive to sample impurities that impede other neutron interrogation methods, and
- the developed system is able to be deployed and operated in a fuel process safeguards inspection use case.

This technique is isotopically specific and quantitative, and can be completed in a reasonable time frame for field measurements (15-60 min, according to [25].) In particular, this research will be scoped to the assessment of fresh fuel only; spent fuels containing the transmuted ^{233}U with various contamination levels of ^{232}U and fission products are also of high safeguards interest, however their high γ-ray background make them ill-suited for a gamma-based measurement technique.

1.5.3 Thesis Outline

This thesis is divided into two sections; the first discusses the motivation, theory, and design of the experiment, and the second characterizes system performance and tests its practical application. The first section begins with the preceding chapter, which discussed the exigency in developing a suite of safeguards measures that are sensitive to the constituents of the thorium fuel cycle. It proposes research into an analytical technique that can be performed on a portable system in conjunction with other isotopic analysis methods. Chapter 2 will discuss the background physics of NRCA, its applications to isotopic analysis and considerations for its use. It also summarizes previous work done on NRTA in this miniaturized configuration. Chapter 3 covers the design of a portable NRCA system and presents MCNP simulations that investigate the optimal experimental setup, including a survey of NRCA detection methods.

The second section of the thesis analyses the performance of the system, using several non-radioactive isotopes to assess the resolving power of the NRCA technique. Chapter 4 characterizes the experimental setup, including a detector study and a comprehensive effort to reduce background effects. Chapter 5 determines the sensitivity of the technique to the changing isotopics and geometry of the target. Finally, Chapter 6 discusses the performance of the technique with respect to safeguards, covering the production of thorium reactor fuel simulants and field portability testing. It presents the results of the research hypotheses and discusses future work and considerations for portable active neutron resonance analysis as a safeguards measure.

Chapter 2

Background

The power of neutron-based material analysis lies in the fundamental nature of a neutron– it is an electrically neutral particle and therefore able to penetrate past the electron fields of an atom to interact with the nucleus itself. The nucleus is isotopically unique and this interaction can provide isotopic identification of a sample if the emitted particles can be detected and interpreted. The likelihood that a neutron interacts with a particular nucleus is based on the energy of the neutron; for some isotopes, even slight changes in energy can result in large increases of reaction probability. These energy-correlated probability variations are the basis for the isotopic assessment research presented in this thesis. The following chapter provides a background on the relevant physics of the nuclear reactions used for material identification and neutron time-of-flight spectroscopy. Gamma detection is also introduced and further applied to different NRCA methodologies in Chapter 3: Experimental Design.

2.1 Nuclear Physics of Resonances

Neutrons can be found naturally and in laboratory settings across a broad spectrum of energies, ranging from ultra-cold levels in the microelectronvolt (μeV) range to high energies exceeding one million electronvolts (eV). In the energy range spanning from one to thousands of eV, most isotopes exhibit distinct and well-defined peaks in their interaction probability, referred to as the cross section (σ). These peaks in cross section, or resonances, are visible in Fig. 2-1 and can change several orders of magnitude over a short span of neutron energy. The width of a resonance, measured at full-width half-maximum (FWHM), is parameterized as Γ in units of eV, with a typical resonance width measuring a few eV [78].

2.1.1 The Origins of Resonances

The compound nucleus model developed by Niels Bohr offers an explanation for the origins of resonance structures. When a neutron of kinetic energy E (in the laboratory system) and rest mass m combines with a target nucleus of mass M, they form a compound nucleus with excitation energy E^*:

$$E^* = S_n + \frac{M}{M+m}E \tag{2.1}$$

where S_n is the binding energy of the neutron [79]. The lifetime of the compound nucleus τ can be approximated by its uncertainty $\Delta\tau$ using the Heisenberg uncertainty principle:

$$\Delta E \Delta\tau > \frac{\hbar}{2} \tag{2.2}$$

where the the resonance width Γ is substituted for the energy uncertainty ΔE. The lifetime of the compound nucleus, therefore, is on the order of $\approx 10^{-15}$ seconds for a Γ of a few eV. This is orders of magnitude greater than a direct nuclear reaction ($\tau \approx 10^{-22}$ seconds) in which the neutron interacts only with one or two nucleons [78]. According to Bohr's compound nucleus model, the additional time allows the nucleus to rearrange S_n among all nucleons [78]. The resulting excited nucleus can decay with varying probabilities through any energetically allowed channel by emission of particle x with a branching ratio Γ_x/Γ. Therefore, the location and magnitude of resonance peaks are a result of the excited energy level structure in the compound nucleus, reflecting particular neutron energies that may access excited compound states [79].

The low energy regions in which neutrons have cross-section resonances account for other important characteristics of the reaction. The total angular momentum of the compound nucleus $\vec{J}$ is the vector sum $\vec{J} = \vec{I} + s + \ell$, or the intrinsic target nucleus spin, the neutron spin (having value 1/2 for a neutron) and the orbital momentum of the compound system, respectively [79]. S-wave reactions are dominant in the low energy regime, for which $\ell = 0$. This results in the resonance parity equalling the target parity[1] and total angular momentum following as $\vec{J} = \vec{I} \pm 1/2$. The probability of arriving at a compound nucleus angular momentum $\vec{J}$ is defined by the statistical spin factor g_J, which reduces to:

$$g_J = \frac{2\vec{J}+1}{2(2\vec{I}+1)} \tag{2.3}$$

---

[1] Where parity is conserved between the resonance π_J and the target π_I as $\pi_J = \pi_I(-1)^\ell$ [79]

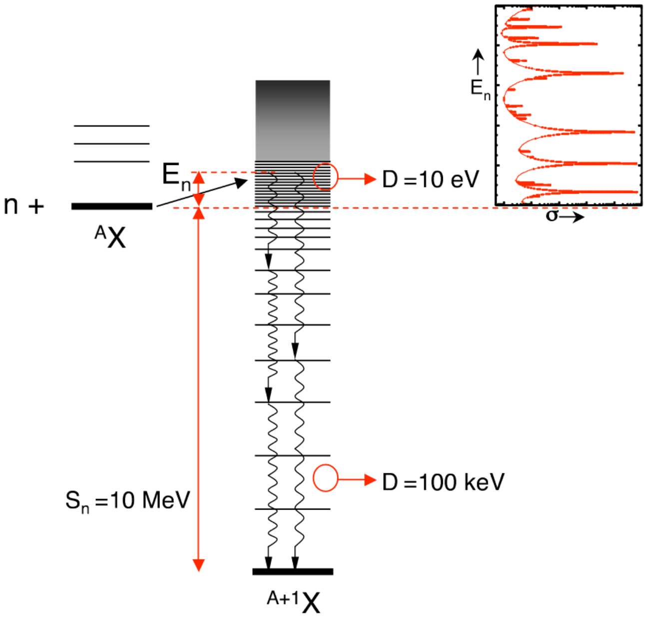

Figure 2-1: A schematic showing the formation of a compound nucleus and subsequent decay by radiative capture. A generalized reaction cross section plot is shown corresponding to excited levels in the compound nucleus. *D* refers to typical values for level spacing. Illustration from [78].

for the case of s-wave reactions [79]. This factor partially determines the magnitude of a cross section in a resonance. It also provides a sense that resonance magnitudes tend to increase with decreasing neutron energy and a higher likelihood of s-wave interactions. Although this is a trend and not categorically true for all isotopes and reaction types, it provides a theoretical basis for the power of using low energy neutrons in this material assay technique.

The Wigner and Eisenbud R-matrix formalism provides a method to use the preceding concepts to parameterize interaction cross sections [80]. Here, the resonance width is the sum of all partial widths $\Gamma = \Sigma_x \Gamma_x$ and when multiplied by $\hbar$ in Eq. 2.2, are the decay rates of a resonance through individual exit channels [81]. Γ_n is the neutron width; like all partial widths, it adheres to the principle of time-reversal invariance and can represent the entrance channel (neutron absorption) or the exit channel (neutron emission) or both (elastic scatter) [81]. The entrance and exit channels are independent of each other. The radiation exit channel Γ_γ results in decay by γ-ray, which is the primary focus of this research. For fissile nuclei, fission Γ_f may occur with a neutron of any kinetic energy. Threshold reactions such as inelastic scattering, (n,2n), or charged particle emission may also occur with sufficient neutron energy [82].

For a well-spaced resonance (one that is further than Γ from its neighbors), the single-level Breit-Wigner (SLBW) expression for the radiative capture cross section is

$$\sigma_\gamma(E) = \pi \lambda\!\!\bar{}^{\,2} g_J \frac{\Gamma_{\mathrm{n}}\Gamma_\gamma}{\left(E - E_\mu\right)^2 + (\frac{\Gamma}{2})^2} \tag{2.4}$$

where $\lambda\!\!\bar{}$ is the reduced de Broglie wavelength of the neutron and E_μ is the resonance energy [79], [83]. This assumes a target at rest in the laboratory system; the effects of thermal motion are discussed in Sec 2.3.4. Overlapping resonances or those involving low-energy fission channels, such as in the case of fissile isotopes, display an asymmetric resonance structure [84]. Vogt, Reich and Moore, and Adler and Adler, among others, have developed successful predictive formalisms for multi-level Breit-Wigner (MLBW) expressions from R-matrix theory [84]. The MLBW expressions for the resolved resonance region are understandably more complex than the SLBW and can be computationally expensive and ill-suited for analytical Doppler broadening [85]. The ENDF-6 manual presents a limited Reich-Moore formalism suitable for evaluating many resonances that experience resonance interference, as well as the more general treatment for complex level and channel structure [85]. The nuclear data libraries used for the simulation and experimental analysis presented in this research use the SLBW and MLBW formalisms where appropriate.

2.1.2 Radiative Capture

Radiative capture, abbreviated (n,γ), describes the reaction in which a target nucleus absorbs a neutron of any energy and immediately decays by γ-ray emission. After neutron capture, the compound nucleus exists in an excited state with excess energy roughly equal to the neutron separation energy S_n plus the neutron kinetic energy, as shown in Eqn. 2.1. For approximately 80% of stable nuclei, this value is between 6 and 10 MeV, peaking at Z=22 and gradually decreasing with increasing atomic number [86]. The lifetime of the compound nucleus is slightly shorter for a thermal neutron capture (10^{-16} s) than for an epithermal resonance capture (10^{-15} to 10^{-14} s). Both lifetimes and their subsequent γ-ray emissions are far shorter than the timing resolution of the detection systems used in this experiment and can be considered to occur promptly after neutron capture. The following section discusses selected physics aspects of thermal and epithermal radiative capture, paired with a short discussion of implications for a materials analysis system.

As indicated above, radiative capture may occur on or off a resonance, with the likelihood of a resonance capture usually several orders of magnitude higher than

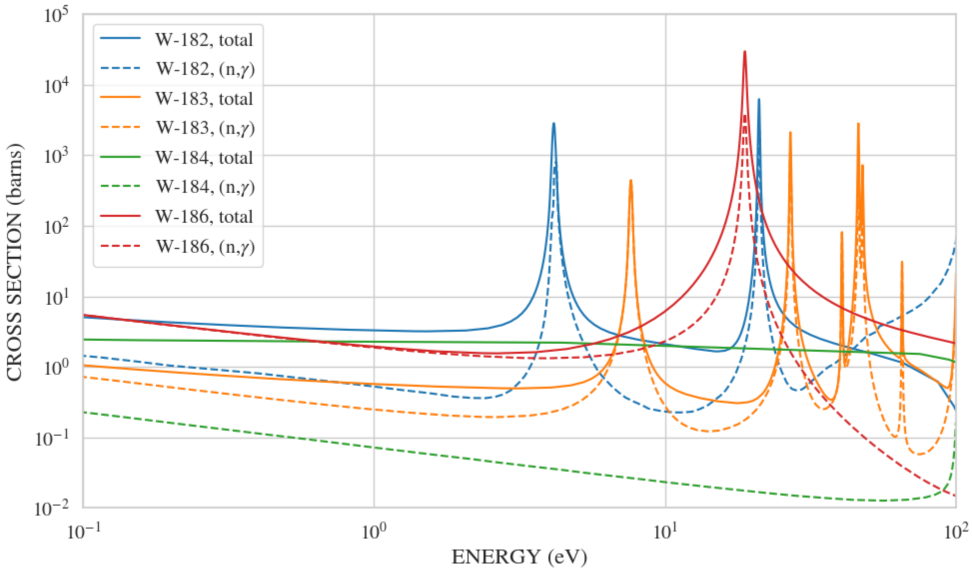

Figure 2-2: Radiative capture versus total cross section for tungsten; each isotope is scaled according to natural abundance. The contributions of the scattering width and capture width in the ^{186}W peak are clearly visible. Color available online, plot generated with data from [87].

the surrounding smooth cross section areas. Elemental tungsten is provided as an indicative example in Fig. 2-2. The four isotopes composing natural tungsten are plotted by total interaction cross section (composed of elastic scattering and (n,γ) at epithermal energies) with the radiative capture cross section contribution plotted below. As in most elements, the smooth capture cross section gradually increases as the interacting neutron approaches thermal energy with a $E^{1/2}$ dependence. The average thermal capture cross section for the tungsten isotopes is approximately 20 barns, significantly less than the capture cross section at the resonance peaks. Both types of capture will occur in a sample, the magnitudes of each depending on the neutron energy flux in the experimental area.

The compound nucleus releases the excitation energy E^* through a cascade of γ-rays with energies corresponding to the discretization of the energy levels of the compound nucleus. These levels are unique to each isotope and therefore the resulting γ-ray energy spectrum is as well. Each transition from level α to β is described by a partial radiation width $\Gamma_{\alpha\gamma\beta}$ with a corresponding intensity I_γ, proceeding in a Markovian process to the ground state [88]. As atomic mass increases, the level structure of an isotope becomes more complex, with a greater number of intermediate levels and finer energy spacing (with the exception of 'magic number' nuceli.) Higher level density results in the de-excitation γ-ray spectrum displaying their characteristic peaks of lower intensities than for an isotope with a less complex level structure. The statistics of the de-excitation path of the final

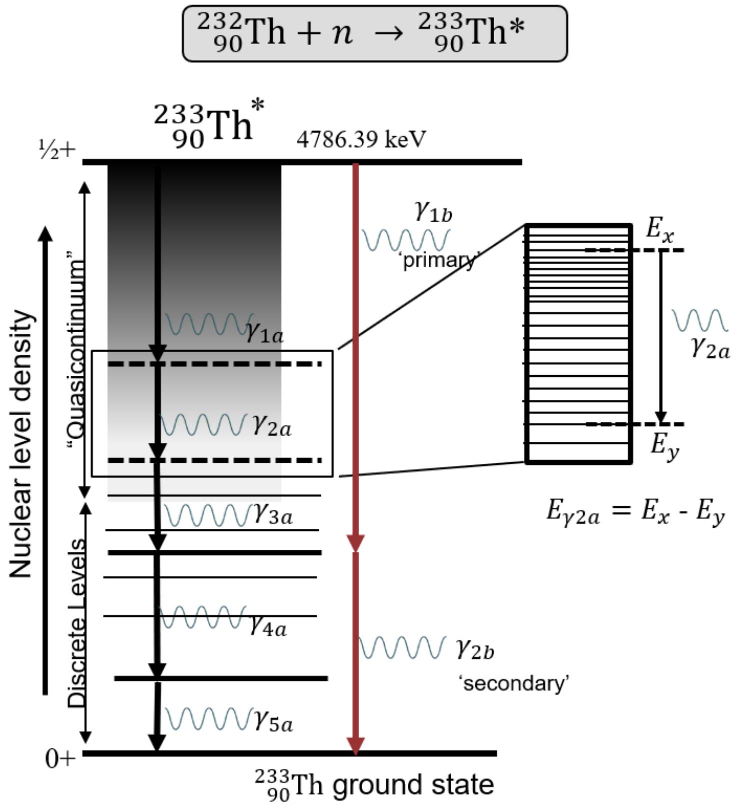

Figure 2-3: Illustration of a multi-step γ-ray cascade (left, in black) and a two-step cascade (red, right) resulting from radiative capture on ^{232}Th. The callout box depicts the unresolvable level structure of the quasicontinuum component. Diagram adapted from [92].

nucleus are impacted by the energy of captured neutron and spin states of particular resonances, such that a thermal capture and different resonances of the same isotope have been observed to have different γ-ray energies and intensity values [89]. Price, *et al.* reported on this phenomenon in U^{238} in 1968 [89], which was more recently studied and characterized by Nauchi *et al.*[90] and Ullmann, *et al.* [91]. The complexity of the (n, γ) spectrum in heavy elements and especially its variability throughout epithermal resonances generates implications for spectroscopic NRCA techniques, discussed in greater detail in Chapters 3 and 4.

The appearance of a quasicontinuum further complicates the γ-ray energy spectrum arising from radiative capture reactions in heavy elements. The clearly defined energy-level structure of lighter isotopes gives way to closer and more numerous levels with the addition of nucleons. This process continues with increasing isotopic mass until there exists a quasicontinuum, or a band of levels so tightly spaced that they cannot be resolved[2] as individual states [93]. An excited nucleus that depopulates through the quasicontinuum region will therefore generate γ-rays corresponding to these transitions that manifest as a continuum of energies, rather than a discrete energy peak correlating to a transition between two defined energy levels [92]. Fig. 2-3 illustrates two depopulation schemata for neutron capture on ^{232}Th, one with five separate transitions and five associated γ-rays, and one with two transitions and γ-rays (the multiplicity of transitions is discussed below). In the figure, $\gamma_{1\alpha}$, $\gamma_{2\alpha}$, and $\gamma_{3\alpha}$ either begin or end in the quasicontinuum levels and will generate continuum component γ-rays. Transitions $\gamma_{1\beta}$ and $\gamma_{2\beta}$ skip the quasicontinuum entirely and, like $\gamma_{4\alpha}$ and $\gamma_{5\alpha}$, are associated with resolvable levels. These γ-rays that deposit their full energy in the detector manifest themselves as energy peaks in the spectrum that may provide additional utility in identifying an isotope.

In isotopes with and without a quasicontinuum, the γ-rays that result from the nucleus depopulating the initial capture state of the compound nucleus and arriving at a known level are called primary rays [94]. A primary γ-ray may either arrive directly at the ground level, carrying the entire Q-value of the reaction, or it may carry the energy of a transition from the initial state to an intermediate level. Conversely, γ-rays that arise from a transition between an intermediate level to another level or to the ground state are secondary rays. In lighter isotopes, the primary and secondary γ-rays may have overlapping energy ranges, such as ^{16}O, which has primary rays at 4.14, 3.27 and 1.09 MeV and secondary rays at 2.18 and 0.88 MeV [95]. For the heavy isotopes examined in this research, the quasicontinuum spanning the levels below the capture state forces any primary γ-ray that can be resolved to have sufficient energy to 'jump' the unresolved region to a known level [92]. As a consequence of this, the observed intensities of radiative capture γ-rays from most heavy elements, including ^{232}Th and ^{238}U, show a MeV-sized gap between the highest secondary γ-ray and the lowest primary ray. This effect is visible in Fig. 2-4. It is important to note that intensity plots such as those in Fig. 2-4 only show γ-ray energies that can be resolved with a spectrometer and do not include quasicontinuum γ-rays. Based on data from the Evaluated Nuclear Structure Data File, 20.6% of capture γ-rays from ^{238}U are from resolved level transitions (therefore contributing to a discrete energy peak in the measured spectrum) and 39.7% of the γ-rays from ^{232}Th.

The γ-ray multiplicity M_γ is the expectation value of the number of γ-rays emitting from a single radiative capture event, where M_γ and the square root of the

---

[2] The boundary between resolvable levels and the quasicontinuum for each isotope is based on the level up to which there exists complete experimental and/or theoretical information [92].

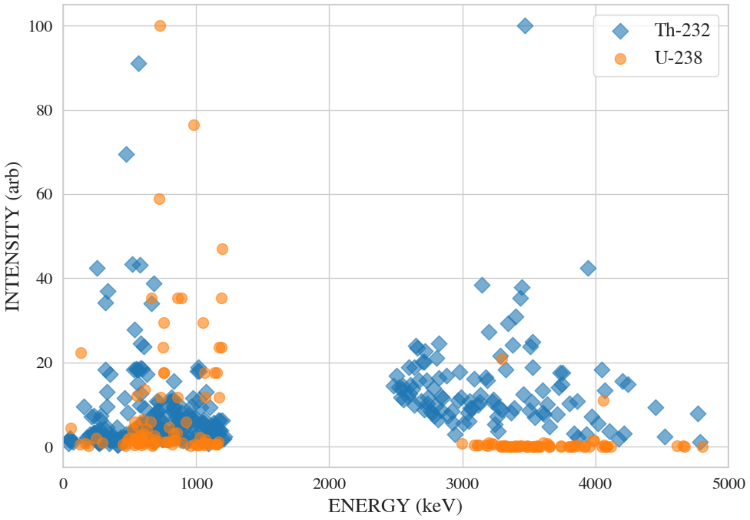

Figure 2-4: The relative intensity distributions for γ-rays from neutron radiative capture on^{238}U and ^{232}Th. The intensities are normalized to the maximum intensity value per nuclide: ^{232}Th: 4.17±0.2% absolute intensity for $E_{\gamma,max}$=3473 keV and ^{238}U: 1.7±0.4% absolute intensity for $E_{\gamma,max}$=726 keV. Transitions which occur via electron capture are not included. Plot generated with data from [96], [97].

variance σ characterize a particular multiplicity distribution [88]. This multiplicity corresponds to the number of energy level steps from the capture state to the ground state, not including possible electron captures from lower energy levels. Like the γ-ray energy spectrum, the distribution of multiplicity values can also show variations from resonance to resonance. Coceva observed a weak correlation between resonances with low spin values and lower values of M_γ in ^{53} Cr, however, he noted the oscillations in multiplicity were too large to assign a fixed relationship [98]. Likewise, Wang, *et al.* observed varying M_γ values for different resonances of ^{149}Sm in both simulation and experiment, with an overall value of 4.8±1.6 [88]. Thorium and uranium similarly exhibit a multiplicity value of 3-5 gammas per capture [91], [99]. Multiplicity has a beneficial effect on resolving an NRCA signal by enhancing the likelihood of detecting a single capture event, however its effects should be considered when comparing captures from one resonance to another. Of particular relevance for NRCA performed on fissile isotopes, the multiplicity of prompt γ-rays accompanying fission has a similar value, with a 2017 study on ^{235}U reporting 6.5 ± 0.2 [100]. Therefore, a fission occurring at the same time of flight as a resonance capture will be indistinguishable in most resonance capture analysis systems without highly detailed, differentiable energy spectra or a fast neutron based method of identifying fission rate.

2.1.3 Other Nuclear Interactions

Radiative capture is the nuclear reaction of interest for this resonance capture research; however, a brief discussion of competing and supplementary reactions is beneficial.

Elastic Scattering

Elastic scattering is an important reaction to consider when selecting the best resonances for NRCA identification of an isotope. According to the R-matrix formalism, a resonance in the total cross section is a sum of all contributing channels; a large total cross section may have a high scattering-to-capture ratio, as observed in the ^{186}W peak (red) in Fig 2-2. An NRCA detector that is sensitive to neutrons may also register a background due to elastic scattering effects. The scattering process has the effect of removing neutrons from the target where they would otherwise create a radiative capture signal, or broaden the time resolution of a resonance due to multiple scatters followed by a capture. In the realm of epithermal neutron production, elastic scattering plays a critical role in moderating the fast 14.1 MeV D-T fusion spectrum six orders of magnitude down to the epithermal region.

For a neutron of energy E scattering on a nucleus at rest in the laboratory system, the final neutron energy E' can be determined through conservation of momentum and energy, leading to:

$$E' = E\left(\frac{m}{M+m}\right)^2\left(\cos\theta + \sqrt{\left(\frac{M}{m}\right)^2 - \sin^2\theta}\right)^2 \tag{2.5}$$

where θ is the angle of the scattered neutron [79]. Scattering is isotropic in the center-of-mass system for s-wave reactions.

The elastic scattering cross section of an isolated resonance is a combination of resonance scattering and potential scattering, and a term which describes the constructive or destructive interference between the two modes. The expression for the SLBW formalism sum of these is:

$$\sigma_n(E) = \pi\lambda\!\!\!^{-2} g_J \frac{\Gamma_n\Gamma_n}{\left(E-E_\mu\right)^2 + \left(\frac{1}{2}\Gamma\right)^2} + 4\pi\lambda\!\!\!^{-} g_J \frac{\Gamma_n\left(E-E_\mu\right)R}{\left(E-E_\mu\right)^2 + \left(\frac{\Gamma}{2}\right)^2} + 4\pi R^2 \tag{2.6}$$

where R is the effective scattering radius [83]. Likewise the total neutron interaction cross section for a resonance may be found by substituting the product of Γ_n and Γ_{total} in the numerator of the first term of Eqn 2.6.

Inelastic Scattering

In the process of elastic scattering, the amount of the lost momentum of the neutron is transferred to the target nucleus in the form of recoil or translation. Inelastic scattering, however, features a transfer of a portion of the neutron's momentum into an excitation of the nuclear energy levels of the target nucleus. The nucleus promptly depopulates this level with one or more γ-rays carrying the characteristic energy of the nucleus' level structure [101]. A neutron exits the nuclear potential with a different energy vector, as depicted in the shorthand $(n,n'\gamma)$.

Inelastic scattering is a threshold reaction in which the neutron must have sufficient kinetic energy to access the energy levels excited in the target nucleus. For light nuclei with well-separated energy levels, the inelastic γ-rays from fast (MeV-range) neutrons can create a distinctive photon energy spectrum indicating qualitative and possibly quantitative information. Inelastic reactions generate a γ-ray background for the NRCA research described here, but are easily removed through timing discrimination and can provide an additional source of target information. A short discussion on time-selected inelastic γ-rays for detector calibration and material identification is presented in Chapter 6.

2.2 Materials Analysis with Neutrons

As discussed in Chapter 1, neutron induced reactions are ideal for nondestructive assay due to their penetrating nature and ability to generate a measurable and isotopically unique signal. An example of a 'neutron in, neutron out' assessment technique is NRTA, discussed in detail in Section 2.3.1. There are also many forms of 'neutron in, gamma out' analysis, in which an interrogating neutron beam generates a γ-ray emission. Generally, the energy of the neutron and the timescale over which the γ-rays are measured dictate the form of the technique. Some methods measure γ-rays and fast neutrons arising from induced fissions, such as the differential die-away analysis introduced in Section 1.4.1. Section 2.2.1 will briefly cover the major analysis techniques based on γ-ray detection resulting from the radiative capture or inelastic scatter of a neutron. This discussion serves to illustrate the uniqueness of the proposed technique and to present some analysis techniques which could be performed concomitantly on the miniaturized setup.

2.2.1 Neutron-Induced Gamma Assay

The principles of neutron-induced γ-ray analysis began shortly after the 1932 discovery of the neutron. In 1934, Fermi, *et al.* identified that the energy of the bombarding neutron was responsible for varying intensities of activation in different elements, discovering the energy-based cross section [102]. By 1936, Hevesy and Levi were using the delayed γ-rays from neutron capture to identify impurities and unknown rare earth elements in samples [103]. γ-rays from neutron capture were soon used to collect nuclear data, such as the 1939 experimental campaign at Columbia University which used various absorbers to preferentially select different neutron energies to build the first cross section plot for ^{238}U [104], [105]. The use of prompt and delayed gamma radiation from neutron interactions to collect nuclear data is still in use today at large beamline facilities such as the Gaerttner Linear Accelerator Facility at the Rensselaer Polytechnic Institute. These data inform our understanding of nuclear structure and are widely used in many domains, including modeling and simulations. With increasing confidence in nuclear data as well as advances in detection and neutron generation, materials analysis techniques based on neutron-induced γ-ray emission have been gathering popularity since the 1970s.

Neutron Activation Analysis

Hevesy and Levi's 1936 work on materials identification through neutron capture γ-rays was the first instance of neutron activation analysis (NAA, sometimes called instrumental or delayed gamma neutron activation analysis). It was reported as a material analysis technique with calculations and sensitivities for various isotopes by Guinn and Wagner in 1960 [106]. In NAA, a sample is first exposed to a neutron field of known energy and fluence and then measured with a γ-ray detector capable of energy discrimination. Rather than measuring the prompt de-excitation γ-rays from a radiative capture (discussed in the next section), traditional NAA is performed after irradiation and analyzes the energies of the γ-rays arising from the decay of an unstable product nucleus.

This technique is qualitative in the isotopic specificity of the decay gamma energies and also quantitative provided accurate neutron energy flux, isotopic cross section data, and measurement of the decay gamma intensity. It can be performed nondestructively on a sample; although some methods may involve sample preparation, for example, loading into a container for in-core reactor irradiation [107]. Candidate materials for NAA assessment are those that have a sufficient neutron capture cross section, with a neutron capture product that is radioactive, and that has a half-life and activity suitable for measurement. Therefore, the practical limits of NAA depend on the methods of each laboratory for irradiation and detection, with approximately 70 elements that possess at least one suitable isotope, some with NAA sensitivities as low as parts per billion [108]. Oak Ridge National Laboratory has demonstrated the effectiveness of NAA in detecting ^{235}U in picogram levels for safeguards applications using swipes irradiated in the High Flux Isotope Reactor [109].

Prompt Gamma Activation Analysis

Prompt gamma activation analysis (PGAA) is a variation on NAA that focuses on immediate γ-ray emission resulting from thermal neutron capture. Rather than using the γ-ray spectrum from the decay of the activated daughter products generated after neutron capture, PGAA examines the de-excitation of the compound nucleus, discussed in Sect. 2.1.2. This technique focuses particularly on radiative capture after thermal neutron capture, as opposed to NRCA, which uses epithermal and resonance energy neutrons. Some PGAA systems are also sensitive to processes competing with prompt radiative capture, such as charged particle emission, delayed isomeric transitions, and neutron-induced fissions [86]. Using spectrometers with a high degree of energy resolution, PGAA correlates the characteristic de-excitation γ-ray spectrum with the isotope of the target nucleus.

PGAA benefits from high thermal neutron flux and is generally performed in facilities with reactors or large accelerators, although there are examples of in situ analysis for bulk material contamination using a neutron generator [110]. Since the excitation and detection occur at the same time, the target area must be sufficiently shielded from background photons associated with neutron production to allow high resolution γ-ray spectroscopy. Every isotope, with the exception of ^{4}He, has a thermal neutron capture cross section which permits analysis with this technique. There are eight orders of magnitude between the highest and lowest thermal capture cross sections; therefore, PGAA will have varying levels of sensitivity. However, Molnár suggests this sensitivity differential can be beneficial when detecting elements with high cross sections embedded within low cross section matrices [86].

Fast Neutron Analysis

Fast neutron analysis (FNA or Pulsed Fast Neutron Analysis, PFNA) is based on the inelastic scatter nuclear reaction. The energy level structure of the target nucleus is isotopically unique, leading to a unique $(n, n'\gamma)$ photon energy spectrum. Light elements have high Q-values and a low number of energy levels, resulting in many emitting a 1 MeV or greater photon after an inelastic scatter. These γ rays are resolved with a high Z detector, even in a high background environment created by proximity to the neutron source. The number of counts in specific energy peaks is correlated with the quantity of an isotope in a sample of known geometry [111].

Inelastic scatter has a neutron energy threshold: neutrons generated by radioisotopic sources such as Am-Be and ^{252}Cf can access inelastic scatter reactions in chlorine, sulfur, iron, etc., but cannot exceed the carbon and oxygen thresholds [112]. The 14.1 MeV neutrons from a deuterium-tritium (DT) neutron generator are well suited for this requirement and are widely used for bulk materials analysis, with applications in manufacturing [113], mining [114], and explosive detection [111]. Certain implementations of the technique include a comparison of the inelastic photon spectrum during the fast neutron production times with one from the intervening times that shows thermal neutron capture data [112].

2.3 Neutron Resonance Spectroscopy

Neutron resonance spectroscopy is the material analysis method that infers isotopic content by measuring the resonance profile of a sample. On a plot of cross section versus neutron energy, the particular combination of resonance magnitude, positioning, and separation is unique to each isotope. To reconstruct such a signature for isotopic identification, researchers must determine the magnitude of the resonance by measuring a nuclear reaction effect and record it against the energy of the neutron that produced such an effect. The energy of a resonance region neutron (1 eV to multiple keV) is difficult to measure experimentally, but the time-of-flight (TOF) can be used to calculate the neutron energy given a pulsed source.

Neutron resonance analysis methods can be further classified by the technique used to measure the magnitude of the resonance. NRTA reconstructs the sum of the neutron scattering and radiative capture resonance widths by plotting the neutron attenuation spectrum against the incident neutron energy. NRCA measures the magnitude of the radiative capture resonance width by time-correlating prompt γ-rays with neutron energy. Both techniques are used for nondestructive quantitative material assay in large beamline facilities on samples that include archaeological and heritage objects, special nuclear materials, and reference samples for the determination of nuclear data [13], [14], [76], [83]. The selection of NRTA or NRCA for a particular object is largely based on the isotopes of concern. The capture method of analysis is typically used for materials containing medium and heavy elements (although NRTA is also sensitive to these isotopes) and the transmission method for light elements or isotopes with or near closed shells [115]. Neutron Resonance Densitometry (NRD) is the combination of NRTA, NRCA, and PGAA, proposed by the Japanese Atomic Energy Agency to characterize fuel debris samples from the Fukushima Daiichi meltdown [116], [117] Although neutron resonance spectroscopy can characterize almost every isotope in high-flux, high-energy resolution experiments at world-class large beamline facilities, it is possible to leverage smaller neutron sources with shorter beamlines to gain isotopic information about a sample. The accuracy of such an experiment will suffer compared to that of large facilities, but it has the advantage of portability. Isotopic safeguards assessment techniques that can be deployed to fuel fabrication and reactor facilities to conduct NDA can deliver results instantaneously. On-site and immediate assay empowers inspectors to take further action in the incidence of a diversion scenario and simplifies chain of custody issues when moving samples to distant measurement facility.

The high-Z isotopes involved in nuclear fuel cycles are particularly well suited to miniaturization efforts. In a compressed beamline, only the slowest neutrons have a sufficient flight time to arrive at the assay target with enough energy separation to distinguish individual resonances. Uranium, thorium, and plutonium are among the elements with the lowest energy resonances, with most of their isotopes having two or more resonance peaks below 50 eV. Our research group has developed a compact and portable DT-based NRTA system and demonstrated it to have isotopic sensitivity to these high-Z isotopes [74], [75].

2.3.1 Neutron Resonance Transmission Analysis

NRTA has a broad range of applications, including arms control verification, safeguards, nuclear physics, and archaeology [118]–[120]. The fundamental principle of NRTA is that the presence of different isotopes in a sample causes neutrons of varying energies to be attenuated as a function of the isotopic resonance profile and linear density. The varying attenuation levels manifest themselves in a series of dips in the neutron transmission spectrum. For an initial neutron flux $I_{o,x}$ in the x direction that impinges on a target of material i and thickness x, the number of neutrons of energy E that are transmitted is given by

$$I_x(E) = I_{o,x} e^{\Sigma_i \Sigma_j n_i \sigma_{i,j}(E) x_i}, \tag{2.7}$$

where n_i is the number density of the material and $\sigma_{i,j}(E)$ is the cross section for interaction type j. Given evaluated cross section data for the isotopes of interest and a spectroscopy system sensitive to neutron energy, these dips are correlated with isotope-specific resonance profiles. The portable neutron generation and data acquisition system discussed here uses TOF to determine neutron energy, discussed in detail in Chapter 3.

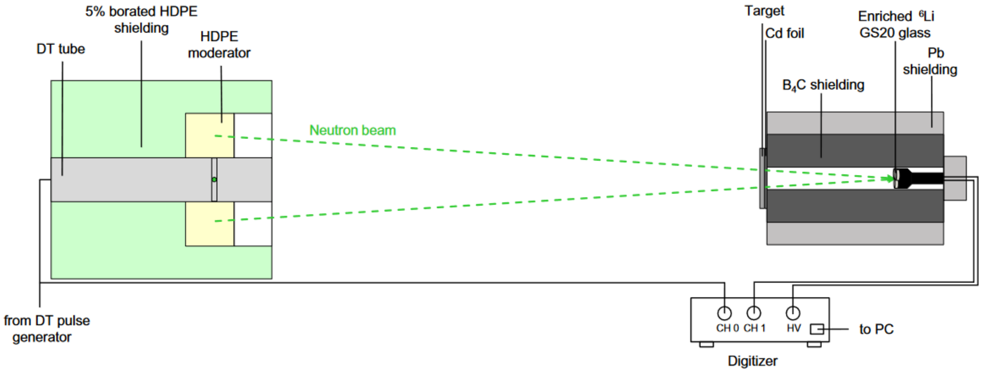

Figure 2-5: A schematic of the NRTA experimental setup focusing on shielding and data acquisition. Figure reprinted from [74].

Fig. 2-5 shows a schematic diagram of the recently developed portable NRTA system. As many aspects of neutron generation are shared between the NRTA experiment and the ongoing NRCA research, a brief overview of only the NRTA-specific findings is presented in this section. Neutron detection was performed using a ^{6}Li-doped GS20 glass scintillator, which is sensitive to epithermal and thermal neutrons, as well as γ-rays. Significant effort was spent in constructing, testing, and optimizing the boron carbide shielding to reduce the ambient thermal neutron background in the detector. Similarly, a large part of this research focused on characterizing the residual background function to provide a correction factor for transmission dips. An accurate background determination is crucial to the ability of NRTA to reconstruct transmission in both resonance and off-resonance areas, which is used to infer the individual linear densities of isotopes in the target.

The NRTA system was applications tested in three major areas of isotopic assessment: the general qualification of shielded uranium, arms control verification, and advanced reactor safeguards. The portable setup was able to detect and quantify 5 mm of uranium shielded by 25 mm of lead with an accuracy greater than 80% in runs of 20-30 minutes [75]. It also showed good agreement in reconstructing ^{235}U abundance (<1%) in samples of depleted uranium. In arms control verification studies, the system demonstrated the ability to confirm the presence of fissile materials in a sample. Furthermore, the set-up was able to reconstruct the isotopic abundance of varying enrichments of ^{235}U/^{238}U and ^{239}Pu/^{240}Pu, showing good agreement with the true values. Finally, the work reported initial results in an ongoing feasibility study for advanced reactor safeguards, showing a minimum detection limit for ^{233}U 1 x 10^{-4} atoms / barn for a measurement time of 2.5 hours [75]. The research concluded with suggestions for follow-up studies on advanced reactor safeguards and a detector trade study to identify an epithermal range neutron detector with lower sensitivity to γ-rays.

2.3.2 Neutron Resonance Capture Analysis

NRCA is based on the changing intensities of prompt γ-ray emissions for different isotopes when exposed to a neutron flux of varying energy. The technique measures the time-correlated γ-rays arising from resonance radiative neutron captures, reconstructing the resonance capture profile of a sample based on the relative strength of γ peaks in the TOF spectrum. Like NRTA, the measurement time of a detected particle, a γ-ray in this case, is recorded relative to the start time of the neutron production pulse and used to calculate the neutron energy at which count peaks occur in the TOF spectrum.

NRCA has its foundations in the first studies to understand the resonance structures of ^{238}U in the 1930s. It is carried out primarily at world-class accelerator facilities as a method to determine nuclear data related to scattering and capture cross sections [121]–[123]. Moxon, *et al.* pioneered NRCA as a material analysis technique in 1974 to determine sample impurities [83]. In 2000, Postma *et al.* demonstrated the utility of NRCA for the evaluation of bulk materials in archaeological objects with the ability to provide immediate results compared to NAA. This analysis was conducted at the 10 m beam station at Delft University of Technology's GELINA accelerator facility, which has a pulse width of 1 ns and an epithermal neutron flux at the target given by $\Phi(E) = 7000/E^{0.91}$ neutrons/eV$\cdot$cm^2 (≈ 105 neutrons/eV$\cdot$cm^2 at 100 eV)[124]. A three-hour run on an ancient copper arrowhead was able to discern bulk quantities of 5% tin and 0.4% arsenic, and silver, antimony, and gold in parts per million. The technique is now used in large beamline facilities around the world for the analysis of objects containing medium and heavy elements.

NRCA, like NRTA, has many beneficial aspects. It is a nondestructive analysis technique, both in that samples do not require special preparation and that the transmutation of isotopes during irradiation does not appreciably[3] change the isotopic concentration. The measurements can be paused and restarted if required and can be monitored in real-time to determine if the signal counts for isotopes of interest meet the desired statistical accuracy. The neutron beam and the solid angle view of the detection system together define the effective area of analysis; large, irregular, and heterogeneous objects can be methodically analyzed by rastering the beam over the entire volume. The range of elements with resonances from 1-100 eV,

---

[3] Assuming a total flux of 10^7cm^{-2} s^{-1} at the target, if every neutron is absorbed over the course of an hour-long measurement the transmutated atoms are still orders of magnitude less than the atoms in the sample [86].

the neutron energy range in which a portable NRCA system can resolve resonance structures, is presented in Appendix B, Fig. B-6.

Both resonance analysis techniques can resolve many isotopes in one measurement of a composite sample, provided that the resonant structures do not obscure each other beyond the resolution of the system. NRCA may be able to constrain NRTA measurements in such situations due to the additive nature of the capture γ-ray measurement as opposed to the neutron removal fraction in NRTA. NRCA and NRTA measurement devices can be positioned orthogonally and performed simultaneously, each collecting different data from the same nuclear interaction. Spectroscopic NRCA has the ability to identify neutron-poisoning contaminants such as boron, which could impact the results of both techniques without identification and consideration.

2.3.3 NRCA Theory

The theoretical capture γ-ray yield Y_γ arising from nuclide k is expressed as the sum of primary capture events $Y_{o,k}$ and the captures that occur after one or more scatters, $Y_{m,k}$: [115]:

$$Y_\gamma = \sum_k (Y_{o,k} + Y_{m,k}). \tag{2.8}$$

The primary capture yield resulting from radiative capture on nuclide k is:

$$Y_{o,k} = \sigma^D_{\gamma,k} n_k x R, \tag{2.9}$$

where $\sigma^D_{\gamma,k}$ denotes the Doppler broadened radiative capture cross section, n_k is the number density of atoms per unit length of the isotope of concern, and x is the thickness of the sample. R is the self-shielding factor, which describes the removal of neutrons available to interact via the desired radiative capture reaction. As discussed in Section 2.1.1, a neutron of the correct energy to interact with a resonance may exit the reaction through any allowable channel. The contributions of scattering, radiative capture, fission, and other reactions to the total cross section of a resonance are unique to each resonance of each isotope. The varying magnitudes of competing reactions relative to the capture cross section have the effect of attenuating the number of energy-specific neutrons available for capture, described by:

$$R = \frac{1 - e^{-\sum_j n_j \sigma^D_{tot,j} x_j}}{\sum_j n_j \sigma^D_{tot,j} x_j}. \tag{2.10}$$

The numerator of this ratio describes the probability of interaction (or, one minus the probability of survival) for any possible reaction on all isotopes in a sample, indexed by j. The denominator is the total macroscopic cross section of the sample, representing the likelihood of interaction per unit path length. R begins at unity for small products of cross section and areal density,[4] diminishing as either multiplicand grows larger. The self-shielding factor has an impact on Eq. 2.9 that the radiative capture yield and the product of cross section and areal density are directly proportional only in sufficiently thin samples or for weak total interaction resonances. Self-shielding is discussed in more detail for its impacts on isotopic quantification studies in Section 5.4.

The quantity of interest in an NRCA experiment is $\sigma_{\gamma,k} n_k x$: the product of the energy-dependent capture cross section, the linear atomic number density, and the thickness of the sample, respectively. Any one of these parameters may be treated as an independent variable, based on the arrangement of the sample relative to other runs in an experimental series. The primary observable is the measured capture yield, $C_\gamma - B_\gamma$, where C_γ is the dead time corrected spectrum with a sample in the neutron beam and B_γ is the background spectrum. The experimental yield, Y_{exp}, for a particular region of a sample may be calculated as a ratio of counts relative to the incident neutron flux φ,

$$Y_{exp} = \frac{C_\gamma - B_\gamma}{\varepsilon \Omega P A \varphi}, \tag{2.11}$$

adjusted by experimental conditions: the detection efficiency ε, the solid angle of detection Ω, the probability P that the prompt γ-rays escape the sample, and A, the area of the sample interacting with the neutron beam [125]. B_γ is strongly influenced by the characteristics of the sample itself, such that subtracting an open beam (sample ‘out’) experimental run is insufficient for removing the non-resonance capture generated γ-ray background in the region of interest. Section 4.3 proposes a custom background function fitting algorithm towards this end.

NRCA is used for two categories of practical applications: determination of cross section information to generate nuclear data tables and for nondestructive isotopic analysis. There are also two general methodologies for analysis of the TOF-associated count data: an absolute method using the least squares fitting of resonance areas and the comparative double ratio method [79]. In a nuclear data determination experiment, the composition and density geometry of the sample and the neutron beam parameters are very well characterized *a priori*, so that the desired quantity is the measured γ-ray flux per incident neutron due to radiative capture. The desired parameters (resonance energy, width, statistical spin factor, etc.) are derived through resonance shape analysis with the REFIT code, which uses least squares adjustment to fit experimental capture yield data [126].

---

[4] Areal density is defined as the product of sample thickness, x and the linear number density of atoms, used here for brevity.

In contrast, isotopic analysis experiments seek to determine isotope type and effective areal density. It is possible to apply the analytical resonance shape method to these experiments as well, holding the resonance parameters fixed and making the free parameters the sample characteristics. Like nuclear data NRCA experiments, detailed characterization of the neutron beam, detection system, and effects of the sample on the measured counts is required [79]. However, the double ratio analysis method is more widely used in practice due to its accessibility, lower computational requirements, and robustness to experimental variations and sample shape [83], [124], [125], [127]. In the double ratio method, the observables are the background subtracted total counts integrated over selected resonances, which are compared with those of a known reference sample. Further discussion on background subtraction is found in Chapter 4 and the choice of limits of integration based on system resolution and overlapping resonances is presented in Chapter 5.

Using the double ratio method, the weight ratio W_I/W_{II} of isotopes I and II in a single object is derived from the ratio of the net areas of resonances μ and λ (where μ is a resonance belonging to isotope I and λ to isotope II). This is done using the equation:

$$\frac{W_I}{W_{II}} = K^{\mathrm{cal}}_{\mu,\lambda} \frac{R_\lambda}{R_\mu} \frac{N_\mu}{N_\lambda}, \tag{2.12}$$

in which the count ratio is corrected by the self-shielding factors for each of the selected resonances (Eq. 2.10), as well as a calibration factor $K^{\mathrm{cal}}_{\mu,\lambda}$. This calibration factor is determined from values measured under the same experimental conditions as the unknown sample, using calibration samples of known isotopic composition and geometry:

$$K^{\mathrm{cal}}_{\mu,\lambda} = \left(\frac{F_\mu}{F_\lambda} \frac{N_\lambda}{N_\mu} \frac{W_I}{W_{II}} \right). \tag{2.13}$$

This calibration factor adjusts for measurement time, solid angle of detection, detection efficiency, and spatial variations of the neutron flux, given the matching experimental conditions [83]. The calibration standard establishes the constant of proportionality between the self-shielding corrected count ratio and the weight ratio.

Note that the effective areal density of the isotope in question appears in the equation to calculate the self-shielding factor. When the sample is thin or a sufficiently weak resonance is analyzed, detected counts are proportional to the effective areal density, and the self-shielding factor remains close to one. Postma, *et al.* have developed a normalization technique for samples exceeding the thin-sample approximation. The effect of self-shielding varies between different resonance strengths of the same isotope. Assuming equal γ-ray detection efficiencies across resonances, the count ratio of two resonances may be used to determine the effective areal density, applying a theoretical self-shielding curve normalized to experimental data. An example of this technique is demonstrated on experimental data in Chapter 5, as well as the introduction of an alternate procedure for effective areal density reconstruction using χ^2 minimization [127].

2.3.4 Considerations and Challenges of Portable NRCA

The novelty of this research lies in the design and development of a miniaturized NRCA system, suited for safeguards applications due to its portability and sensitivity to isotopes in the nuclear fuel cycle. We define 'portable' as a system with a mass and volume small enough to be moved to a nuclear fuel cycle facility without the need for special material handling equipment. In its most portable form, this system could be packed into one or two wheeled cases and transported by a single individual. Perhaps more practically, the neutron production and particle acquisition systems could be housed and operated in a small box truck, a configuration that brings several advantages, as discussed in Chapter 6.

The benefits of compact, portable resonance analysis require compromises that sacrifice some of the analyzing power and sensitivity of the technique compared to NRCA performed at large beamline facilities. Relative to these large accelerator facilities, the component that requires the most miniaturization is the neutron source. We propose the use of a DT generator for this purpose, which affects the energy resolution and counting statistics of the final NRCA system, discussed in Chapters 3 and 4. Incorporating a neutron generator into the suite of safeguards technical measures represents a significant increase in size, but also in capability, of an inspector's kit. With a pulsed DT generator as the neutron source, the technique may be complementary to other concomitantly performed neutron analysis techniques, including NRTA, PFNA, and PGAA.

The second challenge posed by the miniaturization of an NRCA system is a common systems engineering problem: component interference exacerbated by proximity. By reducing the beam path from tens of meters to two meters, the sample and detection systems are moved much closer to the neutron generator and moderator, which increases the background noise from spurious neutron- produced γ-rays. The characterization and mitigation of this γ-ray background is discussed in detail throughout Chapter 4, with considerations for detector selection covered in Section 3.5.

Chapter 3

System Design

The NRCA system developed in this investigation consists of components that perform three primary functions: neutron generation, neutron moderation, and γ-ray detection and digitization. The system design was primarily influenced by two key requirements: portability and improved clarity of the NRCA signal. This chapter explores how these requirements influenced the design and integration of the system's components.

This chapter is structured around the system functions described earlier: neutron production,neutron moderation, and gamma detection. The first section introduces time-of-flight spectroscopy and discusses portable neutron sources. The operational principles of D-T generators are introduced to examine their effects on system design. The second section explores the moderation process and the design considerations that led to the selection of the moderator. The chapter shifts focus to radiative capture γ-ray detection, outlining the special considerations created by system miniaturization. The three primary NRCA detection methodologies and a comparative study are presented, providing an experimental justification for detector selection.

3.1 Design Considerations

The objective of this research is to engineer and test a portable system that uses neutron resonance capture for isotopic analysis. Therefore, the portability of the neutron source, detection system, and associated shielding is of high importance when selecting from the list of candidate options. Portability is supported by several considerations, including mass, ease of setup, safety and dose while in use and in travel configuration, and host support conditions. In addition to satisfying portability needs, the neutron generation system must also meet the requirements to perform neutron resonance analysis on composite materials. Paradela, *et al.* have outlined their requirements for the effective resonance analysis of nuclear fuel cycle materials at the 10 m flight path of the GELINA accelerator, which provide a guideline for a miniaturized system [128]. To analyze nuclear materials in various physical forms, they suggested:

1. a neutron energy range of 0.5 to 500 eV to span the resonance regions of heavy elements with as high a flux as possible,
2. a system resolution "sufficient to analyse complex transmission data below 500 eV," stating that GELINA's resolution of $\Delta E/E \approx 0.008$ was suitable,
3. and an NRTA background of less than 10% throughout the region of interest [128].

An ideal portable system would feature the same neutron intensity and timing resolution as the large accelerator facilities; however, practical considerations dictate there will exist some compromises.

Considering the challenges of emerging fuel cycle safeguards and the benefits of on-site analysis, we outline design requirements to guide the development of a portable NRCA system. Based on Paradela, *et el.*'s guidelines, this system should:

1. generate sufficient epithermal neutron flux to produce an NRCA signal at least two standard deviations above background noise within a reasonable time (less than a few hours),
2. have a system resolution capable of accurately identifying fuel cycle isotopes,
3. be portable by either hand or automobile and able to be transported and used safely by a trained operator.

Without a preexisting requirements document, this list functions as a basic guide that can direct and constrain the research. This work serves as a scoping study, establishing the foundational parameters and assessing the feasibility and potential capabilities of a portable NRCA system.

3.2 Time of Flight Spectroscopy

Prior to discussing the components of the NRCA system, a general explanation of neutron spectroscopy by time-of-flight (TOF) is instructive to understand system operation. Discerning the energy of an epithermal neutron purely on the basis of the energy it deposits in a detector is a difficult process due to the low kinetic energy of the epithermal region and the neutral charge of the particle. TOF spectroscopy provides a solution to this challenge as a versatile and commonly used method that is well suited to the low neutron energies of the resonance region. In a TOF setup, neutrons leave the source or moderator and arrive at the target sample at a time governed by their kinetic energy, which is related to their speed by the relationship $E_n = \frac{1}{2}mv^2$. This non-relativistic neutron energy, E_n, can be calculated using time, T, that a neutron or its reaction particles were detected at a path length, L:

$$E_n = \left(72.298\frac{L}{T - T_o}\right)^2 \tag{3.1}$$

where 72.298 has units of $\sqrt{\mathrm{eV}}\mathrm{\mu s/m}$ and T_0 is the μs latency of the neutron pulse peak from the neutron generator zero-time trigger signal.

Accurate knowledge of the neutron generation pulse start and concise pulse timing are therefore of high importance in determining precise neutron energies. In practice, the start time of the neutrons is determined using a pulsed source or a chopper wheel that divides a continuous neutron flux into discrete packets. For pulsed sources, the faster the mechanism of neutron generation at ramp-up, neutron production, and shut-off, the finer the resolution of energies can be. Tailoring a minimum pulse width comes with neutron flux, operating frequency, and maintenance trade-offs, depending on the type of neutron production used.

The corrected time of flight, t_{TOF} incorporates adjustments for the pulse initiation time and half the pulse width, plus the response time of the detection system, as expressed by:

$$t_{\mathrm{TOF}} = t_{\mathrm{measured}} - t_{\mathrm{pulse}} - t_{\mathrm{detection}}. \tag{3.2}$$

Similarly, the flight path length, L, defined in NRCA as the distance from the front face of the moderator to the target material, requires correction for the neutron moderation path length and the mean free path length in the target medium:

$$l_{\mathrm{TOF}} = l_{\mathrm{measured}} + l_{\mathrm{moderation}} + l_{\mathrm{radial}}. \tag{3.3}$$

Each of these parameters has an associated uncertainty due to statistical processes that occur in neutron generation, moderation, moderator exit position, and capture path length. These uncertainties are summed in quadrature for the time and distance variables and are combined via the method of partial differentials to determine the uncertainty in energy, as discussed in Sect. 4.2.1. Some of these uncertainties are orders of magnitude larger than others and dominate the error propagation process. For example, the rise time of the scintillation response and its subsequent conversion to an electronic signal for all detectors used in this research were on the order of tens of nanoseconds, which is significantly shorter than the microsecond uncertainty associated with the neutron pulse generation time.

3.3 Portable Neutron Sources

A portable neutron source cannot match the neutron flux or the precise system resolution of a large beamline facility that utilizes a fixed accelerator. The most effective neutron source for this research is one that best meets the specific requirements outlined in Sect. 3.1. Neutron production methods are generally categorized into three types: reactors, accelerators, and radioisotopic sources. Each type generates neutrons through one or more specific reactions, including (α, n), (γ, n) and (fission, n). Although reactor-based sources are not portable, the emerging interest in small modular and microreactors may offer regional neutron analysis solutions in the future. Radioisotope sources are the simplest and most compact method, but their operating neutron flux is lower than that of other sources by orders of magnitude. If a source were scaled to 10^8 n/s to match the neutron output of a D-T generator, the 1-meter γ-ray dose from PuBe and AmBe would be 0.1 rem/hr, and 0.5 rem/hr from RaBe, excluding neutron-induced photons and neutron dose [129]. These sources cannot be deactivated during periods of non-use and transport and must be shielded instead. A recent scoping study indicated the potential for resonance analysis using a radioisotope source over a period of days [130].

The remaining category of neutron sources is accelerator-based platforms, the benefits of which include a high degree of control over neutron production. Several excellent literature reviews and studies have highlighted the capabilities of various compact accelerators [130]–[133]. The mechanism of acceleration may be classified as linear accelerator (LINAC), laser, or cyclotron. Systems are further defined by the neutron-producing reaction, including the accelerated particle and target material. Compact cyclotron design has seen steady improvements, with recent models featuring reduced mass and shielding [134]. However, these units still require transportation via a tractor trailer, thus excluding them from this research definition of portability. Laser-driven sources can provide high neutron flux in very short pulses (on the order of femtoseconds in some cases [135]). There has been rapid development over the past two decades in increasing the light intensity of benchtop lasers while miniaturizing power generation and improving target design [136], [137]. Perkins, *et al.* have shown the potential for the portable-scale generation of 10^{15} n cm^{-2} s^{-1} pending the resolution of outstanding issues in fast ion production, laser design, and simulation [136]. Although the state-of-the-art laser-driven neutron

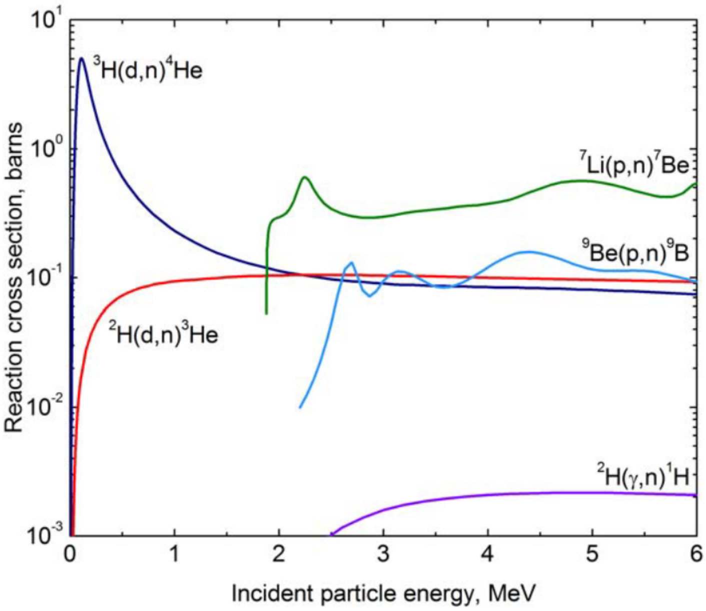

Figure 3-1: Fusion reaction cross sections for neutron producing reactions used in accelerator-based platforms. Plot from [138].

sources today do not meet the cost and size requirements for this research, they are a possible future option should development keep its current pace.

The most viable candidates for portable neutron production are compact accelerator-based neutron sources. Within this category, there exists a range of sizes, from hundreds of kilograms for compact radio-frequency quadrupole accelerators (RFQ) [139], [140] to 40 kg sealed tube neutron generators [141]. These fusion-based neutron sources, also known as electronic neutron generators, are technologically mature and have been ruggedized for various industrial applications, including borehole logging and bulk raw materials assessment. Tube generators primarily use the ^{2}H(d,n)^{3}He (deuterium-deuterium, D-D) or ^{3}H(d,n)^{4}He (deuterium-tritium, D-T) reactions. In D-D reactions, neutrons are generated with an energy of 2.45 MeV when emitted perpendicular to the incident particle's path in the center of mass frame. This energy is closer to the desired epithermal range than the 14.1 MeV neutrons produced by the DT reactions, implying that less moderation is required. However, as shown in Fig. 3-1, D-T fusion exhibits a higher energy-dependent cross section than D-D, corresponding to their respective neutron yields for the same deuteron acceleration.

3.3.1 D-T Generators

A D-T generator is chosen as the optimal neutron source for this project due to its high flux, portability, cost-effectiveness, and technical maturity. Initial NRTA

Table 3.1: Technical Specifications of a P383 Neutron Generator [142]

Parameter	**Specification**
Nominal Max. Yield	3.0E+08 n/s
DT Power Draw	45 watts
Accelerating Voltage	-60 to -130 kV
Control Software	Open-source text & GUI
Pulse Range	0.5 to 20 kHz
Frequency & Duty Cycle	0.5 to 20 kHz; 5% to 90%, continuous
Weight	20 pounds
Operating Temperature	-10 to +50 C
Operating Range	20 to 70 μa, 60 to 130 kV
Minimum Pulse Width	5 μs
Pulse Rise/Fall time	2.0 / 0.5 μs
Input Power	24 VDC
Control Interface	Ethernet (UDPv4)
Typical Tube Life	1,500 hours @ 3E+08 n/s, 4,500 hours @ 1E+08 n/s

Courtesy of Thermo Fisher Scientific

research used a Thermo Fisher Scientific A320 model; however, the research group acquired a Thermo Fisher P383 model in 2022, with which all NRCA research was carried out. The technical specifications for the P383 model are detailed in Table 3.1. Key features of this model, such as a high nominal flux of 3x10^8 n / s, a lightweight design, a long tube life and a power draw of only 45 W, make it particularly suitable for isotopic NRCA.

The D-T system configuration is divided into an accelerator assembly and an electronics assembly in a remote interface unit. Notably, the integration of the high voltage power system inside the accelerator tube is unique to this model family. This improves safety and simplifies the setup and movement of the accelerator, although it complicates component replacement. A 100 foot cable bundle between the accelerator and interface unit provides sufficient length for routing through cable chases in the biological shielding between the control room and experimental laboratory. This research also found that the cable length is adequate to maintain the unshielded, combined neutron/γ-ray dose to an operator at levels below 1 mrem/h, as discussed in Chapter 6.

An understanding of the operation and primary systems of the D-T tube was crucial in optimizing its performance for NRCA and performing field maintenance during this research. A brief overview of the components and their functions is presented in the following section. A discussion on lessons learned in fault prevention, troubleshooting, and recommendations for future D-T generator purchases in Sect. 6.5.3.

3.3.2 Principles of D-T Operation

Within the accelerator assembly of a D-T generator is the vacuum-sealed accelerator tube and the high-voltage power supply (HVPS), surrounded by the housing assembly. The accelerator housing serves to isolate the internal components from physical, electrical, and magnetic interference, while also containing sulfur hexafluoride gas (SF_6) under high pressure. This gas acts as a dielectric, providing sufficient insulation between the HVPS and the acceleration potential in the vacuum tube to enable their connection at high voltages without electrical breakdown [138]. The vacuum envelope, shown in Fig. 3-2, contains an ion source, the ion acceleration section, and a hydride target, cooled by a heat sink. The P383 employs a cold-cathode, Penning ion source, which requires a magnetic field supplied by a surrounding ring magnet [143].

During operation, the control interface receives inputs from the operator and verifies the satisfaction of the safety interlock logic. The control interface also communicates with and powers the HVPS and low-voltage components in the accelerator assembly, regulating neutron production according to programmed and user-specified parameters. Specifically in the P383 model, an open interlock circuit results in a series of open relays that inhibit the 24VDC power from reaching the HVPS [143]. Without the HVPS, the ion source cannot generate the D-T ions necessary for neutron production, protecting from accidental exposure based on the interlock system design. The P383 also receives its source pulser specifications from the remote interface and relays information on temperature, pressure, current, and voltage back to the digital user interface (a computer connected via ethernet). This communications pathway is designed to disable the HVPS in the event of a communications timeout exceeding 5 seconds, preventing a loss of accelerator control.

The deuterium and tritium gases are stored within a gas reservoir as metal hydrides in a getter, which releases the gases upon heating by a thin element controlled by the PID logic of the tube [145]. The cathode in the Penning ion source emits electrons, which are attracted to the anode and redirected by a strong perpendicular magnetic field in the ionizing chamber, ionizing the ambient D-T gas. These ions pass through an exit screen and are accelerated into a D-T impregnated hydride target where neutron-producing fusion occurs [138], [143]. This target is coupled to a copper heat sink and ultimately the accelerator housing, which

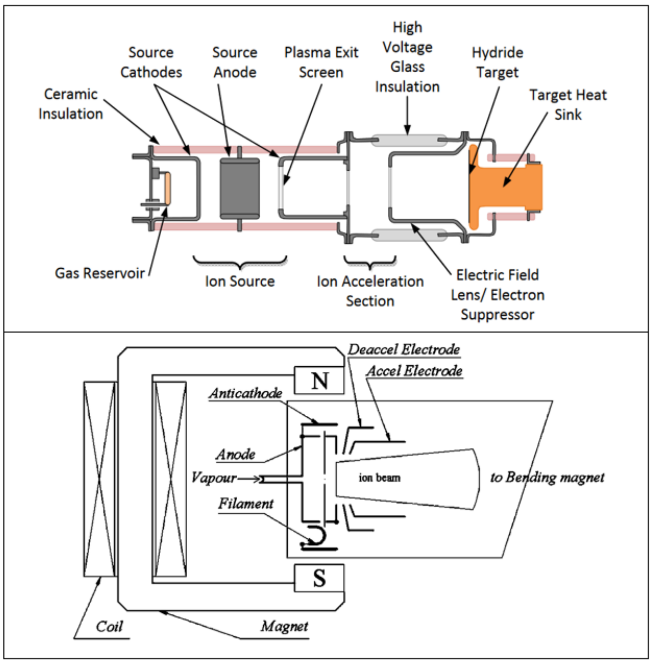

Figure 3-2: Top: schematic cross section of a vacuum-sealed neutron tube by Chichester, based on design by Sandia National Laboratory and sold commercially by Thermo Fisher [138]. Bottom: a schematic of a Penning ion source [144].

dissipates heat convectively. The P383 design uses field effect transistors (FET) for rapid switching of the ion source, giving precise control over when the neutron pulse ends [143].

The user may specify values for beam current and high voltage within the ranges shown in Table 3.1. The user graphical interface displays the output beam current, high voltage, and getter current as calculated by the PID control logic. This feedback loop logic is written to preserve neutron output rate by monitoring the ion current at the target and adjusting the D-T gas available through adjustments to the getter current. The neutron flux scales with the beam current in a generally linear fashion; however, the manufacturer advises that lower currents contribute to the long-term performance of the device [143]. The accelerator voltage contributes to neutron flux through a power-law relationship, where flux increases as the voltage is raised to the power of three-halves. At 90 kV and 50 μ A, the generator will nominally produce 1x10^8 n/s. Overall, the P383 model features advanced control and safety mechanisms that make it an excellent candidate for field-based neutron resonance analysis.

Pulse Width, Flux, and D-T Longevity

The D-T generator is a complex instrument in which operation and output are affected by input parameters in both linear and nonlinear relationships. The shape of the neutron pulse and total flux output are critical characteristics that require analysis to determine their mutual impacts, as well as their effects on the NRCA system effectiveness and the lifespan of the D-T tube. Although operators have the ability to select several tunable parameters, the ultimate flux and pulse shape outputs are governed by the digital control logic. These parameters include beam current and accelerator voltage, which function as previously described, and duty cycle, which adjusts the operational time of the ion source relative to a set pulsing frequency. Notably, the control logic monitors the ion current on target and makes automatic adjustments to maintain consistent neutron flux levels. The shape of the pulse is determined primarily by duty cycle, but the beam current and voltage also contribute.

Multiple parameter studies have been conducted with the goal of optimizing D-T generator settings to provide the highest flux and shortest pulse width while maximizing D-T tube longevity. Figures 3-3, 3-4 and 3-5 show the pulse width and amplitude (corresponding to neutron flux) for varied parameter settings. The limits of the axes on each plot are kept consistent to aid visual comparison. Each measurement was conducted with the P383 D-T generator in the multiplier-moderator cuff assembly with an internal HVPS voltage of 2100 V. A 2x2" EJ-309 liquid organic scintillator, coupled to a photomultiplier tube (PMT) and biased at -1500 V, was placed 1.7 m from the D-T target plane. The detected signals were digitized by a CAEN V1725 14-bit, 250MS acquisition unit, and pulse shape discrimination (PSD) was applied to separate the fast neutron from photon events. The neutron time of flight was calculated relative to a 3.3 V transistor-transistor logic (TTL) trigger signal output by the remote interface unit.

D-T Generator Beam Current

Fig. 3-3 shows the D-T pulse shape as a function of changing beam current while holding voltage constant at 110 kV and the duty cycle at 3.1%. As the beam current increases, the flux increases in the form of a higher pulse amplitude but also a wider pulse width. Conversely, at lower currents the ion source exhibits a higher latency generating plasma relative to the pulse ‘start’ signal. This effect suggests that a lower current is preferred when a shorter pulse is desired but at the expense of reduced neutron flux. The impacts of the solid-state FET switches on the ion source

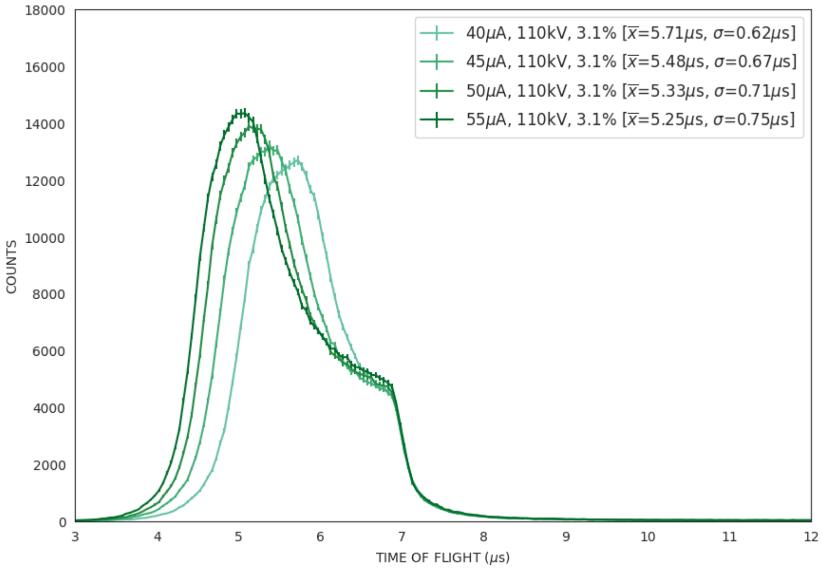

Figure 3-3: Changes to neutron pulse shape as a function of changing beam current. Neutron counts determined by pulse shape discrimination, 2x2" EJ-309 detector, 180 second counts, 50 ns bin widths.

are clear in this plot, resulting in a very sharp neutron cut off, regardless of when the pulse begins.

D-T Generator Acceleration Voltage

Fig. 3-4 shows a varying acceleration voltage while the beam current is maintained at 40 μ A and the duty cycle at 3.1%. The dependence of flux on voltage is apparent in the figure, roughly scaling as a power law for voltages above 90 kV. Likewise, the neutron pulse begins earlier relative to the TTL signal as the accelerator voltage increases. This indicates another instance of trade-off between high neutron flux and short pulse width. An attempt was made to operate the machine at 130 kV as part of this study, but was abandoned due to the indication of an unstable voltage-getter current solution. An example of the GUI readout during an instability condition is available in Appendix B, Fig. B-2. The machine will continue to operate during an unstable PID control logic output until a parameter (usually the getter current) transient exceeds limits, triggering a rapid shutdown.

D-T Generator Duty Cycle

Finally, Fig. 3-5 illustrates the effects of varying duty cycle on the shape of the neutron production pulse. Thermo Fisher has published the nominal duty cycle of the P383 model at no lower than 5%. The pulse width of the generator is dependent

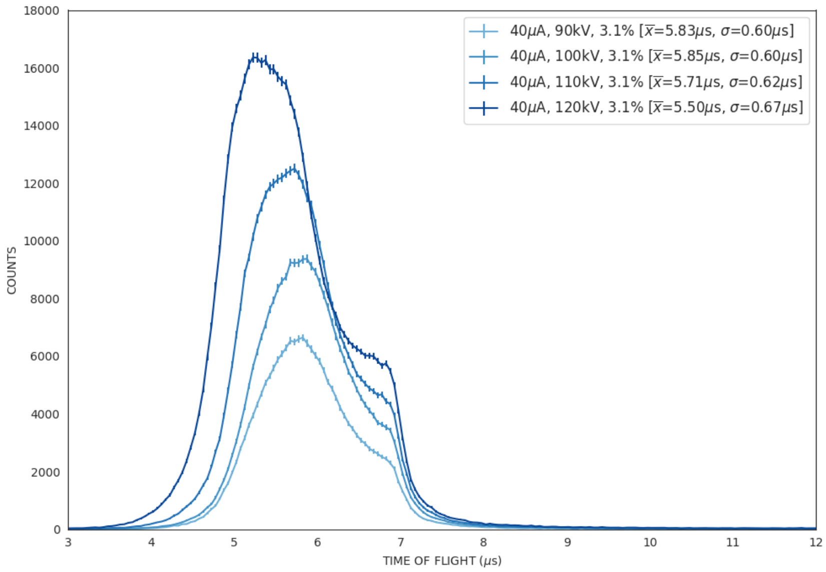

Figure 3-4: Changes to neutron pulse shape as a function of changing accelerator voltage. Neutron counts determined by pulse shape discrimination, 2x2" EJ-309 detector, 180 second counts, 50 ns bin widths.

on the selected operating frequency and duty cycle as

$$t_{\text{pulse}} = \frac{\text{duty cycle }\%/100\%}{f\,[\,\text{s}^{-1}]} \cdot \frac{1\times 10^{6}\text{us}}{1\text{ s}} = \frac{\text{DC}[\%]}{f[\text{kHz}]} \cdot 10 = \text{DC}\cdot T[\mu\text{s}], \tag{3.4}$$

where T is the period of pulse operation and f the corresponding frequency. As evidenced in each of the three plots, the start time of neutrons is not immediate upon initiation of the electrical signal (occurring at TOF $\approx 0\mu$s). This is due to a latency in plasma production at the Penning ion source and is affected by the selected beam current and accelerator voltage. Therefore, selecting a duty cycle of 5% at a repetition frequency of 5 kHz does not equate to 10 μs of neutron production as Eq. 3.4 suggests, but rather ≈6 μs depending on current and voltage. The general course of neutron production is evident in this plot, with a Gaussian component corresponding to the initial plasma formation. This is followed by a secondary plateau during which the getter current is maintained at a near constant level to release the D-T gas to the ion source, thereby producing neutrons until the FET switches disable the source cathode. During an optimization study, it was found that the duty cycle could be tuned lower than the manufacturer-provided 5%, with 3. 1% producing the shortest pulse before reaching an unstable condition.

A comprehensive study of impacts on pulse shape and neutron flux by varying beam current, acceleration voltage, and duty cycle has been published in [75]. The study assigned a merit figure that maximized flux while minimizing the standard

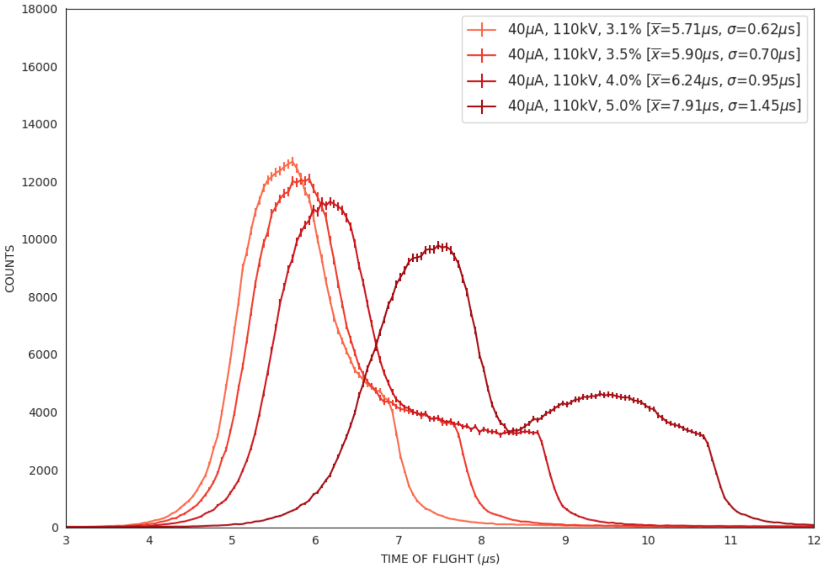

Figure 3-5: Changes to neutron pulse shape as a function of changing duty cycle. Neutron counts determined by pulse shape discrimination, 2x2" EJ-309 detector, 180 second counts, 50 ns bin widths.

deviation of the pulse width. This figure reached a global optimum at 3.1% duty cycle, 45 μA beam current and 120 kV acceleration voltage. Reducing the voltage to 110 kV and the current to 40 μA decreases the flux by 30%, improves the pulse standard deviation by 10%, and decreases the operating stresses on the tube electronics. These parameters were used for all measurements in the NRCA research, unless otherwise noted. They generate a pulse centroid of 5.82 μs (5.76 μs for the Gaussian component only) and a standard deviation of 0.62 μs.

As will be shown in Sect. 4.2, the pulse width of the generator dominates the uncertainty in neutron flight time and has a significant contribution to the energy resolution function of the system. Minimizing the pulse width minimizes uncertainty in energy reconstruction. Considering the variations in shape and plateau of the pulse based on input parameters, it may be modeled as a uniform distribution with standard deviation:

$$\sigma_{pulse} \approx \frac{k \cdot \mathrm{DC} \cdot T}{\sqrt{12}}, \tag{3.5}$$

where k is a proportionality constant between the nominal pulse width in Eq. 3.4 and the measured pulse width. This proportionality is $\frac{1}{3}$ for the parameters used in this research.

3.4 Neutron Moderator

Neutrons are generated in the D-T reaction with a mean energy of 14.1 MeV; six orders of magnitude higher than the targeted epithermal resonance region of 1 to 100 eV. The primary purpose of a source moderator is to slow these neutrons to the desired energy range through successive collisions with the constituent nuclei. According to the conservation of momentum and energy, the maximum fraction of the initial neutron kinetic energy that is transferred to a moderator nucleus of mass number A during a single elastic collision is:

$$\left(\frac{E}{E_o}\right)_{max} = 1 - \left(\frac{A-1}{A+1}\right)^2. \tag{3.6}$$

Eq. 3.6 indicates that for hydrogen ($A = 1$), a maximum of 100% of the incoming neutron energy can be lost in a single collision. The probability of a neutron with energy E_o exiting a collision with energy between E and $E + dE$ varies according to a uniform distribution [146]:

$$P(E_o \to E)dE = \frac{1}{E_o} dE(E_o \geq E). \tag{3.7}$$

In a sufficiently large moderator, fast neutrons undergo enough collisions to equilibrate their kinetic energy with the moderator's temperature. The average logarithmic energy decrease per collision ξ quantitatively describes how much energy a neutron loses on average with each collision. ξ can be used to determine the average number of collisions, $\bar{n}$, to moderate energies from E_o to the target energy E:

$$\bar{n} = \frac{\ln(E_o/E)}{\xi}. \tag{3.8}$$

However, not all neutron interactions result in a scattering event. The effects of absorption in a particular material are quantified using the moderation ratio, which is the product of the logarithmic energy decrement and the ratio of the macroscopic scattering and absorption cross sections, $\xi \frac{\Sigma_s}{\Sigma_a}$. The moderation ratio, plotted for several moderator compositions in Fig. 3-6, provides a metric for the probability of scatter versus absorption for a given neutron energy. The average number of collisions, also plotted in the figure, gives an intuition for the distance and temporal spread of an epithermal neutron exiting the moderator. The more effective a moderator is in slowing a neutron from MeV to eV, the lower the uncertainty in calculating the neutron energy based on its TOF. Polyethylene (approximated here

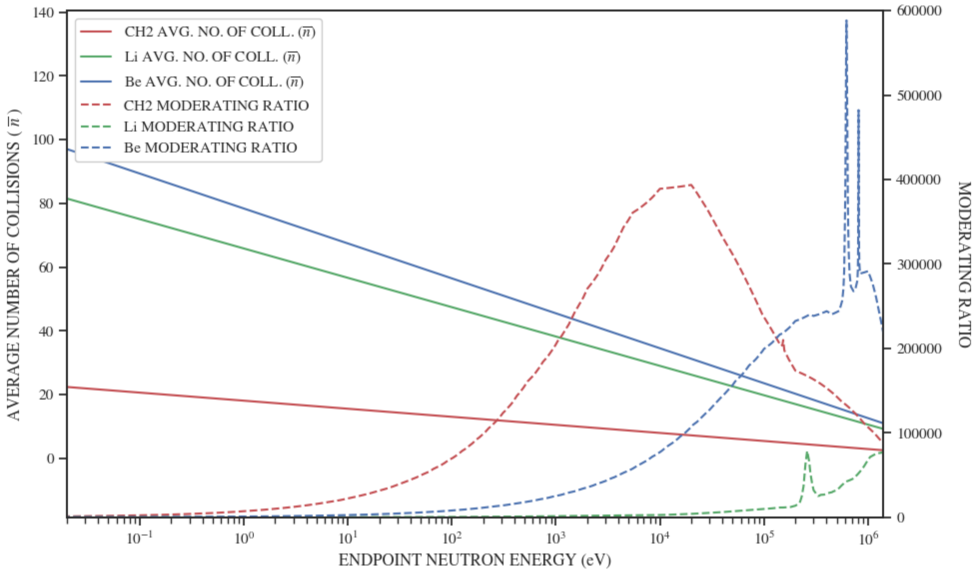

Figure 3-6: Average number of collisions to neutron endpoint energy and moderating ratio for polyethylene (approximated as CH_2), lithium and beryllium. Plot generated using data from ENDF/B-VII.1

as CH_2) is the most effective moderator to slow neutrons to epithermal energies while preserving flux.

The stochastic process of moderation produces a distribution of times that it takes for a neutron of energy E to be 'born' at the fusion target, moderate, and exit the moderator. This distribution of time delays is a function of the energies and velocity vectors of neutrons leaving the D-T target plane, as well as the material properties of the moderator [147]. Groenewold and Groendijk have shown that the time distribution of neutrons moderating in an infinite hydrogenous medium is a function of their energy and λ, the mean free path in the material. The average moderation time is $3\lambda\sqrt{\frac{m}{2E}}$ with a standard deviation of $\sqrt{3}\lambda\sqrt{\frac{m}{2E}}$ [146]. The energy dependence of the time distributions complicates the later reconstruction of the neutron energy based on time; therefore, it is standard practice to represent the moderation process in terms of delay distance. This equation takes the form of a chi-squared function with six degrees of freedom:

$$f(d) = \frac{1}{2\lambda}(d/\lambda)^2 e^{-d/\lambda} \tag{3.9}$$

which has a mean of 3λ and a variance of $3\lambda^2$ [147]. This moderation distance is incorporated into Eq. 3.3 and its variance used in the uncertainty propagation, discussed in Sect. 4.2.1.

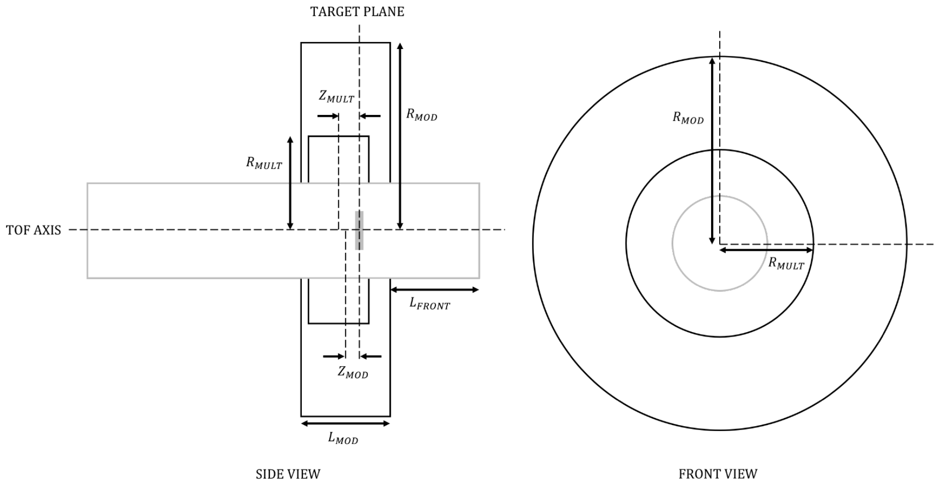

Figure 3-7: Moderator and multiplier geometry relative to the D-T generator housing and target plane. Figure from [75]

A comprehensive moderator study has been performed in Ref. [75] to determine the optimal neutron transport assembly for the D-T-based portable resonance analysis system. MCNP simulations were used to iterate through various geometries, materials, orientations of the D-T tube, and shielding parameters. In particular, the internal layout of the D-T tube significantly influenced the final moderator geometry, shown in Fig. 3-7. The target plane is 12.7 cm behind the front face of the housing assembly, which drove the selection of a radial cuff design to capture a large fraction of the near-isotropically emitted neutrons. A lead multiplier is located between the neutron source and the moderator to leverage the (n,2n) reaction, which occurs in all stable isotopes of lead with a cross section of approximately 2 b for neutrons around 10 MeV [148]. This addition effectively doubles the epithermal neutron flux, with simulations closely aligning with experimental outcomes.

3.5 NRCA Detection Methodology

NRCA is a useful analysis tool for investigating the structure of an atom as well as nondestructively determining the isotopic content of an object. Borella, *et al.* have outlined requirements for the ideal resonance capture photon detection system in large beamline experiments:

- capture event detection efficiency that is independent of the γ-ray cascade (independent of both multiplicity and emitted γ-ray energy),
- low sensitivity to scattered neutrons,

- very good timing response [149].

These requirements can serve as a guideline for detector selection for a compact NRCA system, discussed in Sect. 3.6. Depending on the experimental objectives and setup, there are several types of detector that can meet these specifications. These detectors are grouped into three primary NRCA detection methodologies: total energy detection, total absorption detection, and spectroscopic. The purpose, applications, advantages, and limitations of each technique are presented in the following, along with a short discussion of methodology extensions to portable NRCA.

3.5.1 Total Absorption Detection

The total absorption detection method is based on the detection of all γ-rays emitted during a capture event. Ideally, the detection system has 100% efficiency for each possible energy in a cascade and a 4π geometry around a sample [149]. While the realization of these requirements is not possible in practice, experiments that use this method feature very large arrangements of high-efficiency scintillators to best approximate 4π coverage. A particular use case for this system is exploration of the unresolved resonance and high-energy regions of the neutron spectrum [150]. They are also beneficial for multiplicity determinations and investigations of the quasicontinuum energy levels in medium- and high-Z isotopes [92]. Toward this end, the RPI 16 segment NaI(Tl) detector has been heavily characterized to understand the effects of instrument multiplicity on experimental data [151], [152].

Many large facilities have a total absorption detector comprised of varying types of large-volume scintillators. For example, the Karlsruhe 4π experiment utilizes 42 BaF_2 crystals, while the Los Alamos Neutron Scattering Center operates with 162 BaF_2 elements [149], [150]. The Kurchatov Atomic Energy Institute employs a 48-section 180-liter NaI array [153], and the Japan Spallation Neutron Source uses germanium cluster detectors surrounded by a bismuth germanate coincidence shield [92]. These size of these setups enhances counting statistics for low-probability γ-ray transitions and are useful for the production and verification of nuclear data tables. However, the primary limitation of applying total absorption detection in a portable concept is the considerable size and weight of the detectors, which makes them impractical for mobile applications. In the case of a small truck-mounted safeguard isotopic analysis system, follow-up NRCA investigations could research a small total absorption setup to improve statistics and counting times.

3.5.2 Total Energy Detection

NRCA employs the total energy detection methodology, which is based on the principle that a NRCA using the total energy detection methodology relies on the proportionality of a detector's efficiency and the energy of the detected γ-ray. By selecting a detector with a sufficiently *low* efficiency of detection (so that at most one γ-ray from a given cascade is detected), the capture event detection efficiency becomes proportional to the excitation energy of the reaction [149]. To improve counting statistics, Maier-Leibnitz proposed the use of a more efficient detector (10 - 20%) with a post-processing application of a pulse height weighting function to maintain the proportionality of efficiency and excitation energy [154]. Hydrogen-free liquid scintillators like C_6D_6 and C_6F_6 offer fast time resolution, reduced neutron capture background compared to hydrogenous scintillators, and a well-documented response function [154]. The advantages of this technique include its simplicity, low background noise, and extensive optimization and characterization over decades. It is widely used for both nuclear data collection and isotopic analysis [155]–[157].

Aspects of the total energy detection method offer some extensibility to portable NRCA system development. For the neutron energies used in this research, C_6D_6 detectors have the lowest neutron sensitivity of all known detector types [154]. However, these detectors also have disadvantages, particularly the high cost of deuterated benzene, which has risen from fifty to over one hundred US dollars for 10 grams over the past few years. The low efficiency is also an issue, requiring longer counting times than an inorganic scintillator, for instance. Due to its widespread use and proven record in isotopic analysis NRCA, a C_6D_6 detector was selected as one of the candidates for the following detector study.

3.5.3 Spectroscopic

The gamma-spectroscopic method of detection is used primarily for nuclear data collection, although recent proposals suggest that it is useful for the assessment of contaminants in isotopic analysis [158]. Spectroscopic NRCA is typically performed in the same facilities as traditional NRCA using high purity germanium (HPGe) detectors. These detectors have excellent energy resolution, allowing researchers to identify specific γ-ray energies associated with a level transition in the de-excitation of the compound nucleus. By deconstructing a single TOF-spectrum count peak into individual energies, this method determines information about the level transitions of a specific resonance. Counts are adjusted by a correction factor accounting for total neutron cross section, self-shielding, nonlinearity of efficiency with energy, and

γ-ray attenuation, as well as background rejection through a Compton suppression system. [159]. The partial capture cross sections determined from each primary γ-ray (defined in Sect. 2.1.2) are summed to find the total capture cross section. To account for systematic uncertainties, these cross sections are normalized and reported relative to a well-characterized γ-ray transition from a comparator isotope, often ^{14}N(n,γ) [159].

An advantage of this detection methodology is the additional resonance and nuclear structure information provided by dual TOF- and energy-spectroscopy. These data are used to populate nuclear databases and are of utmost importance for nuclear energy criticality and astronomical nucleosynthesis modeling [90]. As introduced in Chapter 2, nuclear energy level schemes become increasingly complex with increasing atomic number, culminating in the unresolved quasicontinuum region. Spectroscopic methods are limited to γ-ray transitions that have a sufficient probability to be resolved as a peak above the background created by the sample, experimental equipment, and continuous spectrum radiative capture γ-rays. This restricts their utility to isotopes with simple level schemes, or primary and ground state-feeding γ-rays in heavier isotopes [149].

The nuclear resonance densitometry (NRD) experiment, developed by a collaboration of the European Commission-Joint Research Center (ER-JRC) and the Japan Atomic Energy Agency (JAEA), is a notable example of spectroscopic NRCA [90]. This research proposes a method to quantify special nuclear material in fresh and spent reactor fuels, as well as fuel debris after a reactor accident. The technique, performed at a large, pulsed neutron source facility, combines NRTA for fissile and fertile material assay and spectroscopic NRCA for the determination of impurities and to constrain the results of the NRTA. Traditional NRTA is confounded by the particle-like debris from the Fukushima Daiichi accident, which has a large variation in size, shape and contamination of melted structural material, including H, B, Cl, Fe and Ni [90]. Spectroscopic NRCA provides an additional source of information on the sample, including the determination of neutron-absorbing contaminants such as boron by their characteristic thermal capture γ-ray energies. Note that this is a combination of resonance-sensitive NRCA and thermal neutron-driven PGAA techniques.

This NRD research collaboration has developed a custom large-volume $LaBr_3$ scintillator and a graded shield to improve both TOF and energy spectra [160]. The care taken in background reduction, characterization, and peak-to-Compton ratio enhancement provides insights for portable NRCA development. The use of a $LaBr_3$ detector is also notable. HPGe detectors are sensitive to neutron-induced damage that impacts charge collection, thereby reducing energy resolution. While the large-scale facilities have decreased neutron background due to collimation and standoff from the neutron production source, the nature of compact NRCA necessitates that the detector be exposed to prolonged high neutron flux. $LaBr_3$ provides a possible alternative that would allow spectroscopic NRCA in a portable system.

3.6 Detector Comparison and Selection

The objective of the detector comparison study was to determine which detector type is best suited to provide neutron resonance capture information to qualitatively and quantitatively assess an unknown sample. Detectors are usually compared on the basis of criteria such as efficiency, energy resolution, timing, cost, and broad operational considerations. Given the proximity of the detector to the D-T generator in this miniaturized concept, neutron sensitivity was also an important consideration. Together, the neutron sensitivity, efficiency, and energy resolution contribute to a detector's signal-to-noise ratio (SNR). This ratio, along with the remaining criteria, formed the basis of selection.

3.6.1 Comparative Analysis

The detector types analyzed in this study were sodium iodide (NaI), bismuth germanate (BGO, $Bi_4Ge_3O_{12}$), lanthanum bromide ($LaBr_3$), EJ-309 liquid organic scintillator, and EJ-315 deuterated benzene liquid organic scintillator. Each type of detector has been used in NRCA research in other facilities, based on the experimental setup and objectives of the study. Although hydrogen-containing scintillators have been exchanged in favor of C_6D_6 detectors in NRCA total energy detection experiments, EJ-309 was included in this study due to its widespread availability and affordability. EJ-315 was selected for its characteristic low sensitivity to neutrons. An encapsulated 100 cc volume of deuterated benzene was purchased from the manufacturer and optically coupled to a PMT in-house. LaB_3 was chosen for its high efficiency and energy resolution, given its success in the spectroscopic NRCA methodology. NaI(Tl) was also selected for its high efficiency, large volume, and cost-effectiveness. After observing the positive effects of the efficiency and volume of the NaI scintillator on counting statistics, but deterred by its neutron sensitivity, BGO was selected as the last detector obtained for this study. Due to its high effective atomic number and low neutron sensitivity relative to NaI, a large-format BGO detector was custom ordered from the manufacturer. A photo of

Figure 3-8: A photo of the five detectors selected for this study, specifications available in Table 3.2

the five detectors with voltage divider bases attached is provided in Fig. 3-8 and specifications listed in Table 3.2.

Table 3.2: Detector Specifications

Detector Type	**Manufacturer**	**Model**	**Size**	**Density [g/cm^3]**	**Operating Voltage**
EJ-309	Eljen Tech.	510-20x20-11	2 x 2"	0.96	-1300 V
EJ-315	Eljen Tech.	VMF 20x20-1	2 x 2"	0.95	+1500 V
LaBr$_3$	Canberra (Mirion)	LABR-1.5X1.5	1.5 x 1.5"	5.1	+800 V
NaI(Tl)	Bicron	3M3/3-X	3 x 3"	3.7	+1000
BGO	Hilger (Dynasil)	W2513.MK1	3 x 3"	7.1	+1200 V

Most inorganic scintillators have constituent elements with high atomic numbers, taking advantage of the increased photon interaction probability and higher density. These elements typically exhibit more complex level schemes than their lighter counterparts, resulting in more numerous and pronounced resonances in the epithermal region. When choosing a detector for an NRCA application, neutron sensitivity is of the highest importance. Halide and oxide scintillators containing isotopes with epithermal resonances will register a much larger capture signature than a sample isotope of similar isotopic mass and cross section. This effect is due to the resonance capture photons being intrinsically produced in the detector and therefore detected with high geometric efficiency. Depending on the strength of the detector isotope resonance affinity, this may either add to the resonance capture signal from a sample or obscure it entirely. Table 3.4 presents information on isotopes with epithermal and thermal neutron sensitivities for the detector types considered in this research. The epithermal resonances of isotopes of lanthanum,

Table 3.3: Detector Characteristics

Detector Type	**Intrinsic Efficiency**	**Energy Resolution**	**Cost**	**Decay Time**	**Operational Considerations**
EJ-309	Low	Low	Moderate	Very fast	^{1}H-capture
EJ-315	Low	Low	Very High	Very fast	Benzene (toxic)
$LaBr_3$	Very High	High	High	Fast	Resonance captures
NaI	High	High	Low	Slow	Resonance captures
BGO	Very high	Moderate	Moderate	Slow	Low light yield

bromine, iodine, and germanium are listed in the table, with effects visible in Fig. 3-10.

Detector neutron sensitivity is not limited to resonance effects. Thermal neutrons from previous D-T pulses capture on experimental and structural features in the environment, and a detector isotope with a large thermal capture cross section will likewise have a large prompt capture γ-ray contribution. One of the most significant contributions to non-sample background is ^{1}H in the EJ-309 detector, the moderator cuff, and in the concrete of the lab floors, walls, and ceiling. The resulting ^{2}H has an excitation energy of 2.2 MeV but without intermediate level structure, 100% of absorption events are followed by a γ-ray carrying the entire excitation energy. Although other elements prominent in structural materials such as carbon, oxygen, and iron also emit thermal capture γ -rays, they are of varied (usually lower) energies and have significantly lower capture cross sections than hydrogen. Management of the thermal capture γ-rays is discussed thoroughly in Sect. 4.3.

3.6.2 Results

Each detector in the study was used to measure the energy spectrum of two check sources (^{137}Cs and ^{60}Co), digitized by a 14-bit CAEN V1725 250MS acquisition unit. The spectra were calibrated according to the full-energy peaks for the inorganic scintillators and the Compton edges for the organic scintillators. The results are plotted in Fig. 3-9 and display several notable features. The Compton edges of the two liquid organic scintillators are visible; each are able to resolve the ^{60}Co 1.17 and 1.33 MeV γ-rays as two separate peaks. $LaBr_3$ is the only detector capable of resolving the 1.33 MeV ^{60}Co peak from the ambient background 1.47 MeV ^{40}K peak. Note that even with a logarithmic count axis, the increased geometric and intrinsic efficiencies of the 3 x 3" BGO and NaI are apparent, especially at higher energies.

Table 3.4: Neutron Sensitivity of Scintillator Detectors

Detector	**Major Isotopes**	**Thermal (n,γ) Cross Section [b]**	**Epithermal (n,γ) Resonances [eV, b]**	**Capture Product Half-life**
EJ-309	^{1}H (100%)	0.33*	None	Stable
	^{12}C (99%)	0.004	None	Stable
EJ-315	^{2}H (100%)	0.00052	None	12.5 y (β^-)
$LaBr_3$	^{139}La (100%)	8.97	70 eV, 1 kb	1.6 d (β^-)
	^{79}Br (51%)	10	35 eV, 3.7 kb	17 m (β^-,β^+)
	^{81}Br (49%)	2.4	81 eV, 2 kb	35 h (β^-)
NaI	^{23}Na (100%)	0.03	None	15 h (β^-)
	^{127}I (100%)	6.2	Multiple, kb	24 m (β^-,β^+)
BGO	^{209}Bi (100%)	0.03	None	5 d (β^-)
	^{70}Ge (20.5%)	2.7	None	11 d (EC)
	^{72}Ge (27.4%)	0.7	None	Stable
	^{73}Ge (7.7%)	0.2	100 eV, 1 kb	Stable
	^{74}Ge (36.5%)	0.4	None	Stable
	^{76}Ge (7.75%)	0.1	None	11 h (β^-)
	^{16}O (100%)	0.0002	None	Stable

* This capture is followed by a prompt 2.2 MeV γ-ray

The molecular structure of BGO leads to only a small fraction of the deposited photon energy being transferred to visible light and collected by the PMT. The mean energy required to create a photon in BGO is ≈300 eV, compared to NaI(Tl) at ≈25 eV [161]. The energy resolution of the BGO is poor compared to that of the other inorganic scintillators, barely resolving the ^{60}Co 1.17 and 1.33 MeV γ-rays as two separate peaks in Fig. 3-9. The BGO used in this research has a particularly poor resolution compared to other BGO characterizations (90 keV resolution at the 662 keV peak versus 36 keV in Ref. [162].) It also registered high incidents of spurious noise triggers at detection thresholds less than 450 keV, prompting a parameter optimization study to identify the optimal applied voltage and threshold while minimizing reported deadtimes. A 2 x 2" BGO detector from the same manufacturer was used as a comparator to the 3 x 3" BGO, exhibiting a 30% improvement in resolution and a lower limit of detection at 300 keV. Despite the energy spectrum improvements, the 3 x 3" BGO was retained in the study due to its high intrinsic and geometric efficiencies relative to its smaller counterpart.

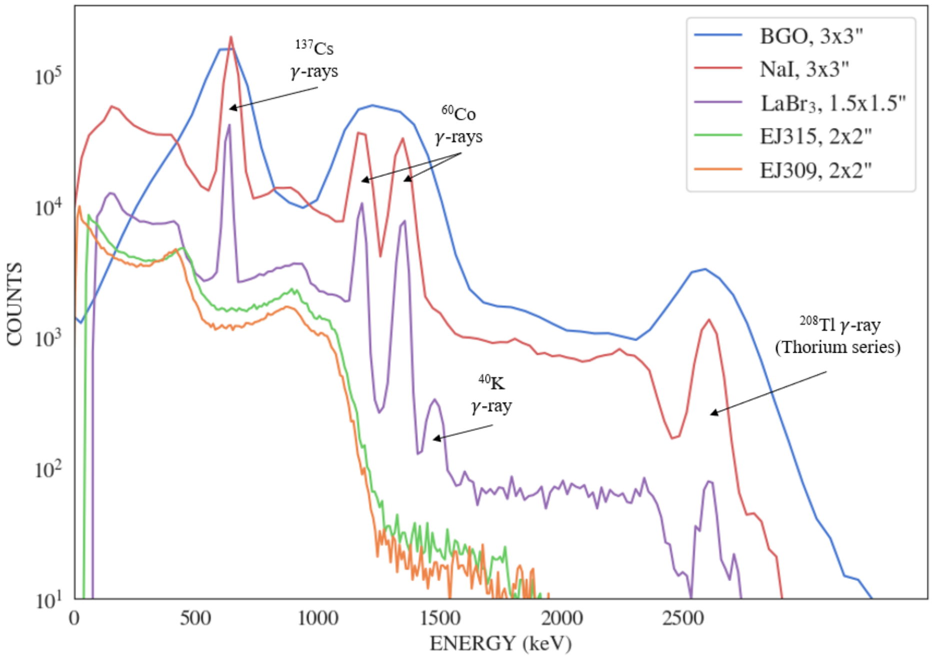

Figure 3-9: Comparative energy spectra of ^{137}Cs and ^{60}Co check sources for each detector in the study with energy peaks indicated. Each plot was acquired for 3 minutes using settings from Table 3.2.

The most important detector attribute to examine is the time-dependant (n,γ) capture signal. Each detector was placed at 1.77 m from the D-T target plane at 180^o to the neutron path direction in the same shielding configuration. A 1 mm thick (1.9 g/cm^2 areal density) tungsten foil was oriented perpendicular to the beam axis, proximal to the front face of the detector. The D-T was operated with the optimal parameters determined in Sect. 3.3.2 and each run acquired for 20 minutes. The TOF spectra for each detector candidate are plotted in Fig. 3-10 with bin widths of 0.5 μ. Each spectrum exhibits a baseline γ-ray background that is consistent in time (the background counts recorded per bin at the end of the 200 μs acquisition period return to the same baseline value they were prior to pulse initiation). This background is subtracted from each spectrum to aid in comparing TOF histogram shape and capture γ-ray count peaks. The dashed gray lines in Fig. 3-10 illustrate the TOF location for each tungsten resonance. Peaks that appear off-resonance are due to the detector's intrinsic isotopes with epithermal resonances, listed in Table 3.4.

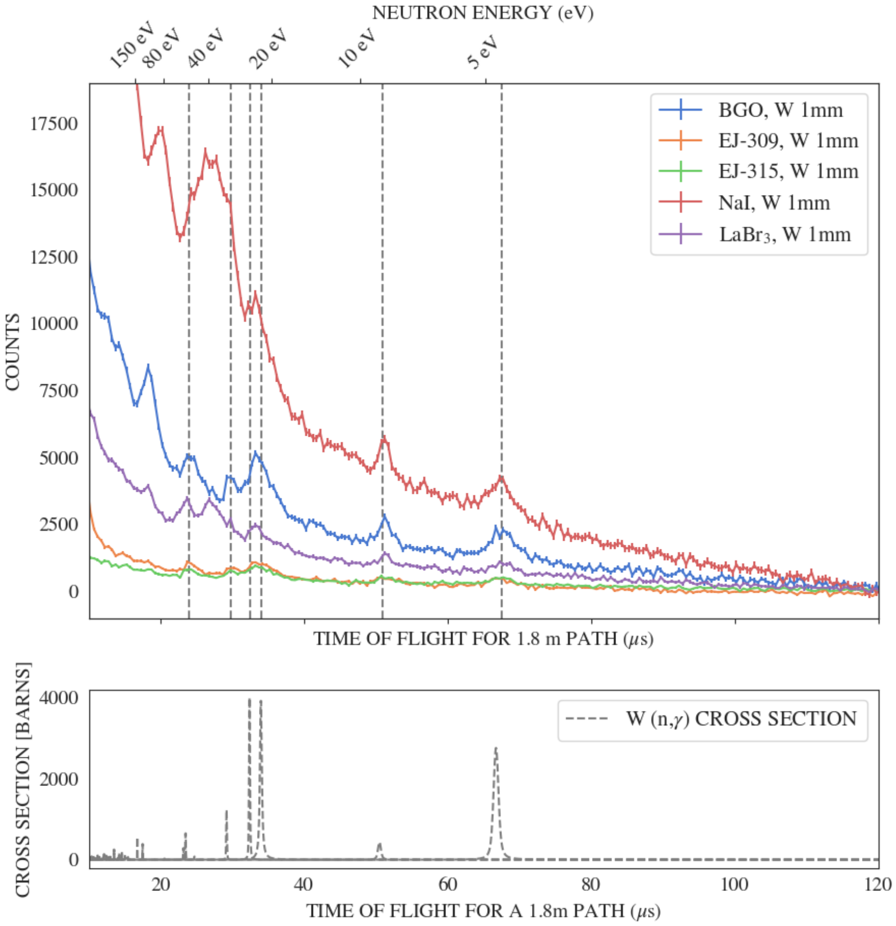

Figure 3-10: Time of flight spectra for each detector studied. Detectors were each oriented in the same position relative to 1 mm foil of tungsten, each run was recorded for 20 minutes with the optimized D-T settings from Sect. 3.3.2. 1σ errors are plotted for each histogram. TOF spectra are background subtracted to enhance visibility of features. The cross sections for the four naturally abundance isotopes of tungsten are plotted below as a function of 1.8 m TOF.

.

3.6.3 SNR and Detector Selection

SNR

The signal-to-noise ratio is a measure of the strength of the radiative capture signal relative to the background noise. The sources of background in this experiment have been extensively researched and characterized in Sect. 4.3. Particular experimental setups, neutron production settings, and targets themselves may influence the SNR; in order to identify the detector yielding the best SNR, all experimental details were held constant. To evaluate each detector's ability to discriminate a true resonance capture signal from the background, a test statistic T is proposed. The test statistic is defined as the ratio of the difference in counts between the sample and the background to the standard deviations of those counts added in quadrature:

$$T = \frac{N_{sample} - N_{bknd}}{\sqrt{\sigma^2_{sample} + \sigma^2_{bknd}}}. \tag{3.10}$$

Here, N_{sample} and N_{bknd} represent the γ-ray counts under the analyte peak for the sample and the same integration region of the background, respectively, while σ^2_{sample} and σ^2_{bknd} are their respective variances. T is therefore a method of quantifying the number of standard deviations a signal is relative to the measurement background. A higher T value indicates a better capability of the detector to resolve the capture signal from the background.

This test statistic is an application of Welch's t-test for unequal means and can be used for hypothesis testing. In an NRCA experiment, the null hypothesis states that there is no statistically significant difference in γ-ray counts between a sample known to exhibit a resonance at neutron energy E_n and a control sample which has similar characteristics affecting γ-ray detection. To test this hypothesis, we set a significance level of $\alpha = 0.1$ and establish a critical value 0f 1.645, which corresponds to the 90$^{\text{th}}$ percentile of the standard normal distribution. A T value above the critical level rejects the null hypothesis. Adjustments to this value can be made to reflect detection confidence standards, including those set by regulatory bodies such as the IAEA.

Selectively reducing noise while preserving the signal is one possible method of improving the signal-to-noise ratio (SNR). Some sources of gamma-ray background are monoenergetic, such as the 2.2 MeV hydrogen capture peak. The BGO detector, characterized by its high effective atomic number, achieves a full energy peak-to-Compton ratio that is 4.5 times higher than that of NaI in the 1-2 MeV range [163]. This attribute allows the BGO detector to maintain more counts in the full energy peak while minimizing counts in the Compton continuum, which underlies the capture gamma-ray signal. This selective removal of energies can also reduce monoenergetic background peaks arising from the sample itself, such as the ^{208}Tl gamma-rays arising from ^{232}Th and ^{232}U. This technique and its applications are discussed in greater detail in the analysis of time-of-flight (TOF) spectra in Chapters 5 and 6.

Detector Selection

The T test statistics for the detectors under evaluation are presented in Table 3.5. Three epithermal tungsten resonances were selected for analysis: the 4.1 eV resonance with a self-shielding value of R = 0.1, the 7.6 eV resonance with a self-shielding value of R = 0.4, and the 46 eV resonance with R = 0.07. Each count peak was integrated to include 1 μs on either side of the peak centroid, applying the same limits of integration to the background count spectrum. Further details on the selection of integration limits are discussed in Chapter 5.

Table 3.5: Detector T-Test Values

Detector		**T-value**	
	4.1 eV	**7.6 eV**	**46 eV**
EJ-309	7.3	5.7	7.6
EJ-315	8.5	6.1	8.5
$LaBr_3$	7.2	5.2	2.4
NaI(Tl)	14.1	12.3	2.2
BGO	17.8	12.7	10.7

The impacts of the detector-intrinsic isotopes with overlapping epithermal resonances are evident in the tungsten 46 eV T test values for NaI and $LaBr_3$. The best SNR values were observed in the 1-100 eV resonance range of interest for the BGO, EJ-315, and EJ-309 detectors. In particular, the BGO detector, with a volume of 347 cm^3, is considerably larger than the two organic scintillators, each with a volume of 102 cm^3. This larger volume, combined with the high density and effective atomic number of BGO, significantly increases its photon stopping power and detection efficiency. Scaling up the EJ-309 or EJ-315 to a size comparable to that of the BGO could potentially increase their geometric efficiency, thereby capturing more radiative capture γ-rays relative to the background; however, this requires modeling or experimentation to verify. This possibility suggests a direction for future research, as discussed in the conclusion of this work.

A weighted criteria matrix was developed to systematically determine the detector best suited for this portable NRCA application. The performance of each detector was evaluated against the following attributes: intrinsic efficiency, energy

Table 3.6: Weighted Criteria Matrix for Detector Evaluation

Detector	**Intrinsic Efficiency**	**Energy Resolution**	**Cost**	**Neutron Insensitivity**	**Peak-to-Compton Ratio**	**Total Score**
Weight	**3**	**2**	**2**	**5**	**2**	
EJ-309	1	2	4	4	1	35
EJ-315	1	2	1	4	1	29
$LaBr_3$	2	4	2	1	2	25
NaI(Tl)	3	3	5	1	2	33
BGO	4	1	4	3	4	42

resolution, cost, neutron sensitivity, and peak-to-Compton ratio. Decay time is not included in the matrix because the pulse-height method of acquisition ensures timely data collection across all detector types. These attributes were weighted on the basis of their importance to the operational effectiveness and accuracy of neutron capture measurements in the portable NRCA setup. For instance, due to the close proximity to the D-T generator, neutron sensitivity was assigned a higher weight, emphasizing its role in minimizing background noise and enhancing the SNR of the system. The BGO was selected as the primary detector for this research due to its superior performance and specific application needs. However, the EJ-315 was also employed in several studies due to its excellent SNR and low neutron sensitivity, making it particularly useful for isolating capture signals.

Chapter 4

System Characterization

Characterizing the sensitivity and resolution of a system allows us to accurately evaluate its empirical performance capabilities. For this portable NRCA system, designed for composite materials analysis, the final evaluation must include the system's sensitivity to both the isotopic composition and isotopic quantity of various target materials. To support this goal, a fundamental understanding of the effects of components on signal and system resolution is required to extract target information from the measured radiative capture counts. This chapter presents a framework for characterizing the NRCA signal, the system resolution, and the background.

4.1 NRCA Signal

The variables of interest in an NRCA experiment are the identities and quantities of isotopes within a sample. These are calculated by the locations and magnitudes of γ-ray count peaks in a time-of-flight (TOF) histogram, respectively. Therefore, the NRCA signal is twofold: the timing of γ-ray count peaks relative to neutron production time and the intensity of these peaks above the background level. System resolution impacts the precision with which the timing of peaks is determined and the corresponding neutron energy is assigned. The background assessment, on the other hand, addresses the accuracy of the peak magnitude quantification amidst the γ-ray noise that is also detected.

Despite the high precision of NRCA experiments at large beamline facilities, TOF histograms do not straightforwardly mirror the radiative capture cross-section plots. Capture resonance structures in the observed data are influenced by several factors:

- the finite resolution of the time-of-flight system, including aspects of neutron production, moderation, and detection timing,

- Doppler broadening effects,
- and neutrons experiencing preliminary scattering interactions in the target or support materials, followed by a capture.

The system resolution function is derived and discussed in Sect. 4.2 using design and characterization data discussed in this chapter and the last. Background characterization and removal algorithms are explored in the next section.

4.1.1 Neutron Characterization

For a neutron to contribute to the radiative capture signal, it must undergo several steps, beginning with moderation to the resonance energy. The neutron must exit the moderator traveling in a direction that leads it to the sample and interact within a time frame consistent with other neutrons contributing to the same resonance peak. This section details system characterization accomplished through MCNP 6.2 models, supported by experimental results where possible. These characterizations and their associated uncertainties support the system resolution characterization in the next section.

Neutron Energy Limits As the kinetic energy of a neutron increases, its time of flight decreases. Due to the shortened beam path and the width of the neutron production pulse in this miniature system, there is an upper energy limit beyond which individual neutron resonances cannot be resolved. Conversely, neutrons with very low energy may not reach the sample before the initiation of the next pulse. Consequently, this limits the operational range of neutron energies to between 1-100 eV. This region aligns with the low-energy portion of the resonance regions for most fuel cycle isotopes. Fig. 4-1 shows arrival times for a 1.8 m beam path of indicated neutron energy groups. As energy increases, neutron energy groups arrive in closer succession and eventually their resonance structures are obscured by the system resolution.

Neutron Moderation and Path Characteristics Neutrons that exit the moderator and are on a trajectory towards the target are termed axial neutrons. Figure 4-2 is an MCNP-6.2 simulation that depicts the flux distribution of these neutrons exiting the moderator. The right-hand image of the figure illustrates the radial spread of epithermal neutrons in the axial direction towards the sample. Over 90% of these neutrons exit the moderator within 10 cm of the central axis, with a median radial distance of 7.2 cm. The mean moderator delay distance for epithermal neutrons prior to exiting is 1.91 cm, with a standard deviation of 1.1 cm, when using a

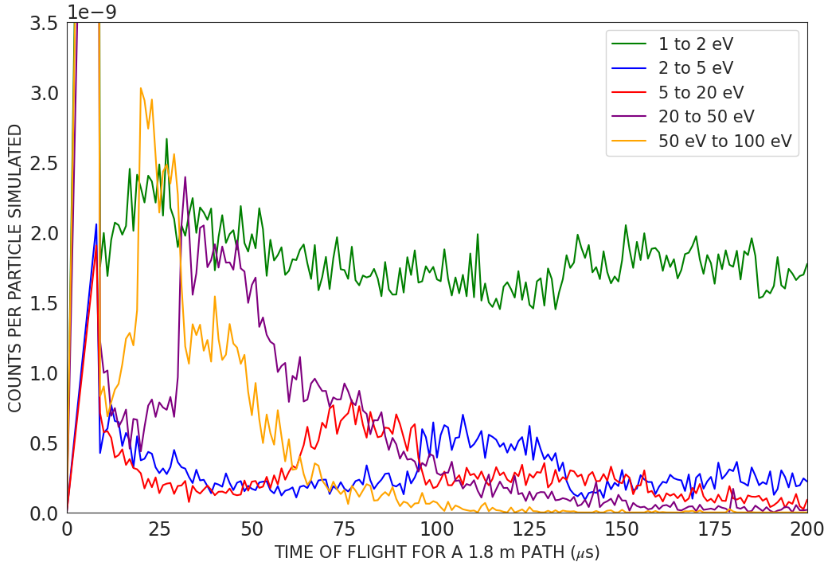

Figure 4-1: MCNP 6.2 simulation of neutron energy group arrival times at a 1.8 m beam path.

pure HDPE moderator. Including the lead multiplier cuff, the mean delay distance slightly increases to 1.96 cm with a standard deviation of 1.2 cm. These values do not significantly vary across the neutron energy range of 1-100 eV.

Neutron Flux at Sample Figure 4-3 shows the simulated energy flux of neutrons from this compact neutron source-multiplier-moderator assembly at a sample positioned 1.8 m from the D-T target plane. The simulation results closely align with the expected 1/E dependence characteristic of a moderated neutron spectrum. For a neutron source strength of 1 x 10$\hat{8}$ neutrons per second and a beam pulse width detailed in Sect. 3.3.2, an estimated 360 neutrons with an energy of approximately 10.0 eV (±0.5 eV) are expected to impinge on a 2.5 x 2.5 cm planar sample during a ten-minute experiment. This underscores the system's capability to deliver a quantifiable neutron flux for effective NRCA experiments.

4.2 System Resolution

System resolution is the ability of the time-of-flight spectrometer to distinguish between different neutron energies. This resolution is influenced by statistical uncertainties within the experimental setup, quantified in the system resolution function [164]. In other words, the resolution function accounts for the probability of detecting a neutron of energy E_n at a time other than expected based on known flight path length. Uncertainty in a system component that affects time or distance

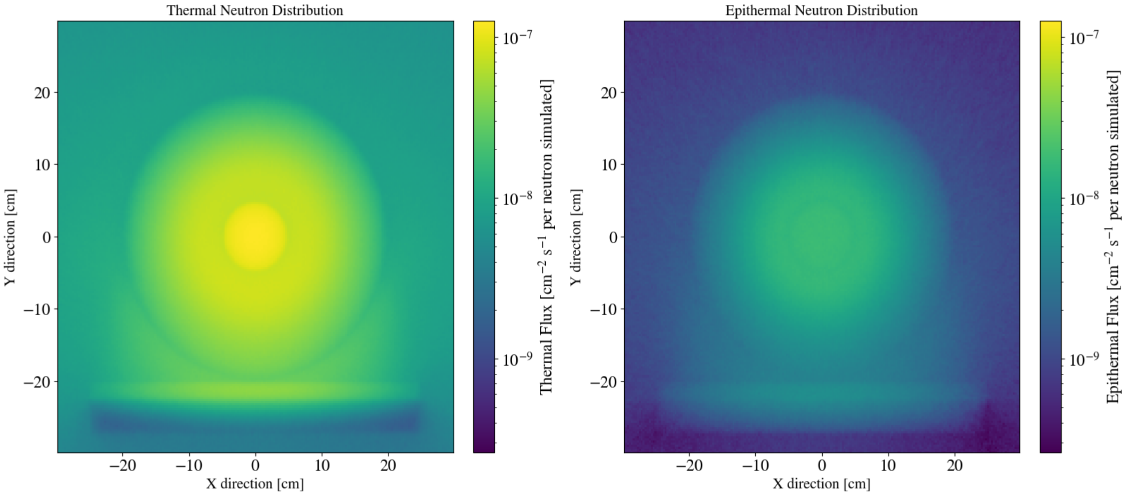

Figure 4-2: The neutron flux distribution of the front view of the moderator and D-T assembly, showing radial spread of axial neutrons. Left figure is the neutron energy group between 1E-2 and 1E-1 eV (generally thermal neutrons) and right figure is the epithermal region, 1-100 eV. Simulated in MCNP 6.2 with 1E10 particles.

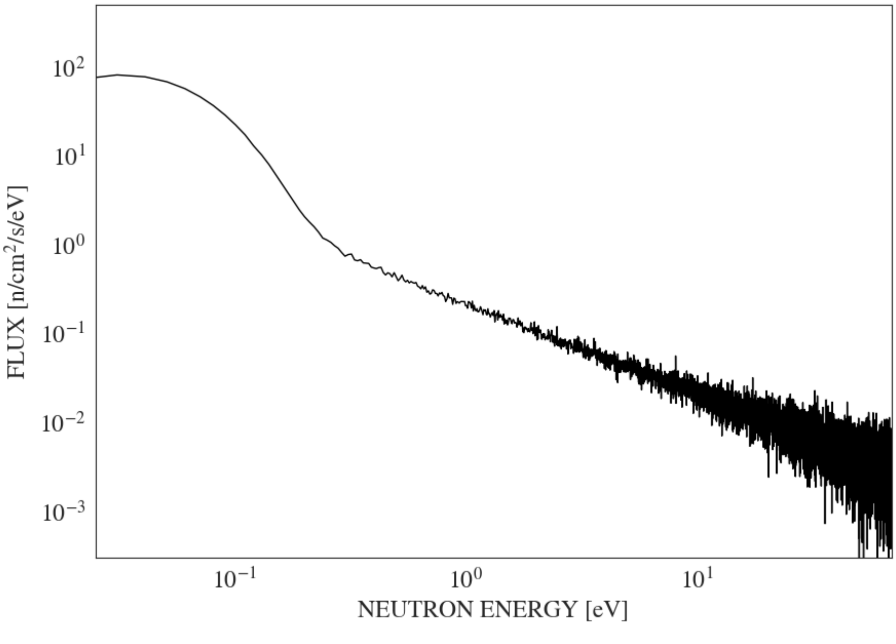

Figure 4-3: MCNP simulation of moderated neutron energy flux showing $1/E$ dependence in the epithermal region

adds to the overall resolution function. Similarly, improvements in these factors can contribute to improving resolution. Combined with Doppler broadening and multiple scatter effects, the system resolution has the effect of broadening the observed resonance width Γ_γ and shortening its amplitude.

Traditional NRCA measurements in large beamline facilities are afforded very high energy resolution by virtue of nanosecond-scale neutron generation pulses and beam paths on the order of tens or hundreds of meters. This precision is crucial to the discovery and exploration missions of these world-class facilities. In the more narrow use case of NRCA as an isotopic assessment method, especially in the case of *a priori* knowledge of the isotopes to be evaluated, looser energy resolution tolerances may be acceptable. There are numerous characterizations of system resolution for large beamline facilities: [13], [149], [164]–[166] as well as a comprehensive derivation of the resolution function for the D-T generator-based NRTA system [75]. Nuclear data evaluation codes, namely REFIT [13] and SAMMY [167], are analytical tools that perform least-squares fitting of resonances using the multilevel R matrix formalism. The codes convolve the calculated resonance structures with a neutron energy resolution function generated using several customized physical parameters of a setup.

4.2.1 System Resolution Function

The uncertainty in calculating the energy of a neutron based on its interaction arrival time is influenced by the time uncertainty δt and distance uncertainty δd. The kinetic energy (E) of a neutron is given by:

$$E = \frac{1}{2} m \left(\frac{d}{t} \right)^2, \tag{4.1}$$

where m is the neutron mass, d is the path length, and t is the flight time. The combined uncertainties in time and distance contribute to the uncertainty in neutron kinetic energy δE as

$$\delta E^2 = \left(\frac{\partial E}{\partial t} \right)^2 \delta t^2 + \left(\frac{\partial E}{\partial d} \right)^2 \delta d^2 \tag{4.2}$$

where the partial derivatives of E with respect to t and d are evaluated based on Eq. 4.1. To determine the relative uncertainty in neutron energy E_n, Eq. 4.2 is divided by E and the square root is taken, which yields

$$\frac{\delta E_n}{E_n} = 2\sqrt{\left(\frac{\delta t_{\mathrm{TOF}}}{t_{\mathrm{TOF}}}\right)^2 + \left(\frac{\delta d_{\mathrm{TOF}}}{d_{\mathrm{TOF}}}\right)^2}, \tag{4.3}$$

where t_{TOF} is the TOF time and d_{TOF} the the path length, each with an associated uncertainty. This expression is frequently presented as a function of neutron energy [164]:

$$\frac{\delta E_n}{E_n} = \frac{2}{L}\sqrt{\frac{E}{\alpha^2} \cdot \delta t^2_{\mathrm{TOF}} + \delta d^2_{\mathrm{TOF}}} \tag{4.4}$$

where α has a value of 72.3 $\mu\mathrm{s\,m}^{-1}$, the time it takes a one eV neutron to travel one meter.

Uncertainty in Flight Time

The time of flight, t_{TOF}, must account for the additions from the pulse width of the D-T generator and the response time of the detection system. The total uncertainty in time of flight is the sum in quadrature of its contributions:

$$\Delta t_{\mathrm{TOF}} \approx \sqrt{\Delta t^2_{\mathrm{pulse}} + \Delta t^2_{\mathrm{detection}}}. \tag{4.5}$$

As discussed in Sect. 3.4, the uncertainty in moderation time is expressed in terms of equivalent decay distance and is included in the path length calculations. The scintillation and digitization process is on the order of hundreds of nanoseconds at most for the detectors used in this research. This makes $\Delta t_{\mathrm{detection}}$ negligible compared to the pulse width uncertainty and Δt_{TOF} approximately equal to $\Delta t_{\mathrm{pulse}}$.

The finite duration of the pulse width and its associated uncertainty are discussed in Sect. 3.3.2. The standard deviation of the pulse time is based on D-T generator duty cycle and period:

$$\sigma_{pulse} \approx \frac{k \cdot \mathrm{DC} \cdot T}{\sqrt{12}}, \tag{4.6}$$

where k is the proportionality constant between the generator's nominal pulse width and empirically assessed one. For the optimal operational parameters of the D-T, $\Delta t_{\mathrm{pulse}} \approx 0.6\mu$s.

Uncertainty in Path Length

The flight path length, d, is defined in NRCA as the distance from the front face of the moderator to the sample material. It requires a correction for the length of the neutron moderation path and the axial location from which the neutron exits the moderator on the flight path to the target. There are three primary sources of uncertainty that can contribute to Δd_{TOF}: the equivalent moderation delay distance, the radial spread of the neutron exit point from the moderator, and any measurement uncertainties in the moderator-to-target distance. These are summed in quadrature as follows:

$$\Delta d_{\mathrm{TOF}} = \sqrt{(\Delta d_{\mathrm{mod}})^2 + (\Delta d_{\mathrm{radial}})^2 + (\Delta d_{\mathrm{measurement}})^2}. \tag{4.7}$$

The uncertainty in the moderation delay distance, Δd_{mod}, is determined by the standard deviation of the delay distance distribution, as detailed in Eq. 3.9. This standard deviation, expressed as $\sqrt{3}\lambda$ reflects the spread of moderation delay distances around the mean. The mean free path λ is assumed to be constant; an assumption which is supported by the consistency of the simulated delay distance across epithermal neutron energies discussed in the preceding section. This delay distance represents the hypothetical path that a moderated neutron would travel in free space and is added to the corrected path length for both energy and energy uncertainty calculations. Simulations of the system with the HDPE moderator and the lead multiplier place Δd_{mod} at 1.2 cm, which is in good agreement with a λ_{HDPE} of $\approx$0.6 cm^{-1} for epithermal neutrons.

The radial spread of a neutron's exit position from the moderator contributes to the total flight path length, expressed as $d_{\mathrm{TOF}} = \sqrt{(d_{\mathrm{measured}})^2 + (d_{\mathrm{radial}})^2}$. A neutron produced at the intersection of moderator and the D-T accelerator housing and one produced at the outer radius of the 15 cm moderator have a path length difference of 0.6 cm for a 177 cm flight path. According to the radial distribution of epithermal neutrons shown in Fig. 4-2, which is predominantly concentrated towards the center of the moderator, the uncertainty $\Delta d_{\mathrm{radial}}$ represents a minor contribution compared to the moderation delay distance.

Resolution Function Calculation

The lowest neutron energy resonance that this system seeks to resolve is approximately 1 eV. This has the implication that the TOF for a 1 eV neutron should not exceed the pulse period (plus the TOF at which high-energy resonances are no longer resolvable). This establishes an inequality that the TOF of the lowest-energy neutrons must be less than or equal to the sum of the pulser period and the time of flight of the high-energy cutoff. The maximum TOF distance $d_{\mathrm{TOF,max}}$ associated with a pulse period that satisfies this inequality is given by:

$$d_{\text{TOF,max}} \approx \frac{T\sqrt{E_{n,lo}}}{\alpha}\left(1+\sqrt{\frac{E_{n,lo}}{E_{n,hi}}}\right), \tag{4.8}$$

where α is defined previously in Eq. 4.4 [75]. The equation for relative uncertainty in reconstructed neutron energy is given in Eq. 4.3 and can be rearranged to isolate the time of flight distance from the square root term:

$$\frac{\Delta E_n}{E_n} = \frac{2}{d_{\text{TOF}}}\sqrt{E_n \cdot \left(\frac{\Delta t_{\text{TOF}}}{\alpha}\right)^2 + \Delta d_{\text{TOF}}^2}. \tag{4.9}$$

Substituting $d_{\text{TOF,max}}$ from Eq. 4.8 and the standard deviation of the pulse width time from Eq. 4.6 yields the relative neutron energy uncertainty,

$$\frac{\Delta E_n}{E_n} = \left(\frac{1}{\sqrt{E_{n,lo}}} - \frac{1}{\sqrt{E_{n,hi}}}\right)\sqrt{E_n \cdot \left(\frac{k \cdot \text{DC}}{\sqrt{3}}\right)^2 + \left(\frac{2\alpha \cdot \Delta d_{\text{TOF}}}{T}\right)^2}. \tag{4.10}$$

Using the epithermal range of 0.5 to 100 eV, a period of 200 μs, and the pulse generation and moderation parameters presented earlier in this section, the relative energy resolution function of the system is:

$$\frac{\Delta E_n}{E_n} = 1.31\sqrt{3.49 \times 10^{-5} \cdot E_n + 7.53 \times 10^{-5}} \tag{4.11}$$

For a resonance occurring at 10 eV, this yields a resolution of 1.4%, or 0.14 eV.

4.2.2 Effects of Doppler Broadening

The system resolution function contributes partially to the difference in representation between the cross section plot and observed resonance captures. Another effect is that of Doppler broadening in which the thermal motion of nuclei causes shifts in their kinetic energy, which widens the measured resonance structure and reduces its amplitude. This may be modeled by convolving the capture cross section with an energy transfer function $S(E')$,

$$\sigma^{\text{D}}(E) = \int S(E')\sigma(E - E')\text{d}E' \tag{4.12}$$

where $S(E')$ is derived using the effective free gas model (EFGM) [79]. In this model, the crystalline solid of the target material is treated with a Maxwellian distribution of velocities as if the nuclei were a free gas [168]. The effective temperature T_{eff} is related to the temperature of the sample by

$$T_{eff} = \frac{3}{8}\theta \coth\left(\frac{3}{8}\theta / T\right) \tag{4.13}$$

where θ is the Debye temperature which correlates elastic properties with thermodynamic ones [79]. The EFGM energy transfer function is

$$S(E') = \frac{1}{\Delta_{\mathrm{D}}\sqrt{\pi}} \exp\left(-\frac{(E'-E)}{\Delta_{\mathrm{D}}^2}\right), \tag{4.14}$$

where Δ_{D}^2 is the Doppler parameter which sets the width of the Gaussian-shaped energy transfer function. The Doppler parameter considers the reduced mass of the neutron-target nucleus system and is proportional to the square root of the effective temperature and energy of the resonance as

$$\Delta_{\mathrm{D}} = \sqrt{\frac{4mME_{\mu}k_{\mathrm{B}}T_{\mathrm{eff}}}{(M+m)^2}} \tag{4.15}$$

where k_{B} is the Boltzmann constant [79].

The single-level Breit-Wigner (SLBW) formula for the radiative capture cross section was introduced in Sect. 2.1.1 and is reprinted here for clarity:

$$\sigma_{\gamma}(E) = \pi \lambda\!\!\!^{-2} g_J \frac{\Gamma_{\mathrm{n}}\Gamma_{\gamma}}{\left(E - E_{\mu}\right)^2 + (\frac{\Gamma}{2})^2}. \tag{4.16}$$

This equation is convolved with the transfer function $S(E')$ from Eq. 4.14 to make an effective Doppler-broadened capture cross section:

$$\sigma_{\gamma}^{\mathrm{D}}(E) = \sigma_{\gamma}\Psi(\beta, x) \tag{4.17}$$

where:

$$\Psi(\beta, x) = \frac{1}{\beta\sqrt{\pi}} \int_{-\infty}^{\infty} \frac{1}{1+y^2} \exp\left(-\frac{(x-y)^2}{\beta^2}\right) \mathrm{d}y. \tag{4.18}$$

The resulting function adopts the shape of a Voigt profile, characterized by a Gaussian-like center with Lorentzian tails [115]. In the Ψ function, β is the width parameter of the Gaussian component and equal to $2\Delta_{\mathrm{D}}/\Gamma$ [79]. The variables x and y are equal to $x = 2(E - E_{\mu})/\Gamma$ and $y = 2(E' - E_{\mu})/\Gamma$ and have the effect of scaling around the resonance energy E_{μ} so that the equation can be applied to different resonance energies and widths.

The width parameter β is a reduction factor that quantifies the ability of $\Psi(\beta, x)$ to reduce the peak cross section of a resonance. Small values of β preserve the

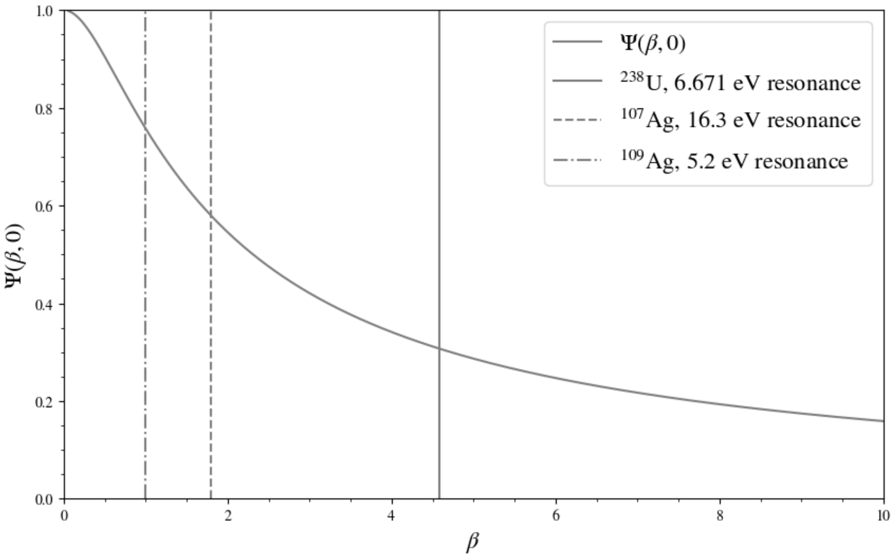

Figure 4-4: Reduction in peak radiative capture cross section due to effects of Doppler broadening. Three important benchmark resonances used in this research are plotted according to their width parameters.

Lorentzian-like qualities of γ-ray count peaks in the TOF histogram (assuming the resonance has a low self-shielding factor) and large values experience more broadening. Evaluating the Voigt profile Eq. 4.18 at $x = 0$ represents the central energy value of a resonance and yields

$$\Psi(\beta,0) = \frac{\sqrt{\pi}}{\beta}\exp\left(\frac{1}{\beta^2}\right)\operatorname{erfc}\left(\frac{1}{\beta}\right), \tag{4.19}$$

where erfc is the complementary error function.

Fig. 4-4 shows the effects of increasing Doppler width parameters on the Voight profile of a resonance. Three benchmark resonances used for system characterization and analysis are plotted according to their β values at room temperature (300 K). The 6.67 eV resonance in ^{238}U experiences a reduction in the radiative capture cross section amplitude of more than half, dramatically altering its shape on a TOF histogram compared to its resonance plot.

4.3 System Background Characterization

The characterization of the background and the development of methods to mitigate or manage it were the most time-intensive components of this research. An accurate understanding of the background was important not only for isolating the capture γ-ray signal, but also for implementing strategies to reduce its effects, thereby improving the signal-to-noise ratio (SNR). To address these challenges, a systematic, iterative strategy termed 'model-mitigate-manage' was implemented, encompassing the following phases:

- **Model:** the detailed characterization of the background using both simulations and empirical data to identify and quantify primary noise sources. This step was essential to understand the factors that contribute to the background and if they could be addressed.
- **Mitigate:** efforts that focused on reducing background interference through modifications to the experimental setup and detector, as detailed in Sect. 3.6.3. This phase also included field studies to test the practical implementation of the portable technique.
- **Manage:** this phase addressed methods for operating with residual background noise that could not be reduced. It involves the development of custom algorithms for the empirical determination of background functions and the integration of automated procedures for resonance identification.

This framework was performed iteratively throughout the research, progressively improving the SNR of the system.

4.3.1 Sources of Background

The background for NRCA measurements originates primarily from neutron interactions in the vicinity of the experiment. By miniaturizing the NRCA system, the neutron production device has been moved closer to the target and detector. This proximity has the effect of creating interference between system components that manifests in the measurement as γ-rays that do not originate from resonance captures in the sample. The detector cannot inherently distinguish between a signal or noise γ-ray, but an accurate characterization of the noise can serve to isolate the signal.

The neutron-induced background can be categorized based on its time dependence relative to the pulsing period of the generator. The time-dependent background is the product of neutrons generated in the current pulse that interact to create a γ-ray prior to the initiation of the next pulse. The time-independent, neutron-based background arises from the 'wrap-around' neutrons remaining from the prior pulses that provide a constant source of capture γ-rays. Photons arising from the decay of short-lived daughter products from neutron activations may also contribute to this background.

Additionally, the γ-ray background includes contributions from natural environmental radiation and passive or induced radioactivity in the sample. The sample itself may generate background through thermal capture γ-rays or by scattering neutrons into the detector. Each of these sources requires careful consideration to accurately quantify and mitigate their impact on the measurements

Table 4.1: Classification of NRCA Background Sources

	Time Independent	**Time Dependent**
Sample Independent	Natural/Room Background b_n	D-T created background on non-sample components b_{open}
Sample Dependent	Passive radioactivity of sample b_p	Off-resonance neutron induced γ-rays from sample $b_{scatter}$

The components of the NRCA measurement background can be classified according to their sample and time dependence, as detailed in Table 4.1. A literature review highlights the methods used in large-beam NRCA experiments to model, estimate, and subtract background components [169]. The background of the room and the radioactivity of the sample, $b_n + b_p$, are quantified just after the final neutrons pass the experimental station. The time dependent component from neutron interactions on non-sample materials b_{open} is estimated through an ‘open beam’ run, where the sample is removed and all other parameters are kept constant. The sample- and time-dependent component is commonly estimated by a scattering fiducial, such as lead or carbon, to measure the effects of neutron sensitivities in the detector. This produces a background correction estimation in the form of:

$$b_\gamma = (b_n + b_p) + b_{open} + S(b_{scatter} - b_{open}), \tag{4.20}$$

where S is a correction factor between the scattering yields of the fiducial and the sample [169]. The scattering data are further analyzed to determine the production of prompt γ-rays from resonance or thermal capture, or delayed decay due to an activated daughter product in the detector or support materials. The literature has many examples of research groups quantifying or improving neutron sensitivities of their detectors and discovering the influence of systematic error in previously reported cross section values [170].

In the portable NRCA setup, thermal neutrons are far more prevalent in the sample-detector region compared to traditional NRCA setups, which typically employ collimation, increased distance between the production source and the detector-target assembly, and a longer pulse period to mitigate wrap-around thermal neutrons. In contrast, the pulse period in the portable system is constrained by the duty cycle's limitations on pulse width. As a result, extending the pulse period to increase the time that thermal neutrons have to dissipate will worsen the system resolution function.

Despite the incorporation of neutron and γ-ray shielding near the detector, only limited background reduction is achieved, a point that will be further discussed in subsequent sections. Both large beam experiments and portable NRTA use fixed isotopic filters to selectively remove neutrons of undesirable energies. An analysis of this technique applied to portable NRCA is provided in Sect. 5.2.2. Given the substantial background of thermal neutron-induced γ-ray noise affecting both the experimental components and the sample itself, the standard background estimation method (Eq. 4.20) requires modifications. In addition, some samples indirectly contribute to shielding the detector from the moderator and room background, which has a subtractive effect. A revised background fitting procedure is proposed in Sect. 4.3.2 to address this and the additional challenges posed by the miniaturization of an NRCA system.

Identification

Identification of neutron-induced γ-ray background sources should include a neutron reaction that produces the γ-ray and a material upon which the reaction occurs. For the purposes of this setup, photon-producing neutron interactions of interest are inelastic scatters, thermal captures, and, indirectly, activation product decays. Resonance radiative captures on detector-intrinsic isotopes (see Sect. 3.6.1) and their daughter product decay photons also contribute.

A benefit of time-based capture analysis is the ability to remove a preponderance of fast neutron interactions. This is done by removing from consideration the γ-rays recorded during the times during the neutron generation pulse and immediately after (approximately the first 12μs of each pulse). The remaining γ-ray energy spectra represent the contributions of neutrons slow enough to survive to the epithermal interaction period. This removes the γ-rays arising from neutron inelastic scatter; however, they are a valuable source of information, the use of which is discussed in Chapter 7.

It is useful to analyze the energy flux of neutrons that generate background during the period of interest after the neutron generation pulse (corresponding to the 12-200 μs following the D-T initiation signal). Fig. 4-5 shows the MCNP simulation of the temporal distributions of various neutron energy groups as they arrive at the target, based on their moderator exit time and TOF. The flux of thermal

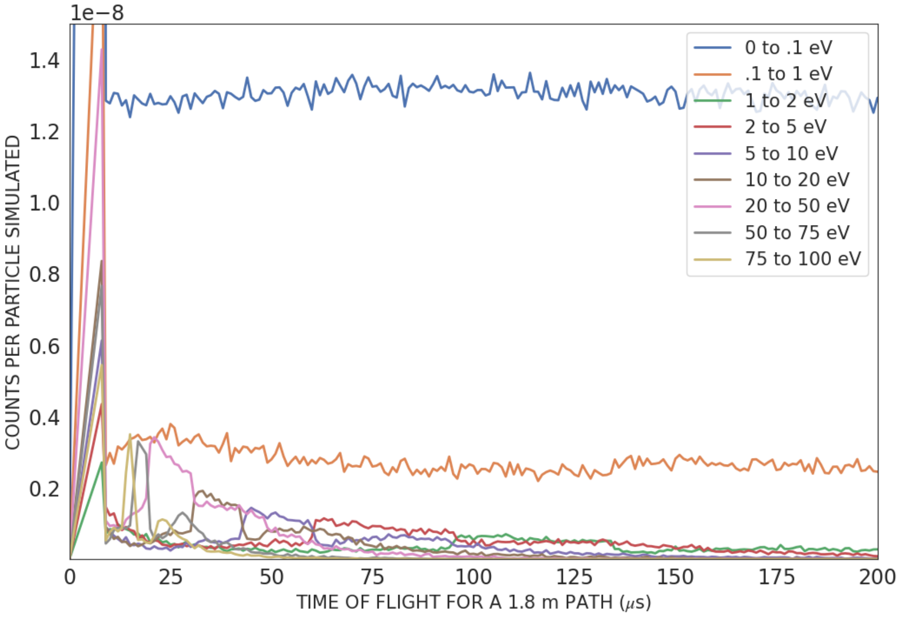

Figure 4-5: An MCNP simulation of neutron energy group arrival times at a 5 x 5 cm sample, 1.8m from target plane of the D-T for a pulser frequency of 5kHz.

neutrons (classified as less than 0.1 eV for this simulation) supports the assertion that thermal contributions are constant with time, excluding the period immediately during the neutron production pulse. The magnitude of thermal flux arriving at the target is approximately six times greater than the on-time epithermal neutrons that arrive at the target at a time commensurate with their moderator exit energy.

The results of these thermal neutrons capturing on experimental materials is shown in Fig. 4-6. The energy spectra for 20 minute acquisitions with an open beam in the MIT Vault Lab from a 3" BGO and a 1.5" $LaBr_3$ are plotted on a logarithmic scale. The spectra have been separated based on their record time relative to the pulse initiation of the D-T generator, so that the dashed line shows events captured during the fast neutron burst and the solid line shows the environment from epithermal and thermal neutron flux only. Gamma-ray lines of probable transitions following thermal capture are matched to their peaks in the BGO spectrum and indicated. In some instances, multiple structural elements, such as aluminum and iron, have isotopes with similar probable decay energies. Fig. 6-10 in Sect. 6.3 provides an example of how the removal of physical structures from the experimental area can affect the thermal neutron-induced background spectrum.

Identification of each peak's contributing reactions and materials can be complex. The 1 MeV peak visible in Fig. 4-6 and later in Fig. 4-9 offers an interesting case study. This peak is present in spectra from all detector types and is enhanced relative to the background continuum when lead is present and also when the experi-

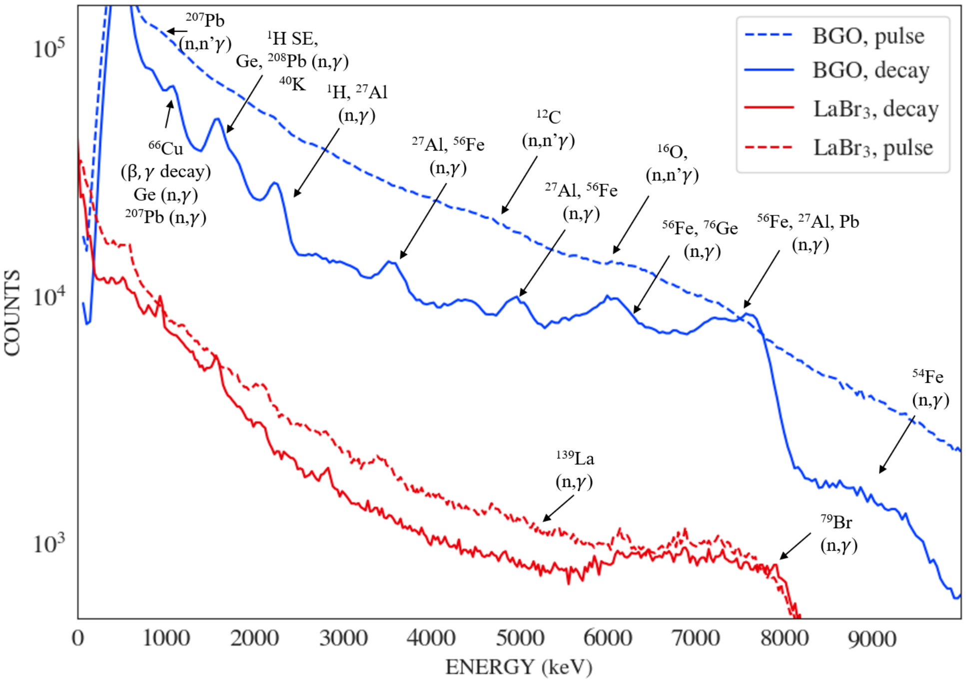

Figure 4-6: BGO and $LaBr_3$ spectra of open beam runs in the MIT Vault, time-separated into pulse (0-12 μs) and decay (13-200 μs) periods. Reactions of interest are labeled on the BGO plots.

ment is performed in the Vault Lab. Analysis shows that the peak is the combination of several effects, notably the gamma decays of two activation products. The first is ^{65}Cu$+n \rightarrow ^{66}$Cu, which decays with a half-life of 5.1 minutes with a γ-ray energy of 1.04 MeV. The second reaction is ^{206}Pb$+n \rightarrow ^{207}$Pb, which emits with high probability 1.064 MeV γ-ray after a half-life of 0.8 seconds, often associated with the decay of naturally radioactive ^{207}Bi (which decays to ^{207}Pb) [86], [171], [172]. The lead reaction has a small cross section of 26 mb, but given its proximity to the detector, the products have a high probability of detection. The copper reaction has a cross section of 2.2 b and can be attributed to the copper windings in the electromagnets of the cyclotron in the Vault Lab, which remains in view for a shielded detector. The 1 MeV peak is further complicated by thermal neutron absorption on several germanium isotopes in the detector which each have a high-probability prompt γ-ray in the 1 MeV region. It is also in the single-escape peak window of the 1.56 MeV de-excitation gamma, which occurs with the highest probability following a thermal capture on ^{208}Pb.

All NRCA data acquired in this research are biparametric: each event is recorded with an associated time relative to the D-T pulse and the photon energy deposited in the detector. Data from an experimental run can be presented as a multivariate, two-dimensional histogram with counts on the z-axis as a function of both neutron

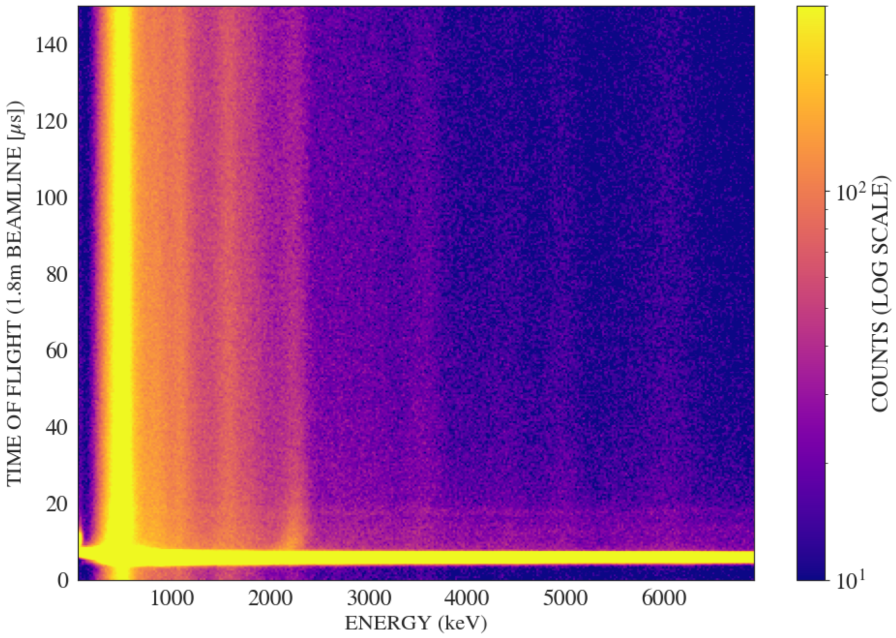

Figure 4-7: Multivariate histogram of γ-ray energy and event time relative to the D-T pulse initiation (corresponding to neutron TOF). Acquired with a 3" BGO detector in the Vault Lab, 20 minute run. Background energy peaks are visible, along with any associated time dependence.

TOF and γ-ray energy. This provides a valuable tool in identifying the time- or energy-dependence of a signal. The thermal neutron-associated γ-ray lines from Fig. 4-6 are visible in Fig. 4-7, plotted as a function of time as well. Analysis of the time-dependence of the 2.2 MeV hydrogen capture line shows a higher flux at early times proximal to the D-T pulse, then weakening as thermal neutrons decay or move away from the moderator assembly, a large hydrogenous component. Understanding the reaction and material that generates γ-ray background assists in mitigating it or adapting to its presence.

Background Mitigation

By understanding the neutron reactions and materials responsible for the off-pulse γ-ray background we can take steps to reduce it. Although there is no elegant solution to remove thermal neutrons from the room environment or the target and detector vicinity, other solutions are available. One possibility is to modify the experimental environment by removing materials that are prone to thermal neutron capture. Another strategy involves shielding the detector, target, or other materials that significantly contribute to background noise. However, this method may involve trade-offs, such as increased system mass and neutron moderation and scattering, which must be considered.

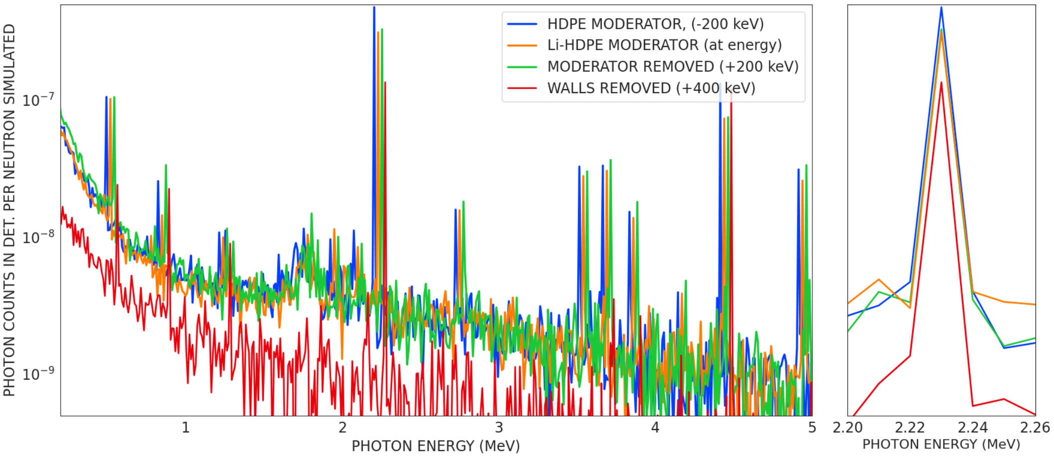

Figure 4-8: MCNP 6.2 simulation of the γ-ray energy spectrum at the detector location for NRCA runs in the MIT Vault Lab. Four different run configurations are presented: an HDPE-only moderator, a 7.5 wt% lithium-loaded HDPE moderator, a moderator-free configuration, and the experiment with all concrete walls, floor, and ceiling replaced with air (using an HDPE moderator). Each run is energy-shifted as indicated in the legend to enhance peak visibility. The inset plot shows a detail of the 2.2 MeV hydrogen capture γ-ray.

Experimental modifications with the goal of removing sources of probable thermal capture have proven beneficial for background improvement. Figure 4-8 shows MCNP simulations of four variations in the MIT Vault Lab NRCA setup: a standard HDPE moderator, a 7.5 wt% lithium-loaded HDPE moderator, a configuration without any moderator, and a version where all concrete walls, floors, and ceilings are replaced with air. By incorporating lithium into the moderator, the reaction ^{6}Li $+n \rightarrow$ ^{3}H + α becomes highly probable for thermal neutrons (with a cross section of 940 barns). This reaction does not produce high-energy gamma rays like hydrogen capture does, thereby effectively reducing the gamma-ray background. The simulations demonstrated that the introduction of a lithium-loaded moderator reduced the gamma-ray background below 2.2 MeV by 45%, a result that aligns well with experimental findings. At the low weight percentage, the lithium loading does not significantly reduce the epithermal flux generated by the moderator and the resulting moderation ratio remains within 10% of the HDPE plot presented in Fig. 3-6. Fig $4-8$ also indicates that the concrete walls of the experimental hall contribute substantially to the background. A field NRCA experiment campaign was conducted to assess portability of the technique and the background reduction afforded by effectively removing the walls, discussed in Sect. 6.3.

Several shielding studies were conducted for the BGO and EJ-315 detectors to assess the effects of lead and hydrogenous shielding on background and signal levels. While large-beamline experiments typically aim to remove as much material

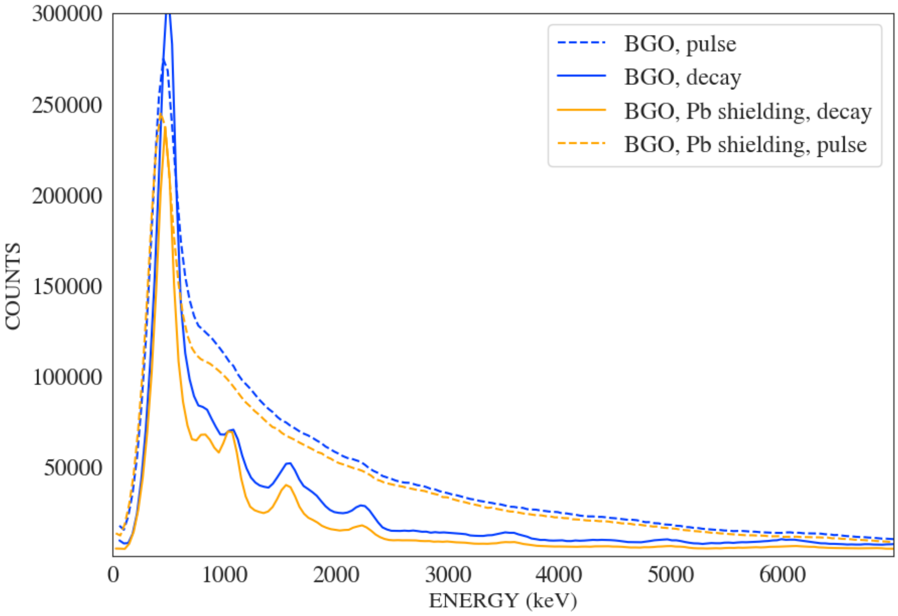

Figure 4-9: Experimental γ-ray spectra of a lead-shielded and unshielded run in the Vault Lab. 20 minutes, 3" BGO detector.

as possible from the vicinity of the target and detectors to reduce scattering impacts [124], [125], some spectroscopic method experiments use substantial shielding around the detector to absorb neutrons and γ-rays [160]. In these cases, the neutron beam is heavily collimated, and the detector shielding is positioned outside the neutron flux to minimize scattering effects. The use of collimation was investigated in this experiment; however, it either reduced or maintained the SNR compared to a non-collimated run.

A moderate shielding of 5 cm of lead surrounding the detector proved to be most effective in reducing background noise while preserving the resolution of the TOF peak shapes. Figure 4-9 illustrates the time-separated γ-ray background from an unshielded and lead-shielded open beam run in the Vault Lab. The lead shielding reduced the background noise during the post-D-T pulse period by 28%. The lead contributions to the 1 MeV peak, discussed in the previous section, are visible here. A more in-depth discussion of shielding and neutron energy reconstruction is provided in Chapter 5.

Further background reduction in NRCA experiments can be achieved through modifications to γ-ray acquisition techniques. Many NRCA studies with the goal of collecting information for nuclear databases have utilized methods such as Compton-coincidence background removal or multiplicity-weighted counts [92], [151]. A Compton-coincidence system offers a low-mass solution for background management and warrants further investigation in future portable NRCA research.

Additionally, adjusting the detection energy threshold, or Lowest Limit of Detection (LLD), can effectively reject regions with a high noise-to-signal ratio, which is particularly beneficial for managing low-energy backgrounds. This approach was applied in studies measuring ^{232}U-contaminated ^{233}U, as discussed in Sect. 6.4.

Inspection of Figures 4-6 and 4-7 demonstrates the utility of the high peak-to-Compton ratio in a BGO detector. For the heavy elements studied in this work, the NRCA gamma signal from resonance radiative captures spans a continuum of energies from 0.2 to 5 MeV. These energies occur with similar probabilities so that they manifest as a continuum in the NRCA energy spectrum (see Fig. 2-4 for a theoretical representation or Fig. 5-9 for an empirical example). A robust peak-to-Compton ratio ensures that more monoenergetic background γ-rays are detected at their full energy, rather than contributing to a Compton continuum. The TOF γ-ray spectrum can be post-processed to selectively remove events associated with monoenergetic noise peaks, thereby reducing the highest background influences while preserving intervening areas with a more favorable SNR. Chapters 5 and 6 contain several examples of energy-cut TOF spectra with the goal of enhancing the resonance capture signal strength.

4.3.2 Algorithm for Empirical Background Determination

Although background sources can be removed by experimental modifications or filtering of the acquired data, an accurate time-dependent background function is required to determine the contents of each γ-ray peak in the TOF spectrum. In many spectroscopic experiments, a background function can be determined by using a control that isolates the effects caused by the background. In the case of NRCA this is typically done with a combination of an open beam run and a scattering fiducial run, as presented in Sect. 4.3.1 and particularly, 4.20.

Fig. 4-10 demonstrates the motivation behind the development of a custom background fitting function. The TOF spectra from an open beam and two sample-containing runs (one with 0.37 g/cm^2 of Ag and one with the same Ag target and 1.9 g/cm^2 added) are corrected for detector deadtimes and plotted. All other experimental parameters remained constant. The figure shows that the γ-ray background at off-resonance times is inconsistent with that of the control run, both in count values and in decay rate of the histograms relative to each other. The observed variations are interpreted as a non-resonance reactions in the sample creating an excess γ-ray background in the detector. In this particular example, the thermal and scattering cross section ratios of the sample isotopes indicate the variation is due to thermal capture (n,γ) reactions as opposed to the sample scattering excess neutrons into the detector (where they interact to produce excess gammas). The relative contributions

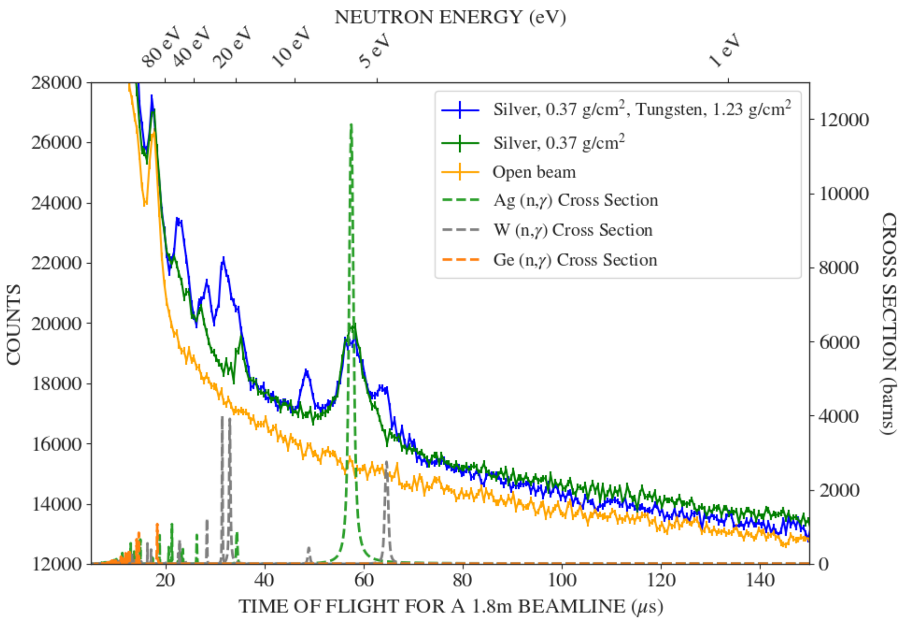

Figure 4-10: Experimental TOF spectra of an open beam, silver, and tungsten samples (the blue plot is a mixed run of both Ag and W), corrected for deadtimes. Neutron capture cross sections for elements of interest are plotted for reference. The off-resonance background counts with a sample do not align with the open beam counts. 20 minutes per run, acquired in the Vault Lab with a 3" BGO detector.

of thermal capture and scattering effects change with target type, geometry, and orientation to the detector.

The discrepancies between the TOF histograms in Fig. 4-10 indicate the presence of sample-dependent background components that cannot be accounted for by the traditional background function methodology. The particular scattering and thermal capture likelihoods of a sample are difficult to reconstruct without the sample itself.[1] This necessitates the development of a custom, time-dependent background function to accurately characterize and subtract the background in portable NRCA measurements. Therefore, a background correction algorithm was developed for this system which approximates the non-resonance γ-ray contributions as a sum of time-dependent analytical functions.

To accurately model the time-dependent background in neutron capture experiments, we employ a parametric fitting approach that adjusts certain parameters to match observed data at specific time points. This method involves solving a system of nonlinear equations derived from our physical model of the experimental setup and γ-ray producing neutron interactions.

---

[1] A geometry study was conducted to use an axially-oriented sample to effectively 'blur' the resonance contributions while still preserving the scattering and thermal capture contributions, however the flux is highly directional and these results did not generate an effective solution.

Background Function Definition The time-dependent model for the background separates the γ-ray contributions of the D-T machine pulse, the late-interacting neutrons and any extremely short-lived activation products, and the constant background. It takes a similar form to an analytical expression used by NRTA experiments at GELINA, used to describe the excess counts underneath saturated resonance dips in the NRTA spectrum [173]. The expression parameterized for this unique NRCA setup is given by:

$$f_{\text{model}}(t) = C_o + C_1 e^{-t/\tau_1} + C_2 e^{-t/\tau_2} \tag{4.21}$$

where C_o is the constant background term, C_1 and C_2 are amplitude coefficients for exponential decays and τ_1 and τ_2 are the decay constants corresponding to gamma-producing processes. Fig. 4-11 shows the overall function and the contribution of each component. The figure shows a TOF histogram acquired with an EJ-315 detector, but the methodology is equally applicable to BGO, NaI, and other detectors.

Methodology for Parameter Estimation For each TOF spectrum, the constant term is fixed to a known value derived from the baseline background measurement. The delay period between the D-T start signal and the plasma production that generates neutrons is useful to measure the aggregate γ-ray background prior to the neutron pulse. The pulse width, flux, and period are such that the γ-ray background returns to this baseline value prior to the next pulse for every spectrum recorded in this research, as seen in Fig. 4-11. The terms C_2 and τ_2 represent the fast decaying contributions of the pulse and are well characterized for a specific D-T generator, detector, and experimental configuration. The fitting process is applied to several sample runs with fixed experimental conditions, and the second exponential component shows excellent agreement between each experiment. For the Vault Lab setting with the D-T at the optimal parameters described in Chapter 3, the 3" BGO C_2 term is 61,500$\pm$600 counts and the time constant τ_2 is 5.7$\pm$0.3 μs. The EJ-315 C_2 amplitude is 4800$\pm$ 100 counts and τ_2 is 5.3$\pm$0.2 μs. These terms change with changing settings, such as in field experiments and when using a different generator, as was the case at Pacific Northwest National Laboratory (PNNL).

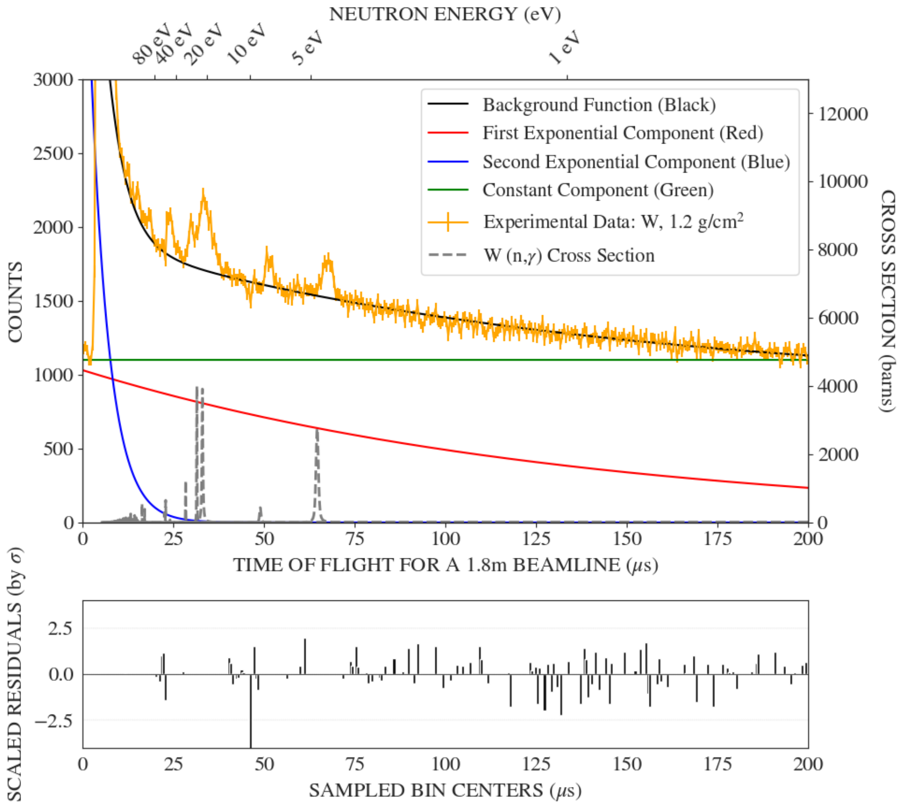

Figure 4-11: Experimental TOF spectra of a tungsten sample measured with an EJ-315 detector. The time-dependent background function is plotted with its component functions. Scaled residuals between the function and experimental data presented below. 20 minute acquisition in the Vault Lab.

Objective Function and Residuals With empirical, physics-based functions for the constant and pulse components, the remaining decay component function must be derived from the TOF histogram. To determine the optimal values for parameters C_1 and τ_1, we establish an objective function that minimizes the residuals between the model and measured data, anchored at specific time points. Specifically, we solve for C_1 and τ_1 such that the model aligns with the empirical data at non-resonance times. The objective function is:

$$\mathscr{L} = \sum_{i=1}^{n} \left[y_{\text{data}}\left(t_i\right) - f_{\text{model}}\left(t_i; C_0, C_1, C_2, \tau_1, \tau_2\right)\right]^2, \tag{4.22}$$

where $y_{\text{data}}(t_i)$ are the data points from the experimental measurement and $f_{\text{model}}(t_i, \ldots)$ is the model function evaluated at time t_i. The residuals are the differences between the measured data and the model values, presented in Fig. 4-11, with each value scaled by the standard deviation of the residuals.

Numerical Solution via Least Squares This method uses the least squares algorithm from the SciPy library, which is suited for solving nonlinear least squares problems; however, any robust least-square solver should suffice. Parameters C_1 and τ_1 are iteratively adjusted to minimize the sum of squared residuals. Initial estimates are provided based on preliminary data and parameter bounds are set to enforce physically meaningful constraints on the solution. The algorithm uses these initial conditions and bounds to converge on the optimal values that best fit the model to the data according to the predefined conditions.

Error Propagation and Considerations for Complex Resonance Structures Sampling each value of a sample-containing TOF histogram introduces bins containing resonance data. The algorithm described in Table 4.3 parses cross section data from the ENDF libraries and transforms them based on neutron energy to a TOF value, broadened appropriately by system resolution. TOF values associated with a cross section in excess of a defined threshold are excluded from the sampled experimental data. This ensures the background fitting procedure is based on non-resonance TOF regions only. The standard errors of the fitted parameters are obtained from the diagonal elements of the covariance matrix [169]. The Jacobian vector $\mathbb{J}$ is used to propagate fitted parameter uncertainty to the estimate of the background, where each element in $\mathbb{J}$ is the partial derivative of $f_{\text{model}}(t_{\text{resonance}})$ with respect to a parameter. The propagated uncertainty in the background estimate, σ_f, is given by:

$$\sigma_f = \sqrt{\mathbb{J}^T \mathbb{C} \mathbb{J}}, \tag{4.23}$$

where $\mathbb{C}$ is the covariance matrix of the fitted parameters and $\mathbb{J}^T$ is the transpose of the Jacobian. Table 4.2 shows the parameters for the NRCA data depicted in Fig. 4-11.

Table 4.2: Background Parameters for EJ315 TOF Histogram with W Target

Parameter	Value	Parameter	Value
c_1	1030.39 ± 18.93	Resonance Energy	7.6 eV (^{183}W)
c_2	4840.25 ± 1651.50	σ_γ	393 b
τ_1	135.81 ± 3.34	Background at $t_{\text{resonance}}$	1604.39 ± 19.40
τ_2	5.14 ± 0.75	Net signal counts	226.61 ± 46.98
c_0 (fixed)	1100 ± 33	SNR	4.82

All time values given in μs and count values are in counts per 0.5 μs bin per 20-minute measurement.

For materials with multiple resonances in clusters, identifying sufficient TOF regions to align the objective function can introduce a source of error. In such cases, a composite background function may be 'built' in the same way as traditional NRCA background functions are constructed. The empirical constant and pulse functions are evident, and the decay function C_1 may be derived from a material with similar scattering and thermal capture characteristics. It should be noted that C_1 and τ_1 do not correspond directly with the sample but describe the aggregate impact of late-interacting neutrons in the environment. This term is largely suppressed in outdoor tests with lower amounts of hydrogenous material in the area relative to the vault lab, as shown in Sect. 6.3. This background composition method provides a ready classification system for various experimental environments that may be encountered while using a portable neutron resonance analysis system. A particular advantage of the technique is that it does not require an open beam run, as long as the environment has been previously characterized.

Table 4.3: Algorithm Description

Background Function Algorithm

Require: 1D array of radiative capture cross sections ($\sigma_{n,\gamma}$) for isotopes present in the experimental data (both in the target and in the detector or experimental setup)
Require: 1D array of energies (E) for the above cross sections
Require: Time of flight offset value (t_{off}) and time of flight distance (L_{TOF})
Require: cross section threshold values (T_σ) to consider a TOF bin for exclusion from the background function
Require: a time resolution value, in microseconds, that corresponds to the time uncertainty of the spectroscopic system and Doppler effects
Require: experimental data in the form of a TOF histogram for which the background is to be fitted
Require: the mathematical form of a background model f_{model}, with parameters and their initial starting values for the fitting algorithm, as well as convergence tolerances in the form of an optimization iteration limit or desired sum of squared residuals

Algorithm Steps:

1. Generate a time of flight array from the energy array associated with each isotope: $TOF_o = \frac{72.298 \cdot L_{\text{TOF}}}{\sqrt{E}}$
2. Adjust TOF arrays for T_{off}: $TOF = TOF_o + T_{\text{off}}$
3. Using threshold value, filter all TOF values which correspond with a cross section value, $\sigma_{n,\gamma}$, above the desired threshold. Create a list of tuples for each range of cross sections.
4. Broaden each tuple with the time resolution value of the system.
5. Concatenate all tuple lists and remove duplicate TOF values. This is the list of excluded TOF values.
6. Sample the histogram to create an array of sampled TOF bins, excluding values from the exclusion list.
7. Iterate through the background model parameters to minimize the sum of the square residuals between the model and the experimental data using the Levenberg-Marquardt optimization algorithm.

Return: a background function, $f(t)$, of gamma counts in terms of neutron time of flight with effects of resonance gammas in the detector and with the sample removed (e.g., $t, C_0, C_1, C_2, \tau_1, \tau_2$).

Chapter 5

Isotopic Analysis

To evaluate the effectiveness of the portable NRCA system in assessing isotopic content and quantifying it, a series of non-radioactive samples were used. This approach allowed scaffolding to improve the technique incrementally using targets that would generate the strongest signal possible. Passive radioactivity in a sample inherently lowers the SNR by generating an addition to the constant background component, therefore, nonradioactive samples were used to determine the most optimal experimental configuration first.

5.1 Experimental Details

5.1.1 Sample Properties

The ideal sample for NRCA measurements is a disc or foil with a thickness small enough to minimize resonance self-shielding for the isotope of concern. Targets, especially powders, should be analyzed prior to use for the incorporation of components that have a high scattering or thermal capture cross section. For example, hygroscopic materials that introduce hydrogen into the sample matrix can create additional neutron moderation in the vicinity of the target and 2.2 MeV hydrogen capture γ-rays. Fig. 5-1 shows examples of the samples used in this research. They range in thickness from an indium foil at 0.01 mm to several millimeters of tungsten. Analyzed samples are reported in areal densities, the product of their volumetric density and thickness relative to the neutron beam path.

This portable system is limited to epithermal resonances, which are generally orders of magnitude stronger than resonances in the 0.5-2 keV range. An indicative example is a prominent ^{63}Cu capture resonance at 578 eV measuring 290 barns, compared to the prominent 5.3 eV ^{109}Ag resonance measuring 11.8 kb. The relative weakness of the higher-energy resonances allows these isotopes to be analyzed at the

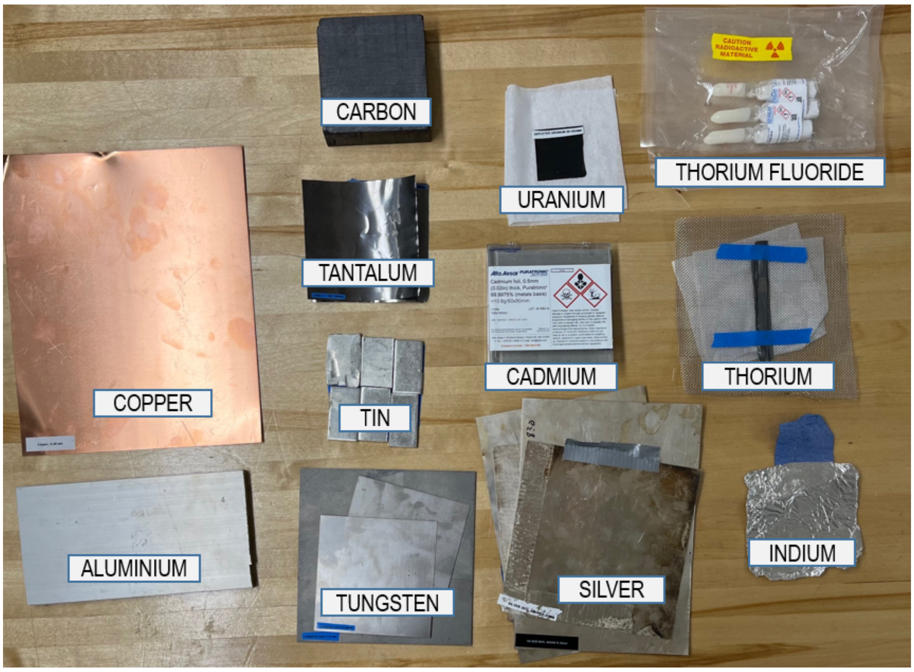

Figure 5-1: Examples of sample materials used in NRCA experiments.

large beamline facilities without large self-shielding corrections. This in turn allows relatively thick objects, including swords, statues, and ancient Roman plumbing taps, to be analyzed using NRCA [127], [174]. Although relatively thick samples with high resonance cross sections were important in detecting and then optimizing the NRCA signal in this primary research, thinner samples should be procured for follow-up research to investigate the technique without high self-shielding impacts. This trend supports one of the primary conclusions of this research: samples with low amounts of self-shielding based on their areal density and resonance strengths can be quantified more accurately.

5.1.2 Data Acquisition

The remaining spectra presented in this research were collected with a 2" BGO, 3" BGO, or 2" EJ-315 detector, with the detector type noted in each plot description. Detector shielding configurations varied from a bare detector, to one lead brick under the detector for field studies, to lead bricks surrounding the detector for the Vault Lab runs. BGO detectors exhibit a strong, nearly linear dependence of light yield on detector temperature, as visible in Appendix B, Fig. B-3 [175]. NRCA runs were conducted at temperatures ranging from -15 C to 24 C throughout the course of the research, and calibration drifts were observed between subsequent runs. Therefore, energy calibrations, when necessary, were performed on a run-to-run basis using characteristic γ-ray peaks arising from fast neutron inelastic scatters detected during the D-T pulse periods.

The beam path length, measured from the target of the D-T generator to the front face of the sample, is generally 1.77 m, with exceptions noted in the plot caption. This path length is derived from the initial NRCA measurements, which were performed in concert with NRTA measurements. The NRTA setup was previously established for a TOF length of 2.00 m, measured from the D-T target to the front face of the neutron detector, which was housed inside a boron carbide shield. To concomitantly measure the sample (which was placed in the well-characterized axial neutron flux for NRTA measurements), the NRCA detector was located at 1.77 m. Subsequent runs maintained this distance to aid in comparison and to leverage the higher flux available closer to the D-T while maintaining the ability to resolve resonances of interest.

The run times are 20 minutes each, unless an exception is noted. Detector data was read with a CAEN DT-5725 desktop digitizer using the Digital Pulse Processing (DPP) mode and the CAEN CoMPASS software. The Python package ComPy was used to process event times associated with each detector pulse into a TOF, based on the D-T TTL pulse output [176]. Cross section data were obtained from the ENDF/B-VII.1 library using the Sigma Evaluated Nuclear Data File Retrieval and Plotting database, hosted by Brookhaven National Laboratory [177].

5.2 NRCA Signal

Gamma ray counts recorded in the detector are plotted corresponding to their time of detection relative to the D-T start signal. For isotopes with resonances in the epithermal region, their capture γ-ray signal is detectable above the background decay continuum arising from the pulse of the D-T. These time-based peaks are the NRCA signal. Fig. 5-2 shows several single-element targets, each with the same flight path length and acquired with the same detection parameters. The isotopes with epithermal resonances show clear variations against the background decay. Elemental tin, the spectrum with the fewest counts, has very weak epithermal resonances at $t = 30$ μs and a low thermal capture cross section, due to its ‘magic’ atomic number of 50. In contrast, cadmium has a visible resonance at 27 eV and a very high thermal neutron capture cross section, which causes its spectrum to show twice as many counts than tin. At the top of the plot are the spectra from 20 grams of depleted uranium metal (^{238}U) and 10 grams of thorium fluoride salt (^{232}Th). These isotopes are unstable and passively radioactive, adding many more counts per

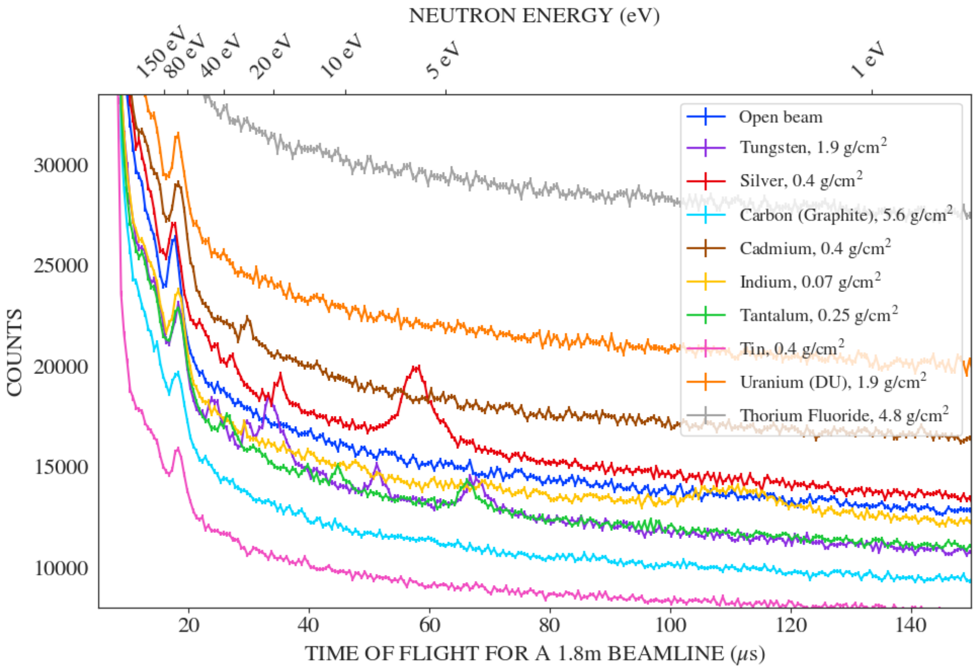

Figure 5-2: TOF capture γ-ray spectra for multiple samples containing either a single element or compound (in the case of thorium fluoride). The 100 eV ^{73}Ge resonance is visible in each spectrum at TOF = 80 μs due to germanium in the detector. Acquired with the 3" BGO in the Field Lab, 20 minutes each run.

bin to their spectra. The following section examines further aspects of the NRCA TOF spectrum and discusses methods to improve signal acquisition.

5.2.1 TOF Histogram Features

Inspection of TOF histograms is useful in understanding the capabilities of the NRCA technique and identifying methods for its improvement. Fig. 5-3 presents a prototypical NRCA TOF spectrum. Compared with Fig. 4-10, which shows spectra from the same targets, detector, measurement times, and D-T settings, Fig. 5-3 was recorded in the outdoor Field Lab. The reduction of hydrogenous material in the experimental area results in a dramatic decrease in the baseline background levels. Additional analysis on the experimental impact of the Field Lab experiments is discussed in Sect. 6.3.

The effects of the γ-ray background, described in Sect. 4.3, are evident in multiple features in Fig. 5-3. In this deadtime-corrected experimental series, the foil-like targets were placed against the front face of the detector, orthogonal to the beam axis. The detector was placed on the opposite side of the target, 180^o to the direction of the flight path. The open beam run has more off-resonance counts per bin than the tungsten-containing run. This can be attributed to the fact that tungsten

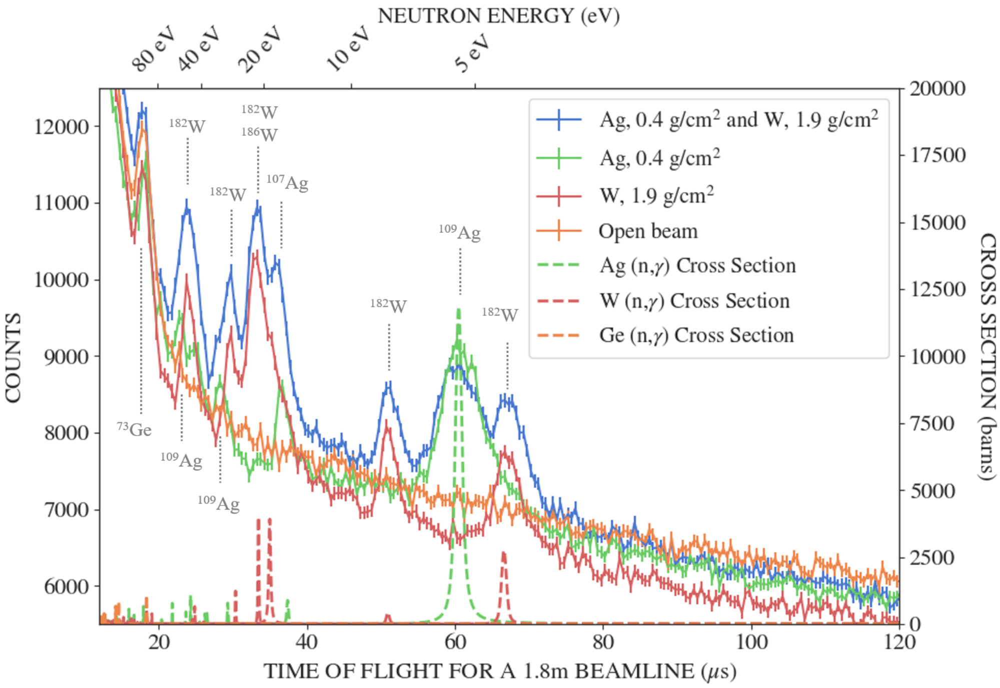

Figure 5-3: Experimental TOF spectra of an open beam, 1.9 g/cm^2 tungsten sample, and 0.4 g/cm^2 Ag sample. 20 minute acquisition in the Field Lab with a 3" BGO detector, deadtime corrected.

shields more γ-rays from entering the detector during these times than it produces. As silver is introduced to the beam, these off-resonance counts per bin increase due to the comparatively high thermal capture cross sections of both ^{107}Ag and ^{109}Ag.

The characteristic ^{73}Ge resonance at 100 eV is visible in all BGO plots. As with scintillator-intrinsic resonances in other detectors, a sample resonance with sufficient counts can be resolved over the intrinsic resonance signature; however, at a detriment to the SNR. Using the ^{73}Ge peak in one of these spectra as an example, we consider a hypothetical sample resonance compounding atop the detector-intrinsic resonance. To resolve the sample resonance with an SNR of 3σ given a background of 12,000 counts per bin, it must produce approximately 480 counts in the detector per bin at its peak. The same resonance occurring at 480 counts per bin in the decay continuum with a background of 7000 counts per bin would yield an SNR of 4σ. The BGO detector remains a suitable choice for this work, as the ^{73}Ge resonance occurs at the top limit of the region in which resonances can be resolved in the portable system.

The reconstruction of resonance structures by the TOF histogram also presents an interesting case study. The effects of resonance overlap, Doppler broadening, system resolution, multiple neutron scatters, and self-shielding are visible in Fig. 5-4. Here, each sample-containing spectrum is presented with the constant back-

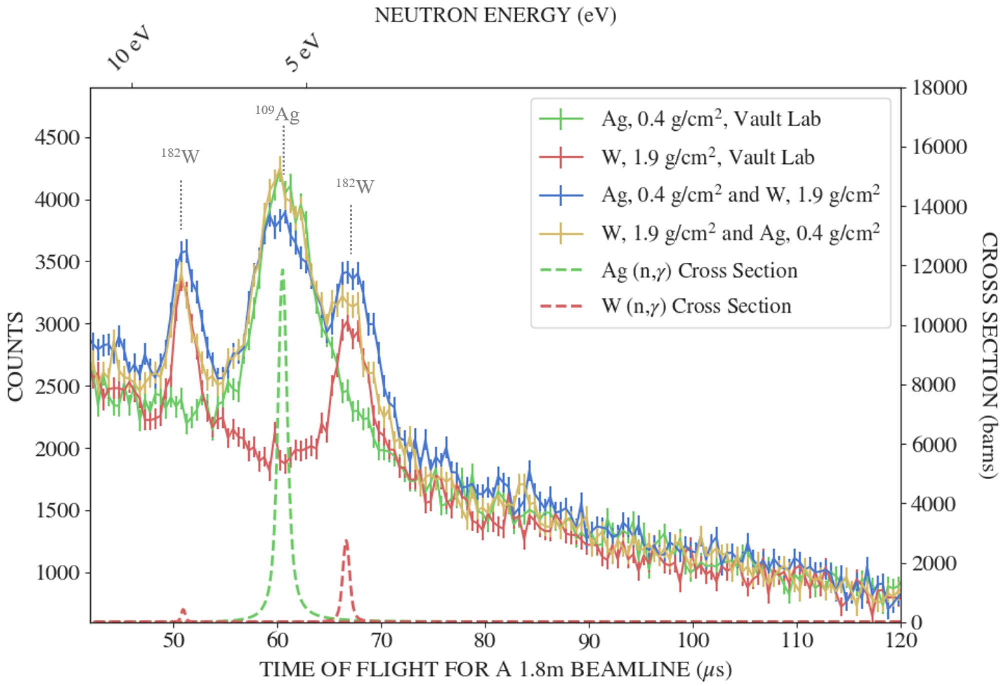

Figure 5-4: A detail of the experimental TOF spectra for a 1.9 g/cm^2 tungsten sample, 0.4 g/cm^2 Ag sample, and both samples combined in two arrangements. The constant background component for each spectra has been removed to aid in resonance comparisons. 20 minute acquisition in the Field Lab with a 3" BGO detector, deadtime corrected.

ground function removed to aid comparison of resonances. This plot contains two arrangements of the combined silver and tungsten target, with the order listed in the legend according to the neutron flight path (e.g.: the blue trace indicates that neutrons interact with silver first, followed by tungsten). The peak of the 5.2 eV ^{109}Ag resonance is attenuated by 15% in the experiment with tungsten acting as shielding between the silver and the detector. This is a reasonable value considering the energy range and distribution of resonance capture γ-rays and the mass attenuation coefficient for tungsten at these energies. This also serves to illustrate that uncharacterized NRCA samples should be evaluated for their effective attenuation coefficients, which may limit the capture γ -rays from escaping the sample.

5.2.2 Signal Improvement

Effects of Shielding

As motivated in previous sections, the neutron flux at the target is just enough to generate an acceptable signal in a reasonable measurement time. The first rule of shielding the detector or target therefore is to ‘do no harm’ to the neutron economy.

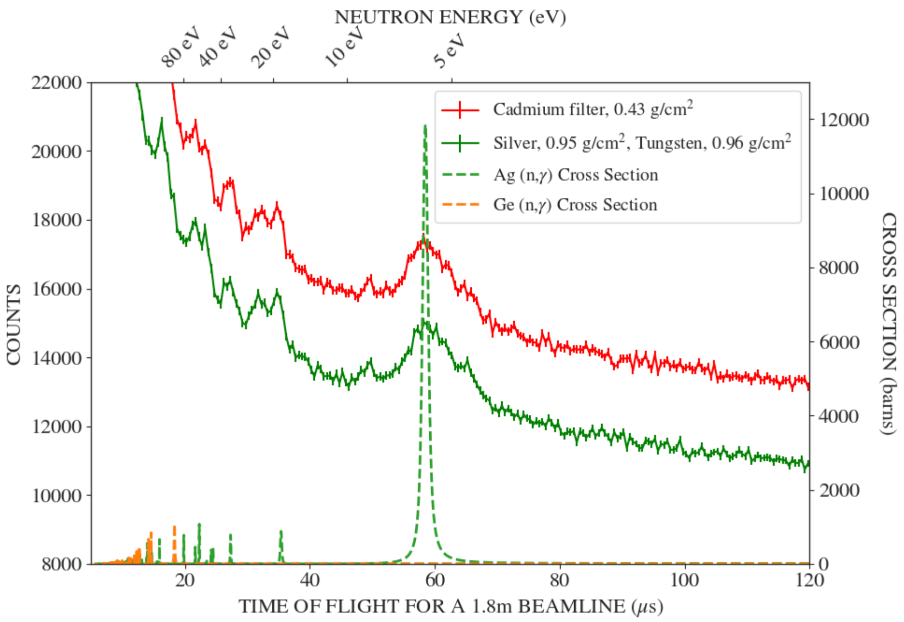

Figure 5-5: TOF spectra of a silver target with and without a cadmium filter. 20 min, BGO detector, Vault Lab.

Every material has some amount of off-resonance, potential scattering cross section regardless of neutron energy, which has the effect of removing eligible signal-producing neutrons from the beam. Thermal neutrons interacting in the target and detector are responsible for one quarter to one third of the background (depending on experimental environment, target, and detector type).

Natural-abundance cadmium has an average potential scattering cross section of 4.8 b across the epithermal range of interest and a 7 kb capture cross section at 0.2 eV. A cadmium filter is used with good effect in NRTA experiments to remove on-axis thermal neutrons from entering the neutron sensitive detector, generating spurious counts. Fig. 5-5 shows silver target with and without a 0.5 mm cadmium filter. The high thermal capture cross section of the material in turn generates prompt capture γ-rays that add to the off-resonance background for NRCA experiments. This has the effect of attenuating 1-5% of the epithermal neutrons producing a resonance signal while creating 20% excess background, thus diminishing the SNR.

Fig. 5-6 shows a silver target with the detector in the 85deg position (relative to the beam path) and several configurations of lead shielding. The SNR for the bare, one brick and four brick configurations is approximately 7.5σ, increasing to 8 σ for the highest amount of shielding. This configuration was used for most Vault Lab experiments. Due to space or weight constraints, the lead was reduced to one brick underneath the detector for the PNNL and Field Lab experiments.

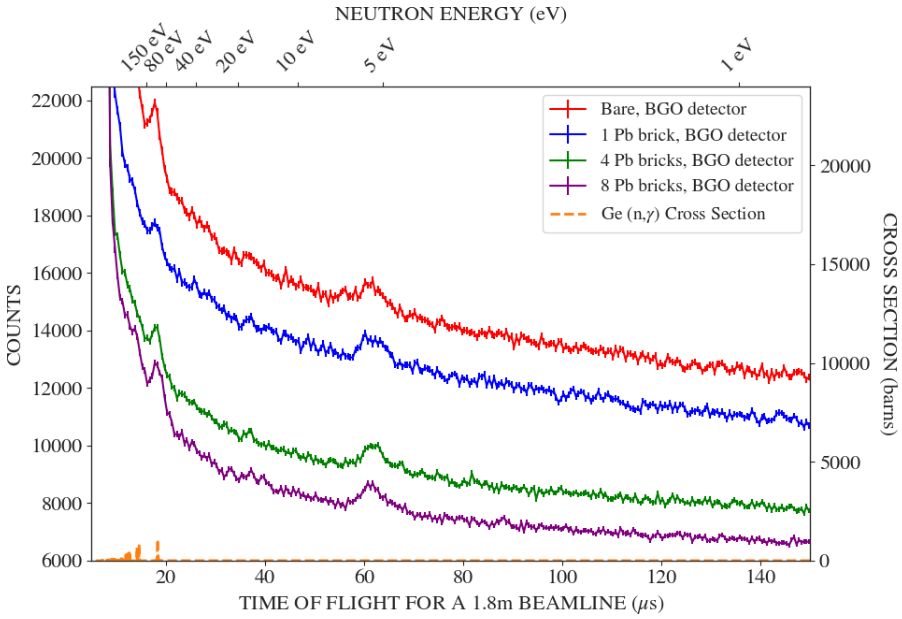

Figure 5-6: TOF spectra with varying amounts of lead shielding. 20 min, BGO detector, Vault Lab.

Filtering TOF by Energy

As introduced in Sect. 4.3.1, methods of γ-ray detection that record event energy information enable the selection of energy windows where the NRCA signal-to-noise ratio differs from that of the rest of the energy spectrum. The most straightforward method to eliminate energy regions that contain more background than noise (compared to the rest of the energy spectrum) is to adjust the lower limit of detection (LLD). By increasing the detector threshold to trigger above a low-energy source of noise, these counts are not registered in the final data output. However, this method is limited to low-energy background, as any count below threshold will not be recorded. Setting a threshold just above the 477 keV γ-ray from ^{10}B(n,γ) is an effective strategy for γ-ray detectors in the vicinity of boron-containing shielding. An application of this technique is presented in Sect. 6.4.

There are two general approaches to energy filtering in post-processing: a selection of the regions in which the NRCA signal is strongest and rejection of other areas, or selecting windows to reject and keeping the rest of the signal. The choice between methods is driven by the preponderance of monoenergetic background sources and the efficiency characteristics of the detector. Fig. 5-7 shows the γ-ray energy spectra and the TOF histograms for both a 1.9 g/cm^2 sample-in and sample-out configuration. The energy spectra reveal a distinct difference in decay-period counts between the two configurations, with the sample-in configuration measuring more counts per bin between the energies of 250 - 1000 keV. This observation

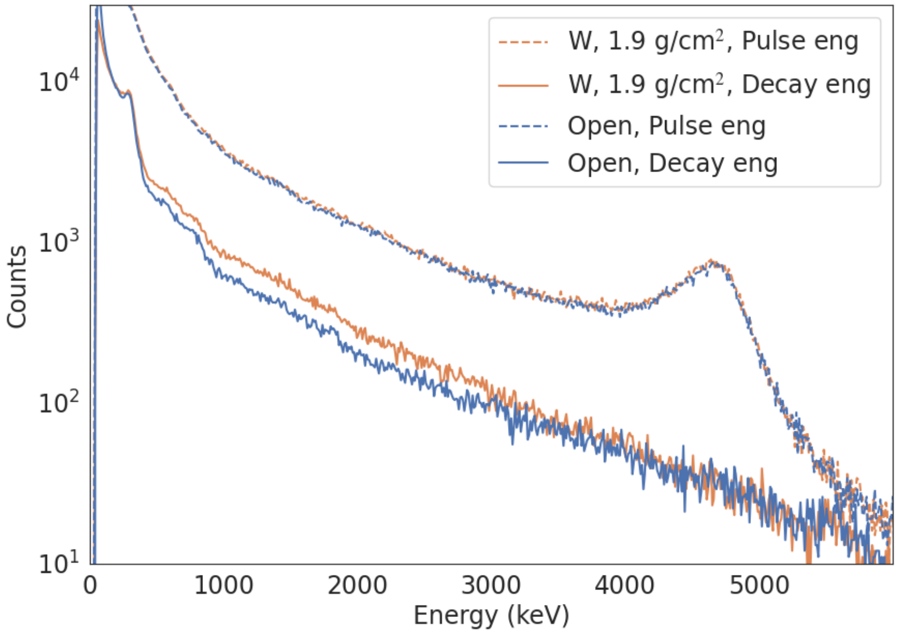

Figure 5-7: Experimental γ-ray energy spectra of an open beam and 1.9 g/cm^2 tungsten sample. Spectra have been separated into pulse periods (0-12 μ s) and decay periods (12.5-200 μ s). 20 minute acquisition in the Vault Lab with a 2" EJ-315 detector, calibrated using Compton edges.

Table 5.1: Resonance Count Values for the 18.8 eV Resonance in ^{186}W

Measurement	**Full Energy TOF**	**Energy Cut TOF**
SNR	8.03 ± 1.17	9.23 ± 2.15
Resonance Count Value	503 ± 72	451 ± 120

suggests that the tungsten sample is effectively shielding low-energy γ-rays and x-rays from the room background.

Fig. 5-8 shows the TOF histograms that correspond to the energy spectra shown in Fig. 5-7. The two sample-containing spectra are from the same measurement, with one displaying the TOF histogram with contributions from γ-rays of all energies. The second shows the TOF spectrum including only γ-rays associated with an energy between 250 and 1000 keV. The background-subtracted counts are plotted at the bottom, representing the contributions of the capture resonances. The background subtracted counts resulting from the energy cut histogram are approximately 80% of the full energy counts for the same integration limits. The SNR and the derived resonance counts for the single bin at the peak of the resonance are presented in Table 5.1.

The relevant metric for noise reduction is its impact on accurate resonance peak measurement, with the ultimate goal of ascertaining the isotopic content in a sample. The energy cuts removed 55% of the background and 11% of the signal, resulting in

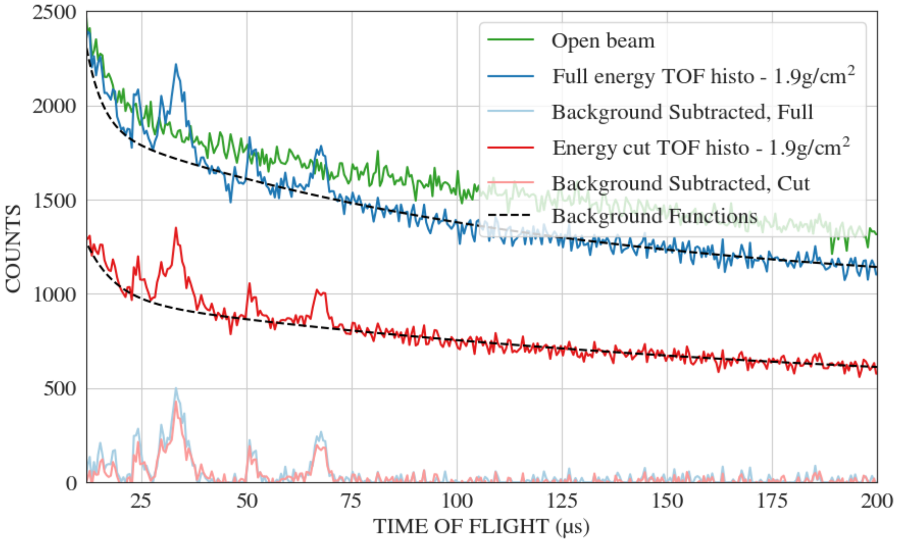

Figure 5-8: TOF spectra from runs corresponding to the energy spectra in Fig. 5-7. The energy-cut TOF histogram is generated using only counts with associated energies between 250 and 1000 keV. The contents of each resonance peak are displayed as a result of subtracting the fitted background function.

an improved SNR. This validates the assumption that the increased counts visible in the energy spectral comparison were due in part to tungsten resonances. By isolating the resonance signals, their peaks are more prominent relative to the background. However, the uncertainties of the energy cut histogram are significantly higher than those of the full-energy data, due to higher relative error in both the measured counts and the parameters of the fitted background function. Despite a clearer signal, the precision of the measurement has decreased as a result of statistical uncertainty.

This discrepancy has implications for inferring isotopic content from the measured signal that are related to the two goals of NRCA: isotopic identification and quantification. A higher SNR leads to more accurate peak fitting, which is important for resonance identification. However, a lower uncertainty leads to greater precision in the final determination of the isotopic content. Ultimately, it is computationally inexpensive to filter histograms by energy, and both strategies may be used based on the research goal. Increasing count statistics by using a more efficient detector or counting for longer can increase the statistics required to bring the uncertainties down to an acceptable range.

When selecting energy regions to exclude or include from the TOF spectrum, it is beneficial to understand the energy distribution of the resonance counts. A multivariate histogram that plots the count energy versus the TOF can display the capture γ energy distributions. Fig. 5-9 shows the subtraction of two single target experimental runs: a 0.37 g/cm^2 silver target and a 1.9 g/cm^2 tungsten target.

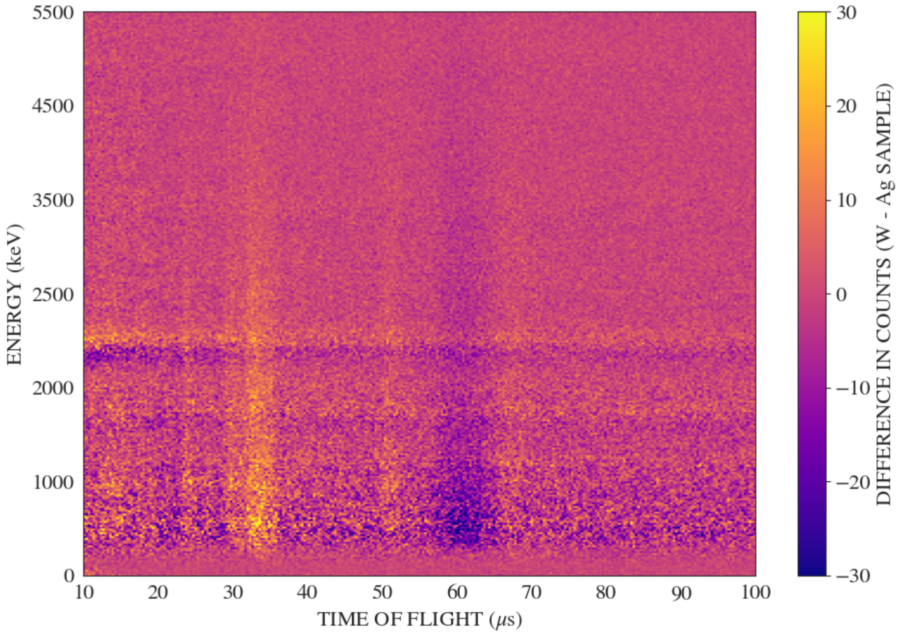

Figure 5-9: Multivariate histograms of a single target tungsten run (1.9 g/cm^2) and a single target silver run (0.37 g/cm^2), subtracted from it. The resonances associated with negative count values are due to silver and the the positive values associated with tungsten. Acquired with the 3" BGO in the Field Lab, 20 minutes each run.

The vertical bands indicate a changing signal in the time domain, highlighting the resonance peaks. The horizontal bands show monoenergetic sources of background, such as the 2.2 MeV hydrogen capture γ-ray and its single escape peak.

While a single run can also be plotted as a two-dimensional histogram, Fig. 5-9 presents the data for the silver experiment subtracted from the tungsten experiment. This provides a visual attribution of each material's contributions to the histogram. The extent of the resonance energies for both elements is visible, highly concentrated at lower energies but extending to greater than 4.5 MeV for the more prominent resonances. Notably, the horizontal bands appear bi-colored due to the attenuation differences between silver and tungsten, with the tungsten target acting as a high-pass filter. The success of this technique for identifying resonances and their capture gamma distributions depends on the relative strengths of the resonances and background. Additional methods for signal enhancement in 2-D histograms are presented in Sect. 5.3.

5.3 Resonance Identification

Given tabulated nuclear cross section data, the peaks occurring in the TOF γ-ray spectrum can be used to determine isotopes with epithermal resonances occurring in the sample. There are several spectrum fitting programs [167], [178] that use system- and Doppler-broadened resolution functions to infer resonance parameters that match the observed data. For all types of neutron resonance analysis, these programs require excellent characterization of the beam, sample, and detection system. For NRCA specifically, they also require an accurate determination of sample capture γ-ray multiplicity if isotopic quantification is desired. To make the issue of quantification more tractable, NRCA research groups have developed calibrated methods, discussed in Sect. 5.4.

Although neutron resonances have a Lorentzian shape in a plot of cross section versus neutron energy, they are broadened by Doppler effects into a Voigt profile, discussed in Sect. 4.2.2. This shape is further convolved with system resolution and multiple scattering such that the final peak may be reasonably described by a Gaussian fit. A single Gaussian fit may be applied to symmetric, well-isolated peaks. In traditional NRCA with access to very long beamlines and the ability to resolve higher energy resonances, researchers preferentially use separated, high cross section magnitude peaks for isotopic identification (and separated, low cross section peaks for isotopic quantification, discussed in the next section). This short beam, portable NRCA concept is limited to epithermal resonances only, in which case overlapping resonances must be used. Here, a double-Gaussian fit is valuable, in which two Gaussian functions are summed, each with a separate amplitude, mean, and standard deviation parameter.

The 7.6 eV resonance of ^{182}W is well separated and does not experience overlap effects from the 5.2 eV silver resonance. In the spectrum presented in Figures 5-3 and 5-4, it has a standard deviation of 2.78±0.26 μs, which converts to 0.895±0.084 eV in energy space. The system resolution at 7.6 eV as calculated by Eq. 4.11 is 0.184 eV. The discrepancy indicates an additional broadening due to Doppler effects and multiple neutron scatters in the target or experimental materials. The overlapping peaks of the 5.2 eV ^{109}Ag resonance and the smaller 4.1 eV resonance of ^{182}W experience higher uncertainties in their fits. The double Gaussian fit applied here yields a centroid for the 5.2 eV peak of 60.3 μs with a standard deviation of 5.49±0.53 μs. The centroid value shows excellent agreement with the true neutron energy location of the resonance for a 1.8 m beam path. The fit reports the 4.1 eV resonance at 68.3 μs and $\sigma_{5.2eV}$ = 2.73±0.69 μs; also good agreement with the reconstructed energy location of the peak, but a poorer relative uncertainty than the isolated peak.

The ability to determine resonance peak characteristics in the TOF spectrum allows the reconstruction of the neutron resonance structure of the sample. The combined energy, spacing, and magnitude of resonances are isotopically unique and allow the identification of sample constituents. In the case of overlapping resonances, an analysis procedure that can identify multiple peaks and their contributions is a useful tool. The multivariate histogram plot may also aid in automatic determination of resonance locations. By applying an edge-finding algorithm, such as a Canny or Sobel filter, the sharp resonance structures in the TOF domain can be easily identified by an automated process.

5.4 Quantity Studies

The count contents of a resonance peak that occurs in the TOF histogram represent the NRCA signal that is used for isotopic quantification. Schillebeeckx, *et al.* have reported the characterization of samples through resonance shape analysis of their capture yields, using the Moxon-Brisland analytical expressions [179]. This method is particularly limited to very thin targets produced by vacuum deposition and a highly characterized detection system with an efficiency that is independent of the capture event and its cascade. Therefore, resonance shape analysis of NRCA data is typically limited to neutron cross section parameter determination for nuclear databases. NRCA quantification of practical items, such as cultural heritage objects, is instead accomplished through an empirical approach. This method requires the use of calibration standards and therefore is not absolute based on a single measurement; however, it has determined the mass ratios of materials in excellent agreement with known values in previous studies [79], [127].

In an ideal measurement, the net area of a resonance peak would be directly proportional to the magnitude of the resonance and the areal density of the isotope. However, the self-shielding factor R, introduced in Sect. 2.3.3, describes the impacts on radiative capture counts made by the contributions of all neutron interaction processes available to a particular neutron energy. These competing interactions have the effect of removing neutrons from the population that otherwise would have resulted in neutron capture and are given by

$$R = \frac{1 - e^{-\sum_j n_j \sigma^D_{tot,j} x_j}}{\sum_j n_j \sigma^D_{tot,j} x_j}, \tag{5.1}$$

where n_j is the number density of isotope j, σ^D_{tot}, is the Doppler-broadened total cross-section for neutron interactions with isotope j, and x_j is the thickness of the material containing isotope j. R is therefore the ratio of the effective neutron capture counts to the ideal neutron capture counts that would be measured without self-shielding. The effect becomes more pronounced with increasing effective

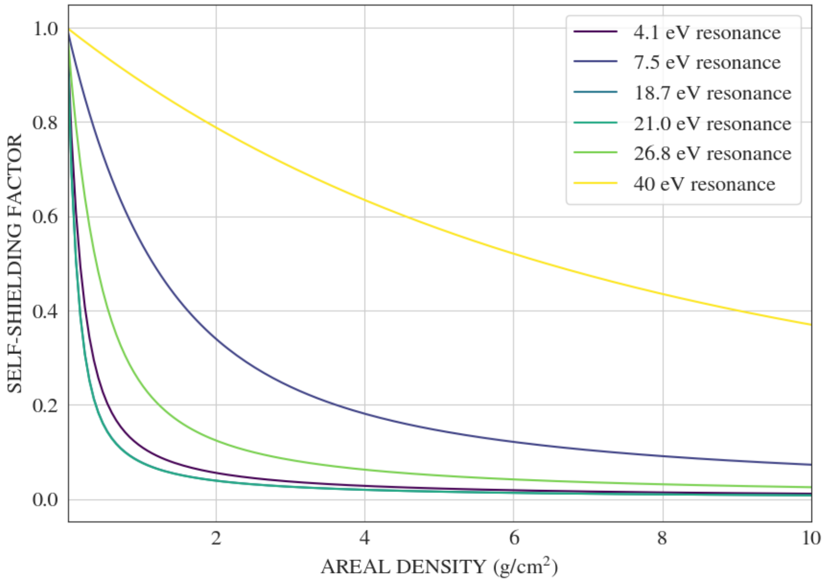

Figure 5-10: Self-shielding factors for selected epithermal neutron resonance energies in tungsten as a function of areal density.

areal densities of each isotope that contributes to neutron removal. Especially for the relatively high resonance magnitudes and thicknesses of samples used in this research, an accurate self-shielding determination is crucial when interpreting a resonance peak area in the context of isotopic quantification.

Fig. 5-10 shows the self-shielding factors for selected epithermal resonances of tungsten as a function of areal density. Each curve corresponds to a different resonance energy, listed in the legend, and is weighted for the natural abundance of each isotope. Visual inspection of the plot shows a range of self-shielding effects, which in turn increase the uncertainty of the ultimate areal density quantification. The high cross section, strongly self-shielded resonances provide high sensitivity to small changes in areal density, but suffer from significant attenuation in thicker samples. Although not a trend for all isotopes, higher energy resonances are usually weaker and will provide more reliable data for samples with high areal densities. The selection of resonances to consider when analyzing a sample must be optimized for the range of sample areal densities and the required sensitivity. A combination of resonances may also be used to provide a more comprehensive analysis, particularly for an unknown sample.

A series of combined silver and tungsten targets were measured using the portable NRCA setup, each with a different material ratio and total areal density. Fig. 5-11 shows the deadtime-corrected TOF spectra from nine of these experiments. The color gradation of the plotted histograms corresponds to increasing silver areal density. The constant background component, C_0, is most closely associated with

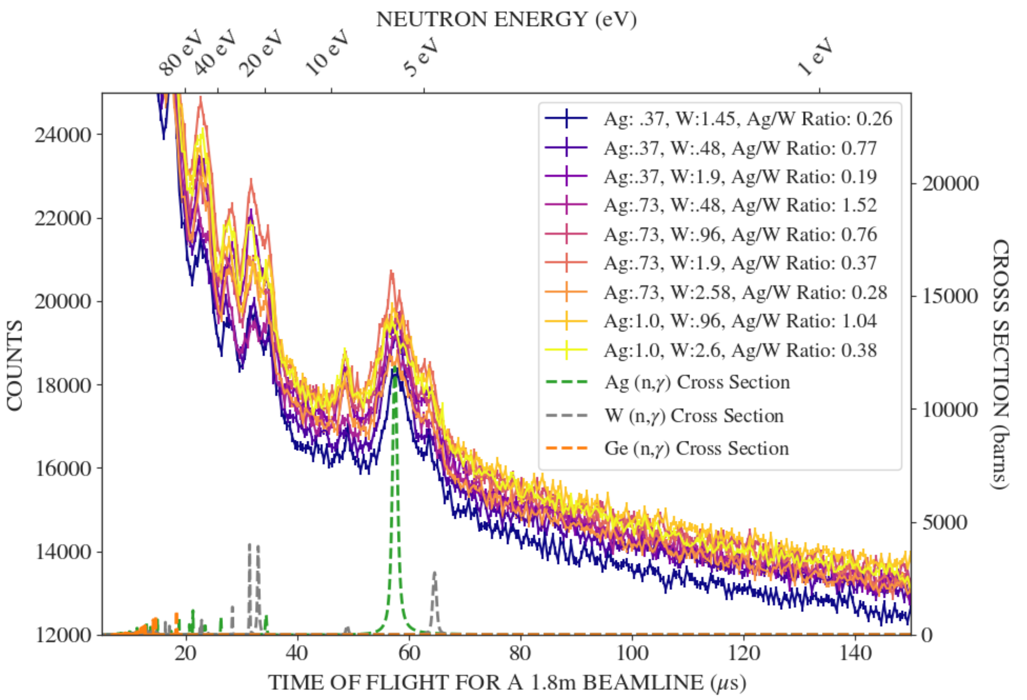

Figure 5-11: Multiple TOF spectra from combined silver and tungsten targets. Values in the legend are reported in units of g/cm^2. Each run taken at the same beam path length for 20 minutes with the 3" BGO in the Vault Lab.

the increase in silver areal density, exhibiting a correlation coefficient of 0.62, compared to the C_0 correlation coefficient for tungsten, which is 0.41. This higher correlation for silver is consistent with its high thermal neutron capture cross section. This analysis indicates that additional isotopic information may be contained in the off-resonance data and comparative spectra from different runs, especially when combined with resonance-derived information.

Each of the spectra from this campaign was analyzed according to the background fitting procedure described in Sect. 4.3. A plot of selected TOF-based measurements and their corresponding background function components is presented in Fig. 5-12. The colors of the plotted histograms represent different sample compositions, and the total and component background functions are shown as dashed lines corresponding to the color of each TOF histogram. The background function component attributable to the D-T pulse, C_2, is the same for each measurement. The constant background component C_0 aligns with each measurement's baseline count value, and the varying contributions of the slow decay component C_1 are visible in the figure. The total function is used to subtract the background component from the histogram resulting in an array of neutron TOF-based γ counts from resonance captures.

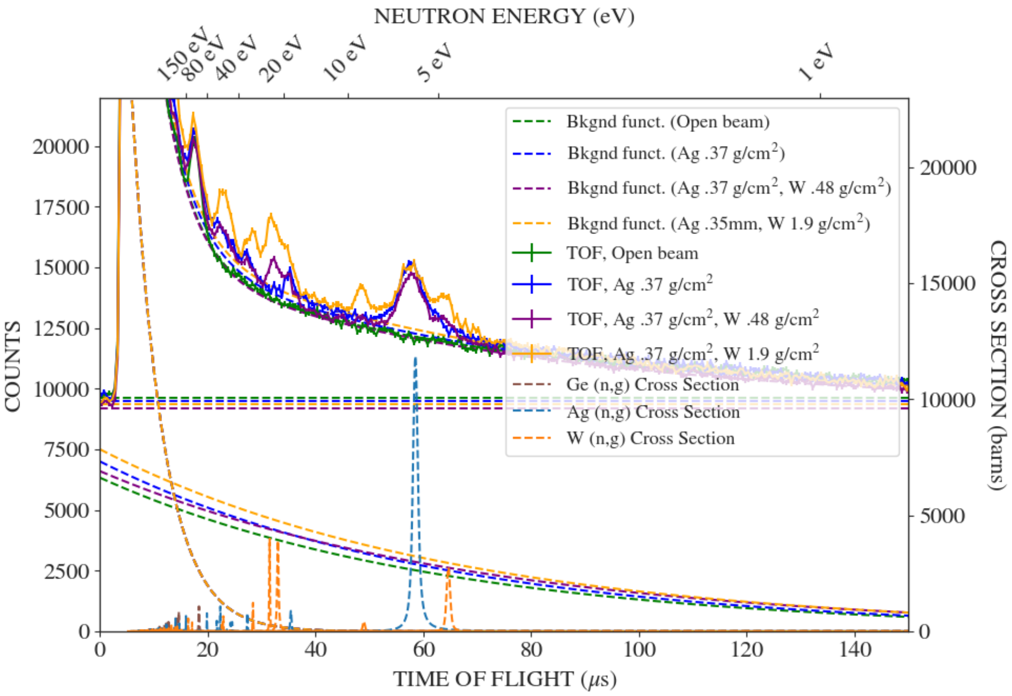

Figure 5-12: Time-of-flight spectra with background functions for various silver and tungsten areal densities. The dashed lines represent the total and component background functions for each measurement. Each measurement was acquired for 20 minutes with the 3" BGO in the Vault Lab.

Seven prominent resonances in silver and tungsten were selected for analysis, and the counts from the bin comprising the resonance peak were recorded. A larger time integration window for peak counts may be applied to improve the counting statistics; however, for this analysis, a single 0.5 μs bin was selected to mitigate the effects of resonance overlap. The count values for each resonance from the nine observations were analyzed using Ordinary Least Squares (OLS) regression to assess their correlation with the areal density of their corresponding isotope. The results of this regression using raw counts and self-shielding corrected counts (R) are presented in Fig. 5-13. The OLS regression model assumes a linear relationship between the dependent and independent variables, resulting in a lower correlation value for the raw count and areal density assessments as a result of the contributions of self-shielding. The R^2 value, the correlation metric used in Fig. 5-13, indicates the proportion of variability in the dependent variable (counts) that can be explained by the independent variable (areal density of the relevant isotope). It should be noted that all values presented in the figure are derived from runs including both silver and tungsten, showing the relative independence of resonance structures, with the exception of silver's 16.3 eV resonance.

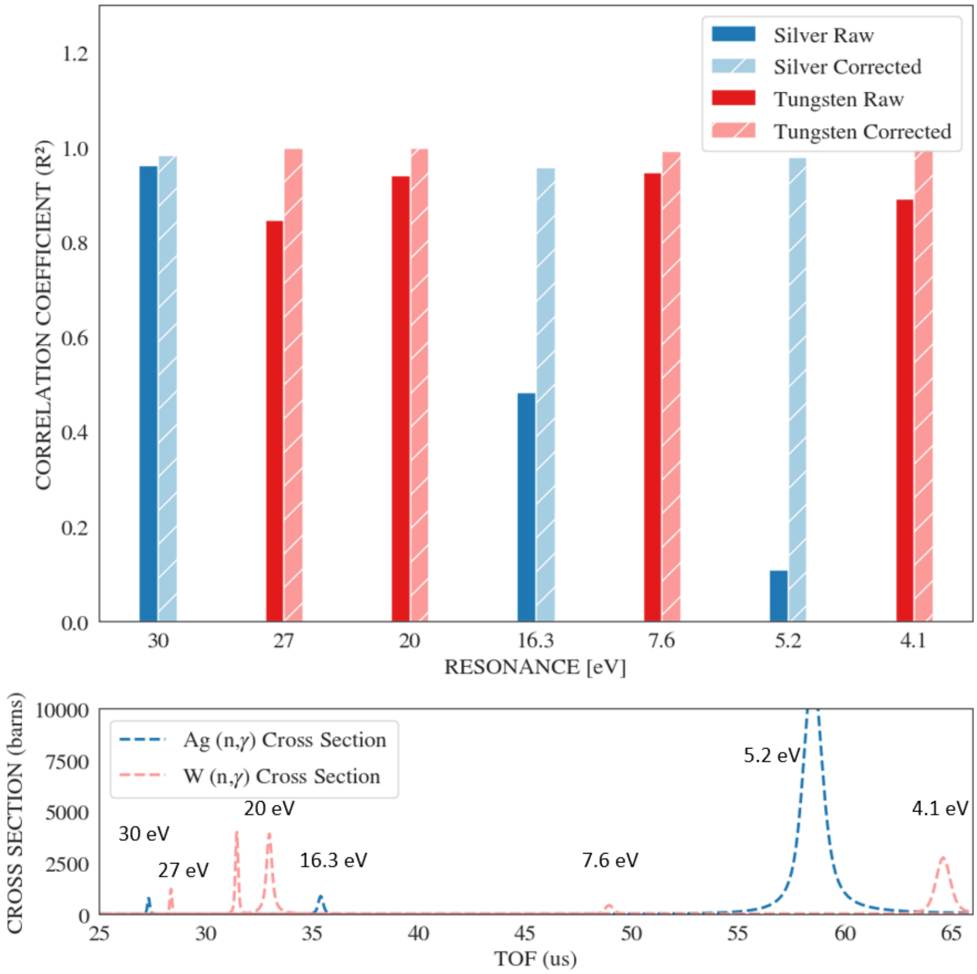

Figure 5-13: Correlation coefficients (R^2 values) for the raw and self-shielding corrected counts of silver and tungsten resonances, obtained through OLS regression. Resonance cross sections as a function of neutron time of flight for a 1.8 meter beamline are presented below, each labeled with their corresponding energy value.

The 5.2 eV resonance of ^{109}Ag, while an excellent benchmark for silver identification and NRCA system optimization, is a poor indicator of silver content at these areal densities. The magnitude of this resonance is so large that the neutron flux of this experimental setup reaches radiative capture saturation even in the thinnest available silver target (0.4 g/cm^2). The counts from this peak showed a stronger correlation magnitude (albeit negative) with increasing tungsten thickness than the correlation with increasing silver content, due to the tungsten's ability to shield resonance capture γ-rays from entering the detector. This is a poor resonance to select for areal density determination in this campaign but can be a powerful indicator of slight areal density changes in thinner targets or targets with trace amounts of silver.

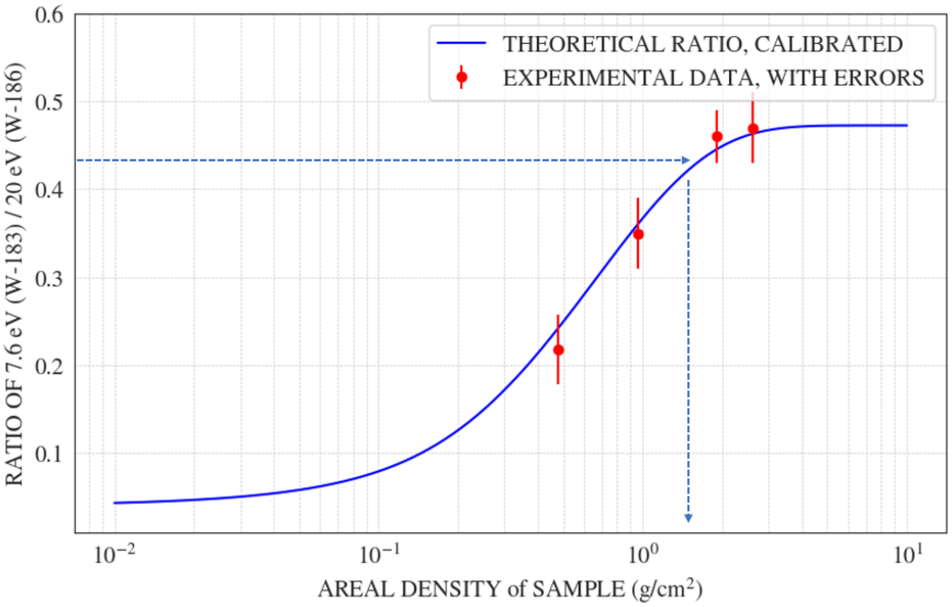

Figure 5-14: Theoretical ratio of counts from the 7.6 and 20 eV resonances in tungsten as a function of tungsten areal density. The theoretical self shielding factor for each resonances is weighted by the natural abundance of each contributing isotope. Experimental data points are shown in red, and the dashed line indicates the experimental ratio of these two resonance counts for a 1.45 g/cm^2 sample of tungsten, showing good agreement with the calibration.

It is expected that the R^2 values for the self-shielding corrected counts would show a strong correlation with the areal densities of the isotopes. This is because the self-shielding correction scales the counts to account for the attenuation effects within the material, thereby normalizing the counts relative to the areal density. Using the areal density-containing R value in a calculation meant to determine the areal density at first appears counter-intuitive; fortunately, there are methods to mitigate this issue. Inspection of Fig. 5-13 shows a strong correlation of raw counts to material thickness, which allows a first-order determination of areal density. .

A more robust approach is the single ratio calibration method, which uses a theoretical self-shielding curve normalized by experimental data. This method was developed by Schillebeeckx [169] and is illustrated using data from this research in Fig. 5-14. Here, the theoretical ratio of counts from the 7.6 and 20 eV resonances in tungsten is plotted as a function of tungsten areal density. The theoretical self-shielding factor for each resonance is weighted by the natural abundance of each contributing isotope (^{183}W for the 7.6 eV, and ^{186}W for the 20 eV). The experimental data points, shown in red, are used to normalize the theoretical curve.

The dashed line indicates the experimental ratio of the raw counts from these two resonances for a 1.45 g/cm^2 sample of tungsten, resulting in an areal density determination of 1.5$\pm$0.3 g/cm^2, where the errors are derived from counting statistics and the covariances of the background fit parameters. This process demonstrates the ability to use calibration standards for an areal density assessment using NRCA data and mitigate the circular logic of the areal density requirement in self-shielding corrections. The method can provide a powerful tool for analyzing samples of appropriate areal density, even when combined with materials that also present with epithermal resonances.

Chapter 6

Safeguards Applications

The identification of isotope types and the quantification of their masses are crucial for nuclear safeguards and security applications, such as port-of-entry inspections. These materials often emit γ, β, α, or neutron radiation from natural decay processes. The particles emitted form passive signatures that can indicate the presence of specific isotopes. However, these signatures can overlap in composite samples, masking the signal of an isotope with lower activity. Another complication arises when the signature of one isotope may closely resemble that of another, as is the case with the passive γ-ray signature of ^{232}Th and ^{232}U, making identification difficult. Active analysis can address these challenges by inducing reactions that generate a clearer signal to identify isotopes of interest.

Traditionally, active nuclear material assays are conducted in large facilities with complex and massive equipment that is not easily moved to the site where the nuclear materials are used, produced, or otherwise evaluated. However, advances in research over the past two decades have challenged this assumption. Portable versions of neutron radiography units, cyclotrons, RFQ linacs, and various compact neutron generators are now available, enabling on-site evaluation techniques [131], [180], [181]. Uranium enrichment is a particularly important topic due to the widespread use of the uranium fuel cycle. Various developments have been made to address the need for accurate information on uranium enrichment, including Active Well Coincidence Counting, the In-Situ Object Counting System, delayed neutron counting of fuel pins, and differential die-away analysis (DAA) [70], [71], [182], [183].

This research proposes NRCA as a method for isotopic identification in locations where a pulsed neutron source is suitable for use. It is sensitive to materials with resonance structures in the epithermal region, which includes all of the fissile and fertile isotopes currently being considered for use in the fuel cycle. Also included in this set are ‘clue’ isotopes that can divulge information about the reactor or processing history of a sample, including ^{232}Pa, ^{233}Pa, and ^{232}U. Portable NRCA has high compatibility with other methods and is capable of being performed concomitantly with NRTA, PGNAA, DAA, and others, should a neutron generator-based assessment platform be added to the safeguards portfolio.

Therefore, the work discussed in this chapter sought to assess the NRCA methodology and the portable system in its proposed application. The first section covers sample selection, design, and considerations for future investigations of this kind. The second section applies the techniques introduced in Chapter 5 to assess NRCA effectiveness in assessing radioactive samples, particularly fertile isotopes in the thorium breeder fuel cycle. This is followed by a section detailing the impacts of a series of field tests and an assessment of the portability, safety, and effectiveness of the technique. The fifth section presents results from an NRCA campaign carried out at Pacific Northwest National Laboratory using the NRTA-based D-T set up there and a series of unique fuel-cycle targets. Finally, a short discussion covers practical considerations for deployment of a D-T-based system and its use in a safeguards capacity. Issues and troubleshooting steps for operating the D-T in this uniquely taxing pulsing regime are also covered, as well as considerations for the purchase of future neutron generators.

6.1 Sample Selection and Design

Not only will the isotopic and chemical forms of the advanced fuel materials proposed vary significantly, but so will their physical shapes, sizes, and densities. Figure 6-1 shows three such fuel forms, indicating that future reactor fuels may range from liquid salts, axially heterogeneous fuel pellets, and metal oxide plates. Other forms and shapes are possible, such as TRISO balls and ceramic fuels. A robust isotopic analysis system for nuclear material is one that can reasonably assay multiple forms and compositions. This section discusses radioactive sample design for experiments at MIT, the samples used at PNNL are covered in Sect. 6.4.

As indicated by the geometry studies presented in Chapter 5, plate or foil-like samples yield a cleaner signal as a result of neutron interaction timing. Therefore, the ideal samples to assess this technique were thin sheets of uranium and thorium metal. Depleted uranium (99.8% ^{238}U, 0.2% ^{235}U) was available in 1 mm thick, 100 cm^2 sheets, one of which was cut into several 20-30 g samples for this research, each ranging from 6-8 cm^2. Small, 1 g samples were also obtained from this cutting process. A small uranium sample and two thorium samples from this research are shown alongside other samples in Fig. 5-1.

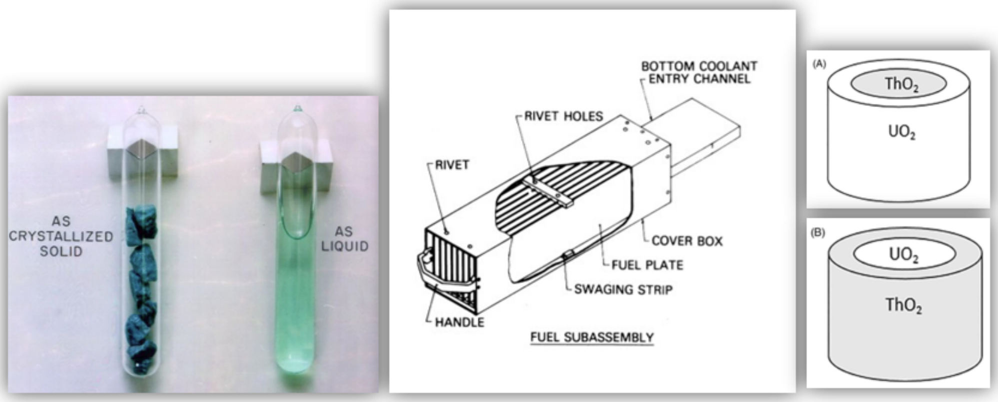

Photo: ORNL / DOE

(Baghwat, Nuc. Tech., 1993)

(Rabir, Eng. Rsrch., 2020) also, (van der Walt, Nuc. Eng., 2023)

MSR Fuel (LiF –BeF-ThF$_4$-UF$_4$)

Kamini Th LWR Plate Fuel (Al-clad ^{233}U)

Duplex fuel pins (ThO$_2$-UO$_2$)

Figure 6-1: Photos and schematics of various fuel forms proposed for use in advanced nuclear reactor concepts [47], [184].

A 1 kg thorium metal rod ($\approx$ 15 cm height and 2.5 cm diameter) with a thin layer of oxidization was available at MIT and was used for the initial NRCA experimentation. The passive activity and poor geometry of the sample resulted in these experiments yielding a negative result, with no ^{232}Th resonances visible over the immense background. Efforts were made to purchase sheets of metallic thorium or thorium oxide; however, most vendors had discontinued thorium sales. Thorium hexaflouride (ThF_4) was commercially available from Strem Chemicals. As the chemical form most commonly proposed for thorium-bearing molten salt reactors (see Table 1.2,) this salt was an excellent option for applications testing the NRCA technique. It arrived in 10 g units, each packaged in a glass vial under argon. Initial preparations were made to vacuum seal the salt in polytetraflouroethylene (PTFE, C_2F_4) sheets in a flat, uniform thickness configuration inside a radioactive materials fume hood. However, inspection of the salt grain size showed it to be on the order of tens to hundreds of micrometers, creating a possible inhalation hazard. The salts were kept in their glass vial packaging and double sealed in PTFE to reduce breakage hazards. Future researchers working with actinide salts are advised to specify the grain size or inquire about manufacturer packaging in a more favorable geometry. Toward the end of the research, several 0.5-1 gram strips of metallic thorium became available for use.[1] These provided clear thorium resonance signatures and their use is indicated in the plots below.

---

[1] Thorium metal strips courtesy of MIT Environmental Health and Safety.

Keeping the thorium fluoride salt in the glass vials rather than sealing in a disc-like configuration increased the complexity and uncertainty of measurement. The vials were oriented horizontally across the front face of the detector so that the powder was evenly distributed across the lower half of the vial. This can be approximated as a semi-circle; integrating the chord lengths over the height of the semicircle and dividing by the radius yields an average width or effective thickness seen by an orthogonal neutron beam. For the 1.5 cm diameter vials used in this research, the effective thickness of the thorium fluoride powder is $\frac{\pi r}{2}$ = 1.18 cm and the powder density is approximately 1.9 g/cm^3. Assuming a wide margin of error and propagating the uncertainty from the density and geometry measurements, the ThF_4 salts are presumed to have an effective areal density of 4.8±0.4 g/cm^2 per vial.

6.2 Results With Actinide Samples

Passively radioactive samples that decay by γ-ray emission present a challenge to this assessment technique, which is based on the detection and interpretation of induced γ-rays. The decay particle type and the magnitude of the specific activity of the isotopes under evaluation can significantly add to the background noise of a measurement. As such, the SNR for NRCA signals from radioactive samples is comparatively lower than that of a non-radioactive isotope with similar areal density and resonance cross section.

In traditional NRCA experiments used to determine cross section information, samples containing fissionable materials require additional data analysis over non-fissionable ones. When analyzing materials in which single resonances share both radiative capture and fission widths, research groups apply special measurement and data processing steps to accurately link γ-ray yield to each process [169]. A benefit of the calibrated method of isotopic quantification presented in Chapter 5 is that fission and capture γ-rays alike support the positive quantification of an isotope, assuming experimental parameters remain constant during the calibration and sample runs.

Thorium presence in a sample can often be determined with gamma spectroscopy (both passively and from neutron activation analysis). In this method, the γ-ray energy spectrum is used to identify the characteristic decay energies of ^{232}Th daughter products, including ^{212}Pb at 212 keV, ^{228}Ac at 911 and 968 keV, ^{212}Bi at 1620 keV and ^{208}Tl at 2615 keV. However, thorium that has recently been chemically processed will have a markedly different spectrum than natural thorium, as most of the energy peak features are generated by its progeny isotopes. Further

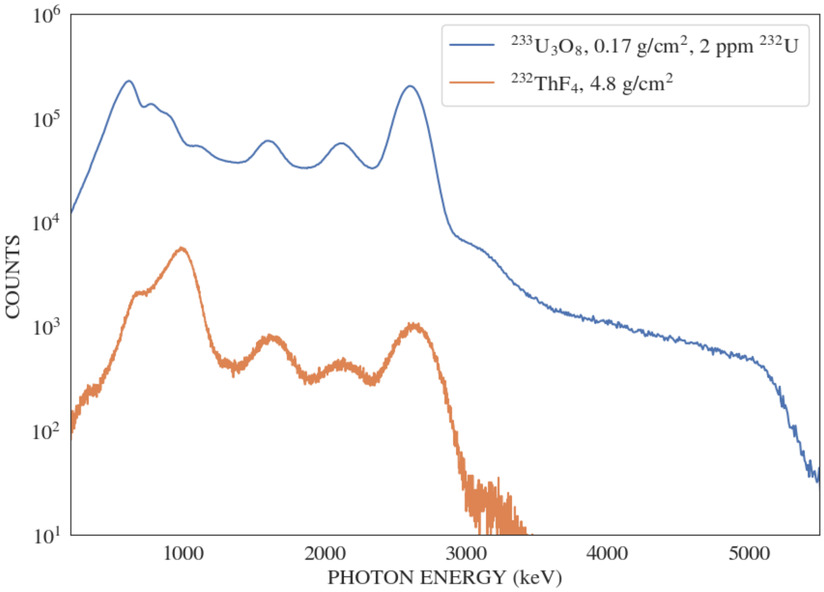

Figure 6-2: Experimental energy spectra from 10 g of ThF_4 acquired in the Vault Lab with a 2" BGO (corrected for volume,) and from 2 g of $^{233}U_3O_8$ acquired in the PNNL LSF with the 3" BGO. Each spectrum measured for 5 minutes.

complicating the assay of advanced fuel materials, ^{232}Th and ^{232}U decay through the same 4*n* actinide decay series, with the same daughter products from ^{228}Th onward, leading to similar passive spectra, as seen in Fig. 6-2. Although it has one-fifth the mass of the thorium sample, the uranium sample is 15 times more active due to the relatively short half-life of ^{232}U (visible in Appendix B, Fig. B-1.) The evaluation of thorium independently of its daughter products is therefore an important capability for nondestructive assessment of fuel cycle materials. Likewise, identifying uranium isotopes in mixed samples with thorium is also an important assessment function for safeguards applications.

The 21, 23, and 58 eV resonances of ^{232}Th are theoretically resolvable in an NRCA system sensitive to epithermal neutron energies. ^{238}U also has three prominent epithermal resonances at 6.6, 20, and 37 eV, with other higher energy resonances that are more difficult to resolve given the constraints of the portable system (discussed in Sect. 4.2.1). ^{235}U has more epithermal resonances than the former isotopes, but at lower cross section magnitudes. Fig. 6-3 demonstrates the self-shielding factor based on magnitudes of the total neutron interaction cross section for selected ^{232}Th and ^{238}U resonances. The relative strength of the ^{238}U resonances implies that self-shielding effects are crucial to consider for accurate isotopic quantification, especially as the areal density increases. Resonances that have overlapping tails from isotopes comingled in the same sample will contribute to self-shielding. Using the 20.4 eV resonance in ^{238}U as an indicative example, the

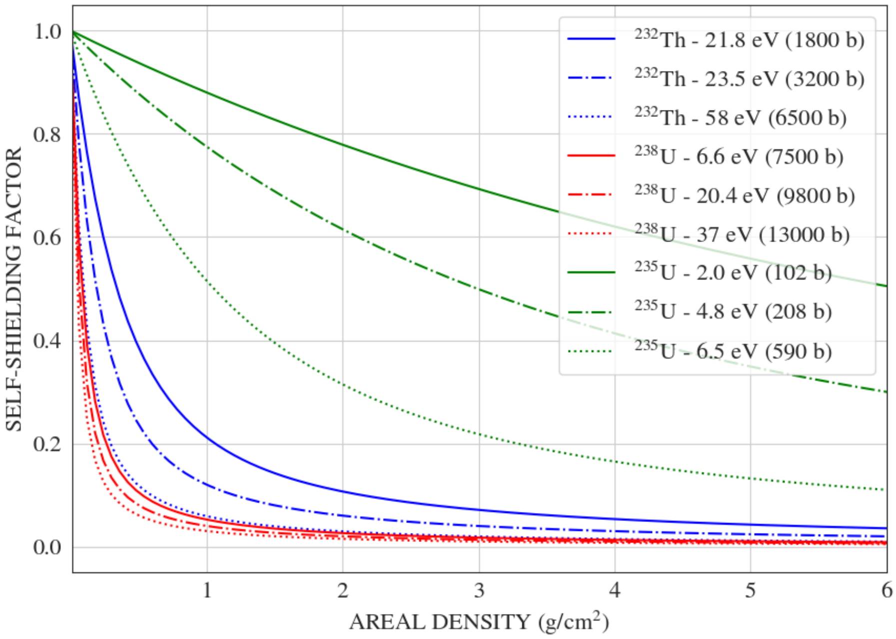

Figure 6-3: Self-shielding factors of selected ^{232}Th, ^{235}U, and ^{238}U resonances as a function of areal density. Resonance peak cross sections are indicated in the legend; values are for (n,total) reactions.

(n,tot) cross section as a function of neutron energy contributes an additional 29 barns of self-shielding to the 21.8 eV resonance in ^{232}Th. However, the Gaussian-like tail of this cross section shape has returned to the uranium potential scattering baseline value by the occurrence of the thorium 23.5 eV resonance, contributing only marginally to its self-shielding. When using NRCA-derived capture γ-ray count values for isotopic quantification, self-shielding is an important consideration.

The results of Fig. 6-3 indicate that the linear relationship between background-removed counts and sample thickness is best preserved in thin samples of uranium (as is the case for any material with strong resonances). This effect is further compounded by a passively radioactive sample. Adding additional sample thickness beyond the linear density at which a particular resonance reaches the self-shielding limit will continue to contribute to background counts with very little additional signal. This places a practical sample thickness limit on NRCA's quantification ability. However, NRCA can still provide useful isotopic qualification information for objects that have exceeded self-shielding thicknesses, even for very large objects that cannot be imaged with transmission techniques.

A particular benefit of the high peak-to-Compton ratio of the BGO detector is the greater percentage of photon counts that deposit their full energy into the sensitive volume. This feature allows background removal by placing cuts on energies in which a preponderance of background occurs, such as the 2.2 MeV

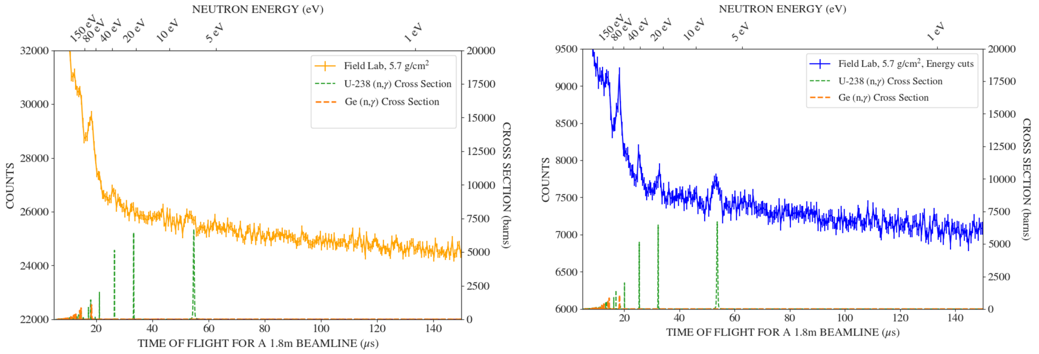

Figure 6-4: Two TOF spectra for a single experiment, the left without energy cuts applies and the right including only counts that deposited between 1 - 2.2 MeV and greater than 2.6 MeV. The target is 5.7 g/cm^2 DU, 20 minute duration, Vault Lab, 3" BGO detector.

hydrogen capture peak, or decay lines from uranium. Fig. 6-4 shows two uranium TOF spectra from the same experimental run. The left is the raw spectrum and the right includes only events that deposited between 1 - 2.2 MeV and greater than 2.6 MeV. These energy windows were selected to remove the photons arising from hydrogen capture and the passive decay of ^{238}U (primarily less than 1 MeV), highlighting the probabilities for the decay energies of the primary radiative capture gamma from ^{238}U and ^{232}Th, shown in Fig. 2-4. The characteristic resonances of ^{238}U are visible in both plots, but enhanced relative to the background in the energy-cut spectrum. Using the 6.6 eV resonance as a benchmark, the SNR improves from $(2.8 \pm 0.9)\sigma$ to $(3.6 \pm 1.1)\sigma$ after background removal. In the cases where energy cuts are used on the TOF spectrum to reject areas of low SNR, consideration of each energy spectrum is warranted if calibration shifts are indicated between runs.

Fig. 6-5 shows TOF spectra from experiments analyzing increasing areal densities of metallic DU plates. The constant background component has been removed to aid in comparison, and the energy cuts discussed above have been applied. These data are presented in their raw histograms in Appendix B, Fig. B-7. As inferred by the self-shielding factors presented in Fig. 6-3, resonance peak counts become increasingly nonlinear as target areal density increases. This effect is pronounced in the 6.6 and 21 eV resonances. The 36 eV resonance has diminished self shielding effects due to its lower cross section magnitude. For this target configuration and experimental setup, quantity determination reaches a practical limit at approximately 4 g/cm^2. This concept is further explored in Sect. 6.4 using thinner samples of HALEU powder.

The TOF spectra presented in Fig. 6-6 illustrate the radiative capture γ-ray response due to varying areal densities of ThF$_4$. The plots indicate the sensitivity of

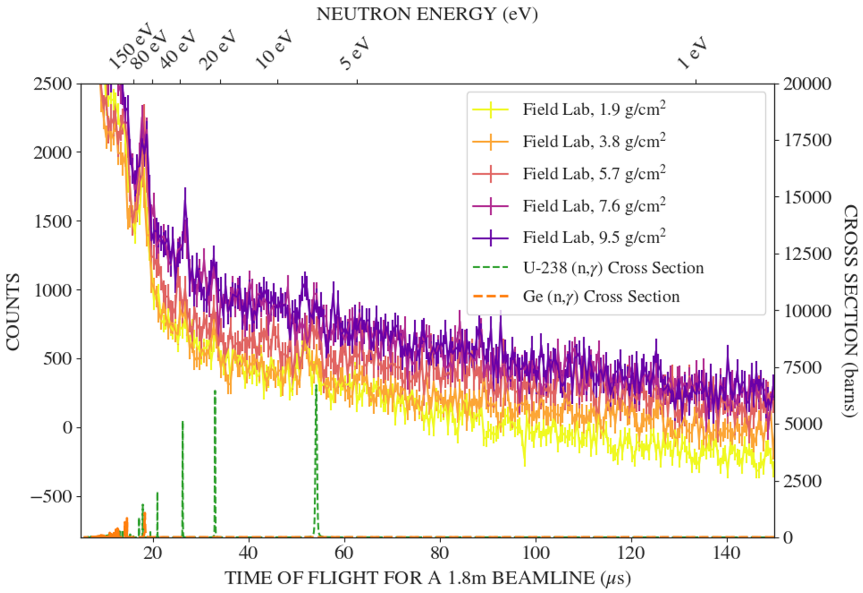

Figure 6-5: TOF spectra from increasing areal densities of depleted uranium metal sheets, each approximately 5x5 cm. The C_o background component has been subtracted from each for comparison purposes and the energy cuts discussed in Fig. 6-4 have been applied. 20 min runs in the Vault Lab with the 3" BGO detector.

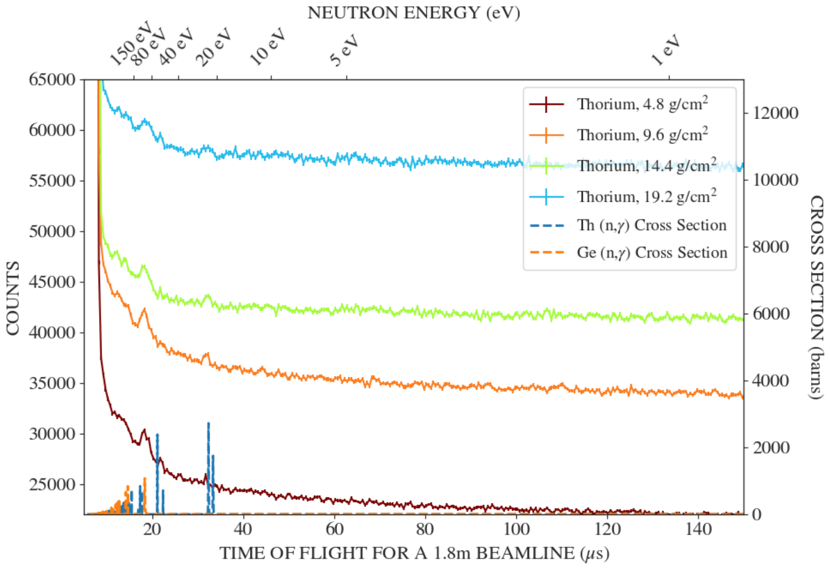

Figure 6-6: TOF spectra from various areal densities of 10 g vials of ThF_4 powder. 20 min runs in the Vault Lab with the 3" BGO detector.

the technique to the presence of thorium, indicated by distinct resonance peaks corresponding to the resonance profile of ^{232}Th. However, there is limited sensitivity to the areal density of the thorium on the basis of count values of the resonance peaks using the methods described in Sect. 5.4. Although additional thorium thickness adds to the overall counts per time bin (the C_o constant background term in the background function), this does not contribute to a positive identification of the thorium isotope, only an indication that the overall activity of the sample is increasing. This experiment used the vials of powdered thorium fluoride, which potentially contributed to the broadening of resonance peaks in the final TOF spectra.

Fig. 6-7 shows TOF spectra from three different experiments, each with a constant areal density of metallic thorium and an increasing areal density of depleted uranium. The TOF spectrum from each experiment has been filtered based on the energy values of the contributing γ-ray count, with the darker line trace representing counts with deposited energies between 1 and 2.4 MeV and the lighter trace composed of only counts with energies registering 2.6 MeV and higher. The resonance peaks associated with ^{238}U are more pronounced in the lower energy cuts, and those for thorium are preferenced in the high energy cut. This observation supports the expected energies from the primary de-excitation γ-rays from both thorium and uranium (see Fig. 2-4), however, this will require further experimentation to establish correlation. It should be noted that the lengths of the thorium strips were such that 4 cm of the sample was not covered by uranium and exposed to the full neutron beam, therefore not undergoing compounding self-shielding effects from the uranium metal. Shielding effects from other isotopes with nearby resonances are important to consider in safeguards applications.

6.3 Field Testing

Three series of field testing campaigns were conducted at MIT Bates Research and Engineering Center in Middleton, MA in November and December of 2023 and February of 2024. Operations were supported by the radiation protection staff from MIT's Environmental Health and Safety (EHS) office, as well as technicians from Bates. The purpose of the field testing campaigns was to assess the portability of the technique and to empirically validate the background reduction effects compared to the Vault Lab on MIT main campus.

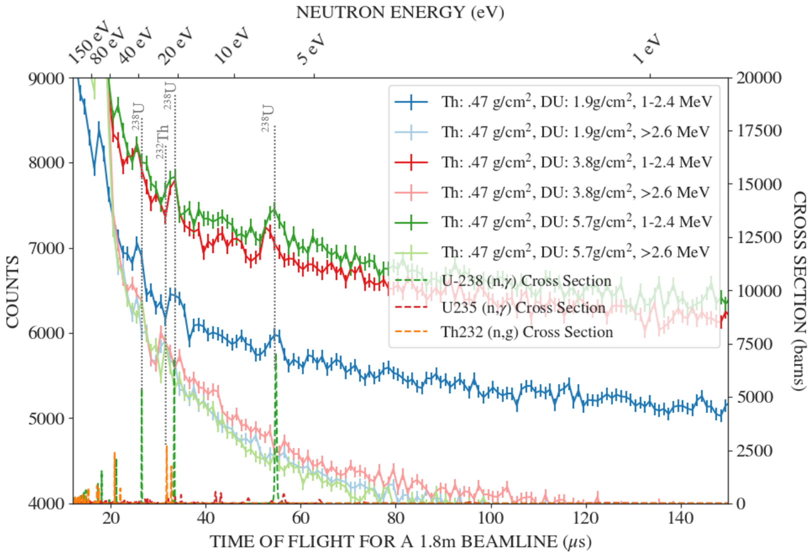

Figure 6-7: Spectra from three experimental runs with 0.47 g/cm^2 of thorium oxide and various areal densities of depleted uranium oxide. Two TOF spectra are displayed for each run, the bold colors have an energy cut to select γ-rays from 1-2.4 MeV and the light colors are energies greater than 2.6 MeV. Resonances of interest are highlighted. Acquired with a 3" BGO detector, 20 minutes in the Vault Lab.

6.3.1 Portable Configuration

The portable experimental setup was as closely matched as possible to that in the Vault Lab, using the same D-T generator, control head, and cables, as well as the same detectors and digitization setup. Packing and moving these items from MIT main campus to the field site 30 miles away provided an excellent practical exercise in portability testing. Aside from the lead multiplier ring (with a weight of 60 pounds) the entire neutron generation and γ-ray acquisition setup fits into two cases and can be moved by a single person. A photograph of the D-T generator equipment and all cables required for the setup inside a single, wheeled case is available in Appendix B, Fig. B-8. The D-T tube itself was transported in a separate hard case by EHS personnel, due to radiation transportation considerations for the sealed tritium source (2 Curies) inside the tube.

The experimental configuration took approximately 30 minutes to set up, with the majority of the time spent on cable management. The radiation protection team took neutron and γ-ray dose measurements with the D-T in its lowest power configuration and another set of measurements at normal operating parameters, resulting in a total set-up time of one hour from arrival to the first NRCA measurements. The photograph in Fig. 6-8 shows one of two field experiment configurations. In this format, the detector and target are offset from the generator on a small camp table

Figure 6-8: Photo of field experimental setup with the D-T generator, moderator-multiplier assemble and detector HV power supply on the left and detector and target on the right. The D-T power supply, control head and digitizer are located 30 feet away at the operator's station. The facility in the background is a portion of the Bates 500 MeV electron linear accelerator beamline.

to replicate a low-mass, high-portability setup. Experiments were also conducted with the D-T tube oriented 90^o to the left and the detector and target at the other end of the large aluminum work stand. This setup mimicked the neutron-induced γ-ray background from a neutron resonance analysis setup in the back of a box-truck.

6.3.2 Dose Field Calculation and Measurement

During feasibility studies to obtain EHS approval for the field experiments, several photon and neutron dose modeling studies were conducted. The particle flux studies were performed in MCNP 6.2 (as opposed to MCNP 6.3, which was used for TOF modeling) and visualized and analyzed in MeshTal Viewer and GXS View. Dosimetry modeling was performed using the FMESH capability in MCNPX using ICRP 116 flux-to-dose conversion factors. These data were visualized and animated in TecPlot 360 EX.

The initial source term for the D-T generator and the associated experimental geometry were first tested inside a model of the Vault Lab at MIT. The dose fields from this study were compared to several measurements both inside the Vault concrete walls and at the operator station, validating the model parameters. The source term and experimental geometry were then tested in models of an open field and a box truck to determine the effective dose profiles for these setups. These

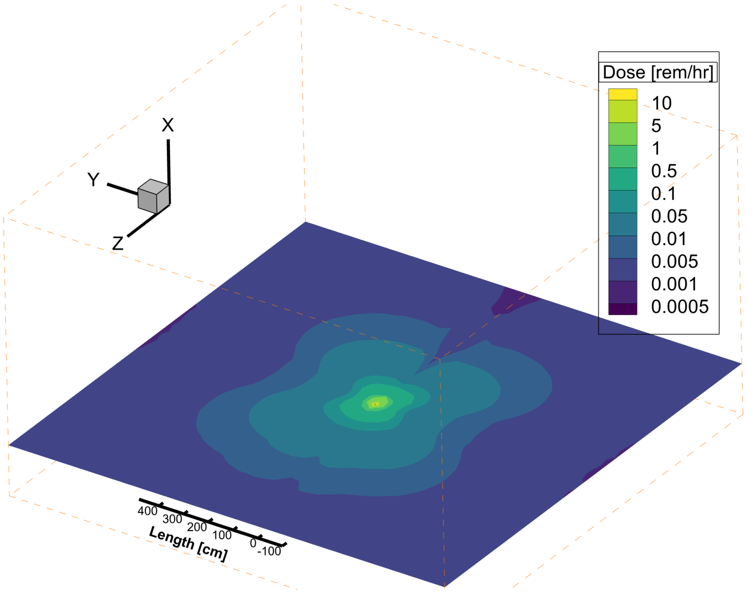

Figure 6-9: The neutron effective dose profile as calculated using the FMESH utility in MCNPX with ICRP 116 flux-to-dose conversion factors. Visualized in TecPlot 360 EX, showing the dose profile at the *x*-plane of the D-T generator centerline (approximately 1 m off the ground). The D-T generator tube is aligned in the *y*-direction and the anisotropic flux profile is due to the moderator and multiplier cuff assembly.

predicted values were within instrument error of the measured photon and neutron dose, although measured dose values in the neutron ‘shadow’ of the aluminum work stand were understandably lower.

Radiation effective dose is useful for the general evaluation of potential health impacts of radiation exposure. Publication 103 of the International Commission on Radiological Protection (ICRP) recommends the use of the H*(10) ambient dose equivalent for area monitoring and assessing radiation protection in a workplace [185]. This value is calculated using the corresponding expanded and aligned radiation field incident on an ICRP sphere at a depth of 10 mm on the radius vector opposing the direction of the aligned field. It provides a conservative estimate of dose to a worker and is useful in understanding the impacts of protective measures. The modeled H*(10) for an operator at the Vault Lab control station is 1.3 mrem/hr and 1.1 mrem/hr for the 30 ft (9 m) operator station in the field setting. The field value does not include shielding other than air and can easily be decreased by adding distance or personnel shielding. In the current configuration, the dose to an operator and the general public is well within practical limits.

6.3.3 Results

The field testing campaign showed a marked improvement in the isotopic quantification ability of the technique through the reduction of background noise. Comparative energy spectra between the Vault Lab and the Field Lab are shown in Fig. 6-10. The γ-ray events corresponding to each spectrum have been separated on the basis of the detection time relative to the D-T start signal, so that the solid lines represent photons detected after the pulse. There are several notable features between the two datasets. The γ-ray peaks corresponding to iron isotopes are diminished in magnitude and prominence due to the lack of the cyclotron and other experimental materials in the Vault Lab. Interestingly, the magnitude of the 2.2 MeV hydrogen capture γ-ray peak and its single escape peak are decreased in the field experiments, but their relative prominence is enhanced. The peaks are attributable to the hydrogen present in the field soil and the relative decrease in the Compton continuum from higher energy γ-rays allows them to stand out more distinctly. The reduction in background noise and the simplification of the spectra in the field conditions underscore the technique's improved capability for detecting and analyzing specific isotopic signatures in field-deployed environments.

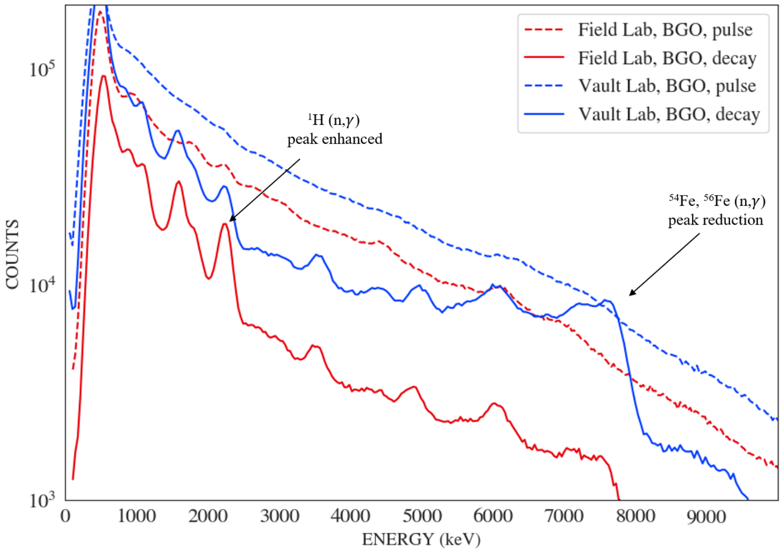

Figure 6-10: Energy spectra from an open beam run in the Vault Lab and one in the Field Lab, time-separated into pulse (0-12 μs) and decay (13-200 μs) periods. Acquired with the 3" BGO detector, 20 minutes.

The NRCA results follow as expected: there is an approximately 35% drop in constant background counts from the Vault Lab to the Field Lab setting. The C_1 background component displays a shorter amplitude and a shorter decay constant in the field tests, possibly due to the decreased number of neutrons experiencing multiple scatters back into the detector and target area. This effect is visible in Fig. 6-11 and Fig. 6-13, presented in the following section. Most notably, the prominence of the higher energy, lower magnitude resonance peaks is significantly enhanced relative to the background continuum, contributing up to a 4x SNR improvement.

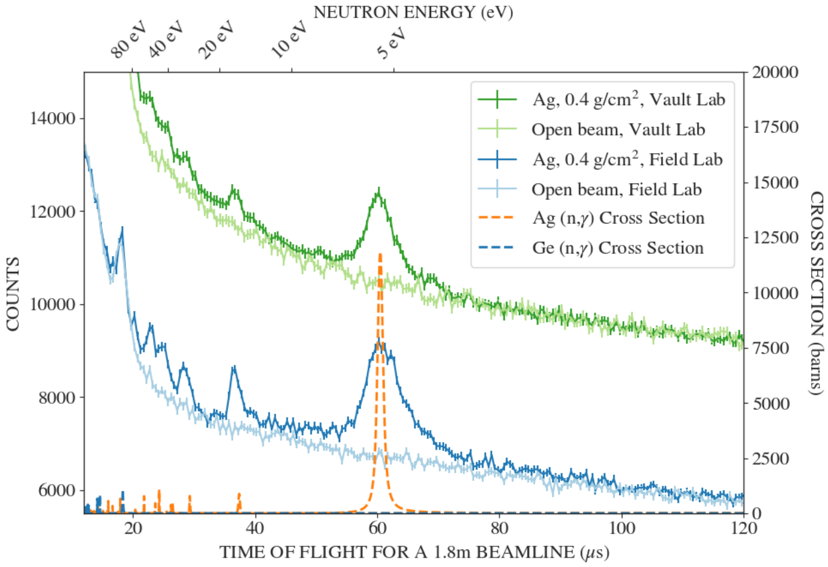

Figure 6-11: TOF spectra from an open beam and 0.4 g/cm^2 silver run in the Vault Lab and in the Field Lab. Acquired with the 3" BGO detector, 20 minutes.

6.4 PNNL Experiments

6.4.1 Experimental Methods and Environment

A series of NRCA experiments were performed at the Pacific Northwest National Laboratory (PNNL) Low Scatter Facility (LSF) in Richland, WA. This work was supported by a joint collaboration between MIT and PNNL under the auspices of a Department of Energy National Nuclear Security Administration (NNSA) grant. The LSF facility is a large, concrete-walled room with an aluminum and steel platform on which the D-T generator, target, and detectors are placed. Measurements were acquired over 30 minute periods unless otherwise noted. The D-T was operated at a duty cycle of 3. 5% and 5 kHz frequency, resulting in a nominal pulse width of 7.0 μs. The beam current was 35 μA and the acceleration voltage was set at 130 kV, which were the parameters resulting from a neutron flux optimization study at the National Lab. The data were acquired on the same CAEN DT-5725 digitizer used in the other portions of this research.

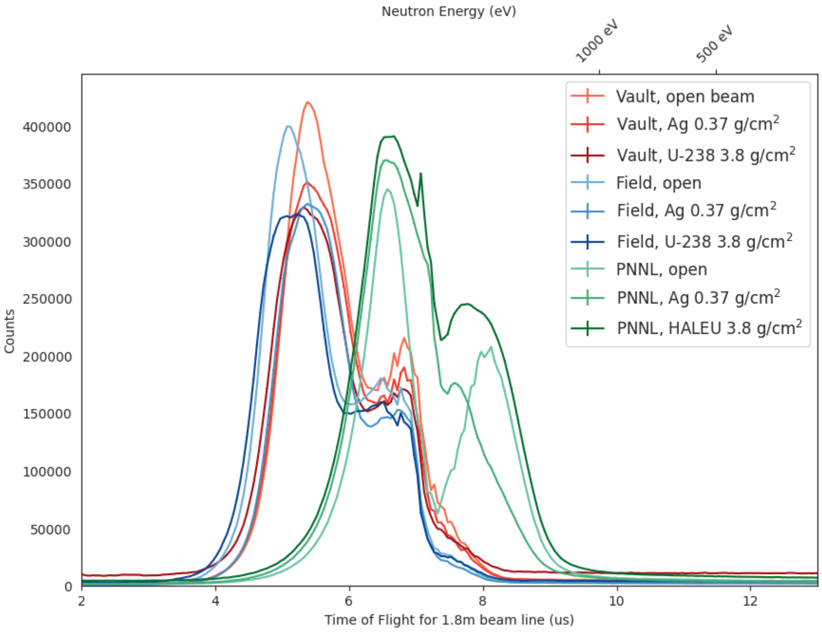

Figure 6-12: Pulse shape from a open beam, silver, and uranium target for PNNL and MIT neutron generators. The MIT neutron generator pulse is shown in both Vault and Field Lab conditions.

Prior to examining the NRCA data acquired during this campaign, it is instructive to compare the γ-ray signals arising from different D-T parameters and operating environments. Fig. 6-12 shows several γ-ray histograms of the D-T pulse shapes in the MIT Vault, Field Lab (using the same D-T generator) and the PNNL neutron generator in the LSF. The γ-rays associated with fast neutron interactions are a suitable proxy for the shape and timing of neutron generation. When using the PNNL D-T generator, the centroid of the entire pulse shape is shifted later in time to 7.01 ± 0.04 μs (standard deviation is 1.08 ± 0.04 μs). Although this method operating the generator results in a slightly lower system resolution than the parameters used at MIT, it preserves the generator electronics and results in the longevity of the tube. It is recommended that future neutron resonance analysis research be conducted using these operating settings to preserve the D-T generator. Of note, the appearance of a bimodal pulse in the PNNL experiments is an artifact of the detector experiencing high deadtimes and is not indicative of the D-T generator's pulse shape.

Fig. 6-13 shows three TOF histograms of an open beam run from MIT's Vault and Field Labs and the PNNL LSF. The constant background component has been removed to highlight the shape of the remaining histograms. As also noted in [75], the neutron background of the LSF differs slightly from that of the Vault Lab. In an NRCA measurement, this manifests as a longer decay component to the C_1

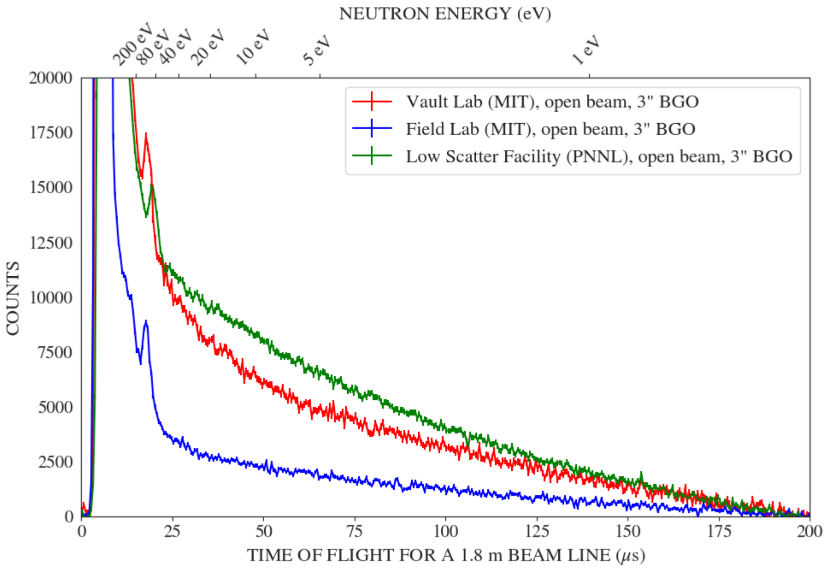

Figure 6-13: TOF open beam histograms for the PNNL, MIT Vault and MIT Field experimental setups. The constant background has been removed from each histogram to allow comparison of decay constants. Each run was acquired for 20 min using the 3" BGO detector.

background. This observation is in part attributable to the larger volume of the LSF. The larger mass of concrete (and therefore hydrogen) in the LSF increases the number of hydrogren captures. Furthermore, the greater distance to the walls that a partially moderated neutron must travel before being captured could have the effect of extending the decay constant of the background relative to the D-T pulse. The minimization of the C_1 component in the Field Lab tests is noticeable.

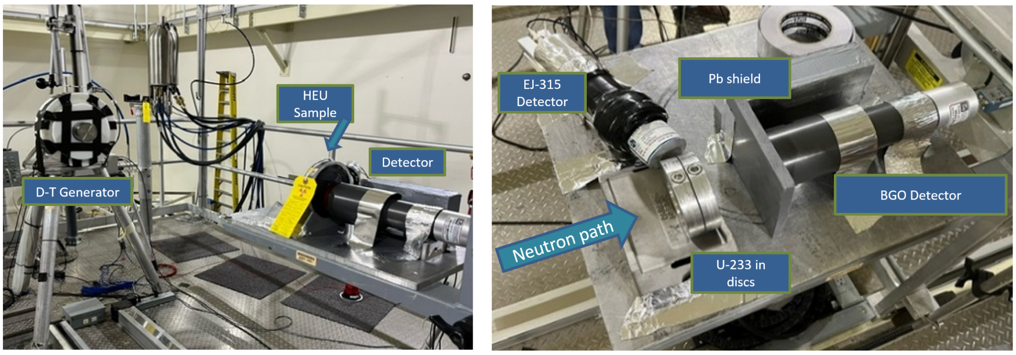

Figure 6-14: Photograph of the experimental set up in the PNNL LSF. (Left) a view of the D-T generator and detector with the HEU sample in place. (Right) A detail of a two detector setup and the ^{233}U samples.

The experimental setup for the LSF runs is shown in Fig. 6-14. The D-T generator is visible with a moderator and small lead multiplier cuff. The highly enriched uranium (HEU) target in the left hand photograph is approximately 94 g of 93% ^{235}U and 7% ^{238}U. Just under 1% of the uranium in the target is ^{234}U, a byproduct of the isotopic separation process required to enrich natural uranium. A resonance of this isotope is visible in Fig. 6-15. The EJ-315 and BGO detectors are visible in the right hand photo, along with a 3.5 g sample of ^{233}UO$_2$ (2.5 g of ^{233}U). For this target, a 16mm lead shield is used between the sample and the detector to prevent high rates of deadtime, discussed in detail in Sect. 6.4.2.

6.4.2 Results

The PNNL experiments offered an opportunity to assess the NRCA technique on unique isotopes, including fissile materials. At the LSF, various materials were combined to create samples that approximated the isotopic composition of fuel proposed for advanced reactors. Notably, the high-assay, low-enrichment uranium (HALEU) samples provided a valuable assessment due to their thin form factor and the ability to stack them in different areal densities. The plots presented below are selected highlights of this research campaign.

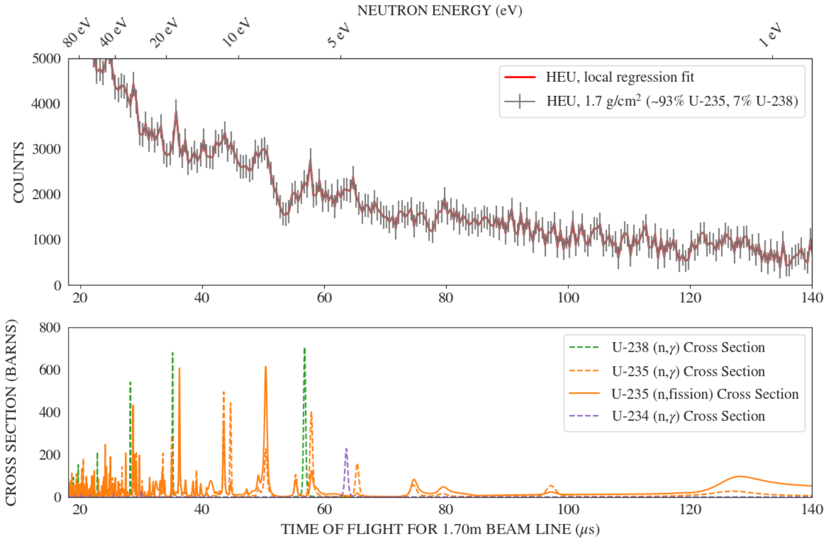

Figure 6-15: Background-subtracted TOF histogram for a 1.7 g/cm^2 sample of powdered highly enriched uranium. A LOESS (local regression) fit to the data is included. The cross sections plotted for reference have been scaled for their abundance in this sample. Acquired with the 3" BGO detector at the PNNL LSF, 30 minutes.

Fig. 6-15 shows the TOF histogram for the 1.7 g/cm^2 sample of HEU discussed earlier. The plot indicates a good reconstruction of the epithermal resonance profile of the isotopes present. A comparison of two enrichments of uranium is presented in Fig. 6-16, which shows HEU and HALEU in the closest-matching areal densities.

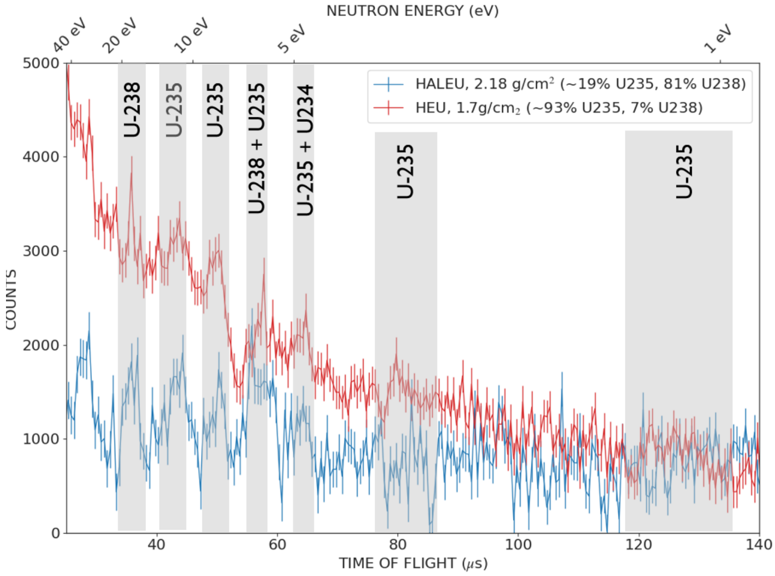

Figure 6-16: Background-subtracted TOF histogram for a 1.7 g/cm^2 sample of HEU and a 2.2 g/cm^2 sample of HALEU. Characteristic resonance peaks for each material are highlighted. Each sample acquired with the 3" BGO detector at the PNNL LSF, 30 minutes.

The plot is also presented in Appendix B, Fig. B-11 with cross section magnitudes included. The count values of selected resonances of ^{238}U and ^{235}U show good agreement with changing enrichment values. Future research should include additional values of enrichment to verify the sensitivity of the technique for this application.

The HALEU samples available at the LSF were thin sheets that were suitable for stacking to create compositions of different areal densities. Each sample was enriched to a value of 19.8% ^{235}U. The uranium was present in a compound with molybdenum, which has five stable isotopes including ^{95}Mo, which has an epithermal resonance indicated in Fig. 6-17. This figure shows the background-subtracted TOF histograms for four areal densities of HALEU acquired with the 3" BGO detector. A photo of the configuration used for HALEU experiments is shown in Appendix B, Fig. B-10. The areal density correlation values for count values of four selected resonances of ^{238}U and ^{235}U are presented in Fig. 6-18. This figure depicts both raw correlation coefficients and those obtained after performing self-shielding corrections using Eq. 5.1. The resonance count values show a good correlation with changing areal density, even prior to self-shielding corrections.

Using the raw resonance count data from the varying thicknesses of HALEU, Fig. 6-19 shows a linear regression for each resonance. The shaded areas around each line represent a 95% confidence interval. The uncertainty is higher for ^{238}U

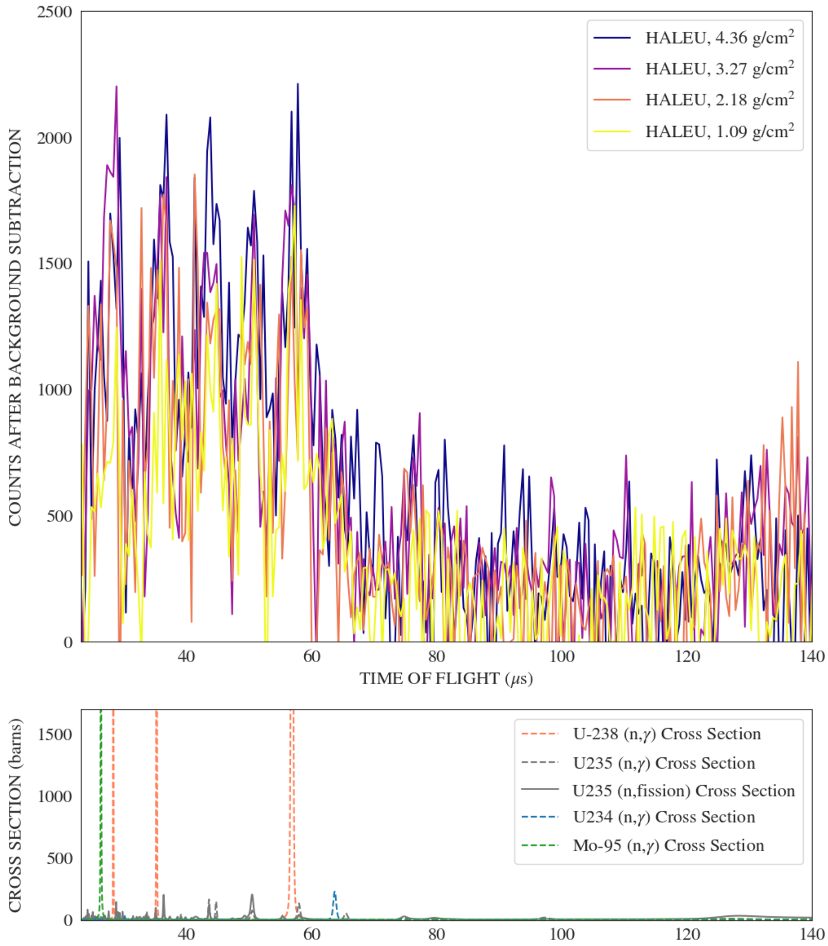

Figure 6-17: Background-subtracted resonances for varying areal densities of HALEU metal. Acquired with the 3" BGO detector at the PNNL LSF, 30 minutes each thickness of HALEU.

across the range of effective thicknesses due to the saturation of these resonances. The linear regression plots for the self-shielding corrected count values are presented in Appendix B, B-12.

A plot illustrating the use of the single ratio calibration method for areal density determination is presented in Fig. 6-20. This method proceeds in the same fashion as described in Sect. 5.4, except rather than using the ratio of two resonances from the same isotope to calibrate the theoretical self-shielding curve, one resonance from each of the primary HALEU isotopes is used in conjunction with their known weight ratios. With this method, a reverse calculation of enrichment may be possible using a set of samples of the same substance in varying areal densities or (provided a well-collimated neutron beam) a single sample oriented at different angles such that the effective areal density changes from run to run. This bears further investigation

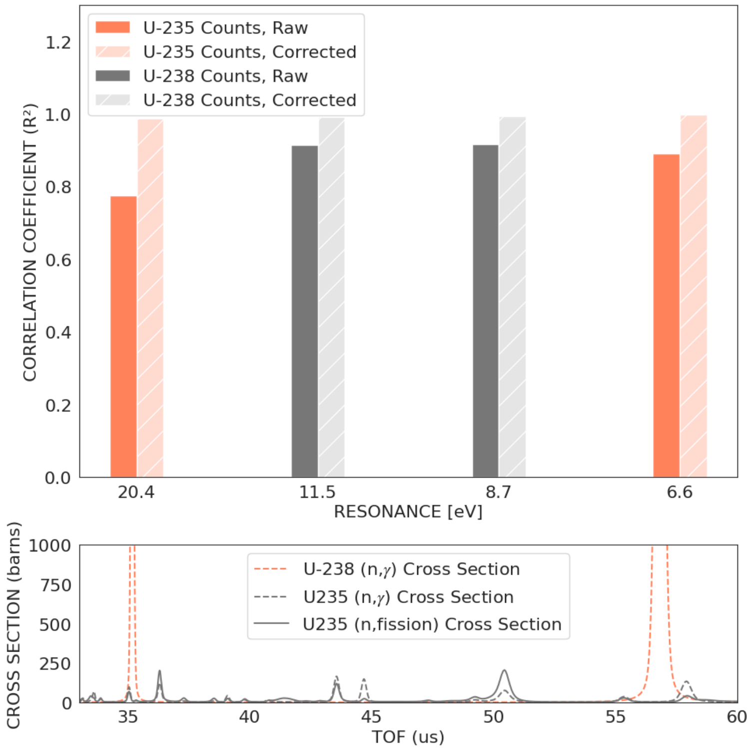

Figure 6-18: Correlation measurements for four selected resonances from ^{238}U and ^{235}U) before and after counts are corrected for self-shielding

given samples of varying enrichments. The errors shown in Fig. 6-20 are the result of counting statistics and the covariances of the background fit parameters.

The unique samples at the LSF provide an opportunity to demonstrate how NRCA behaves with thorium fuel cycle materials. The sample of ^{233}U discussed earlier was assessed individually and stacked with HEU and 3.5 g/cm^2 of metallic ^{232}Th in compositions meant to replicate fuel materials. The ^{233}U sample was produced in the mid-20th century in a thorium breeder reactor and, as discussed in Chapter 1, contaminated with ^{233}U. Although the ^{233}U content has been assessed at 1.8 ppm, at the time of this research, it contributed 1.52x10^6 Bq/g to the activity of the sample. This was the most active sample measured in this research and initially yielded detector deadtimes of over 80%. The deadtimes were mitigated by placing a 16 mm lead shield between the sample and the detector, as indicated in Fig. 6-14. When this modification resulted again in unacceptably high deadtimes, the acquisition threshold was set to a lower limit of detection (LLD) of 2.7 MeV, just above the ^{208}Tl γ-ray.

The raw TOF histograms of these uranium and thorium compositions are presented in Appendix B, Fig. B-13, and the background subtracted histograms in Fig. B-14. Fig. 6-21 shows the locally-weighted scatterplot smoothing (LOWESS) fits to

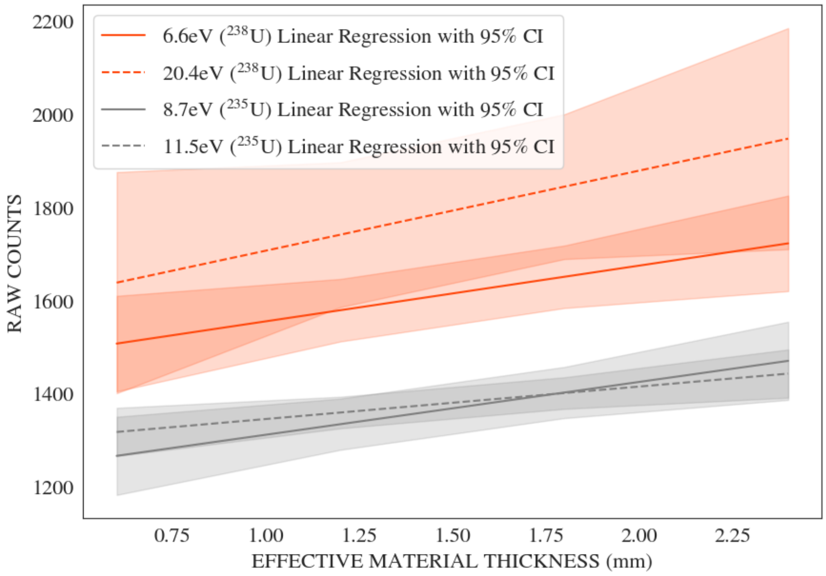

Figure 6-19: Linear regression of raw count values for selected resonances of ^{238}U and ^{235}U, based on data from NRCA measurements. Shaded areas represent 95% confidence intervals.

each histogram. Due to the noise in the histograms from the high γ-ray background, a LOWESS fit is used to determine trends. This method was selected due to the fit's flexibility without a predetermined model, it's local focus to highlight rapid changes such as a resonance peak, and its robustness in handling outlying data points. The fits show heavy influence from noise, however the thorium/^{233}U composition shows promising indications of thorium resonances. Further investigation is required to determine if the late-time (low energy) ^{235}U and ^{233}U resonances can be resolved in this setup, which would provide an important nondestructive method of distingushing between the two isotopes in mixed batches.

A potential research extension of NRCA is to understand the contribution of fissions to the time-based γ-ray signal. Resonances with a fission exit channel component may exhibit higher counts relative to radiative capture-dominant resonances in a TOF histogram. The detection configuration used primarily in this research placed the target either proximal or a short distance from the front face of the detector. In this configuration, it is possible that post-fission β-rays are detected via their bremsstrahlung radiation in the target material, detector housing or scintillator material. Fig. B-5 in Appendix B compares the BGO detector spectrum from the natural background and from a pure beta-emitter, showing a high sensitivity to bremsstrahlung radiation below 1 MeV. The fission-bearing resonances appear to experience a stronger count magnitude increase relative to non-fission resonances when the TOF spectrum is filtered to include photons of 1 MeV or lower (see

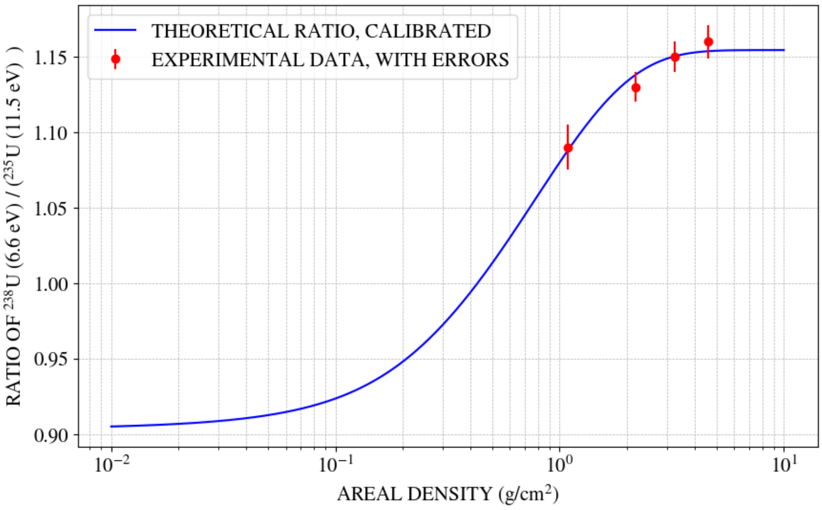

Figure 6-20: Theoretical ratio of counts from the 6.6 eV and 11 eV resonances in ^{238}U and ^{235}U, respectively, as a function of sample areal density. The theoretical self shielding factor for each resonances is weighted by the enrichment value of each contributing isotope. Experimental data points used for calibration are shown in red.

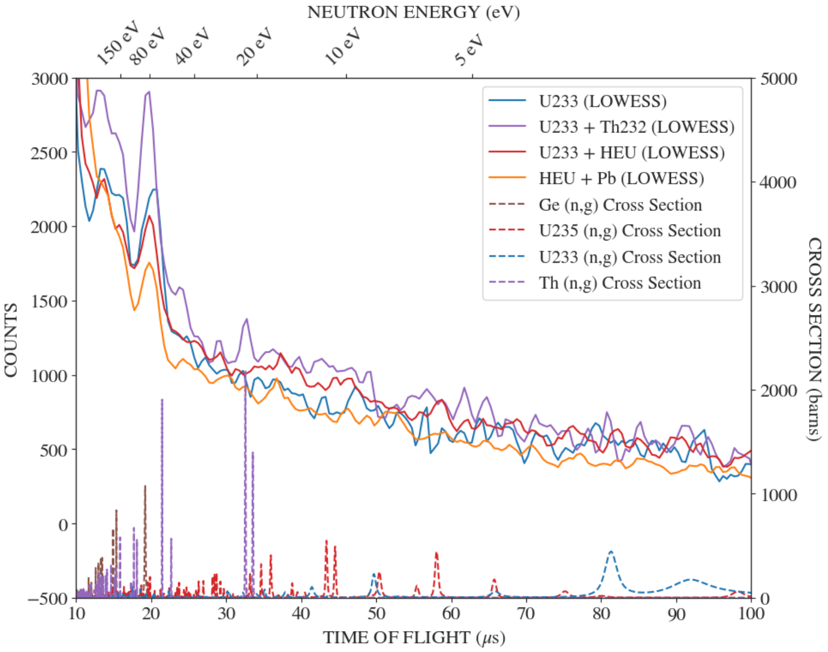

Figure 6-21: LOWESS fits to the background subtracted TOF histograms from thorium, HEU, and ^{233}U compositions. Acquired for 30 minutes each at the LSF using the 3" BGO.

Appendix B, Fig. B-9.) Using the calibrated quantity analysis methods outlined in Sect. 5.4 any β-rays detected will contribute to the overall quantification of the sample. This effect should be further investigated if researchers have access to fissile samples.

The research undertaken at PNNL was beneficial in understanding the limits and extensions of the NRCA technique. Several research extensions are presented throughout this chapter and the next that will further characterize or improve the sensitivity of portable NRCA if another opportunity arises to evaluate fissile and fissionable materials. NRCA was demonstrated to have good sensitivity to the characteristic epithermal resonance signatures of several fuel cycle isotopes, as well as an ability to analyze the quantity of HALEU samples using the calibrated ratio assessment method. Futher research is needed to determine the technique's discrimination ability between HEU and ^{233}U in mixed batches.

6.4.3 Neutron Detection

The EJ-315 detector is an organic scintillator and is capable of discriminating between fast neutrons and γ-rays. By applying time gates to the detected waveforms as they arrive at the digitizer, pulse shape discrimination (PSD) can be performed as a post-processing step. This ability provided a ready opportunity to determine if fast neutrons arising from resonance fissions in ^{233}U and ^{235}U could be detected at epithermal neutron flight times commensurate with the resonance energy. This approach was concurrently explored while recording radiative capture γ-rays with the EJ-315 detector, although it did not yield positive outcomes.

6.5 Applications Discussion

6.5.1 Practical Considerations for Deployment

To support the research goal of evaluating a portable NRCA system, the portability aspect was rigorously assessed. A field-deployable system must address radiation field reduction and monitoring to ensure safety for operators, nuclear fuel facility personnel, and the general public. Applications involving ionizing radiation should adhere to the principle of ALARA (As Low As Reasonably Achievable) to minimize radiation exposure. Next-generation ALARA planning tools are available to optimize work activities and process flows, thereby reducing overall radiation doses to personnel [186]. The results of this research, along with several other fieldability tests for neutron generator-based systems, indicate the potential for safe and effective operation in various settings [187]–[189]. Key factors such as mass, ease of setup, operational safety, and compliance with travel regulations must be considered to enhance the practicality of deploying these systems in the field.

Compliance with U.S. shipping regulations mandates that SF_6 gas be removed or depressurized for transport, except for certain models such as those from Thermo-Fisher, which have a Department of Transportation exemption [141], [142]. Sealed tube generators should be chosen to meet host nation requirements, ensuring regulatory compliance during international operations. For true field use applications without access to mains or generator-supplied power, many electric neutron generator models can be adapted to accept high-capacity batteries. Operators should confirm that low-power generators can meet the necessary specifications for duty factor, pulse rate, and neutron flux to ensure effective operation. As with any neutron resonance analysis system, thorough verification of these parameters is essential for reliable and efficient field deployment.

Although it was not tested as a sample during this research, this portable NRCA system will also be highly sensitive to gold (^{197}Au. This system could be a tool of possible interest to the archaeological community for a rapid, in-field, nondestructive assessment of uncovered objects. The system in its current epithermal configuration is sensitive to gold, silver, tin, platinum, and mercury, metals commonly used in ancient artifacts. A modification to the pulsing mechanism of a D-T generator to allow arbitrarily long periods between pulses would permit the beam line to be extended to a length in which the first copper and zinc resonances become visible. Although a longer beamline would diminish the epithermal neutron flux at the target, longer counting times can provide better statistics.

6.5.2 Practical Considerations for Safeguards Applications

Safeguards-like accountancy measures might be applied to intermediate fuel material processing, either prior to first use in a reactor or in spent fuel reprocessing [190]. During these steps, fuel isotopes are generated in multiple chemical forms. Uranyl nitrate ($UO_2(NO_3)_2$) is an important fuel isotope intermediary that is highly hygroscopic. It readily absorbs moisture from the ambient air, which introduces neutron moderating and capturing hydrogen to the sample, possibly altering the results of the neutron resonance analysis. A thorough understanding of the characteristics of materials under test is required before drawing conclusions about a substance. Likewise, while sample activation is limited by the low flux of the neutron generator, the NRCA and thermal background signals indicate that neutron transmutation is occuring. A sample exposed to a neutron-based interrogation should be noted as such and avoided for future analysis, especially by a method with high sensitivities to isotopic presence and quantity. Furthermore, additions to the IAEA inspector's toolkit, especially a system of this size, will require modifications to complementary access under the Additional Protocol.

6.5.3 Issues and Troubleshooting

A future fuel isotope analysis system based on a neutron generator should have the benefit of design consultation with the company producing the neutron generator. This section outlines the primary neutron generator issues encountered in this research to provide a starting point for future neutron generator design and purchasing specifications.

The Thermo-Fisher P383 used in this research ran for hundreds of cumulative hours on NRTA/NRCA studies with a 3.1% duty fraction. This parameter was in excess of the 5% specified by the manufacturer and created an overly taxing operations regime for its system components. Our neutron generator also operated on a monthly basis as a secondary neutron source for an unrelated molten salt-tritium breeding experiment, running at 100% duty fraction for 12 hours each day over the course of three days. It was packed and moved between field and lab conditions over twenty times and operated in ambient temperatures ranging from -15 to 27 C. The generator assembly suffered multiple short (10 cm) drops, hundreds of cable detach/reattach cycles, and a 25 kg lead multiplier cuff resting on the housing over the D-T getter plane and heat sink. It is a remarkable piece of engineering from a physics, electrical, and packaging perspective. Without the robustness of this generator, this research would not have been possible. Likewise, the professionalism and knowledge of Thermo-Fisher engineers while troubleshooting generator issues was instrumental to the success of the research.

The digital design of the P383 incorporates control algorithms meant to provide stable but flexible closed-loop performance of the accelerator. Due to the requirement of this research to optimize TOF energy resolution, the neutron generator was run at a duty cycle and pulser frequency in excess of the specifications quoted by the manufacturer. Understandbly, this unique operations regime taxed the D-T components to such an extent that after a year of use, the PID loop began to produce erratic getter current outputs. A screen capture of the D-T control interface during this instablility is provided in Appendix B, Fig. B-2. In three instances, these getter current incursions were severe enough that the machine could not be ramped above its lowest flux settings. This issue was solved by obtaining the LEVEL III passcode from Thermo Fisher engineers (this must be done over the phone each time) and manually adjusting the tube voltage, placing the control loop into a different solution regime.

Future design requests should include a level of equipment hardening equal to or greater than that of the P383. A generator with as narrow a pulse width as possible is ideal, even if it requires sacrificing some of the neutron flux. Furthermore, increasing the maximum time between pulses (in effect, decreasing the duty factor) would allow extending the beamline distance to access neutron resonance energies above epithermal.

Chapter 7

Conclusion

Renewed interest in nuclear power and the state of nuclear technologies suggests that advanced nuclear reactors will be commercially available within the next decade. Nuclear engineers and scientists have a professional obligation to ensure that nuclear technology can be monitored or otherwise safeguarded to prevent inappropriate or nefarious use. Multiple US national lab studies have identified technological gaps in the capabilities of current uranium and plutonium safeguards methods in accounting materials in the thorium fuel cycle. Toward this goal, portable neutron resonance capture analysis is presented as a method of on-site isotopic assessment.

The main objective of this research was to assess the feasibility of performing NRCA with a portable neutron source, which is a novel setup and application. The primary challenge in this configuration was to reduce the background noise to a level that allowed sufficient resolution of isotopic content for practical use. The system demonstrated strong sensitivity to thorium fuel cycle products and other advanced uranium fuel cycle products, as well as good sensitivity to changes in isotopic quantities in appropriately sized samples. Although this research focused on evaluating the feasibility of NRCA within the context of the thorium fuel cycle, the technique has a wide range of potential applications. The use of NRCA as an isotopic assessment method in a portable setup marks a significant advancement in on-site, active assessment for nuclear materials safeguards. This work represents another step in the development of a comprehensive suite of portable neutron assessment techniques that can be performed concomitantly and with complementary information outputs. The particular advantage of NRCA is its sensitivity to very thin or small samples. It is also a 'one-sided' technique, and can obtain some isotopic information about an object that cannot otherwise be transmission imaged.

There are multiple extensions to this research that have been presented throughout the preceeding chapters. Each spectrum gathered in this research contained a wealth of information, with more analysis methods available to understand what other conclusions may be drawn. The passive γ-ray spectrum of a material, when used in conjunction with time-dependent resonance capture data, can serve to enhance and constrain findings from NRCA. Peak-shape analysis codes offer a powerful tool to determine the isotopic content and quantity of a sample without the need for calibration. However, these codes are highly sensitive to experimental arrangement and the multiplicity of the radiative capture decay, requiring a high degree of sample and detector characterization if used.

A detection methodology sensitive to low-energy γ rays will allow exploration of this region of the spectrum to determine if there is additional NRCA signal. A phoswitch is a detector which uses a thin material to preferentially measure low-energy γ -rays and beta particles when the background is composed of higher-energy photons [191], [192]. A phoswitch shielded from the room background may be sensitive to β-rays released during fissions and be able to correlate the time dependence of this signature to fission resonances. Cerium-doped Yttrium Orthosilicate (YSO) is one possible detector alternative to BGO and EJ-315. The constituent isotopes do not have epithermal resonances and it has a high light yield and fast decay time. Future research should investigate the suitability of this detector type for NRCA uses. A multi-detector matrix of any suitable scintillator material in a grid or other layout will allow position-sensitive capture γ-analysis.

^{233}Pa is of particular importance to determine the sensitivity and specificity of assessment techniques. This protactinium isotope will decay to fissile ^{233}U with a half-life of 27 days; depending on the operating parameters and separation history of a thorium-breeder reactor, concentrations of ^{233}Pa can be relatively pure (e.g.: without heavy contamination from ^{232}U, the effects of which are discussed in 1.2.1). Future material accountancy procedures for the thorium fuel cycle should include quantification of ^{233}Pa. Neutron resonance analysis methods are hypothesized to be sensitive to this isotope, which has a 5200 b resonance at 1.6 eV, and should be evaluated when a quantity of the isotope is made available.

This work has successfully designed and evaluated a first-of-a-kind portable Neutron Resonance Capture Analysis System. A detector study and D-T generator parameter optimization were conducted to understand their impacts on the NRCA signal. To address significant background noise, extensive environmental studies and MCNP models were developed. These enabled the design of a customized background fitting methodology to support more accurate isotopic quantification. The system was rigorously tested across a variety of sample combinations, sizes, and shielding configurations. Analysis methods, including the calibrated ratio technique, were examined for their efficacy in determining isotopic quantities using the data generated by this novel system.

The NRCA technique developed here has demonstrated the capability to identify multiple mid- and high-Z materials by reconstructing their neutron resonance profiles in measurements as brief as 20 minutes. While the technique successfully differentiated between nuclear fuel cycle isotopes in composite samples, it encountered limitations in quantifying the areal densities of the available uranium and thorium samples. The portability of this system was confirmed by extensive field tests. These exercises also validated dosimetry models, ensuring safe operation in a deployed configuration, maintaining operator doses well within occupational limits. These findings suggest that NRCA, particularly when combined with NRTA and other neutron interrogation techniques, holds significant potential for the rapid, nondestructive quantification and characterization of isotopes of interest in support of safeguards material accountancy.

Acknowledgements Portions of this research were made possible under the auspices of the Consortium for Monitoring, Technology, and Verification under Department of Energy National Nuclear Security Administration award number DE-NA0003920. The author would like to extend her gratitude to the PNNL, MIT Bates, and MIT EHS teams for their consummate professionalism and expertise and to the NNSA MTV consortium for the ample opportunities to publicize this work in the scientific and defense communities.

Appendix A

Tables

Table A.1: Percentage of neutron energy flux for selected thorium reactor designs. Adapted from: [20]

Spectrum Type	$E \leq 1$ eV	1 eV $< E \leq 6$ MeV	$E > 6$ MeV
Fission Spectrum	-	97.4	2.6
HWR			
Fuel (7% ThO_2)	41.0	58.0	0.4
Target channel	81.5	18.5	0.02
PWR			
Fuel (70% ThO_2, 30% UO_2)	8.4	90.8	0.8
LMFBR†			
Core fuel (ThO_2, UO_2)	-	99.6	0.4
Radial blanket (ThO_2)	-	99.9	0.01

† Liquid Metal Fast Breeder Reactor

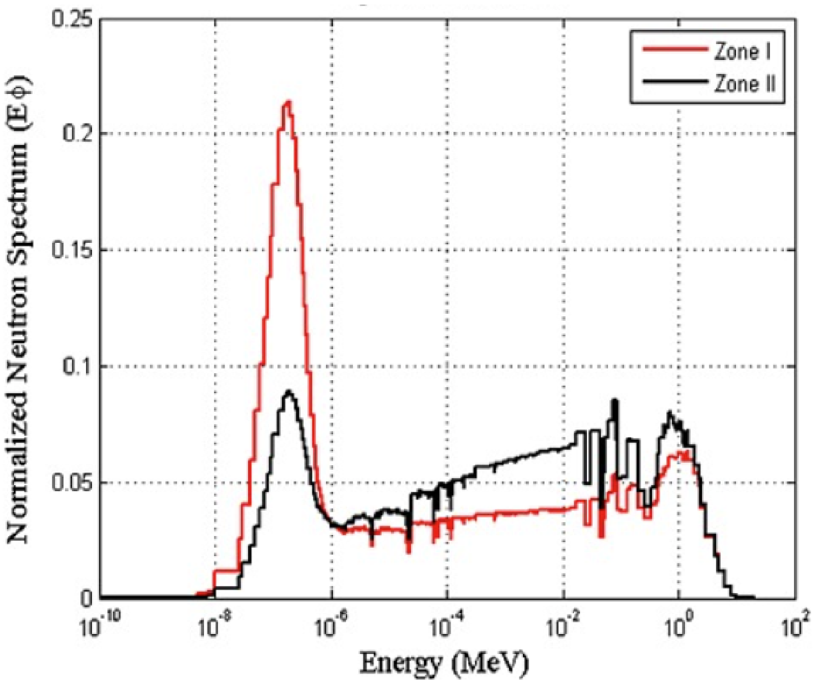

Figure A-1: Normalized flux distribution for a single fluid, dual zone, graphite moderated, thermal TMSR. Simulated with MCNP (plot and methodology available in [193].) Most fissions occur in Zone I and the same fuel circulates through Zone II which has a more favorable neutron flux for breeding. This plot is presented to give a sense of MSR neutron spectra as tabulated data for an MSR is unavailable.

Appendix B

Figures

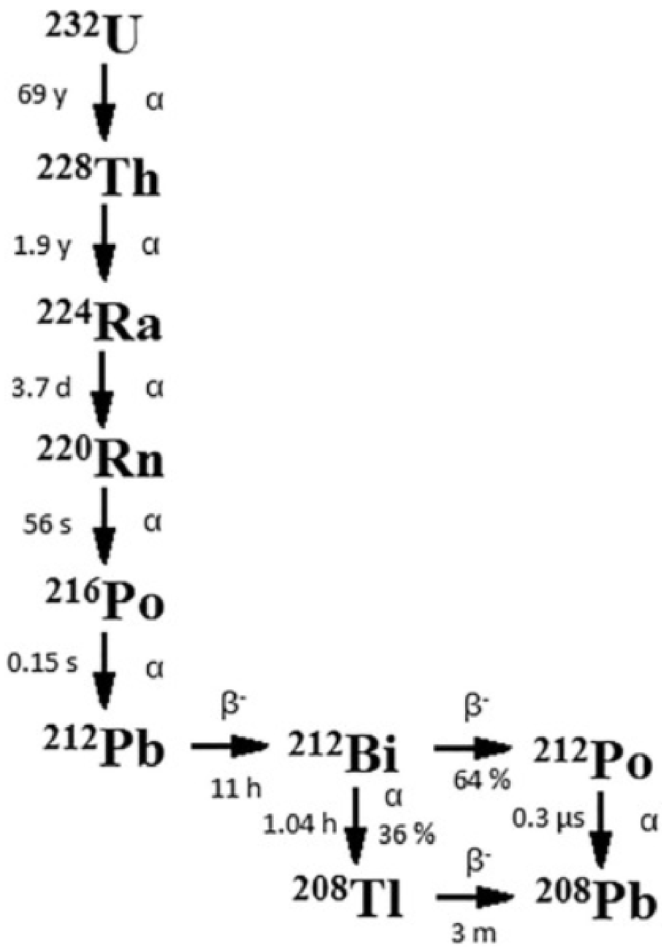

Figure B-1: A decay chain for ^{232}U decay, from [41]

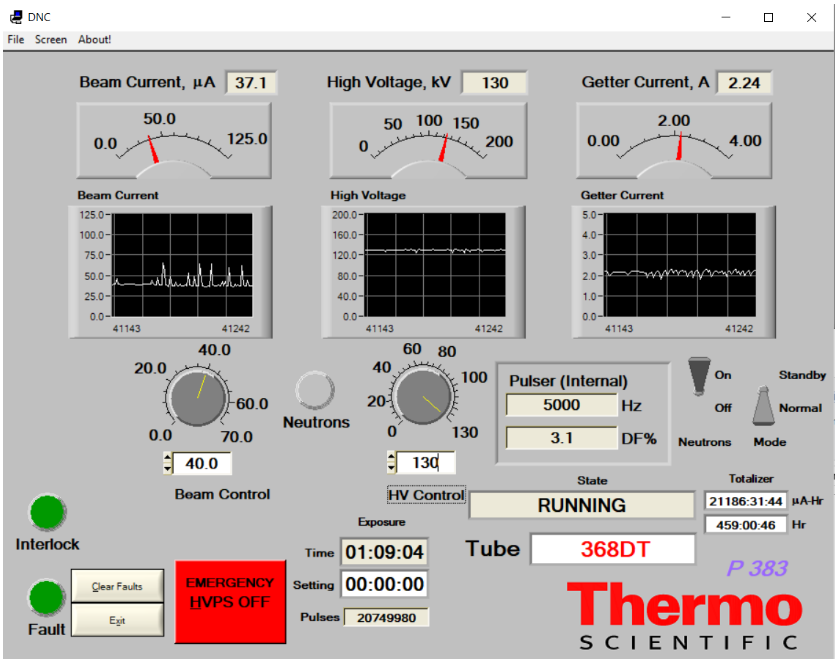

Beam Current, µA 37.1

High Voltage, kV 130

Getter Current, A 2.24

Beam Control 40.0

HV Control 130

Pulser (Internal) 5000 Hz

3.1 DF%

State RUNNING

Totalizer 21186:31:44 µA-Hr

459:00:46 Hr

Exposure

Time 01:09:04

Setting 00:00:00

Pulses 20749980

Tube 368DT

Figure B-2: GUI screen capture of an instability condition generated by application of a high-limit voltage (130 kV) and short duty cycle (3.1%). The machine will continue to operate in this fashion until a transient getter current excursion exceeds limits, triggering a fault condition and rapid shutdown.

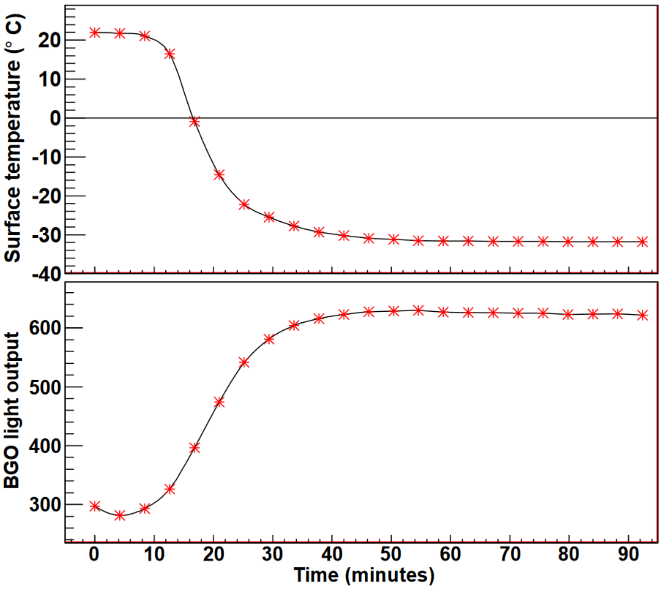

Figure B-3: The variation of the surface temperature of a BGO detector and its light output with time. Detector is 25x25x600mm, used in a dark matter electromagnetic calorimetry system. Reprinted from [175].

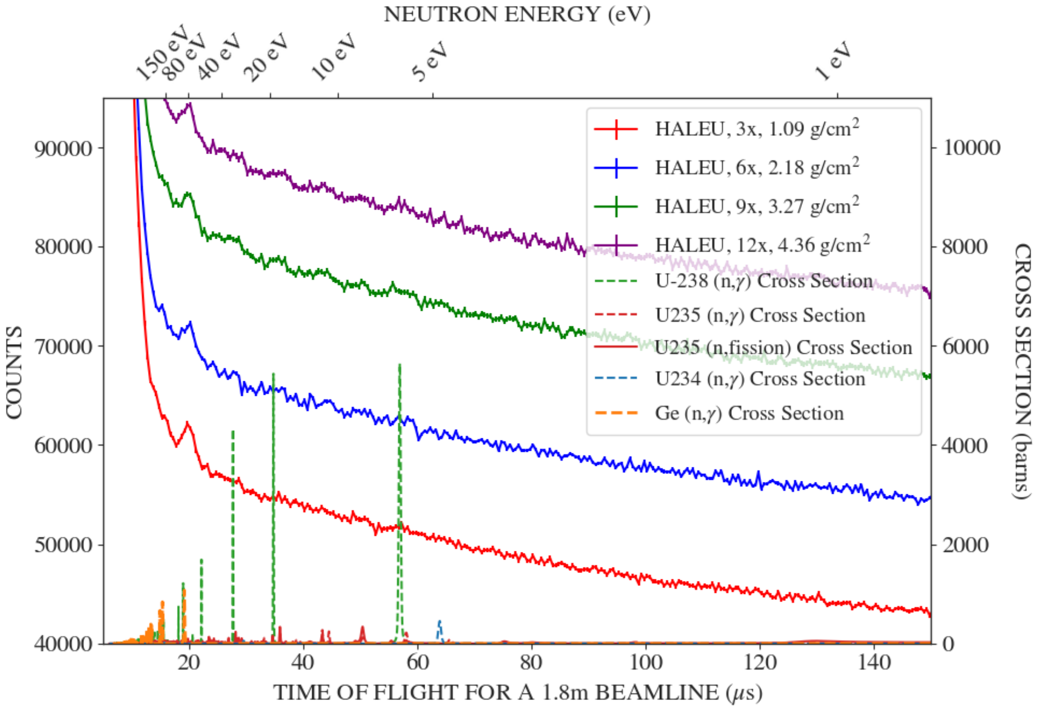

Figure B-4: TOF spectra for HALEU plates in increasing areal densities. No energy cuts or background removal has been performed. Acquired with a 3" BGO detector, 30 minutes each, in the PNNL LSF.

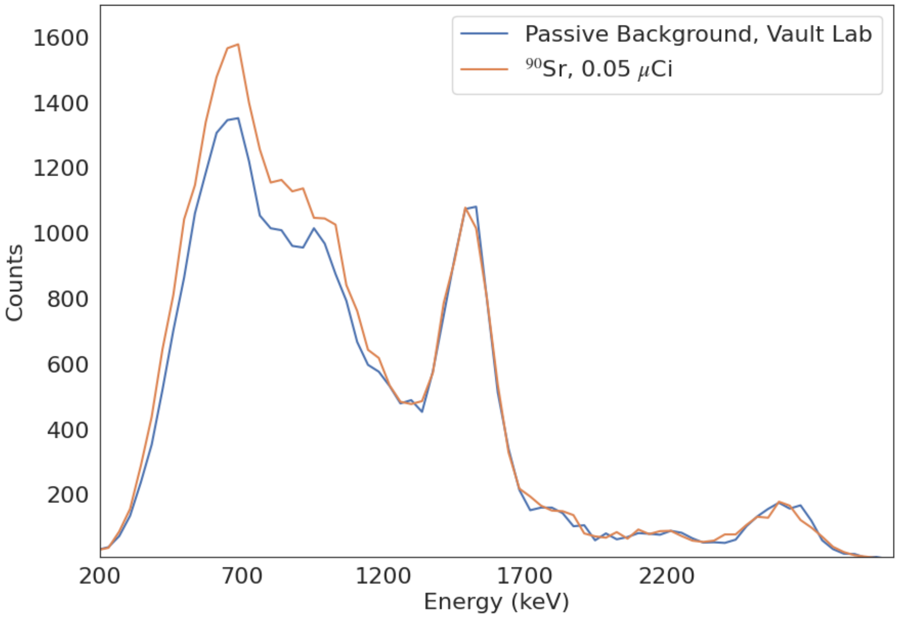

Figure B-5: Vault Lab natural background (prior to D-T use for the day) and a 0.05 μCi ^{90}Sr source, located directly against the front face of the detector. The additional counts in the source spectrum are commensurate with a bremsstrahlung spectrum of ^{90}Sr β-rays in mid-Z elements. Acquired with a 3" BGO detector, 5 minutes in the Vault Lab.

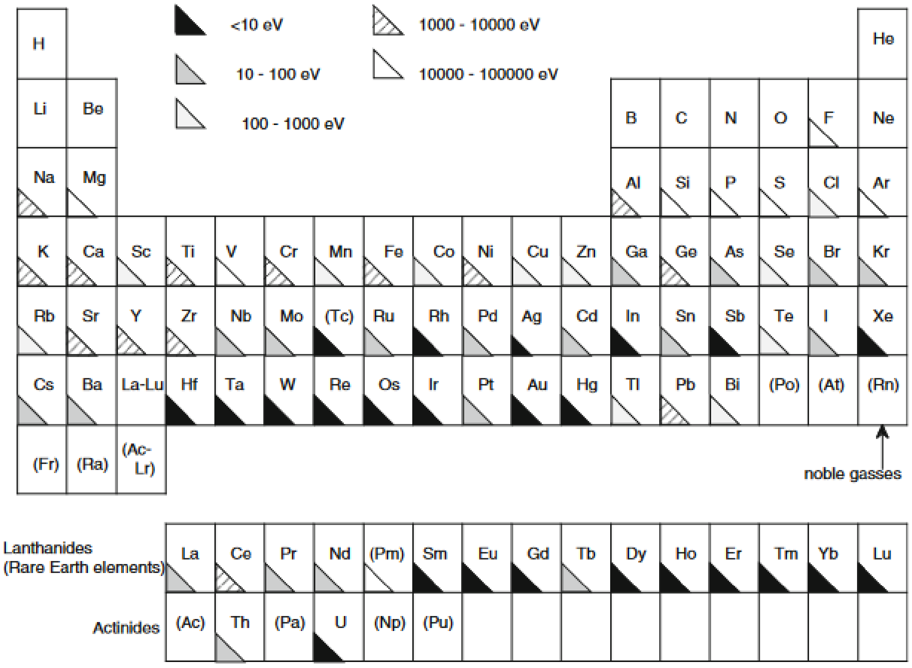

Figure B-6: Periodic table with elements shaded according to lowest energy resonances suitable for NRCA. In this portable system, resonances at energies 1-100 eV are resolvable.

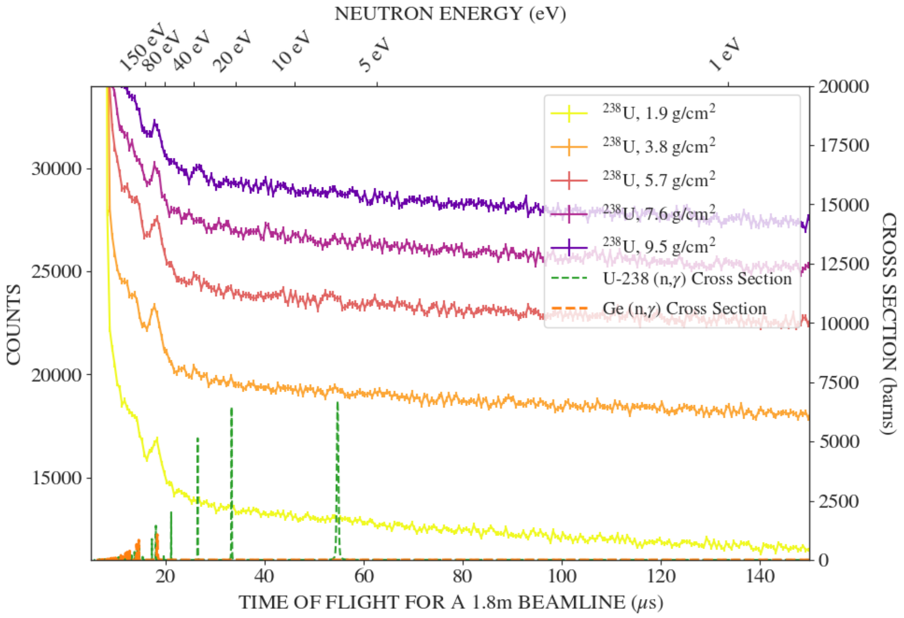

Figure B-7: TOF spectra from increasing areal densities of depleted uranium metal sheets, each approximately 5x5 cm. 20 min runs in the Vault Lab with the 3" BGO detector.

Figure B-8: Photograph of the D-T Generator equipment and cables inside a wheeled protective case. Foam packing has been removed for visibility. There is sufficient room for the D-T tube itself, however this was transported in a separate wheeled case by EHS personnel during field experiments.

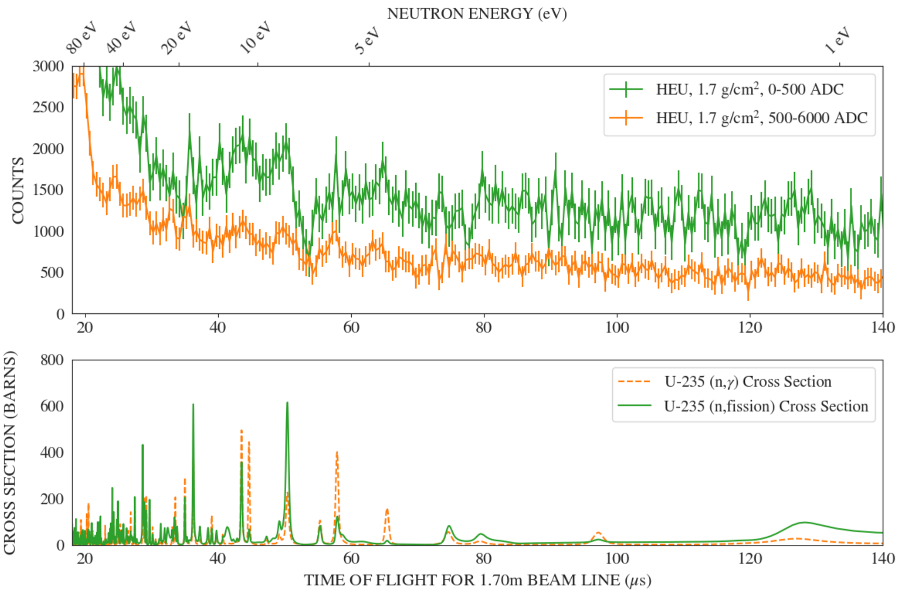

Figure B-9: TOF histograms of the same experimental run using 1.7 g/cm^2 of highly enriched uranium. The green trace shows all counts depositing less than 1 MeV and the orange trace shows all counts above 1 MeV. This analysis method can be used to determine the importance of fission-associated β-rays in generating an NRCA signal.

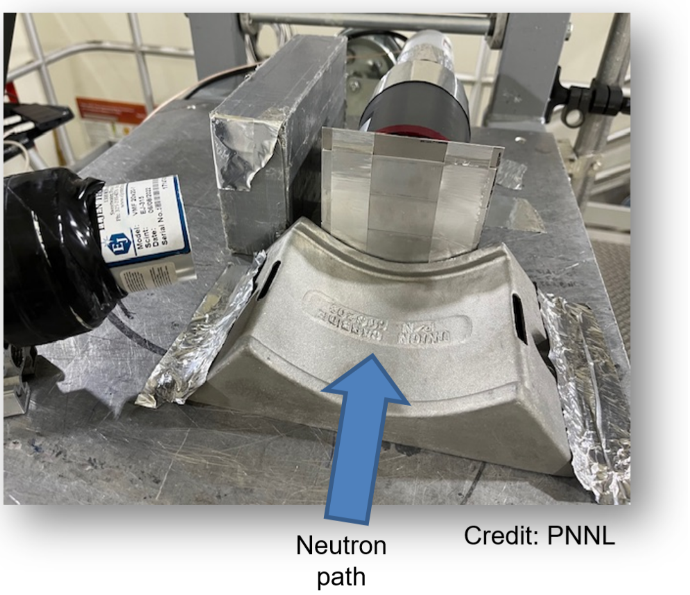

Credit: PNNL

Figure B-10: Photograph of the setup for experiments using high-assay, low-enriched uranium (HALEU) at the LSF.

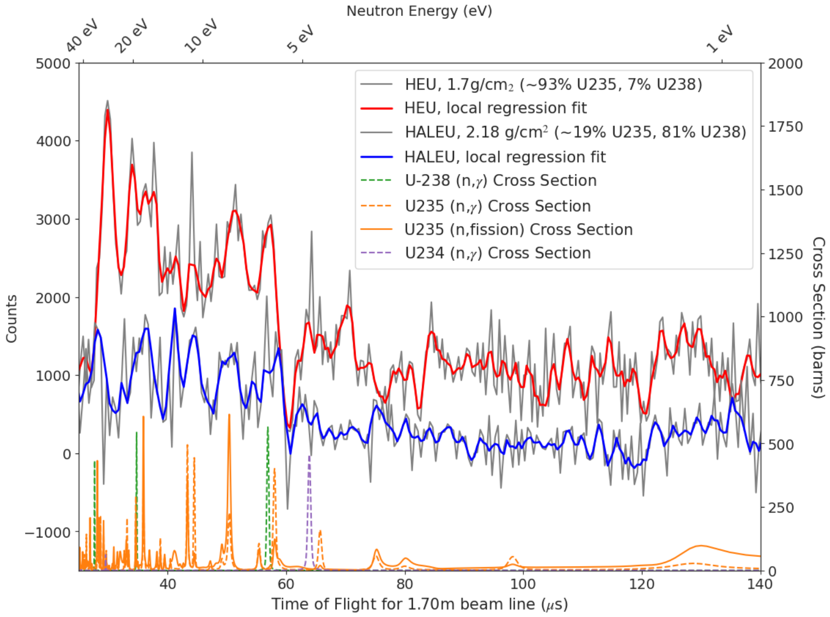

Figure B-11: TOF spectra for high enriched uranium and HAELU reactor fuel blend. Resonances are plotted below for reference. Acquired with the 3" BGO detector at the PNNL LSF, 30 minutes each run.

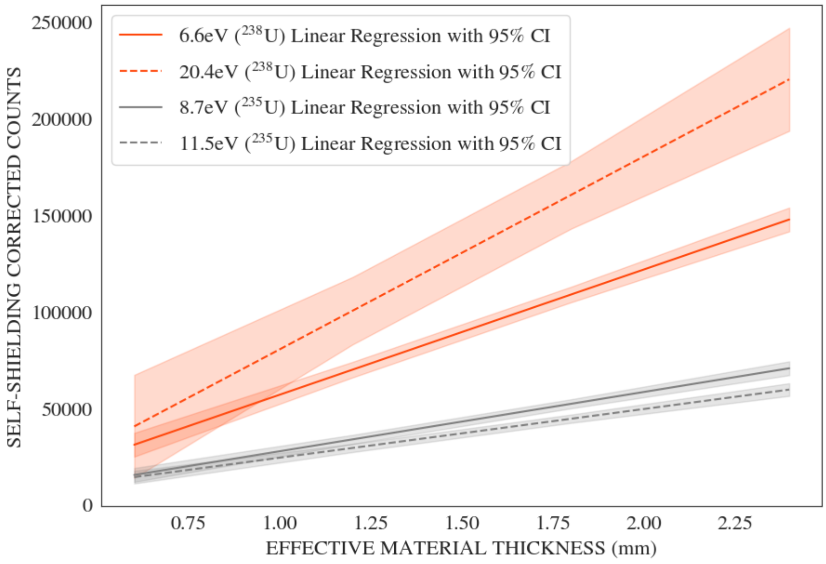

Figure B-12: Linear regression of raw count values for selected resonances of ^{238}U and ^{235}U, based on data from NRCA measurements. Shaded areas represent 95% confidence intervals.

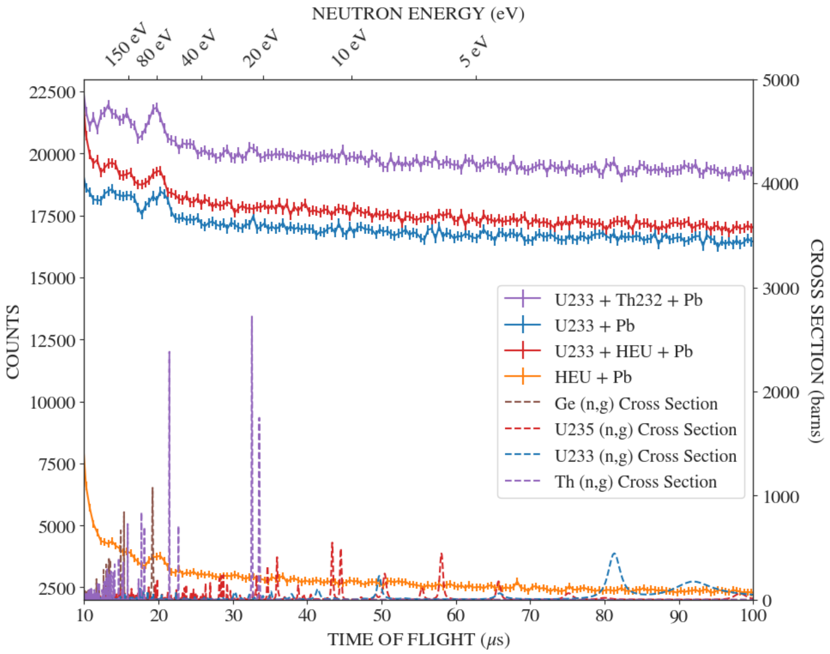

Figure B-13: Raw TOF histograms from thorium, HEU, and ^{233}U compositions. Acquired for 30 minutes each at the LSF using the 3" BGO.

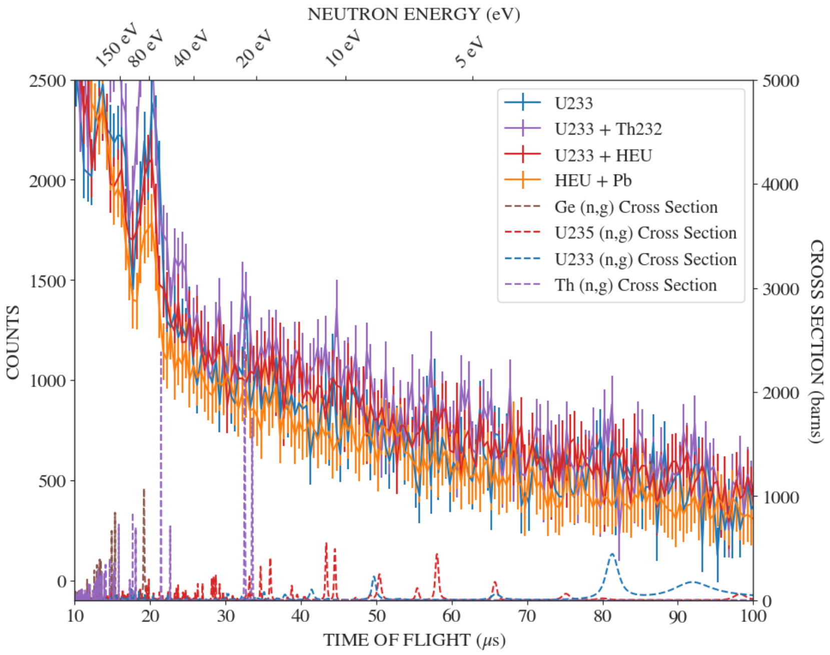

Figure B-14: Background subtracted TOF histograms from thorium, HEU, and ^{233}U compositions. Acquired for 30 minutes each at the LSF using the 3" BGO.

References

[1] “Operating permit issued for Chinese molten salt reactor : New Nuclear - World Nuclear News.” (), [Online]. Available: `https://www.world-nuclear-news.org/Articles/Operating-permit-issued-for-Chinese-molten-salt-re` (visited on 12/11/2023).

[2] “China’s 2 Megawatt Molten-salt Thorium Nuclear Reactor Has Start up Approval | NextBigFuture.com.” (Aug. 24, 2022), [Online]. Available: `https://www.nextbigfuture.com/2022/08/chinas-2-megawatt-molten-salt-thorium-nuclear-reactor-has-start-up-approval.html` (visited on 08/08/2023).

[3] “China Thorium Molten Salt Experimental Reactor is Licensed for Operation | NextBigFuture.com.” (Jun. 15, 2023), [Online]. Available: `https://www.nextbigfuture.com/2023/06/china-thorium-molten-salt-experimental-reactor-is-licensed-for-operation.html` (visited on 12/11/2023).

[4] “Clean Core’s ANEEL fuel to begin pre-licensing review by Canadian regulator - Nuclear Engineering International.” (), [Online]. Available: `https://www.neimagazine.com/news/newsclean-cores-aneel-fuel-to-begin-pre-licensing-review-by-canadian-regulator-10602596` (visited on 12/11/2023).

[5] “Clean Core and Canadian Nuclear Laboratories Sign Strategic Partnership on Advanced Nuclear Fuel Development,” Canadian Nuclear Laboratories. (Apr. 12, 2023), [Online]. Available: `https://www.cnl.ca/clean-core-and-canadian-nuclear-laboratories-sign-strategic-partnership-on-advanced-nuclear-fuel-development/` (visited on 12/11/2023).

[6] S. Tuberville. “Text - S.4242 - 117th Congress (2021-2022): Thorium Energy Security Act of 2022.” (May 18, 2022), [Online]. Available: `https://www.congress.gov/bill/117th-congress/senate-bill/4242/text` (visited on 12/11/2023).

[7] M. B. Schaffer, "Abundant thorium as an alternative nuclear fuel: Important waste disposal and weapon proliferation advantages," *Energy Policy*, vol. 60, pp. 4–12, Sep. 1, 2013, ISSN: 0301-4215. DOI: `10.1016/j.enpol.2013.04.062`.

[8] S. Gangotra, R. B. Grover, and K. L. Ramakumar, "Analysis of measures to enhance safeguards, and proliferation resistance in thorium based fuel fabrication plants," *Progress in Nuclear Energy*, vol. 77, pp. 20–31, Nov. 1, 2014, ISSN: 0149-1970. DOI: `10.1016/j.pnucene.2014.06.012`.

[9] IAEA, "INFCIRC/153(Corrected) - The Structure and Content of Agreements Between the Agency and States Required in Connection with the Treaty on the Non-Proliferation of Nuclear Weapons," Jun. 1972.

[10] "Enhancing Capabilities for Nuclear Verification: Resource Mobilization Priorities," International Atomic Energy Agency, STR-399, Jan. 2022.

[11] L. Evans-Worrall, *Safeguards Technology Considerations and Research Needs for Thorium Fuel Cycles and Molten Salt Reactors*, National Academy of Sciences, Oct. 2021. [Online]. Available: `https://www.nationalacademies.org` (visited on 05/19/2023).

[12] D. Reilly, N. Ensslin, H. Smith Jr, and S. Kreiner, "Passive nondestructive assay of nuclear materials," Nuclear Regulatory Commission, Washington, DC (United States), 1991.

[13] E. P. Cippo, A. Borella, G. Gorini, *et al.*, "Imaging of cultural heritage objects using neutron resonances," *J. Anal. At. Spectrom.*, vol. 26, no. 5, pp. 992–999, 2011. DOI: `10.1039/C0JA00256A`.

[14] H. Harada, F. Kitatani, M. Koizumi, *et al.*, "Neutron Resonance Densitometry for Particle-like Debris of Melted Fuel," *Nuclear Data Sheets*, vol. 118, pp. 502–504, Apr. 1, 2014, ISSN: 0090-3752. DOI: `10.1016/j.nds.2014.04.118`.

[15] T. J. Dolan, "1 - Introduction," in *Molten Salt Reactors and Thorium Energy*, T. J. Dolan, Ed., Woodhead Publishing, Jan. 1, 2017, pp. 1–12, ISBN: 978-0-08-101126-3. DOI: `10.1016/B978-0-08-101126-3.00001-4`.

[16] S. F. Ashley, R. A. Fenner, W. J. Nuttall, and G. T. Parks, "Open cycle thorium–uranium-fueled nuclear energy systems," *Proceedings of the Institution of Civil Engineers. Energy*, vol. 166, no. 2, pp. 74–81, 2013, ISSN: 1751-4223. DOI: `10.1680/ener.13.00003`.

[17] V. Ashley, R. Ashworth, D. Coates, and J. Earp, “The accelerator-driven thorium reactor power station,” *Proceedings of the Institution of Civil Engineers. Energy*, vol. 164, no. 3, pp. 91–135, Aug. 2011. DOI: `10.1680/ener.2011.164.3.127`.

[18] Z. Dai, “17 - Thorium molten salt reactor nuclear energy system (TMSR),” in *Molten Salt Reactors and Thorium Energy*, T. J. Dolan, Ed., Woodhead Publishing, Jan. 1, 2017, pp. 531–540, ISBN: 978-0-08-101126-3. DOI: `10.1016/B978-0-08-101126-3.00017-8`.

[19] *IAEA Safeguards Glossary* (International Nuclear Verification Series 3 (Rev. 1)). Vienna: International Atomic Energy Agency, 2022, ISBN: 978-92-0-122122-3. [Online]. Available: `https://www.iaea.org/publications/15176/iaea-safeguards-glossary`.

[20] J. Kang and F. N. von Hippel, “U-232 and the proliferation-resistance of U-233 in spent fuel,” *Science & Global Security*, vol. 9, no. 1, pp. 1–32, 2001, ISSN: 0892-9882. DOI: `10.1080/08929880108426485`.

[21] W. B. Arthur, “Uranium-232 production in current design LWRS,” Oak Ridge Gaseous Diffusion Plant, TN (USA), 1977.

[22] S. F. Ashley, G. T. Parks, W. J. Nuttall, C. Boxall, and R. W. Grimes, “Thorium fuel has risks,” *Nature*, vol. 492, no. 7427, pp. 31–33, 7427 Dec. 2012, ISSN: 1476-4687. DOI: `10.1038/492031a`.

[23] R. Hargraves and R. Moir, “Liquid Fluoride Thorium Reactors,” *American Scientist*, vol. 98, no. 4, p. 304, 2010, ISSN: 0003-0996, 1545-2786. DOI: `10.1511/2010.85.304`.

[24] A. Rykhlevskii, A. Lindsay, and K. Huff, “Full-core analysis of thorium-fueled molten salt breeder reactor using the SERPENT 2 Monte Carlo code,” *Transactions of the American Nuclear Society*, 2017. [Online]. Available: `https://www.semanticscholar.org/paper/Full-core-analysis-of-thorium-fueled-molten-salt-2-Rykhlevskii-Lindsay/b9775d77ad3a77f9e226147eecc71180dcef8b06` (visited on 01/03/2024).

[25] L. G. Worrall, V. Henzl, A. Swift, *et al.*, “Safeguards Technology for Thorium Fuel Cycles: Research and Development Needs Assessment and Recommendations,” Oak Ridge National Lab.(ORNL), Oak Ridge, TN (United States), 2021.

[26] "Thorium - World Nuclear Association." (), [Online]. Available: `https://world-nuclear.org/information-library/current-and-future-generation/thorium.aspx` (visited on 12/21/2023).

[27] D. Wang, "Optimization of a seed and blanket thorium-uranium fuel cycle for pressurized water reactors," Thesis, Massachusetts Institute of Technology, 2003. [Online]. Available: `https://dspace.mit.edu/handle/1721.1/29956` (visited on 12/19/2023).

[28] I. A. E. Agency, "Status of Molten Salt Reactor Technology," International Atomic Energy Agency, Text, 2023, pp. 1–315. [Online]. Available: `https://www.iaea.org/publications/14998/status-of-molten-salt-reactor-technology` (visited on 12/16/2023).

[29] L. Jorgensen, "19 - ThorCon reactor," in *Molten Salt Reactors and Thorium Energy*, T. J. Dolan, Ed., Woodhead Publishing, Jan. 1, 2017, pp. 557–564, ISBN: 978-0-08-101126-3. DOI: `10.1016/B978-0-08-101126-3.00019-1`.

[30] A. Sowder, "Technology Assessment of a Molten Salt Reactor Design: The Liquid-Fluoride Thorium Reactor (LFTR)," EPRI, Technical Report 3002005460, Oct. 2015.

[31] R. Wigeland, T. Taiwo, H. Ludewig, *et al.*, "Nuclear Fuel Cycle Evaluation and Screening – Final Report," *Final Report*, 2014.

[32] K. K. Hogue, P. W. Gibbs, M. P. Dion, and W. P. Poore III, "Domestic Safeguards Material Control and Accountancy Considerations for Molten Salt Reactors," Oak Ridge National Laboratory (ORNL), Oak Ridge, TN (United States), ORNL/SPR-2020/1881, Feb. 1, 2021. DOI: `10.2172/1797666`.

[33] J. L. Kloosterman, "20 - Safety assessment of the molten salt fast reactor (SAMOFAR)," in *Molten Salt Reactors and Thorium Energy*, T. J. Dolan, Ed., Woodhead Publishing, Jan. 1, 2017, pp. 565–570, ISBN: 978-0-08-101126-3. DOI: `10.1016/B978-0-08-101126-3.00020-8`.

[34] O. Beneš and R. J. M. Konings, "4 - Thermodynamic Calculations of Molten-Salt Reactor Fuel Systems," in *Molten Salts Chemistry*, Elsevier Inc, 2013, pp. 49–78, ISBN: 978-0-12-398538-5. DOI: `10.1016/B978-0-12-398538-5.00004-4`.

[35] R. Yoshioka, M. Kinoshita, and I. Scott, “7 - Materials,” in *Molten Salt Reactors and Thorium Energy*, T. J. Dolan, Ed., Woodhead Publishing, Jan. 1, 2017, pp. 189–207, ISBN: 978-0-08-101126-3. DOI: `10.1016/B978-0-08-101126-3.00007-5`.

[36] A. Swift, K. Hogue, T. Folk, and J. Cooley, “Safeguards Technical Objectives for Thorium Molten Salt Reactor Fuel Cycles,”

[37] G. Kessler, *Proliferation-Proof Uranium/Plutonium and Thorium/Uranium Fuel Cycles: Safeguards and Non-Proliferation*. KIT Scientific Publishing, 2017, ISBN: 978-3-7315-0516-7. DOI: `10.5445/KSP/1000054131`.

[38] J. S. Herring, P. E. MacDonald, K. D. Weaver, and C. Kullberg, “Low cost, proliferation resistant, uranium–thorium dioxide fuels for light water reactors,” *Nuclear Engineering and Design*, vol. 203, no. 1, pp. 65–85, Jan. 1, 2001, ISSN: 0029-5493. DOI: `10.1016/S0029-5493(00)00297-1`.

[39] IAEA, “INPRO Collaborative Project: Proliferation Resistance and Safeguardability Assessment Tools (PROSA),” International Atomic Energy Agency, Text, 2021, pp. 1–106. [Online]. Available: `https://www.iaea.org/publications/14895/inpro-collaborative-project-proliferation-resistance-and-safeguardability-assessment-tools-prosa` (visited on 12/29/2023).

[40] R. Moir, “U232 Nonproliferation Features,” LLNL-TR–438648, 1124839, Jun. 25, 2010, LLNL-TR–438 648, 1 124 839. DOI: `10.2172/1124839`.

[41] C. Lloyd, B. Goddard, and R. Witherspoon, “The effects of U-232 on enrichment and material attractiveness over time,” *Nuclear Engineering and Design*, vol. 352, p. 110 175, Oct. 1, 2019, ISSN: 0029-5493. DOI: `10.1016/j.nucengdes.2019.110175`.

[42] “WISE Uranium Project,” Uranium Calculator. (), [Online]. Available: `https://www.wise-uranium.org/index.html` (visited on 12/28/2023).

[43] S. Grape and C. Hellesen, “10 - Nonproliferation and safeguards aspects of the MSR fuel cycle,” in *Molten Salt Reactors and Thorium Energy*, T. J. Dolan, Ed., Woodhead Publishing, Jan. 1, 2017, pp. 261–279, ISBN: 978-0-08-101126-3. DOI: `10.1016/B978-0-08-101126-3.00010-5`.

[44] *Plutonium Fuel: An Assessment*, OECD Nuclear Energy Agency, 1989.

[45] J. Doyle, *Nuclear Safeguards, Security and Nonproliferation: Achieving Security with Technology and Policy*. Elsevier, Apr. 8, 2011, 615 pp., ISBN: 978-0-08-088811-8.

[46] L. Avrami, H. Jackson, and M. Kirshenbaum, "Radiation-Induced Changes in Explosive Materials," US Army, Picatinny Aresenal, Technical Report 4602, Nov. 1973. [Online]. Available: `https://royalsocietypublishing.org/doi/10.1098/rspa.1958.0124` (visited on 12/30/2023).

[47] A. M. Bhagwat, K. V. Kamath, K. N. Kutty, *et al.*, "Radiological Safety Experience in the Fabrication of Alloy Plate Fuels Bearing 233U/Pu," *Nuclear Technology*, vol. 103, no. 2, pp. 246–256, Aug. 1, 1993, ISSN: 0029-5450. DOI: `10.13182/NT93-A34846`.

[48] J. R. Engel, H. F. Bauman, J. F. Dearing, W. R. Grimes, H. E. McCoy, and W. A. Rhoades, "Conceptual design characteristics of a denatured molten-salt reactor with once-through fueling," Oak Ridge National Lab. (ORNL), Oak Ridge, TN (United States), ORNL/TM-7207, Jul. 1, 1980. DOI: `10.2172/5352526`.

[49] "Status Report- ThorCon," Martingale, Inc., Jul. 19, 2016, p. 26. [Online]. Available: `https://aris.iaea.org/PDF/ARISThorCon9.pdf` (visited on 01/04/2024).

[50] D. E. Serfontein and E. J. Mulder, "Thorium-based fuel cycles: Reassessment of fuel economics and proliferation risk," *Nuclear Engineering and Design*, SI : HTR 2012, vol. 271, pp. 106–113, May 1, 2014, ISSN: 0029-5493. DOI: `10.1016/j.nucengdes.2013.11.018`.

[51] A. B. Lovins, "Thorium cycles and proliferation," *Bull. At. Sci.; (United States)*, vol. 35:2, Feb. 1, 1979. DOI: `10.1080/00963402.1979.11458583`.

[52] A. Ahmad, E. B. McClamrock, and A. Glaser, "Neutronics calculations for denatured molten salt reactors: Assessing resource requirements and proliferation-risk attributes," *Annals of Nuclear Energy*, vol. 75, pp. 261–267, Jan. 1, 2015, ISSN: 0306-4549. DOI: `10.1016/j.anucene.2014.08.014`.

[53] C. G. Bathke, B. B. Ebbinghaus, B. A. Collins, *et al.*, "The Attractiveness of Materials in Advanced Nuclear Fuel Cycles for Various Proliferation and Theft Scenarios," *Nuclear Technology*, Jul. 1, 2012. DOI: `10.13182/NT10-203`.

[54] G. Flanagan, "Presentation on MSR Reactor Technology: Module 8: Fuel Cycle and Safeguards," presented at the NRC: Package ML17331B100 -Overview of Molten Salt Reactor Technology Training Materials (Washington DC), Nov. 7, 2017. [Online]. Available: `https://www.nrc.gov/docs/ML1733/ML17331B100.html` (visited on 12/29/2023).

[55] T. Gozani, “Active nondestructive assay of nuclear materials: Principles and applications,” Science Applications, Inc., Palo Alto, CA (USA); Mound Plant (MOUND), Miamisburg, OH (United States), NUREG/CR-0602; SAI-MLM-2585, Jan. 1, 1981. DOI: `10.2172/6215952`.

[56] M. Zendel, “IAEA Safeguards Equipment,” Workshop, presented at the JAEA-IAEA Workshop on Advanced Safeguards (Tokai-mura, Ibaraki, Japan), Nov. 13, 2007. [Online]. Available: `https://www-pub.iaea.org/mtcd/meetings/PDFplus/2007/cn1073/Presentations/4A.4%20Pres_%20Zendel%20-%20IAEA%20Safeguards%20Equipment.pdf`.

[57] L. G. Worrall, A. Worrall, G. F. Flanagan, *et al.*, “Safeguards Considerations for Thorium Fuel Cycles,” *Nuclear Technology*, vol. 194, no. 2, pp. 281–293, 2016. DOI: `10.13182/NT15-103`.

[58] K. Hogue, “Introduction to Safeguards by Design,” presented at the Global Security Programs & Strategic Partnerships (Y-12 National Security Complex). [Online]. Available: `https://www.osti.gov/servlets/purl/1478634`.

[59] D. N. Kovacic, A. Worrall, L. G. Worrall, *et al.*, “Safeguards Challenges for Molten Salt Reactors,” Aug. 2018. [Online]. Available: `https://www.osti.gov/biblio/1474868`.

[60] L. M. Scott, M. P. Dion, K. K. Hogue, S. E. O’Brien, and G. T. Westphal, “Infrastructure and Testing Needs for Molten Salt Reactor Safeguards,” United States, Mar. 2021. DOI: `10.2172/1782030`.

[61] “Thorium Fuel Cycle - Potential Benefits and Challenges,” International Atomic Energy Agency, Text, 2005, pp. 1–112. [Online]. Available: `https://www.iaea.org/publications/7192/thorium-fuel-cycle-potential-benefits-and-challenges` (visited on 01/08/2024).

[62] *International Safeguards in the Design of Nuclear Reactors*. International Atomic Energy Agency, 2014, 50 pp., ISBN: 978-92-0-106514-8. Google Books: `PxbToQEACAAJ`.

[63] “Code of Federal Regulations: Part 74—MATERIAL CONTROL AND ACCOUNTING OF SPECIAL NUCLEAR MATERIAL,” NRC Web. (), [Online]. Available: `https://www.nrc.gov/reading-rm/doc-collections/cfr/part074/full-text.html` (visited on 01/09/2024).

[64] V. Yu. Blandinskiy, E. A. Bobrov, O. V. Davidenko, T. Yu. Karpushkin, and S. V. Tsybulskiy, “Light Water Reactors with Thorium–Uranium Heterogeneous Fuel in a Nuclear Energy System,” *Physics of Atomic Nuclei*, vol. 85, no. 8, pp. 1335–1341, Dec. 1, 2022, ISSN: 1562-692X. DOI: `10.1134/S1063778822080051`.

[65] D. N. Kovacic, P. W. Gibbs, and L. M. Scott, “Model MC&A for Pebble Bed Reactors (Technical Direction No. 5 Task 2.6 Letter Report),” Oak Ridge National Laboratory (ORNL), Oak Ridge, TN (United States), ORNL/SPR-2019/1329, Mar. 1, 2020. DOI: `10.2172/1606926`.

[66] M. L. Lockhart, H. R. Trellue, V. Henzl, *et al.*, “Advanced Neutron Nondestructive Assay Methods for 233U Mass Quantification in Emerging Thorium Fuel Cycles,” Los Alamos National Laboratory (LANL), Los Alamos, NM (United States), LA-UR-23-32874, Nov. 13, 2023. [Online]. Available: `https://www.osti.gov/biblio/2208780` (visited on 01/06/2024).

[67] O. Searfus, P. Marleau, E. Uribe, H. Reedy, and I. Jovanovic, “Passive and active neutron signatures of U-233 for nondestructive assay,” *Physical Review Applied*, vol. 20, no. 6, p. 064 038, Dec. 21, 2023. DOI: `10.1103/PhysRevApplied.20.064038`.

[68] P. Mortreau and R. Berndt, “Determination of the uranium enrichment with the NaIGEM code,” *Nuclear Instruments and Methods in Physics Research Section A: Accelerators, Spectrometers, Detectors and Associated Equipment*, vol. 530, no. 3, pp. 559–567, Sep. 11, 2004, ISSN: 0168-9002. DOI: `10.1016/j.nima.2004.04.229`.

[69] S. Gangotra, R. B. Grover, and K. L. Ramakumar, “Comparison for thorium fuel cycle facilities of two different capacities for implementation of safeguards,” *Nuclear Engineering and Design*, vol. 262, pp. 535–543, Sep. 1, 2013, ISSN: 0029-5493. DOI: `10.1016/j.nucengdes.2013.04.038`.

[70] B. Goddard, S. Croft, A. Lousteau, and P. Peerani, “Evaluation of Am–Li neutron spectra data for active well type neutron multiplicity measurements of uranium,” *Nuclear Instruments and Methods in Physics Research Section A: Accelerators, Spectrometers, Detectors and Associated Equipment*, vol. 830, pp. 256–264, Sep. 11, 2016, ISSN: 0168-9002. DOI: `10.1016/j.nima.2016.05.100`.

[71] K. A. Jordan and T. Gozani, “Pulsed neutron differential die away analysis for detection of nuclear materials,” *Nuclear Instruments and Methods in Physics Research Section B: Beam Interactions with Materials and Atoms*,

vol. 261, no. 1-2, pp. 365–368, Aug. 2007, ISSN: 0168-583X. DOI: `10.1016/J.NIMB.2007.04.294`.

[72] M. Delarue, E. Simon, B. Pérot, *et al.*, “New measurements of cumulative photofission yields of 239Pu, 235U and 238U with a 17.5 MeV Bremsstrahlung photon beam and progress toward actinide differentiation,” *Nuclear Instruments and Methods in Physics Research Section A: Accelerators, Spectrometers, Detectors and Associated Equipment*, vol. 1040, p. 167 259, Oct. 1, 2022, ISSN: 0168-9002. DOI: `10.1016/j.nima.2022.167259`.

[73] M. Chadwick, M. Herman, P. Obložinský, *et al.*, “ENDF/B-VII.1 Nuclear Data for Science and Technology: Cross Sections, Covariances, Fission Product Yields and Decay Data,” *Nuclear Data Sheets*, vol. 112, no. 12, pp. 2887–2996, Dec. 2011, ISSN: 00903752. DOI: `10.1016/j.nds.2011.11.002`.

[74] E. A. Klein, F. Naqvi, J. E. Bickus, H. Y. Lee, A. Danagoulian, and R. J. Goldston, “Neutron-Resonance Transmission Analysis with a Compact Deuterium-Tritium Neutron Generator,” *Physical Review Applied*, vol. 15, no. 5, p. 054 026, May 13, 2021, ISSN: 2331-7019. DOI: `10.1103/PhysRevApplied.15.054026`.

[75] E. A. Klein, “Neutron Resonance Transmission Analysis of Nuclear Material Using a Portable D-T Neutron Generator,” Thesis, Massachusetts Institute of Technology, Sep. 2023. [Online]. Available: `https://dspace.mit.edu/handle/1721.1/152884` (visited on 01/11/2024).

[76] N. Kardjilov and G. Festa, Eds., *Neutron Methods for Archaeology and Cultural Heritage* (Neutron Scattering Applications and Techniques). Cham: Springer International Publishing, 2017. DOI: `10.1007/978-3-319-33163-8`.

[77] B. S. McDonald, A. Danagoulian, A. J. Gilbert, *et al.*, “Neutron resonance transmission analysis prototype system for thorium fuel cycle safeguards,” *Nuclear Instruments and Methods in Physics Research Section A: Accelerators, Spectrometers, Detectors and Associated Equipment*, vol. 1062, p. 169 148, May 1, 2024, ISSN: 0168-9002. DOI: `10.1016/j.nima.2024.169148`.

[78] F. Gunsing, *Neutron Resonance Spectroscopy*, Mémoire d’Habilitation à Diriger des Recherches présenté à l’Université Paris 7, Jun. 1, 2005. [Online]. Available: `https://inis.iaea.org/collection/NCLCollectionStore/_Public/39/107/39107575.pdf`.

[79] H. Postma and P. Schillebeeckx, “Neutron Resonance Capture and Transmission Analysis,” *Encyclopedia of Analytical Chemistry*, 2009. DOI: `10.1002/9780470027318.a9070`.

[80] E. P. Wigner and L. Eisenbud, “Higher Angular Momenta and Long Range Interaction in Resonance Reactions,” *Physical Review*, vol. 72, no. 1, pp. 29–41, Jul. 1, 1947. DOI: `10.1103/PhysRev.72.29`.

[81] I. J. Thompson, “Introduction to R-matrix Theory,” in *Conference Proceedings*, Santa Fe, NM: US Department of Energy, Jul. 1, 2016.

[82] J. E. Lynn, *The Theory of Neutron Resonance Reactions*. Clarendon Press, 1968.

[83] H. Postma and P. Schillebeeckx, “Neutron Resonance Analysis,” in *Neutron Methods for Archaeology and Cultural Heritage*, N. Kardjilov and G. Festa, Eds., Cham: Springer International Publishing, 2017, pp. 235–283, ISBN: 978-3-319-33163-8. DOI: `10.1007/978-3-319-33163-8_12`.

[84] M. R. Bhat, Ed., *Multi-Level Effects In Reactor Calculations and the Probability Table Method*. Brookhaven National Laboratory: National Neutron Cross Section Center, Apr. 1973.

[85] A. Trkov, M. Herman, and D. A. Brown, Eds., *ENDF-6 Formats Manual*, 215th ed. Brookhaven National Laboratory: National Nuclear Data Center, Feb. 1, 2018.

[86] G. L. Molnár, Ed., *Handbook of Prompt Gamma Activation Analysis: With Neutron Beams*. Boston, MA: Springer US, 2004. DOI: `10.1007/978-0-387-23359-8`.

[87] *Evaluated Nuclear Data File*, version B-V.II.1, National Nuclear Data Center, Dec. 2011. [Online]. Available: `nndc.bnl.gov`.

[88] S. Wang, M. Lubert, Y. Danon, *et al.*, “The RPI multiplicity detector response to gamma-ray cascades following neutron capture in and,” *Nuclear Instruments and Methods in Physics Research Section A: Accelerators, Spectrometers, Detectors and Associated Equipment*, vol. 513, no. 3, pp. 585–595, Nov. 2003, ISSN: 01689002. DOI: `10.1016/S0168-9002(03)01941-7`.

[89] D. Price, R. Chrien, O. Wasson, *et al.*, “Neutron capture in 238U,” *Nuclear Physics A*, vol. 121, no. 3, pp. 630–654, Dec. 1968, ISSN: 03759474. DOI: `10.1016/0375-9474(68)90113-9`.

[90] Y. Nauchi, J.-i. Hori, K. Terada, and T. Sano, "Gamma-Ray Spectrum Measurement from Capture Reactions of Uranium-238 for Thermal and Resonance Energy Neutrons," *EPJ Web of Conferences*, vol. 284, p. 08 010, 2023, ISSN: 2100-014X. DOI: `10.1051/epjconf/202328408010`.

[91] J L Ullmann, Toshihiko Kawano, Todd Bredeweg, *et al.*, "Cross section and gamma-ray spectra for U238(n,g) measured with the DANCE detector array at the Los Alamos Neutron Science Center," *Physical review. C, Nuclear physics*, vol. 89, 2014, ISSN: 0556-2813. DOI: `10.1103/physrevc.89.034603`.

[92] K. Hagiwara, T. Yano, T. Tanaka, *et al.* "Gamma Ray Spectrum from Thermal Neutron Capture on Gadolinium-157." arXiv: `1809.02664 [hep-ex, physics:nucl-ex, physics:physics]`. (Sep. 10, 2018), [Online]. Available: `http://arxiv.org/abs/1809.02664` (visited on 01/25/2024), pre-published.

[93] M. Guttormsen, L. Bernstein, A. Görgen, *et al.*, "Scissors resonance in the quasi-continuum of Th, Pa and U isotopes," *Physical Review C*, vol. 89, Oct. 26, 2013. DOI: `10.1103/PhysRevC.89.014302`.

[94] K. Furutaka, H. Harada, and S. Raman, "Prompt Gamma Rays Emitted in Thermal-neutron Capture Reaction by 99Tc and Its Reaction Cross Section," *Journal of Nuclear Science and Technology*, vol. 41, no. 11, pp. 1033–1046, Nov. 1, 2004, ISSN: 0022-3131. DOI: `10.1080/18811248.2004.9726328`.

[95] C. Sheu, J. Kelley, and J. Purcell, "ENSDF - O-16," Aug. 5, 2021.

[96] E. Browne and J. Tuli, "U-238 Nuclear Data Sheet 122, 293," 2014.

[97] B. Singh, J. Tuli, and E. Browne, "Th-232 Nuclear Data Sheet 170, 499," 2020.

[98] C. Coceva, "Radiative transitions from neutron capture in53Cr resonances," *Il Nuovo Cimento A*, vol. 107, no. 1, pp. 85–116, Jan. 1994, ISSN: 0369-3546, 1826-9869. DOI: `10.1007/BF02813075`.

[99] T. Rosener, "U-238 Neutron Capture Gamma Cascade Generation and Transport Simulation for Capture Tank Response," Rensselaer Polytechnic Institute, May 1992.

[100] J. A. Ryan, "Measuring the energies and multiplicities of prompt gamma-ray emissions from neutron-induced fission of U-235 using the STEFF spectrometer," CERN Thesis 2017-354, University of Manchester, 2017.

[101] S. F. Parker, "Inelastic Neutron Scattering, Instrumentation*," in *Encyclopedia of Spectroscopy and Spectrometry (Second Edition)*, J. C. Lindon, Ed., Oxford: Academic Press, Jan. 1, 2010, pp. 1035–1044, ISBN: 978-0-12-374413-5. DOI: `10.1016/B978-0-12-374413-5.00173-1`.

[102] E. Amaldi, O. D'Agostino, E. Fermi, B. Pontecorvo, F. Rasetti, and E. Segrè, "Artificial Radioactivity Produced by Neutron Bombardment. II," *Proceedings of the Royal Society of London. Series A, Mathematical and Physical Sciences*, vol. 149, no. 868, pp. 522–558, 1935, ISSN: 0080-4630. JSTOR: `96379`. [Online]. Available: `https://www.jstor.org/stable/96379` (visited on 01/28/2024).

[103] G. Hevesy and H. Levi, "Action of Slow Neutrons on Rare Earth Elements," *Nature (London)*, vol. 137, no. 3457, pp. 185–185, 1936. DOI: `10.1038/137185a0`.

[104] E. T. Booth, J. R. Dunning, A. V. Grosse, and A. O. Nier, "Neutron Capture by Uranium (238)," *Physical Review*, vol. 58, no. 5, pp. 475–476, Sep. 1, 1940. DOI: `10.1103/PhysRev.58.475.2`.

[105] H. L. Anderson, "Resonance Capture of Neutrons by Uranium," *Phys. Rev.*, vol. 80, no. 4, pp. 499–506, Nov. 1950. DOI: `10.1103/PhysRev.80.499`.

[106] V. P. Guinn and C. D. Wagner, "Instrumental Neutron Activation Analysis," *Analytical Chemistry (U.S.) Formerly Ind. Eng. Chem., Anal. Ed*, vol. 32, no. 3, pp. 317–323, 1960. DOI: `10.1021/ac60159a005`.

[107] L. Hamidatou, H. Slamene, T. Akhal, *et al.*, "Concepts, Instrumentation and Techniques of Neutron Activation Analysis," in *Imaging and Radioanalytical Techniques in Interdisciplinary Research - Fundamentals and Cutting Edge Applications*, IntechOpen, Mar. 13, 2013, ISBN: 978-953-51-1033-0. [Online]. Available: `https://www.intechopen.com/chapters/43467`.

[108] S. D. Moody. "Neutron Activation Analysis | The McClellan Nuclear Research Center." (May 10, 2017), [Online]. Available: `https://mnrc.ucdavis.edu/neutron-activation-analysis`.

[109] D. Glasgow, "Delayed neutron activation analysis for safeguards," *Journal of Radioanalytical and Nuclear Chemistry*, vol. 276, no. 1, pp. 207–211, 2008.

[110] T. Congedo, "Treatability Study Using Prompt Gamma Neutron Activation Analysis: Phase 1," Westinghouse Science and Technology Center for the U.S. Depatment of Energy, Pittsburg, PA, Topical Report DE-AC21-93MC30177, Jun. 1995.

[111] M. Litz, C. Waits, and J. Mullins, "Neutron-Activated Gamma-Emission: Technology Review:" Defense Technical Information Center, Fort Belvoir, VA, Jan. 1, 2012. DOI: `10.21236/ADA554870`.

[112] G. Vourvopoulos, "Pulsed fast/thermal neutron analysis: A technique for explosives detection," *Talanta*, vol. 54, no. 3, pp. 459–468, May 10, 2001, ISSN: 00399140. DOI: `10.1016/S0039-9140(00)00544-0`.

[113] D. Hei, W. Jia, C. Cheng, *et al.*, "Design of an inelastic neutron scattering system based on DT neutron generator for metallic materials analysis," *Journal of radioanalytical and nuclear chemistry*, vol. 329, no. 1, pp. 301–308, 2021, ISSN: 0236-5731. DOI: `10.1007/s10967-021-07755-3`.

[114] *PGNAA and PFTNA Technology*. Thermo Fisher Scientific, 2019, 26 pp. [Online]. Available: `https://www.thermofisher.com`.

[115] P. Schillebeeckx, A. Borella, F. Emiliani, *et al.*, "Neutron resonance spectroscopy for the characterization of materials and objects," *Journal of Instrumentation*, vol. 7, no. 03, p. C03009, Mar. 2012. DOI: `10.1088/1748-0221/7/03/C03009`.

[116] P. Schillebeeckx, B. Becker, H. Harada, and S. Kopecky, *Neutron Resonance Spectroscopy for the Characterisation of Materials and Objects*. Joint Research Centre, European Commission, 2014.

[117] H. Tsuchiya, H. Harada, M. Koizumi, *et al.*, "A Monte Carlo simulation to study a design of a gamma-ray detector for neutron resonance densitometry," *Nuclear Instruments and Methods in Physics Research Section A: Accelerators, Spectrometers, Detectors and Associated Equipment*, vol. 729, pp. 338–345, Nov. 2013, ISSN: 0168-9002. DOI: `10.1016/J.NIMA.2013.07.075`.

[118] H. G. Priesmeyer and U. Harz, "Isotopic Content Determination in Irradiated Fuel By Neutron Transmission Analysis.," *Atomkernenergie*, vol. 25, no. 2, pp. 109–113, 1975, ISSN: 00047147. [Online]. Available: `https://inis.iaea.org/search/search.aspx?orig_q=RN:6210353`.

[119] D. L. Chichester and J. W. Sterbentz, "Assessing the Feasibility of Using Neutron Resonance Transmission Analysis (NRTA) for Assaying Plutonium in Spent Fuel Assemblies," in *Journal of Nuclear Materials Management*, vol. 40, 2012, pp. 41–52. [Online]. Available: `https://inldigitallibrary.inl.gov/sites/sti/sti/5517268.pdf`.

[120] J. J. Hecla and A. Danagoulian, “Nuclear disarmament verification via resonant phenomena,” *Nature communications*, vol. 9, no. 1, pp. 1–7, 2018. [Online]. Available: `https://www.nature.com/articles/s41467-018-03680-4`.

[121] J. L. Tain, F. Gunsing, D. aniel-Cano, *et al.*, “Accuracy of the Pulse Height Weighting Technique for Capture Cross Section Measurements,” *Journal of Nuclear Science and Technology*, vol. 39, pp. 689–692, sup2 Aug. 2002, ISSN: 0022-3131, 1881-1248. DOI: `10.1080/00223131.2002.10875193`.

[122] J. Lee, J.-i. Hori, T. Sano, Y. Takahashi, H. Unesaki, and K. Nakajima, “Resonance Analysis for Neutron Capture Cross Sections of Th-232,” *Energy Procedia*, "Special Issue of for the Fifth International Symposium on Innovative Nuclear Energy Systems", vol. 131, pp. 306–311, Dec. 1, 2017, ISSN: 1876-6102. DOI: `10.1016/j.egypro.2017.09.435`.

[123] K. Kobayashi, S. Lee, S. Yamamoto, and T. Kawano, “Neutron Capture Cross-Section Measurement of ^{99} Tc by Linac Time-of-Flight Method and the Resonance Analysis,” *Nuclear Science and Engineering*, vol. 146, no. 2, pp. 209–220, Feb. 2004, ISSN: 0029-5639, 1943-748X. DOI: `10.13182/NSE04-A2404`.

[124] H. Postma, M. Blaauw, P. Bode, P. Mutti, F. Corvi, and P. Siegler, “Neutron-resonance capture analysis of materials,” *Journal of Radioanalytical and Nuclear Chemistry*, vol. 248, no. 1, pp. 115–120, Apr. 1, 2001, ISSN: 1588-2780. DOI: `10.1023/A:1010690428025`.

[125] P. Schillebeeckx, A. Borella, F. Emiliani, *et al.*, “Neutron resonance spectroscopy for the characterization of materials and objects,” in *Journal of Instrumentation*, 3, vol. 7, Springer, Berlin, Heidelberg, 2015, pp. 10–66. DOI: `10.1088/1748-0221/7/03/C03009`.

[126] L. Šalamon, B. Geslot, J. Heyse, *et al.*, “107Ag and 109Ag resonance parameters for neutron induced reactions below 1 keV,” *Nuclear Instruments and Methods in Physics Research Section B: Beam Interactions with Materials and Atoms*, vol. 446, pp. 19–28, May 2019, ISSN: 0168583X. DOI: `10.1016/j.nimb.2019.03.012`.

[127] P. A. C. Schut, W. Kockelmann, H. Postma, D. Visser, P. Schillebeeckx, and R. Wynants, “Neutron resonance capture and neutron diffraction analysis of Roman bronze water taps,” *Journal of Radioanalytical and Nuclear Chemistry*, vol. 278, no. 1, pp. 151–164, Oct. 1, 2008, ISSN: 1588-2780. DOI: `10.1007/s10967-007-7190-3`.

[128] C. Paradela, G. Alaerts, J. Heyse, *et al.*, “Neutron Resonance Analysis System Requirements,” JRC Technical Reports, EUR 28239 EN, 2016 Search PubMed, 2016. [Online]. Available: `https://publications.jrc.ec.europa.eu/repository/bitstream/JRC103484/jrc103484_report_nd_517_2016_v06%20%283%29.pdf`.

[129] J. Hoste, “Isotopic neutron sources for neutron activation analysis,” International Atomic Energy Agency, 1988. [Online]. Available: `https://inis.iaea.org/collection/NCLCollectionStore/_Public/19/088/19088950.pdf`.

[130] P. Levine, “Feasibility study of compact Neutron Resonance Transmission Analysis using a linac, a fusion-based neutron generator, and an isotopic source,” Ph.D. dissertation, Massachusetts Institute of Technology, Cambridge, MA USA, May 2022.

[131] D. L. Chichester, J. D. Simpson, and M. Lemchak, “Advanced compact accelerator neutron generator technology for active neutron interrogation field work,” *Journal of Radioanalytical and Nuclear Chemistry*, vol. 271, no. 3, pp. 629–637, Mar. 2007, ISSN: 1588-2780. DOI: `10.1007/s10967-007-0318-7`.

[132] International Atomic Energy Agency, *Neutron Generators for Analytical Purposes*. 2012, ISBN: 978-92-0-125110-7. [Online]. Available: `http://www-pub.iaea.org/MTCD/Publications/PDF/P1535_web.pdf`.

[133] D. L. Chichester and E. H. Seabury, “Active interrogation using electronic neutron generators for nuclear safeguards applications,” in *AIP Conference Proceedings*, vol. 1099, AIP, 2009, pp. 851–856. [Online]. Available: `https://aip.scitation.org/doi/pdf/10.1063/1.3120173`.

[134] C. Johnstone, S. V. Kutsaev, R. Lanza, S. Boucher, and R. Johnson, “High-current light-ion cyclotron for applications in nuclear security and radioisotope production,” *IEEE transactions on nuclear science*, 2021.

[135] A. Macchi, “A femtosecond neutron source,” *Applied Physics B*, vol. 82, no. 3, pp. 337–340, Mar. 2006, ISSN: 1432-0649. DOI: `10.1007/s00340-005-2092-y`.

[136] L. J. Perkins, B. G. Logan, M. D. Rosen, *et al.*, “The investigation of high intensity laser driven micro neutron sources for fusion materials research at high fluence,” *Nuclear Fusion*, vol. 40, no. 1, p. 1, Jan. 2000. DOI: `10.1088/0029-5515/40/1/301`.

[137] M. Zimmer, "Laser-Driven Neutron Sources-A Compact Approach to Non-Destructive Material Analysis," 2020.

[138] D. L. Chichester, "Production and applications of neutrons using particle accelerators," in *Industrial Accelerators and Their Applications*, World Scientific, 2012, pp. 243–305. [Online]. Available: `https://inldigitallibrary.inl.gov/sites/sti/sti/6302373.pdf`.

[139] A. Zografos, A. Hening, V. Joshkin, *et al.*, "Engineering Prototype for a Compact Medical Dielectric Wall Accelerator," *AIP Conference Proceedings*, vol. 1412, no. 1, pp. 71–78, Dec. 13, 2011, ISSN: 0094-243X. DOI: `10.1063/1.3665298`.

[140] R. W. Hamm, *Threshold Neutron Linac*, Feb. 2023.

[141] C. E. Moss, W. L. Myers, G. M. Sundby, D. L. Chichester, and J. P. Johnson, "Survey of Neutron Generators for Active Interrogation," Los Alamos National Laboratory, 2017. [Online]. Available: `https://permalink.lanl.gov/object/tr?what=info:lanl-repo/lareport/LA-UR-17-23592`.

[142] *P383 Data Sheet*, Thermo Fisher Scientific.

[143] T. F. Scientific, "P383 Neutron Generator Operation Manual," Manual P/N 120009-A2, 2021.

[144] V. Gushenets, A. Bugaev, E. Oks, A. Hershcovitch, and T. Kulevoy, "Molecular phosphorus ion source for semiconductor technology," *The Review of scientific instruments*, vol. 83, 02B311, Feb. 1, 2012. DOI: `10.1063/1.3672112`.

[145] "Periodic Operation Of Neutron Generators For Extended Operating Life," Thermo Fisher Scientific, Technical Bulletin 155, Aug. 10, 2020, p. 2.

[146] H. Groenewold and H. Groendijk, "Non-thermal neutron cascade," *Physica*, vol. 13, no. 1-3, pp. 141–152, Mar. 1947, ISSN: 0031-8914. DOI: `10.1016/0031-8914(47)90075-X`.

[147] C. Coceva, R. Simonini, and D. Olsen, "Calculation of the ORELA neutron moderator spectrum and resolution function," *Nuclear Instruments and Methods in Physics Research*, vol. 211, no. 2-3, pp. 459–467, Jun. 1983, ISSN: 0167-5087. DOI: `10.1016/0167-5087(83)90275-2`.

[148] S. Carmona and S. Yiftah, "The (n,2n) and (n,3n) Reactions of Lead, A Potential Neutron Amplifier for Fusion Blankets," *Nuclear Technology*, vol. 71, no. 1, pp. 289–295, Oct. 1, 1985, ISSN: 0029-5450. DOI: `10.13182/NT85-A33727`.

[149] A. Borella, G. Aerts, F. Gunsing, M. Moxon, P. Schillebeeckx, and R. Wynants, “The use of C6D6 detectors for neutron induced capture cross-section measurements in the resonance region,” *Nuclear Instruments and Methods in Physics Research Section A: Accelerators, Spectrometers, Detectors and Associated Equipment*, vol. 577, no. 3, pp. 626–640, Jul. 2007, ISSN: 01689002. DOI: `10.1016/j.nima.2007.03.034`.

[150] K. Wisshak, F. Voss, F. Käppeler, and G. Reffo, “Measurements of keV neutron capture cross sections with a 4Pi barium fluoride detector: Examples of Nb-93, Rh-103, and Ta-181,” *Physical Review C*, vol. 42, no. 4, pp. 1731–1750, Oct. 1, 1990. DOI: `10.1103/PhysRevC.42.1731`.

[151] S. Wang, M. Lubert, Y. Danon, *et al.*, “The RPI multiplicity detector response to gamma-ray cascades following neutron capture in and,” *Nuclear Instruments and Methods in Physics Research Section A: Accelerators, Spectrometers, Detectors and Associated Equipment*, vol. 513, no. 3, pp. 585–595, Nov. 2003, ISSN: 01689002. DOI: `10.1016/S0168-9002(03)01941-7`.

[152] R. Block, M. Bishop, D. Barry, *et al.*, “Neutron transmission and capture measurements and analysis of Dy from 0.01 to 550 eV,” *Progress in Nuclear Energy*, vol. 94, pp. 126–132, Jan. 2017, ISSN: 01491970. DOI: `10.1016/j.pnucene.2016.09.019`.

[153] G. V. Muradyan, Yu. V. Adamchuk, Yu. G. Shchepkin, and M. A. Voskanyan, “Multiplicity Spectrometer for Measuring Neutron Cross Sections,” *Nuclear Science and Engineering*, vol. 90, no. 1, pp. 60–74, May 1985, ISSN: 0029-5639, 1943-748X. DOI: `10.13182/NSE85-A17431`.

[154] R. Plag, M. Heil, F. Käppeler, P. Pavlopoulos, R. Reifarth, and K. Wisshak, “An optimized C6D6 detector for studies of resonance-dominated (n,g) cross-sections,” *Nuclear Instruments and Methods in Physics Research Section A: Accelerators, Spectrometers, Detectors and Associated Equipment*, vol. 496, no. 2-3, pp. 425–436, Jan. 2003, ISSN: 01689002. DOI: `10.1016/S0168-9002(02)01749-7`.

[155] L. Šalamon, B. Geslot, J. Heyse, *et al.*, “107Ag and 109Ag resonance parameters for neutron induced reactions below 1 keV,” *Nuclear Instruments and Methods in Physics Research Section B: Beam Interactions with Materials and Atoms*, vol. 446, pp. 19–28, May 2019, ISSN: 0168583X. DOI: `10.1016/j.nimb.2019.03.012`.

[156] European Commission. Joint Research Centre. Institute for Reference Materials and Measurements., *Neutron Resonance Spectroscopy for the Characterisation of Materials and Objects.* LU: Publications Office, 2014. [Online]. Available: `https://data.europa.eu/doi/10.2787/98278` (visited on 01/25/2024).

[157] S. T. Mazhen, P. V. Sedyshev, N. V. Simbirtseva, A. M. Yergashov, A. Yu. Dmitriev, and V. L. Ivchenkov, “Application of non-destructive neutron resonance capture analysis for investigation of women’s Old Believer cross dating back to the second half of the 17th century,” *Eurasian Journal of Physics and Functional Materials*, vol. 5, no. 4, pp. 181–187, Dec. 9, 2021, ISSN: 2616-8537, 2522-9869. DOI: `10.32523/ejpfm.2021050402`.

[158] M. Koizumi, F. Kitatani, H. Harada, *et al.*, “Proposal of neutron resonance densitometry for particle-like debris of melted fuel using NRTA and NRCA,”

[159] A. Borella, A. Moens, P. Schillebeeckx, *et al.*, “Determination of the 209Bi(n,g) capture cross section at a cold neutron beam,” *Journal of Radioanalytical and Nuclear Chemistry*, vol. 265, no. 2, pp. 267–271, Jul. 1, 2005, ISSN: 1588-2780. DOI: `10.1007/s10967-005-0819-1`.

[160] H. Tsuchiya, M. Koizumi, F. Kitatani, and H. Harada, “Performance of large volume LaBr3 scintillation detector equipped with specially-designed shield for neutron resonance capture analysis,” *Nuclear Instruments and Methods in Physics Research Section A: Accelerators, Spectrometers, Detectors and Associated Equipment*, vol. 932, pp. 16–26, Jul. 2019, ISSN: 0168-9002. DOI: `10.1016/J.NIMA.2019.04.048`.

[161] M. Krammer, “Scintillators: Detectors for Particle Physics,” Presentation (Institute of High Energy Physics, Vienna, Austria).

[162] H. Vincke, E. Gschwendtner, C. W. Fabjan, and T. Otto, “Response of a BGO detector to photon and neutron sources: Simulations and measurements,” *Nuclear Instruments and Methods in Physics Research Section A: Accelerators, Spectrometers, Detectors and Associated Equipment*, vol. 484, no. 1, pp. 102–110, May 21, 2002, ISSN: 0168-9002. DOI: `10.1016/S0168-9002(01)01966-0`.

[163] A. E. Evans, “Gamma-Ray Response of a 38-mm Bismuth Germanate Scintillator,” *IEEE Transactions on Nuclear Science*, vol. 27, no. 1, pp. 172–175, 1980, ISSN: 0018-9499. DOI: `10.1109/TNS.1980.4330822`.

[164] A. Brusegan, G. Noguere, and F. Gunsing, “The Resolution Function in Neutron Time-of-Flight Experiments,” *Journal of Nuclear Science and Technology*, vol. 39, pp. 685–688, 2002, ISSN: 00223131. DOI: `10.1080/00223131.2002.10875192`.

[165] C. Coceva, R. Simonini, and D. K. Olsen, “Calculation of the ORELA neutron moderator spectrum and resolution function,” *Nuclear Instruments and Methods in Physics Research*, vol. 211, no. 2, pp. 459–467, Jun. 15, 1983, ISSN: 0167-5087. DOI: `10.1016/0167-5087(83)90275-2`.

[166] A. Brusegan, G. Noguere, and F. Gunsing, “The Resolution Function in Neutron Time-of-Flight Experiments,” *Journal of Nuclear Science and Technology*, vol. 39, pp. 685–688, 2002. [Online]. Available: `https://www-tandfonline-com.libproxy.mit.edu/doi/abs/10.1080/00223131.2002.10875192` (visited on 03/15/2024).

[167] ORNL, *SAMMY 8.1.0: Code System for Multilevel R-Matrix Fits to Neutron and Charged-Particle Cross-Section Data Using Bayes'Equations.* Oak Ridge National Laboratory, Apr. 1984.

[168] W. E. Lamb, “Capture of Neutrons by Atoms in a Crystal,” *Physical Review*, vol. 55, no. 2, pp. 190–197, Jan. 15, 1939. DOI: `10.1103/PhysRev.55.190`.

[169] P. Schillebeeckx, B. Becker, Y. Danon, *et al.*, “Determination of Resonance Parameters and their Covariances from Neutron Induced Reaction Cross Section Data,” *Nuclear Data Sheets*, Special Issue on Nuclear Reaction Data, vol. 113, no. 12, pp. 3054–3100, Dec. 1, 2012, ISSN: 0090-3752. DOI: `10.1016/j.nds.2012.11.005`.

[170] P. E. Koehler, R. R. Winters, K. H. Guber, *et al.*, “High-resolution neutron capture and transmission measurements, and the stellar neutron-capture cross section of ${}^{88}\mathrm{Sr}$,” *Physical Review C*, vol. 62, no. 5, p. 055 803, Oct. 13, 2000. DOI: `10.1103/PhysRevC.62.055803`.

[171] V. E. Guiseppe, S. R. Elliott, N. E. Fields, and D. Hixon, “Fast-neutron activation of long-lived nuclides in natural Pb,” *Astroparticle Physics*, vol. 64, pp. 34–39, Apr. 1, 2015, ISSN: 0927-6505. DOI: `10.1016/j.astropartphys.2014.11.002`.

[172] J. Brückner, H. Wänke, and R. C. Reedy, “Neutron-induced gamma ray spectroscopy: Simulations for chemical mapping of planetary surfaces,” *Journal of Geophysical Research: Solid Earth*, vol. 92, no. B4, E603–E616, 1987, ISSN: 2156-2202. DOI: `10.1029/JB092iB04p0E603`.

[173] F. Ma, S. Kopecky, G. Alaerts, *et al.*, "Non-destructive analysis of samples with a complex geometry by NRTA," *J. Anal. At. Spectrom.*, vol. 35, no. 3, 2020. DOI: `10.1039/C9JA00342H`.

[174] H. Postma, M. Blaauw, P. Schillebeeckx, G. Lobo, R. B. Halbertsma, and A. J. Nijboer, "Non-destructive elemental analysis of copper-alloy artefacts with epithermal neutron-resonance capture," *Czechoslovak Journal of Physics Supplement*, vol. 53, A233–A240, Jan. 1, 2003. DOI: `10.1007/s10582-003-0030-y`.

[175] P. Wang, Y. Zhang, and Z. Xu, "Study on temperature dependence of BGO light yield," *Science China Physics, Mechanics & Astronomy*, vol. 57, Sep. 29, 2013. DOI: `10.1007/s11433-014-5548-4`.

[176] E. A. Klein, *ComPy: The CoMPASS Python Companion*, version v.1.0.4, Cambridge, MA: MIT, Dec. 6, 2022. [Online]. Available: `https://github.com/eaklein/compy`.

[177] D. A. Brown, M. B. Chadwick, R. Capote, *et al.*, "ENDF/B-VIII.0: The 8th Major Release of the Nuclear Reaction Data Library with CIELO-project Cross Sections, New Standards and Thermal Scattering Data," *Nuclear Data Sheets*, vol. 148, pp. 1–142, 2018, ISSN: 0090-3752. DOI: `10.1016/j.nds.2018.02.001`.

[178] M. C. Moxon, T. Ware, and C. Dean, *REFIT-2009: A Least-Square Fitting Program for Resonance Analysis of Neutron Transmission, Capture, Fission, and Scattering Data*, Apr. 2010.

[179] P. Schillebeeckx, A. Borella, J. C. Drohe, *et al.*, "Target requirements for neutron-induced cross-section measurements in the resonance region," *Nuclear Instruments and Methods in Physics Research Section A: Accelerators, Spectrometers, Detectors and Associated Equipment*, Target and Stripper Foil Technologies for High Intensity Beams, vol. 613, no. 3, pp. 378–385, Feb. 11, 2010, ISSN: 0168-9002. DOI: `10.1016/j.nima.2009.09.080`.

[180] J. G. Fantidis, G. E. Nicolaou, and N. F. Tsagas, "Optimization study of a transportable neutron radiography unit based on a compact neutron generator," *Nuclear Instruments and Methods in Physics Research Section A: Accelerators, Spectrometers, Detectors and Associated Equipment*, vol. 618, no. 1-3, pp. 331–335, 2010. [Online]. Available: `https://www.sciencedirect.com/science/article/pii/S0168900210003633`.

[181] H. P. Li, H. Q. Su, Y. S. Lv, *et al.*, “Design of a compact RFQ linac for the transportable neutron source,” *Nuclear Instruments and Methods in Physics Research Section A: Accelerators, Spectrometers, Detectors and Associated Equipment*, vol. 1042, p. 167 254, 2022.

[182] E. Braverman, A. Lebrun, V. Nizhnik, and F. Rorif, “In Situ Object Counting System (ISOCS) Technique: Cost-Effective Tool for NDA Verification in IAEA Safeguards,” International Atomic Energy Agency (IAEA), 2010, p. 8.

[183] T. Bily, O. Huml, and B. Belko, “Delayed neutron counting of uranium pins using moderated neutrons from portable DD neutron generator in high frequency mode,” *Applied Radiation and Isotopes*, vol. 191, p. 110 527, 2023, ISSN: 0969-8043. DOI: `10.1016/j.apradiso.2022.110527`.

[184] M. H. Rabir, A. F. Ismail, and M. S. Yahya, “Review of the microheterogeneous thoria-urania fuel for micro-sized high temperature reactors,” *International Journal of Energy Research*, vol. 45, no. 8, pp. 11 440–11 458, 2021, ISSN: 1099-114X. DOI: `10.1002/er.5923`.

[185] “The 2007 Recommendations of the International Commission on Radiological Protection,” Internation Commission on Radiological Protection, ICRP Publication 103, 2007.

[186] M. Hale, P. Tran, T. Rahon, and D. Quinn, “3D Radiation Exposure Modeling Tool for ALARA Planning: Kewaunee Pilot,” Electric Power Research Institute, 2011.

[187] D. L. Chichester and E. H. Seabury, “Using electronic neutron generators in active interrogation to detect shielded fissionable material,” in *2008 IEEE Nuclear Science Symposium Conference Record*, IEEE, 2008, pp. 3361–3367.

[188] D. L. Chichester and B. W. Blackburn, “Radiation fields from neutron generators shielded with different materials,” *Nuclear Instruments and Methods in Physics Research, Section B: Beam Interactions with Materials and Atoms*, vol. 261, pp. 845–849, 1-2 SPEC. ISS. 2007, ISSN: 0168583X. DOI: `10.1016/j.nimb.2007.04.222`.

[189] J. A. Mullens, D. H. Austin, and J. T. Mihalczo, “Active Interrogation Safety: DT Generator Dosimetry Measurements,” Oak Ridge National Lab. (ORNL), Oak Ridge, TN (United States), ORNL/LTR-2014/669, Feb. 1, 2015. DOI: `10.2172/1479813`.

[190] J. L. Warburton, "Spectroscopic methods of process monitoring for safeguards of used nuclear fuel separations," ProQuest Dissertations Publishing, 2011, ISBN: 9781267170736.

[191] S. Usuda, S. Sakurai, and K. Yasuda, "Phoswich detectors for simultaneous counting of -, (gamma)-rays and neutrons," *Nuclear Instruments and Methods in Physics Research Section A: Accelerators, Spectrometers, Detectors and Associated Equipment*, vol. 388, no. 1, pp. 193–198, Mar. 21, 1997, ISSN: 0168-9002. DOI: `10.1016/S0168-9002(97)00327-6`.

[192] J. Maslin, J. Henderson, and M. P. Taggart, "A phoswich for thermal-neutron and gamma-ray detection," *Nuclear Instruments and Methods in Physics Research Section A: Accelerators, Spectrometers, Detectors and Associated Equipment*, vol. 1058, p. 168 898, Jan. 1, 2024, ISSN: 0168-9002. DOI: `10.1016/j.nima.2023.168898`.

[193] J. Park, Y. Jeong, H. C. Lee, and D. Lee, "Whole core analysis of molten salt breeder reactor with online fuel reprocessing: Whole core analysis of MSBR with online fuel reprocessing," *International Journal of Energy Research*, n/a–n/a, Jul. 2015, ISSN: 0363907X. DOI: `10.1002/er.3371`.